INSTITUTO SUPERIOR TÉCNICO

UNIVERSIDADE TÉCNICA DE LISBOA

INSTITUTO SUPERIOR TÉCNICO

Measurement of the Gluon Polarisation Through High p_T Hadron Production in COMPASS

Luís Miguel Faria Pereira Lopes da Silva

Supervisor: Doctor Sérgio Eduardo de Campos Costa Ramos

Thesis approved in public session to obtain PhD Degree in

Physics

Jury final classification: Pass with Distinction

Jury

Chairperson: Chairman of the IST Scientific Board

Members of the Committee:

Doctor Alfredo Barbosa Henriques
Doctor Maria Paula Frazão Bordalo e Sá
Doctor Eva Maria Kabuß
Doctor Krzysztof Kurek
Doctor Sérgio Eduardo de Campos Costa Ramos
Doctor Marcin Stolarski

2011

UNIVERSIDADE TÉCNICA DE LISBOA
INSTITUTO SUPERIOR TÉCNICO

Measurement of the Gluon Polarisation Through High p_T Hadron Production in COMPASS

Luís Miguel Faria Pereira Lopes da Silva

Supervisor: Doctor Sérgio Eduardo de Campos Costa Ramos

Thesis approved in public session to obtain PhD Degree in
Physics
Jury final classification: Pass with Distinction

Jury

Chairperson: Chairman of the IST Scientific Board
Members of the Committee:

Doctor Alfredo Barbosa Henriques, Professor Catedrático do Instituto Superior Técnico, da Universidade Técnica de Lisboa

Doctor Maria Paula Frazão Bordalo e Sá, Professora Associada (com Agregação), do Instituto Superior Técnico, da Universidade Técnica de Lisboa

Doctor Eva Maria Kabuß, Professora Associada da Universidade Johannes Gutenberg Mainz, Alemanha

Doctor Krzysztof Kurek, Professor Associado da Universidade de Varsóvia, Polónia

Doctor Sérgio Eduardo de Campos Costa Ramos, Professor Auxiliar (com Agregação) do Instituto Superior Técnico, da Universidade Técnica de Lisboa

Doctor Marcin Stolarki, Investigadora do Laboratório de Instrumentação e Física Experimental de Partículas

Funding Institutions

FCT Fundação para a Ciência e a Tecnologia
MINISTÉRIO DA EDUCAÇÃO E CIÊNCIA

2011

No lugar dos palácios desertos e em ruinas à beira do mar,
Leiamos, sorrindo, os segredos das sinas
De quem sabe amar.
Qualquer que ele seja, o destino daqueles
Que o amor levou
Para a sombra, ou na luz se fez a sombra deles,
Qualquer fosse o voo.
Por certo eles foram mais que reais e felizes.

Fernando Pessoa
as Álvaro de Campos

To Jeronimo Pombo Lopes da Silva.

Acknowledgements

I would like to start by thanking my supervisor Prof. Doutor Sérgio Eduardo de Campos Costa Ramos for his support, guidance and for the fruitful discussions full of *parentheses* —as he uses to call them—, because sometimes most of the interesting issues are hidden there.

A special thanks to Prof. Doutora Paula Bordalo, for having given me the opportunity to join the COMPASS collaboration, her support and her high level of demand, which enhances the level of quality of my work.

Thanks also to my colleagues in the Lisbon group at LIP: Catarina Quintans and Helena Santos for their criticism and suggestions that most of the time allowed me to have a new view, which led me to overcome the problems. A special thanks to Marcin Stolarski for the fruitful discussions and for his patience to my questions. Thanks to Celso Franco, my dear office companion, for the nice company and also nice discussions on physics and many other things.

To my colleagues of the COMPASS collaboration, thank you, in particular to colleagues from the high p_T: to Konrad Kilmaszewski, for the nice discussions about the analytical method, to Krzysztof Kurek, for the insight in the theoretical and phenomenological aspects of the analysis, to Ewa Rondio and to Eva-Maria Kabuß, for their experience about the spin experiments previous to COMPASS, SMC, NMC and EMC.

Thank you to my family, my father and my mother who always supported me in all aspects; to my little daughter who tought my to see physics using a child lens, always eager to know.

A very special thanks to my wife (thank you! from the bottom of my heart!) for her kindness, patience, and for her support too.

Resumo

Uma das peças fundamentais para a atual compreensão da estrutura do spin do nucleão é a contribuição devida aos gluões: a chamada polarização do gluão. Esta quantidade pode ser determinada em dispersões inelásticas profundas (DIS) através do processo físico da fusão do fotão com o gluão (PGF). Dois métodos de análise podem ser usados: (i) identificação de eventos de charme aberto or (ii) a seleção de eventos com hadrões de alto momento transverso (high p_T). Os dados usados na presente tese foram tomados pela experiência COMPASS, na qual um feixe de muões naturalmente polarisado de 160 GeV colide num alvo fixo com nucleões polarisados. Os resultados da polarização do gluão usando hadrões de alto momento transverso são apresentados em três bins independentes de x_G em primeira ordem de Born. O método de análise desenvolvido é baseado no método de pesos usando um rede neuronal.

Palavras-chave: gluão, polarização, spin, nucleão, high pT, COMPASS.

Abstract

One of the missing keys in the present understanding of the spin structure of the nucleon is the contribution from the gluons: the so called gluon polarisation. This quantity can be determined in DIS through the Photon-Gluon Fusion (PGF) process, in which two analysis methods may be used: (i) identifying open charm events or (ii) selecting events with high p_T hadrons. The data used in the present work were collected by the COMPASS Experiment, where a naturally polarised muon beam of 160 GeV, impinging on a polarised nucleon fixed target, is used. The results for the gluon polarisation from high p_T are presented. The gluon polarisation result for high p_T hadrons is divided, for the first time, into three independent x_G bins at leading order (LO). A new weighted method based on a neural network approach is used.

Keywords: gluon, polarisation, spin, nucleon, high pT, COMPASS.

Contents

List of Tables

List of Figures

CHAPTER 1

INTRODUCTION

Deep inelastic scattering (DIS) of leptons on nucleons is an important tool to unveil the structure of the nucleon. The *electron-proton* (ep) DIS experiment at SLAC in the 60's showed us that the form factors exhibit an approximate scaling at high Q^2, as predicted by J. Bjorken; this discovery was celebrated in 1990 by awarding the Nobel Prize in Physics to the experimentalists J.I. Friedman, H.W. Kendal and R.E. Taylor. The observation of this scaling behaviour is an evidence of the point-like constituents of the nucleon, the partons, proposed by R.P. Feynman. Thus the quarks postulated by Gell-Mann and Zweig were proven real existence.

DIS of *polarised* leptons on *polarised* nucleons brought also insight into the *spin* structure of the nucleon. The first experiments using polarised ep scattering were made by the E80 and E130 Collaborations at SLAC. They measured significant spin-dependent asymmetries in DIS ep scattering cross section; their results were consistent with the Ellis-Jaffe sum rule [1]. Surprisingly, on 1987, the EMC experiment at CERN, with an extended kinematic range down to $x \simeq 0.01$, announced that, contradicting previous results and predictions, the measured quark contribution to nucleon spin is small (0.12 ± 0.17) [2] and this result has been confirmed by other experiments [3–8]. In 2007, the COMPASS collaboration measured this contribution with a remarkable precision using a NLO QCD fit with all world data available [9]: 230 points from different experiments (43 of them from COMPASS). This measurement of the quark contribution to the nucleon spin was found indeed smaller than the predicted by the Ellis-Jaffe sum rule and compatible with the EMC measurement with a better precision.

Since the quark contribution does not account for the total nucleon spin, other contributions need to be found to explain this "spin crisis". As nucleons are also made of gluons together with quarks, the most natural would be to include the gluon contribution to the nucleon spin; also it is natural to think that the orbital angular momentum of the partons could carry some missing spin. Based on this hypothesis, the nucleon spin can be heuristically written in ref. [10] as :

$$\frac{1}{2} = \frac{1}{2}\Delta\Sigma + \Delta G + L, \tag{1.1}$$

where $\Delta\Sigma$ is the quark contribution, ΔG is the gluon contribution and L is the contribution coming from orbital angular momentum from the partons (quarks and gluons).

The aim of this study is to estimate the gluon contribution using high transverse momentum (also known as *high* p_T) hadrons. The analysis is performed in two complementary kinematic regions: $Q^2 < 1\ (\mathrm{GeV}/c)^2$ (low Q^2 region) and $Q^2 > 1\ (\mathrm{GeV}/c)^2$ (high Q^2 region). The present work is mainly focused on the analysis for high Q^2. The analysis at low Q^2 region is completely described in [11].

In the last fourty years many developments about the structure of the nucleons and of the parton distributions functions (PDF) were achieved. Nevertheless, the knowledge about the polarisation of the gluon in the nucleon and the transverse PDFs ia still poorly known.

Part I

Theoretical Framework

CHAPTER 2

THE NUCLEON SPIN STRUCTURE

Le véritable voyage de découverte
ne consiste pas à chercher de
nouveaux paysages mais à avoir de
nouveaux yeux.

Marcel Proust.

In order to establish a complete and useful approach to the subject of this work the main theoretical concepts of the nucleon spin structure are described in detail in this chapter to provide a solid background regarding the physics aspects. Deep Inelastic Scattering (DIS) is used as a tool to access the information for the nucleon structure, therefore the kinematics of this process is explained in section 2.1. The cross section expression is derived in section 2.2 The spin asymmetries and the fundamental relations are shown in section 2.3. The simple and the improved, using the Quantum Chromodynamics (QCD), quark parton models are discussed.

2.1 Kinematic Variables in Deep Inelastic Scattering

In DIS experiments an incoming beam of leptons with energy E scatters off a nucleon in a fixed hadronic target. A lepton l having a 4-momentum $k = (E, \vec{\mathbf{k}})$, neglecting its mass (*i.e.* $\vec{\mathbf{k}} \simeq \vec{0}$), scatters off a nucleon at rest, N, having a 4-momentum $p = (M, \vec{0})$. The incoming lepton interacts with the target nucleon through the exchange of a virtual photon. The scattering lepton l' has an angle θ with respect to the incoming lepton and a 4-momentum $k' = (E', \vec{\mathbf{k}'})$. Particularly in the *inelastic* case, the nucleon absorbing the energy of the virtual photon breaks up producing the final state X. This process can be written in this way

$$l + N \to l' + X$$

and schematically illustrated by figure 2.1.

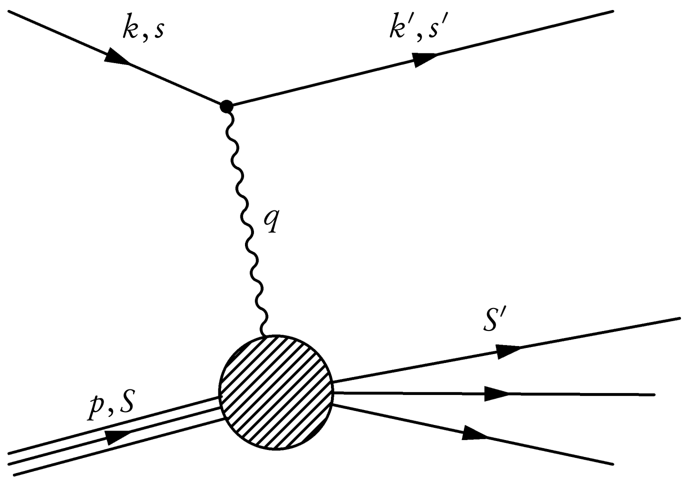

Figure 2.1: DIS process.

The 4-momentum vector that describes the exchanged virtual photon is given by $k - k' = q = (\nu, \vec{\mathbf{q}})$.

In the case of a fixed target and energy beam experiment two variables, the energy E' and the polar angle θ of the scattering lepton are sufficient to determine entirely the kinematics of an event. In practise it becomes feasible to use the two independent *Lorentz invariants*:

$$Q^2 = -q^2 = -(k-k')^2 \overset{\text{lab}}{\simeq} 4EE' \sin^2\frac{\theta}{2}, \tag{2.1}$$

$$\nu = \frac{p \cdot q}{M} \overset{\text{lab}}{=} E - E', \tag{2.2}$$

where ν represents the lepton energy loss.

Also an alternative pair of dimensionless variables can define the kinematics:

$$x = \frac{Q^2}{2p \cdot q} = \frac{Q^2}{2M\nu}, \tag{2.3}$$

$$y = \frac{\nu}{E}, \tag{2.4}$$

The variable x was introduced by Bjorken, it measures the property of elasticity of the collision; if $x \to 0$ the collision is elastic, if $x \to 1$ the collision is inelastic. y measures the fraction of energy loss of the incoming lepton.

The invariant mass of the hadronic system is $W^2 = (p+q)^2 = M^2 + 2p \cdot q + q^2$. Since the invariant mass cannot be less than the nucleon's, due to baryon number conservation in the scattering process,

$$W^2 > M^2 \Rightarrow M^2 + 2p \cdot q - Q^2 \geq M^2 \Rightarrow x \leq 1 .$$

As Q^2 and y are positive, the physical kinematic accessible region is defined by

$$0 \leq x, y \leq 1 .$$

2.2 DIS Cross Section

In this section the expression for the DIS cross section will be derived.

The scattering cross section by two particles, a and b, producing a final hadronic state of n particles is given by

$$d\sigma(a+b \to 1+\ldots+n) = \Phi \prod_{i=1}^{n} \frac{d^3 p_i}{(2\pi)^3 (2p_j^0)} |\mathcal{M}|^2 (2\pi)^4 \delta^4 \left(p_a + p_b - \sum_{j=1}^{n} p_j\right), \quad (2.5)$$

with the flux

$$\Phi = \frac{1}{4\sqrt{(p_a \cdot p_b)^2 - (m_a m_b)^2}}. \quad (2.6)$$

In the DIS case of muons on a fix nucleon target, a and b are related to the muon and the nucleon, repectively. Therefore $p_a = k$ and $p_b = p$. The DIS of polarised muons on a polarised fix nucleon target is

$$d\sigma = \frac{(2\pi)^4}{(2E)(2M)} |\mathcal{M}|^2 \delta^4 \left(p + q - \sum_{i=1}^{X} p_i\right) \frac{d^3 k'}{(2\pi)^3 (2E')} \prod_{j=1}^{X} \frac{d^3 p_j}{(2\pi)^3 (2E_j)} \quad (2.7)$$

The scattering amplitude $\mathcal{M}$ for the DIS process depicted in figure 2.1 is

$$i\mathcal{M} = (-ie)^2 \left(\frac{-i g_{\mu\nu}}{q^2} \right) \langle k' s' | j_l^{\mu}(0) | k, s \rangle \langle X S' | j_h^{\nu}(0) | p, S \rangle, \quad (2.8)$$

which represents the interaction between the leptonic and the hadronic currents j_l^{μ} and j_h^{ν} through the electromagnetic field of the photon introduced by the $\frac{-i g_{\mu\nu}}{q^2}$ propagator. The polarisation states are $s(s')$ and $S(S')$, respectively the lepton and nucleon initial (final) states.

The differential scattering cross section is obtained by squaring the amplitude $\mathcal{M}$ in expression (2.8), and using it in equation (2.7). Since the polarisations of the final states of the scattering muon and the hadrons are not determined in the expression of $d\sigma$, a sum over all possible states needs to be performed. The result is

$$d\sigma = \frac{e^4}{4Q^4} \frac{(2\pi)^4}{(2E)(2M)} \frac{d^3 k'}{(2\pi)^3 (2E')} \sum_X \sum_{s',S'} \int \prod_{j=1}^{X} \frac{d^3 p_j}{(2\pi)^3 (2E_j)} \delta^4 \left(p + q - \sum_{i=1}^{X} p_i\right) \times$$

$$\langle k, s | j_l^{\mu}(0) | k\prime, s' \rangle \langle k', s' | j_l^{\nu}(0) | k, s \rangle \langle p, S | j_{\mu h}(0) | X, S' \rangle \langle X, S' | j_{\nu h}(0) | p, S \rangle, \quad (2.9)$$

in which the fact that the currents are hermitian was used , *i.e.* $j_{\mu}^{\dagger} = j_{\mu}$ thus $\langle \alpha | j^{\mu} | \beta \rangle^* = \langle \beta | j^{\mu} | \alpha \rangle$.

At this point it is convenient to introduce two tensors: the leptonic tensor, $L_{\mu\nu}$ and the hadronic tensor, $W_{\mu\nu}$.

$$L^{\mu\nu}(k,s;k',s') = \sum_{s'}\langle k',s'|j_l^{\nu}(0)|k,s\rangle\langle k,s|j_l^{\mu}(0)|k',s'\rangle \tag{2.10}$$

$$W_{\mu\nu}(p,q) = \frac{(2\pi)^3}{2M}\cdot\frac{1}{4}\sum_X\sum_{S'}\int\left[\prod_{j=1}^{X}\frac{d^3p_j}{(2\pi)^3(2E_j)}\delta^4\Big(p+q-\sum_{i=1}^{X}p_i\Big)\times\right.$$
$$\left.\langle p,S|j_{\mu h}(0)|X,S'\rangle\langle X,S'|j_{\nu h}(0)|p,S\rangle\right] \tag{2.11}$$

The leptonic and hadronic tensors $L_{\mu\nu}$ and $W_{\mu\nu}$ describe leptonic and hadronic interactions, by the inclusion of the leptonic and hadronic currents. The tensor $L^{\mu\nu}$ carries the information about the virtual photon, emitted by the lepton, the hadronic tensor $W^{\mu\nu}$ describes the internal structure of the nucleon. Both tensors can be represented as a combination of a symmetric and an anti-symmetric part, having the form

$$L^{\mu\nu} = L^{\mu\nu\,(S)} + i L^{\mu\nu(A)} \tag{2.12}$$
$$W^{\mu\nu} = W^{\mu\nu\,(S)} + i W^{\mu\nu(A)} \tag{2.13}$$

The leptonic tensor $L^{\mu\nu}$ comes directly from Feynman rules in QED having the following symmetric and anti-symmetric components:

$$L^{\mu\nu\,(S)} = 2k'^{\mu}k^{\nu} + 2k'^{\nu}k^{\mu} + 2(m^2 - k'\cdot k)g^{\mu\nu} \tag{2.14}$$
$$L^{\mu\nu\,(A)} = 2m\epsilon^{\mu\nu\alpha\beta}q_\alpha s_\beta \tag{2.15}$$

The hadronic tensor $W^{\mu\nu}$ can be parametrised in terms of the structure functions, having then the following components:

$$W^{\mu\nu\,(S)} = -g^{\mu\nu}F_1 + \frac{F_2}{p\cdot q}p^\mu p^\nu \tag{2.16}$$
$$W^{\mu\nu\,(A)} = g_1\frac{M}{p\cdot q}\epsilon^{\mu\nu\alpha\beta}q_\alpha S_\beta + g_2\frac{M}{(p\cdot q)^2}\epsilon^{\mu\nu\alpha\beta}q_\alpha(p\cdot q S_\beta - S\cdot q p_\beta) \tag{2.17}$$

The functions F_1, F_2, g_1, and g_2 are the set of structure functions of the nucleon measured experimentally. For illustration, in figures 3.1, 2.3 and 3.5 these structure functions are shown. It is worth to mention that, for a spin-1 target, there are extra structure functions to consider, namely $b_{1\ldots4}$.

The set of equations (2.16) and (2.17) were obtained using the following constrains on the $W^{\mu\nu}$ tensor [12]: (*i*) parity conservation; (*ii*) time reversal invariance; (*iii*) hermiticity; (*vi*) translational invariance, and (*v*) current conservation. The last constraint also was applied to the $L^{\mu\nu}$ tensor.

Using equations (2.10), (2.11) and preforming a variable change to $dx\,dy\,d\phi$ into equation (2.9) the inclusive DIS cross section of muons on fix nucleon target reads as follows:

$$\frac{d^3\sigma}{dx\,dy\,d\phi} = \frac{e^4}{16\pi^2Q^4}\left[\frac{y}{2}\right]L^{\mu\nu}W_{\mu\nu} \tag{2.18}$$

In equation (2.18), the contraction of the symmetric part $L^{\mu\nu\,(S)}$ with the anti-symmetric part $W^{(A)}_{\mu\nu}$, and vice-versa results in null tensor. Therefore the symmetric and anti-symmetric terms of $L^{\mu\nu}W_{\mu\nu}$ are well defined. The symmetric term $L^{\mu\nu}W^{(S)}_{\mu\nu}$ corresponds to the unpolarised cross section while the anti-symmetric term $L^{\mu\nu}W^{(A)}_{\mu\nu}$ corresponds to the differences of cross sections with opposite target spins.

The lepton and nucleon initial spin polarisations are:

$$s \overset{\text{lab}}{=} h_l \frac{1}{m}(|\vec{\mathbf{k}}|, 0, 0, E)\,, \tag{2.19}$$

$$S \overset{\text{lab}}{=} (0, \sin\alpha\cos\beta, \sin\alpha\cos\beta, \cos\alpha)\,. \tag{2.20}$$

The incoming lepton spin is polarised along the direction of its 3-dimensional momentum vector, having helicity values according to $h_l = \pm 1$. The incoming nucleon spin is parametrised according to the set of angles α and β defined in figure 2.2.

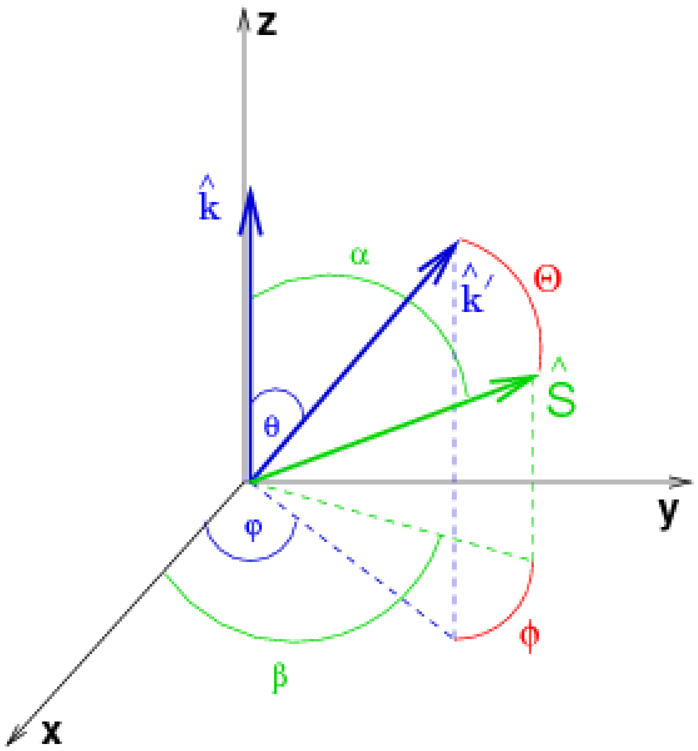

Figure 2.2: Reference system used to represent spin polarisations and their associated angles.

Considering this parametrisation the inclusive DIS cross section written in equation (2.18) can be expressed as follows:

$$\frac{d^3\sigma}{dx\,dy\,d\phi} = \frac{d^3\overline{\sigma}}{dx\,dy\,d\phi} - h_l\cos\alpha\frac{d^3\Delta\sigma_{\parallel}}{dx\,dy\,d\phi} - h_l\sin\alpha\cos\phi\frac{d^3\Delta\sigma_{\perp}}{dx\,dy\,d\phi}\,, \tag{2.21}$$

with

$$\frac{d^3\overline{\sigma}}{dx\,dy\,d\phi} = \frac{e^4}{4\pi^2 Q^4}\left\{\frac{y}{2}F_1 + \frac{1}{2xy}\left(1-y-\frac{y^2\gamma^2}{4}\right)F_2\right\} = \boldsymbol{\overline{\sigma}}\,, \tag{2.22}$$

$$\frac{d^3\Delta\sigma_{||}}{dx\,dy\,d\phi} = \frac{e^4}{4\pi^2 Q^4}\left\{\left(1-\frac{y}{2}-\frac{y^2\gamma^2}{4}\right)g_1 - \frac{y}{2}g_2\right\} = \boldsymbol{\Delta\sigma}_{||}\,, \tag{2.23}$$

$$\frac{d^3\Delta\sigma_{\perp}}{dx\,dy\,d\phi} = \frac{e^4}{4\pi^2 Q^4}\left\{\gamma\sqrt{1-y-\frac{y^2\gamma^2}{4}}\left(\frac{y}{2}g_1 + g_2\right)\right\} = \boldsymbol{\Delta\sigma}_{\perp}\,, \tag{2.24}$$

where the term $\boldsymbol{\overline{\sigma}}$ corresponds to the so-called spin-averaged differential cross section. The terms $\boldsymbol{\Delta\sigma}_{||}$ and $\boldsymbol{\Delta\sigma}_{\perp}$ are respectively the differential cross section terms for the longitudinal and transverse configurations of the nucleon spin with respect to the muon spin. And

$$\gamma^2 = \frac{4M^2x^2}{Q^2}\,. \tag{2.25}$$

2.3 Spin Asymmetries

Generally speaking, asymmetries are a tool which allows to access very small differences. In the context of the nucleon spin structure, these differences on the spin balance resolve the spin contribution of the partons.

The spin asymmetries can be defined according to two perspectives: The *lepton-nucleon* and the *photon-nucleon* asymmetries, which will be discussed next. The first one represents the asymmetry measured in the lab frame. The second one gives us the asymmetry in the photon reference frame.

Lepton-Nucleon Asymmetry

To measure the spin-dependent effects asymmetries are used, which take into account the difference between cross sections with specific spin configurations. These cross sections are evaluated with parallel and anti-parallel spin configuration of the lepton ($\leftarrow$) with respect to the nucleon ($\Rightarrow$ or $\Leftarrow$) polarisations.

The double longitudinal and transverse spin asymmetries, A_{LL} and A_{T} are:

$$A_{\mathrm{LL}} = \frac{\sigma^{\overset{\leftarrow}{\Rightarrow}} - \sigma^{\overset{\leftarrow}{\Leftarrow}}}{\sigma^{\overset{\leftarrow}{\Rightarrow}} + \sigma^{\overset{\leftarrow}{\Leftarrow}}} \tag{2.26}$$

$$A_{\mathrm{T}} = \frac{\sigma^{\leftarrow\Downarrow} - \sigma^{\leftarrow\Uparrow}}{\sigma^{\leftarrow\Downarrow} + \sigma^{\leftarrow\Uparrow}} \tag{2.27}$$

Experimentally, it is useful and direct to measure these double spin asymmetries defined by equations (2.26) and (2.27) due to the fact that the observables (the kinematic variables x, Q^2 and the angle of the scattered lepton) can be obtained from the event in a very straightforward way.

Photon-Nucleon Asymmetry

The photon-nucleon asymmetry is defined in the frame of the interaction between the virtual photon and the nucleons. Contrarily to the previous asymmetry, the photon-nucleon asymmetry gives a higher resolution. Thus it allows to extract the asymmetry information with respect to the partons inside the nucleon. First, the cross sections for this case are described. Then the asymmetries are defined.

Photon-Nucleon Cross Sections

Looking at figure 2.1 illustrating the DIS, the lower vertex represents also the absorption of the virtual photon by the nucleon.

$$\gamma^{\star}(h)+N(H)\rightarrow\gamma^{\star}(h')+N(H'). \tag{2.28}$$

In this process a virtual photon, $\gamma^{\star}$, moving in the z-axis with 4-momentum vector $q=(\nu,0,0,\sqrt{\nu^2+Q^2})$ and helicity h is absorbed by a nucleon, N, with helicity H. Afterwards, the nucleon emits a new virtual photon with helicity h' and its helicity is changed to H'.

The helicity amplitude can be determined in terms of the tensor $\mathscr{T}_{\nu\mu}$, as

$$\mathscr{M}_{\mathrm{h,H;h',H'}}=\epsilon^{\mu\star}_{h'}\epsilon^{\nu}_{h}\mathscr{T}_{\nu\mu} \tag{2.29}$$

The polarisation 4-vector of the incoming (outgoing) virtual photon is represented by $\epsilon^{\mu}_{h\,(h')}$. Three polarisations are possible:

$$\epsilon^{\mu}_{\pm} = \mp\frac{1}{\sqrt{2}}(0,1,\pm i,0), \tag{2.30}$$

$$\epsilon^{\mu}_{0} = \frac{1}{Q}(|\vec{\mathbf{q}}|,0,0,\nu), \tag{2.31}$$

where the subscripts $-,0,+$ are respectively $h=-1,0,1$ polarisations states. The polarisations must satisfy $q_{\mu}\epsilon^{\mu}=0$ and $\epsilon^2=-1$.

Using the *optical* theorem the cross section can be expressed as the imaginary or absorptive part of the forward virtual photon-nucleon Compton scattering amplitude,

$$W_{\mu\nu}=\frac{1}{2\pi}\Im\mathfrak{m}(\mathscr{T}_{\mu\nu}). \tag{2.32}$$

Equation (2.18) states the relation between the cross section and the hadronic tensor, $W_{\mu\nu}$, which allows to express the photo-absorption cross sections in terms of the structure functions.

$$\sigma^{T}_{\frac{1}{2}} = \tfrac{4\pi^2\alpha}{MK}\Im\mathfrak{m}\left(\mathscr{M}_{1,\frac{1}{2},1,\frac{1}{2}}\right) = \frac{4\pi^2\alpha}{MK}\left(F_1+g_1-\gamma^2 g_2\right), \tag{2.33}$$

$$\sigma^{T}_{\frac{3}{2}} = \tfrac{4\pi^2\alpha}{MK}\Im\mathfrak{m}\left(\mathscr{M}_{1,-\frac{1}{2},1,-\frac{1}{2}}\right) = \frac{4\pi^2\alpha}{MK}\left(F_1-g_1+\gamma^2 g_2\right), \tag{2.34}$$

$$\sigma^{L}_{\frac{1}{2}} = \tfrac{4\pi^2\alpha}{MK}\Im\mathfrak{m}\left(\mathscr{M}_{0,\frac{1}{2},0,\frac{1}{2}}\right) = \frac{4\pi^2\alpha}{MK}\left[(1+\gamma^2)\frac{F_2}{2x}-F_1\right], \tag{2.35}$$

$$\sigma^{TL}_{\frac{1}{2}} = \tfrac{4\pi^2\alpha}{MK}\Im\mathfrak{m}\left(\mathscr{M}_{0,\frac{1}{2},0,-\frac{1}{2}}\right) = \frac{4\pi^2\alpha}{MK}\gamma(g_1+g_2). \tag{2.36}$$

The subscripts $\frac{1}{2}$ and $\frac{3}{2}$ correspond to the total angular momentum of the photon-nucleon system along the virtual photon projection. The superscripts T and L are related to the transverse and longitudinal virtual photon polarisations. The term σ^{TL} corresponds to the cross section term arising from the interference between the transverse and the longitudinal amplitude. The K factor is the incoming virtual photons flux defined by Hand [13].

The total transverse cross section, σ^T, is defined as

$$\sigma^T = \frac{1}{2}(\sigma^T_{\frac{1}{2}} + \sigma^T_{\frac{3}{2}}) = \frac{4\pi^2\alpha}{MK}F_1\,, \tag{2.37}$$

while σ^L is defined simply as $\sigma^L = \sigma^L_{\frac{1}{2}}$.

It is also convenient to define R as the ratio of the absorption cross section by the nucleon of the longitudinal over the transverse polarised photons, *i.e.*

$$R = \frac{\sigma^L}{\sigma^T} \tag{2.38}$$

Thus equation (2.38) can be rewritten as a function of F_1 and F_2.

$$R = \frac{F_2(1+\gamma^2)}{2xF_1} - 1. \tag{2.39}$$

It is usual to define the longitudinal structure function, F_L as

$$F_L = F_2(1+\gamma^2) - 2xF_1. \tag{2.40}$$

Then using equations (2.39) and (2.40) the following relations can be written:

$$R = \frac{F_L}{2xF_1}, \tag{2.41}$$

$$F_1 = \frac{F_2(1+\gamma^2)}{2x(1+R)} \tag{2.42}$$

The Cross Section Asymmetries A_1 and A_2

As discussed before, the double spin asymmetries in the lepton-nucleon system, defined by equations (2.26) and (2.27) are extracted directly from experimental observables, therefore these asymmetries depend strongly on the kinematic range of the experiment. Thus they lose physical meaning while comparing different experiments. To avoid such situation of lack of consistency the asymmetries A_1 and A_2 are defined as functions of the photon-nucleon cross section

$$A_1 = \frac{\sigma^T_{\frac{1}{2}} - \sigma^T_{\frac{3}{2}}}{\sigma^T_{\frac{1}{2}} + \sigma^T_{\frac{3}{2}}}\,, \tag{2.43}$$

$$A_2 = \frac{\sigma^{TL}_{\frac{1}{2}}}{\sigma^T_{\frac{1}{2}} + \sigma^T_{\frac{3}{2}}}\,. \tag{2.44}$$

Using equations (2.33) to (2.36), the two previous equations can be stated as:

$$A_1 = \frac{g_1 - \gamma^2 g_2}{F_1}\,, \tag{2.45}$$

$$A_2 = \frac{\gamma\,(g_1 + g_2)}{F_1}\,. \tag{2.46}$$

In figure 2.3, 3.5 and 3.1, the spin dependent and independent structure functions, g_1 and F_2, are shown.

Relation between Lepton-Nucleon and Virtual Photon-Nucleon asymmetries

The longitudinal and transverse asymmetries A_{LL} and A_{T} can be defined with respect to the A_1 and A_2 asymmetries as

$$A_{\mathrm{LL}} = D\,(A_1 + \eta A_2)\,, \tag{2.47}$$

$$A_{\mathrm{T}} = d\,(A_1 - \xi A_2)\,, \tag{2.48}$$

where

$$D = \frac{y(2-y)\left(1+\frac{1}{2}\gamma^2 y\right)}{(1+\gamma^2)\left[2\left(1-y-\frac{\gamma^2 y^2}{4}\right)\left(\frac{1+R}{1+\gamma^2}\right)+y^2\right]}\,, \tag{2.49}$$

$$d = \frac{\sqrt{1-y-\frac{\gamma^2 y^2}{4}}}{1-\frac{y}{2}}D\,, \tag{2.50}$$

$$\eta = \frac{\gamma\left(1-y-\frac{\gamma^2 y^2}{4}\right)}{\left(1-\frac{y}{2}\right)\left(1+\frac{1}{2}\gamma^2 y\right)}\,, \tag{2.51}$$

$$\xi = \frac{\gamma\left(1-\frac{y}{2}\right)}{1+\frac{1}{2}\gamma^2 y}\,. \tag{2.52}$$

D is the depolarisation factor, while d, η and ξ are the other kinematic factors. In DIS experiments the target mass M is small when compared to the Q^2 of the process, therefore $\gamma \to 0$ as Q^2 increases. In this sense relation (2.47) becomes

$$A_{\mathrm{LL}} \simeq DA_1\,. \tag{2.53}$$

The depolarisation factor describes the polarisation amount transferred from the incoming muon to the virtual photon. Thus the depolarisation factor D allows us to commutate between two reference systems: the muon-nucleon (the laboratory system) and the photon-nucleon one.

2.4 The Quark Parton Model

In this section the Quark Parton Model (QPM) [14, 15] is introduced. In this model, the nucleon structure is composed by point-like, massless particles, called partons. An important

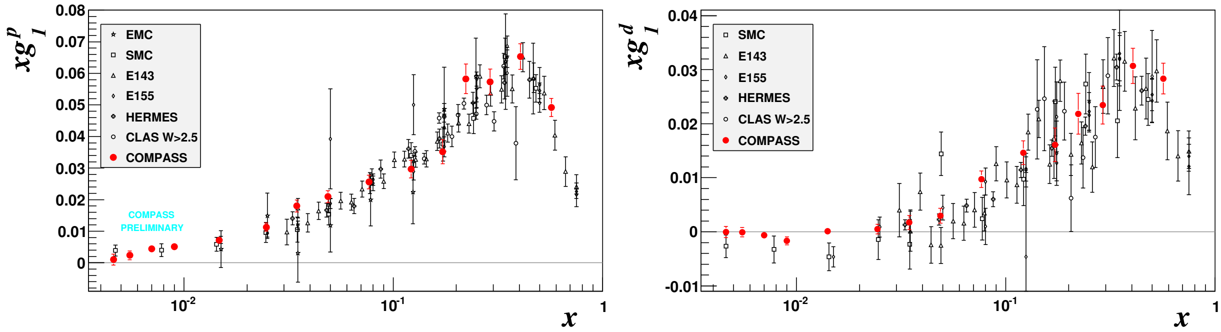

Figure 2.3: Spin dependent structure function g_1 for proton (left) and deuteron (right) data.

peculiarity of this model is that partons are free particles when probed in the Bjorken limit ($\nu, Q^2 \to \infty$, fixed x). The QPM is formulated in the infinite momentum frame, in which the nucleon moves with an infinite momentum, neglecting the quark transverse momentum component and the rest masses. Therefore, during the time period of the virtual photon, partons are assumed to be free and not interacting with each other. An important result of the QPM is the Bjorken *scaling* behaviour of the structure functions F_1 and F_2 [16],

$$F_{1,2}(x, Q^2) \stackrel{(\nu,Q^2\to\infty)}{\longrightarrow} F_{1,2}(x) \, .$$

The second important result is the Callan-Gross relation [17], in the Bjorken limit

$$F_2(x) = 2xF_1(x) \, .$$

An interesting result comes from using the Callan-Gross relation in equation (2.39), $R \simeq 0$ in the QPM, due to the Bjorken limit leading to ($\gamma \to 0$). This result states that the spin-$\frac{1}{2}$ partons, in this context naturally identified as quarks, can only absorb transversely polarised virtual photons. In this case the lepton-nucleon scattering is interpreted as a virtual photon scattering off free partons. Thus the lepton-nucleon cross section can be regarded as a incoherent sum of virtual photon-quark cross section scattering.

In this frame the scattering variable x can be identified as the fraction of nucleon momentum carried by the struck quark. The hadronic tensor $W^{\mu\nu}$ can be calculated leading to the expressions for the structure functions

$$F_1(x) = \frac{1}{2}\sum_f e_f^2 \left[q_f^+(x) + q_f^-(x)\right] = \frac{1}{2}\sum_f e_f^2 q_f(x) \, , \tag{2.54}$$

$$F_2(x) = x\sum_f e_f^2 \left[q_f^+(x) + q_f^-(x)\right] = x\sum_f e_f^2 q_f(x) \, , \tag{2.55}$$

$$g_1(x) = \frac{1}{2}\sum_f e_f^2 \left[q_f^+(x) - q_f^-(x)\right] = \frac{1}{2}\sum_f e_f^2 \Delta q_f(x), \tag{2.56}$$

$$g_2(x) = 0 \, , \tag{2.57}$$

The quark distribution functions $q_f(x)$ represent the probability density to find a quark or antiquark of flavour f with a momentum fraction x inside the nucleon. The superscript $+(-)$ is related to the quark distribution functions with spin parallel (anti-parallel) with respect to the nucleon spin. The electric charge of the quark with flavour f is described by e_f. Expression (2.57) reflects the lack of interpretation of the structure function g_2 in the frame of the QPM.

2.5 The First Moment of $g_1(x)$ and the Nucleon Spin

The first moment of the spin dependent structure function g_1, defined as

$$\Gamma_1 = \int_0^1 g_1(x)dx = \frac{1}{2}\sum_f e_f^2 \int_0^1 \Delta q_f(x)dx \; , \tag{2.58}$$

has an important information: the quark helicity contribution to the nucleon spin.

Defining Δq_f as

$$\Delta q_f = \int_0^1 \Delta q_f(x)dx \; , \tag{2.59}$$

and neglecting the heavy quarks, the first moment for the proton can be written as

$$\Gamma_1^p = \frac{1}{2}\left(\frac{4}{9}\Delta u + \frac{1}{9}\Delta d + \frac{1}{9}\Delta s\right) \; , \tag{2.60}$$

$$= \frac{1}{12}(\Delta u - \Delta d) + \frac{1}{36}(\Delta u + \Delta d - 2\Delta s) + \frac{1}{9}(\Delta u + \Delta d + \Delta s) \; . \tag{2.61}$$

Assuming the isospin symmetry, the first moment for the neutron can be obtained by $\Delta u \longleftrightarrow \Delta d$.

A very useful mathematical tool is the Operator Product Expansion (OPE). This tool allows to relate the three terms in equation (2.61) with the expectation values a_i of the proton matrix element of a SU(3) octet of quark axial-vector currents [12]. These expectation values are defined as

$$\langle P,S|J^i_{5_\mu}|P,S\rangle = Ma_i S_\mu, \qquad i = 1\ldots 8 \; , \tag{2.62}$$

where M is related to the mass of the quarks. The currents $J^i_{5_\mu}$ are given by the λ_i, the Gell-Mann matrices as

$$J^i_{5_\mu} = \bar{\Psi}\gamma_\mu\gamma_5\frac{\lambda_i}{2}\Psi \; , \tag{2.63}$$

Ψ is a column vector in the flavour space

$$\Psi = \begin{pmatrix} \Psi_u \\ \Psi_d \\ \Psi_s \end{pmatrix} \tag{2.64}$$

The element a_0 is given by the singlet operator

$$J^0_{5_\mu} = \bar{\Psi}\gamma_\mu\gamma_5\Psi \; . \tag{2.65}$$

Therefore equation (2.65) represents the axial vector current and the matrix element

$$\langle P,S|J^0_{5_\mu}|P,S\rangle = Ma_0 S_\mu \tag{2.66}$$

measures the spin.

Finally the correspondence of the expectation values a_i of equations (2.62) and (2.66) to the terms of eq. (2.61) is as follows

$$a_3 = \Delta u - \Delta d \; , \tag{2.67}$$

$$a_8 = \Delta u + \Delta d - 2\Delta s \; , \tag{2.68}$$

$$a_0 = \Delta u + \Delta d + \Delta s = \Delta\Sigma \; . \tag{2.69}$$

The last relation represents, in the naïve parton model, the quarks' helicity contribution to nucleon spin, also known as $\Delta\Sigma$.

The elements a_3 and a_8 are well known from the neutron β decay and the spin-$\frac{1}{2}$ hyperon decays (*e.g.* $\Lambda \to p$, $\Sigma \to n$, $\Xi \to \Lambda$) in the SU(3) baryon octet. These can be expressed in terms of the parameters F and D, obtained from the aforementioned decays [12, 18, 19].

$$a_3 = F + D = |g_A| = 1.2694 \pm 0.0028\ , \tag{2.70}$$

$$a_8 = 3F - D = 0.585 \pm 0.025\ , \tag{2.71}$$

where g_A is the axial coupling constant. Thus the knowledge of a_3 and a_8 allows to determine a_0 and Γ_1^p.

The QCD improved parton model leads to some corrections [20–22] modifying equation (2.61), using the terms defined in equations (2.67)to (2.69), leads to

$$\Gamma_1^p = \frac{1}{12}\{\left(a_3 + \frac{1}{3}a_8\right)E_{NS}(Q^2) + \frac{4}{3}a_0 E_S(Q^2)\}\ , \tag{2.72}$$

with

$$E_{NS}(Q^2) = 1 - \frac{\alpha_s(Q^2)}{\pi} - \begin{pmatrix}3.58\\3.25\end{pmatrix}\left(\frac{\alpha_s(Q^2)}{\pi}\right)^2 \dots\ , \tag{2.73}$$

$$E_S(Q^2) = 1 - \begin{pmatrix}0.333\\0.040\end{pmatrix}\frac{\alpha_s(Q^2)}{\pi} - \begin{pmatrix}1.10\\-0.07\end{pmatrix}\left(\frac{\alpha_s(Q^2)}{\pi}\right)^2 \dots\ , \tag{2.74}$$

where the upper and lower values correspond to the cases in which the number of quark flavours are three and four, respectively.

The first measurement of Γ_1 was performed by the European Muon Collaboration (EMC) [23, 24]. The value of a_0 was found to be compatible with zero ($\Delta\Sigma = 0.12 \pm 0.17$). This value was unexpectedly small. The naïve QPM indicates $\Delta\Sigma = 1$. Applying the Ellis-Jaffe sum rule [25] or taking into account relativistic effects [26] leads to $\Delta\Sigma \approx 0.6$. Thus the EMC measurement led to the so called *spin crisis in the parton model*, which arouse a profuse experimental and theoretical effort and work (*e.g.* [4, 27–31] and references therein). The COMPASS Collaboration in 2007 published a result on $\Delta\Sigma$, improving the accuracy of the measurement done by EMC

$$\Delta\Sigma(Q^2 = 4(\mathrm{GeV}/c)^2) = 0.237^{+0.024}_{-0.029} \tag{2.75}$$

and established the small contribution of the quarks to the nucleon spin, obtained from the measurement of Γ_1 given in the Modified-Minimal-Subtraction scheme ($\overline{MS}$); see section 3.1 for details.

2.6 The Bjorken Sum Rule

Taking into account equations (2.67), (2.68) and (2.69) the first moment of the proton can be rewritten as

$$\Gamma_1^p = \frac{1}{12}a_3 + \frac{1}{36}a_8 + \frac{1}{9}a_0\ . \tag{2.76}$$

Using the isospin symmetry the first moment of the neutron is

$$\Gamma_1^n = -\frac{1}{12}a_3 + \frac{1}{36}a_8 + \frac{1}{9}a_0\ . \tag{2.77}$$

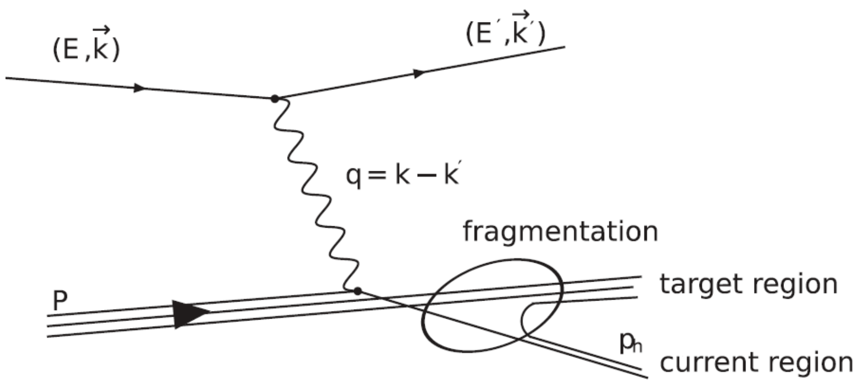

Figure 2.4: Schematic representation of the fragmentation process. The hadrons production in DIS.

Therefore

$$\Gamma_1^p - \Gamma_1^n = \frac{1}{6} a_3 = \frac{1}{6} |g_A| \ . \tag{2.78}$$

In the next chapter the results for the first moments of the proton and neutron and consequently for the Bjorken sum rule are covered taking into account the improved QPM.

2.7 Fragmentation Process

The scattering picture that so far has been shown is the inclusive DIS, in which only the incoming and scattering muons are measured. Let us imagine for a moment the possibility of detecting a hadron in coincidence with the incoming and scattering muons; this can provide important information about different flavours in the nucleon structure.

The hadron production in DIS is explained by the fragmentation process illustrated in figure (2.4). To describe this process, two variables are not sufficient, a third one is therefore needed. This variable is related to one property of the newly produced hadrons. Normally two options are available: the energy fraction of the virtual photon carried by the hadron

$$z = \frac{E_h}{\nu} \ , \tag{2.79}$$

or alternatively, the Feynman x, x_F

$$x_F = \frac{p_L^{c.m.}}{p_{L,max}^{c.m.}} \simeq \frac{2 p_L^{c.m.}}{W} \ . \tag{2.80}$$

Where $p_L^{c.m.}$ is the longitudinal momentum of the hadron and $p_{L,max}^{c.m.} \simeq W/2$ is the maximum allowed $p_L^{c.m.}$ in the virtual photon-nucleon centre of mass system.

This last variable is particularly useful to distinguish between two regions: $x_F < 0$ selects hadrons from the target fragmentation region, which were originated from the target remnant; $x_F > 0$ selects hadrons produced in the current fragmentation region, which were originated by the struck quark.

According to QCD, quarks are confined, *i.e.* there is no evidence of quarks in unbound states. After the interaction, the struck quark and the target remnants have to produce colour neutral bound states. This process of hadronisation cannot be described in perturbative QCD, nevertheless it can be parametrised in the form of fragmentation functions. In this way, the factorisation of the hard process and fragmentation are assumed. Therefore the hard process can be calculated using perturbative QCD and the soft part, the fragmentation, is parametrised independently.

The cross section for the production of a hadron h can be written at leading order (LO) QCD as

$$\sigma^h(x,Q^2,z) \propto \sum_f e^2 q_f(x,Q^2) D_f^h(z,Q^2)\,,$$

where $D_f^h(z,Q^2)$ is the fragmentation function parametrising the fragmentation process. The fragmentation function gives the probability density that a struck quark of flavour f, probed at Q^2, fragments into a hadron h, carrying a fraction z of the photon energy. As an example, one of the most recent parametrisation of fragmentation functions is described in ref. [32]. The precision of the fragmentation functions is one of the important issues related to the flavour separation of the spin dependent quark distribution analysis, since it constitutes one of the main sources of systematic uncertainties [33].

CHAPTER 3

THE GLUON IN THE NUCLEON

You can tell the mailman not to call,
I ain't comin' home until the fall,
And I might not get back home at all, ['cause]
Lulu's back in town.

Al Dubin and Harry Warren, in "Broadway Gondolier".

In the previous chapter the spin asymmetries were defined and the physics background related to the nucleon spin was drawn. In this chapter a new player comes into the theory: the gluon. In this sense, the naïve QPM described in section 2.4 is enriched, in chapter 3.1, using the quark interaction theory described in *Quantum Chromodynamics* theory. In this section also the small violation of the scale invariance of the structure functions predicted by Bjorken is discussed; a consequence of this fact is a dependence on Q^2 in the parton distribution functions. A development of a new tool to cope with this dependence is described.

The gluon polarisation is presented in section 3.2. Using the knowledge described in the previous section the gluon polarisation quantity is defined. The direct techniques for measuring this quantity are described.

3.1 The QCD improved Quark Parton Model

In this section, the simple Quark Parton Model will be improved by introducing the quark interaction described in the theory of strong interactions, *Quantum Chromodynamics* (QCD). The relevant ideas of the QCD theory are highlighted. The evidence of the gluons inside the nucleons emerges from the Bjorken scaling violation. In the frame of these violations, the quark and gluon distribution functions will not only depend on x, but also on Q^2. Therefore the evolution in this new dependence needs to be taken into account. These two facts are described below.

Scaling Violations

The measurements of F_2 for proton and deuteron targets show a weak logarithmic Q^2 dependence. This violation of the Bjorken scaling is an indication that the quark interaction is done via gluon exchange. Looking at figure 3.1 it is possible to see that for a fixed value of x (in particular for lower values), increasing Q^2 leads to an increase in F_2. This is explained as follows: increasing Q^2 allows higher photon resolution, a parton that is probed at a low Q^2 seems to be a single quark, when probed at high Q^2 is seen as a quark that emits a gluon, which in its turn may create a $q\bar{q}$ pair. Figure 3.2 illustrates this aspect. Therefore, for low x, the parton distribution functions increase as Q^2 increases and for high x the parton distribution functions decrease as Q^2 increases. This last assertion is due to the fact that quarks carrying high momentum fraction x loose momentum due to gluon radiation.

Q^2 Evolution of the Parton Distributions

As consequence of the Bjorken scaling violation, the description of the parton distribution functions $q_f(x)$ and $g(x)$ also depend on Q^2. The Q^2 evolution of those distributions is performed by the Dokshitzer-Gribov-Lipatov-Altarelli-Parisi (DGLAP) equations [34–36]:

$$\frac{dq_f(x,Q^2)}{d\ln Q^2} = \frac{\alpha_s(Q^2)}{2\pi}\int_0^1 \frac{dy}{y}\left(q_f(y,Q^2)P_{qq}(z)+g(y,Q^2)P_{qG}(z)\right) , \tag{3.1}$$

$$\frac{dg(x,Q^2)}{d\ln Q^2} = \frac{\alpha_s(Q^2)}{2\pi}\int_0^1 \frac{dy}{y}\left(\sum_f q_f(y,Q^2)P_{Gq}(z)+g(y,Q^2)P_{GG}(z)\right) . \tag{3.2}$$

Where $z = x/y$ and α_s is the running QCD coupling constant. $P_{ij}(z)$ are the splitting functions, representing the probability to find a parton i carrying a momentum fraction z of a parent parton j with momentum $y > x$. The splitting functions are calculated from the Feynman rules, in figure 3.3 the Feynman diagrams of the splitting are depicted.

For the polarised case, the Q^2 evolution equations are drawn in analogous way with respect to the unpolarised case. The Q^2 dependence of the spin dependent parton distribution functions of the quarks $\Delta q_f(x)$ and gluons $\Delta g(x)$ is given

$$\frac{d\Delta q_f(x,Q^2)}{d\ln Q^2} = \frac{\alpha_s(Q^2)}{2\pi}\int_0^1 \frac{dy}{y}\left(\Delta q_f(y,Q^2)\Delta P_{qq}(z)+\Delta g(y,Q^2)\Delta P_{qG}(z)\right) , \tag{3.3}$$

$$\frac{d\Delta g(x,Q^2)}{d\ln Q^2} = \frac{\alpha_s(Q^2)}{2\pi}\int_0^1 \frac{dy}{y}\left(\sum_f \Delta q_f(y,Q^2)\Delta P_{Gq}(z)+\Delta g(y,Q^2)\Delta P_{GG}(z)\right) \tag{3.4}$$

where the spin dependent splitting function are defined as $\Delta P_{ij}(x) = P^+_{ij}(x) - P^-_{ij}(x)$. It is convenient to separate the polarised quark distributions in a flavour singlet $\Delta q^S(x)$ and non-

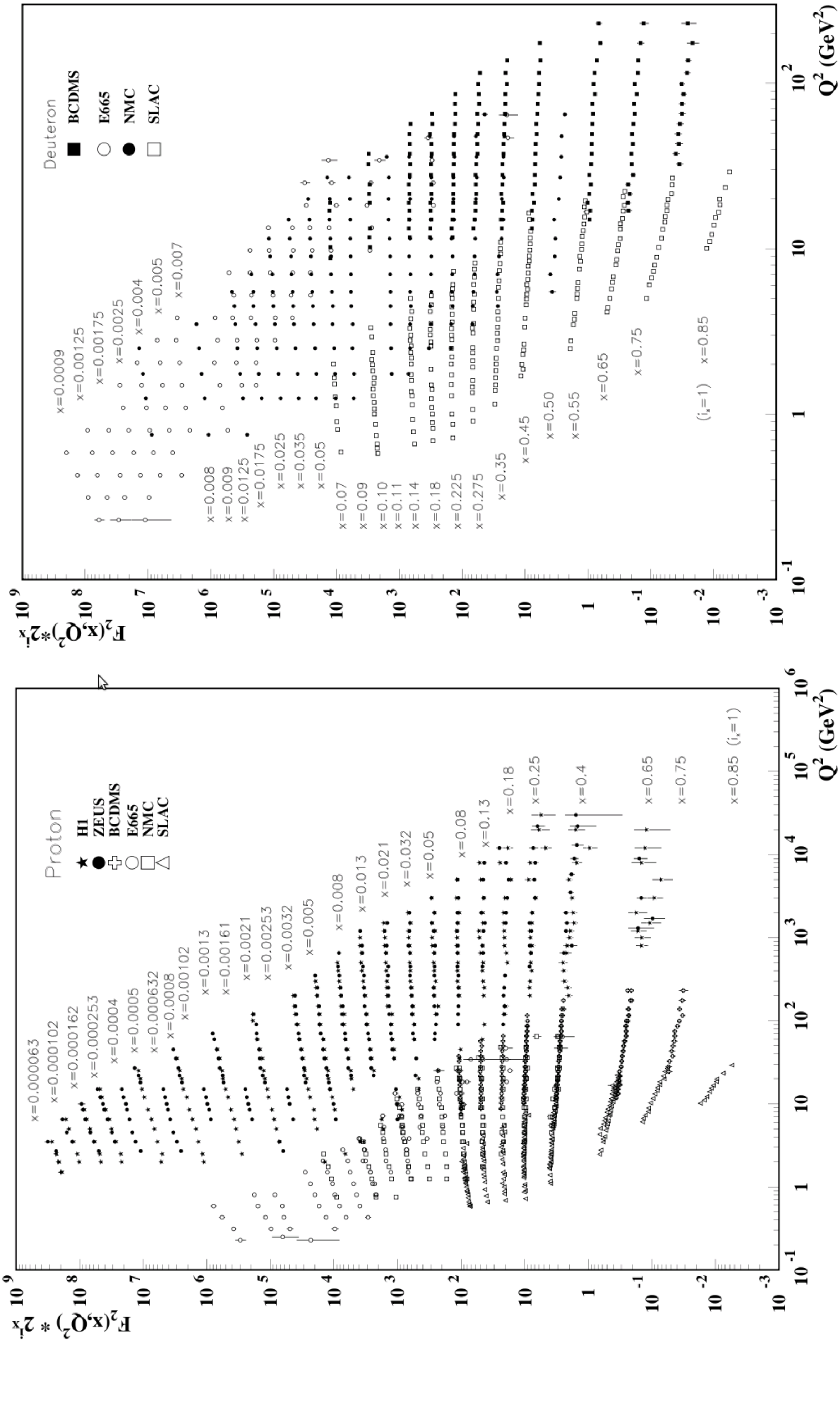

Figure 3.1: Spin in dependent structure function F_2, for proton (left) and deuteron (right) data.

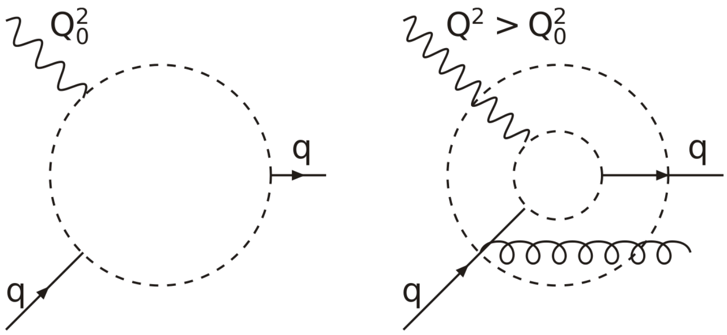

Figure 3.2: In a lepton-nucleon scattering, increasing Q^2 reveals the gluon radiation which explains the small violation in the Bjorken Scaling.

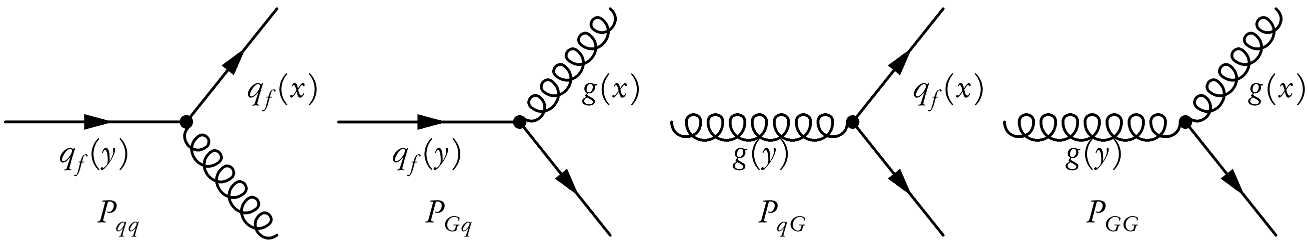

Figure 3.3: The Feynman diagrams for splitting functions.

singlet $\Delta q^{NS}(x)$ defined as

$$\Delta q^S(x) = \sum_f \Delta q_f(x, Q^2), \tag{3.5}$$

$$\Delta q^{NS}(x) = \sum_f \left(\frac{e_f^2}{\langle e^2 \rangle}\right) \Delta q_f(x, Q^2). \tag{3.6}$$

The average $\langle e^2 \rangle = \frac{1}{n_f}\sum e_f^2$, n_f being the number of flavours. Hence the evolution equations for the spin dependent case read now

$$\frac{d\Delta q^{NS}(x,Q^2)}{d\ln Q^2} = \frac{\alpha_s(Q^2)}{2\pi}\int_0^1 \frac{dy}{y} \Delta q^{NS}(y,Q^2)\Delta P_{qq}^{NS}(z), \tag{3.7}$$

$$\frac{d\Delta q^{S}(x,Q^2)}{d\ln Q^2} = \frac{\alpha_s(Q^2)}{2\pi}\int_0^1 \frac{dy}{y} \left(\Delta q^S(y,Q^2)\Delta P_{qq}^S(z) + 2n_f \Delta g(y,Q^2)\Delta P_{qG}^S(z)\right), \tag{3.8}$$

$$\frac{d\Delta g(x,Q^2)}{d\ln Q^2} = \frac{\alpha_s(Q^2)}{2\pi}\int_0^1 \frac{dy}{y} \left(\Delta q^S(y,Q^2)\Delta P_{Gq}^S(z) + \Delta g(y,Q^2)\Delta P_{GG}^S(z)\right). \tag{3.9}$$

From the previous set of equations it is seen that the flavour non-singlet terms evolve independently from the gluons while the flavour singlet and the gluon ones evolve coupled.

The spin dependent structure function g_1 can be written in terms of the singlet and non-singlet coefficient functions ΔC_S, ΔC_{NS} and ΔC_G [37]

$$g_1(x,Q^2) = \frac{1}{2}\langle e^2 \rangle\{\Delta C_{NS}\otimes\Delta q^{NS}(x,Q^2) + \Delta C_S\otimes\Delta q^S(x,Q^2) + 2n_f\Delta C_G\otimes\Delta g(x,Q^2)\}. \tag{3.10}$$

The coefficient functions depend on x and $\alpha_s(Q^2)$, which can be expanded in power series in α_s

$$\Delta C(x,\alpha_s) = \Delta C^{(0)}(x) + \frac{\alpha_s}{2\pi}\Delta C^{(1)} + \mathcal{O}(\alpha_s^2)\,. \tag{3.11}$$

At LO,

$$\Delta C_S^{(0)}\left(\frac{x}{y}\right) = \Delta C_{NS}^{(0)}\left(\frac{x}{y}\right) = \delta\left(1-\frac{x}{y}\right) \qquad \text{and} \qquad \Delta C_G^{(0)}\left(\frac{x}{y}\right) = 0\,,$$

and one obtains a similar equation to equation (2.56), apart from the Q^2 dependence,

$$g_1(x,Q^2) = \frac{1}{2}\sum_f e_f^2 \Delta q_f(x,Q^2)\,.$$

This result shows, as expected, that in LO the gluons do not contribute to the spin dependent structure function g_1. The splitting and the coefficient functions have been calculated up to next-to-leading order in α_s [38–40]. In NLO QCD, the splitting and the coefficient functions depend on the so called factorisation and renormalisation scheme, thus the interpretation of the measurements performed in DIS is scheme dependent. In the gauge invariant so called Modified-Minimal-Subtraction ($\overline{MS}$) scheme [41] also the second term in the expansion (eq. (3.11)) of ΔC_G, namely $\Delta C_G^{(1)}$ vanishes, thus $\Delta g_1(x,Q^2)$ does not contribute directly to the first moment Γ_1. Yet in the Adler-Bardeen (AB) scheme [42], the chirality is conserved, in contrast with the $\overline{MS}$ scheme, and $\Delta C_G^{(1)} \neq 0$, and thus the first moment Γ_1 depends directly on $\Delta g_1(x,Q^2)$. The first moments of the flavour singlet quark distribution $\Delta\Sigma(Q^2) = \int_0^1 \Delta q^S(x,Q^2)dx$ in the two schemes are related by

$$\Delta\Sigma_{\overline{MS}}(Q^2) = a_0 = \Delta\Sigma_{\overline{AB}}(Q^2) - n_f\frac{\alpha(Q^2)}{2\pi}\Delta G(Q^2)\,, \tag{3.12}$$

where $\Delta G(Q^2)$ is the first moment of the gluon distribution $g_1(x,Q^2)$

$$\Delta G(Q^2) = \int_0^1 g_1(x,Q^2)dx\,. \tag{3.13}$$

The first moment $\Delta G(Q^2)$ is the same in both schemes, *i.e.* $\Delta G_{\overline{MS}}(Q^2) = \Delta G(Q^2)_{\overline{AB}}$.

A similar result to equation (3.12) is obtained using the OPE. Consider the axial current from equation (2.63)

$$J_{5\mu}^f = \overline{\Psi}_f(x)\gamma_\mu\gamma_5\frac{\lambda}{2}\Psi_f(x)\,, \tag{3.14}$$

made up of quark operators of definite flavour f. Using the free Dirac equation of motion

$$\partial^\mu J_{5\mu}^f = 2im_f\overline{\Psi}_f(x)\gamma_\mu\gamma_5\frac{\lambda}{2}\Psi_f(x)\,, \tag{3.15}$$

m_f is the mass of the quark of flavour f.

In the chiral limit, $m_f \to 0$, equation (3.15) seems to be conserved, however this is not true. An anomalous contribution comes from the triangle diagram shown in figure 3.4, leading to a non vanishing result in equation (3.15). This phenomenon was first observed in QED by Adler [43]. In QCD [44, 45] equation (3.15) can be written as

$$\partial^\mu J^f_{5\mu} = \frac{\alpha_s}{4\pi} G^a_{\mu\nu} \tilde{G}^{\mu\nu}_a = \frac{\alpha_s}{2\pi} \mathrm{Tr}\left[G_{\mu\nu}\tilde{G}^{\mu\nu}\right] , \tag{3.16}$$

where the gluonic field tensor obeys the condition $\tilde{G}^{\mu\nu}_a = \frac{1}{2}\epsilon_{\mu\nu\rho\sigma} G^{\rho\sigma}_a$.

Summing over all quark flavour, $n_f = 3$, the gluonic contribution to a_0 is

$$a_0^{gluons}(Q^2) = -3\frac{\alpha_s}{2\pi}\Delta G(Q^2) . \tag{3.17}$$

The previous equation is believed to be an exact result and not to be affected by higher order QCD corrections [46].

Therefore, as a consequence of equation (3.17), a_0 has contributions from quarks and gluons. Then adding both contributions, in the $\overline{AB}$ scheme,equation (3.12) is regained.

$$a_0 = \Delta\Sigma_{\overline{AB}}(Q^2) - 3\frac{\alpha(Q^2)}{2\pi}\Delta G(Q^2) . \tag{3.18}$$

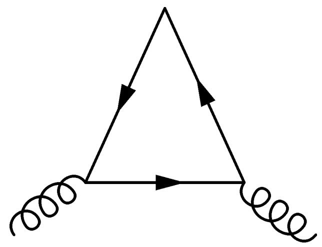

Figure 3.4: Triangle diagram which gives rise to the axial anomaly.

3.2 Direct Measurement of the Gluon Polarisation in DIS: The Photon-Gluon Fusion process

The gluon polarisation can be regarded as the spin helicity asymmetry of the gluon inside the nucleon. The purpose of this chapter is to explain how the gluon polarisation can be measured in different experimental scenarios. The content of this section is as follows. Firstly the direct measurement of the gluon polarisation in DIS is discussed. The main process for such measurements is the *photon gluon fusion* process, which is introduced. The techniques to select events associated to such process are stated. Then the measurement using $p-p$ collisions is summarised.

The gluon polarisation $\Delta G/G$ is measured directly via the Photon-Gluon Fusion process (PGF), depicted in figure 3.6. In the process, a photon interacts with the nucleon gluon exchanging a quark and producing a $q\bar{q}$ pair. This allows to probe the gluon inside the nucleon in DIS. In this way, the information carried by the gluon is available.

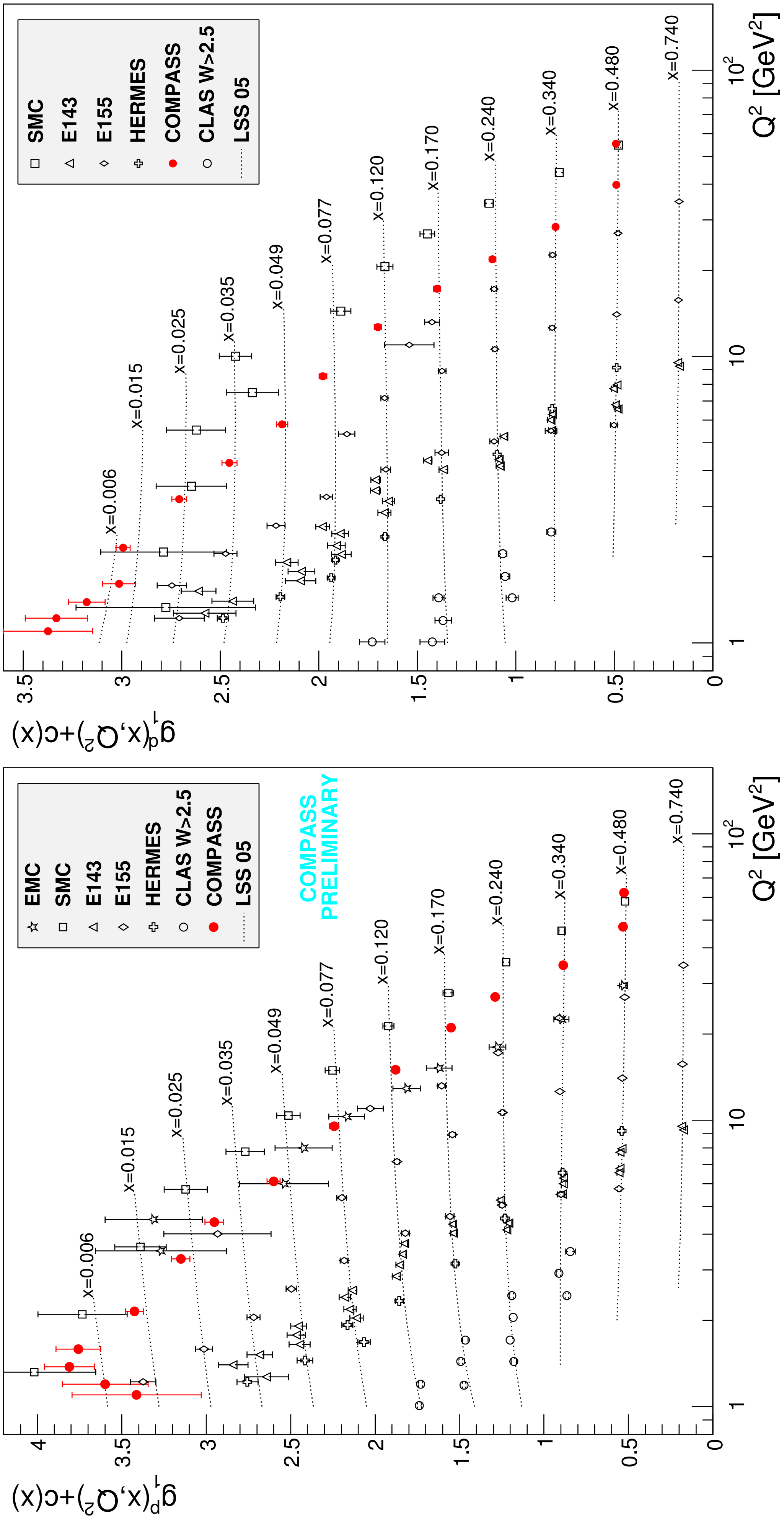

Figure 3.5: Spin dependent structure function g_1 for proton (left) and deuteron (right) data.

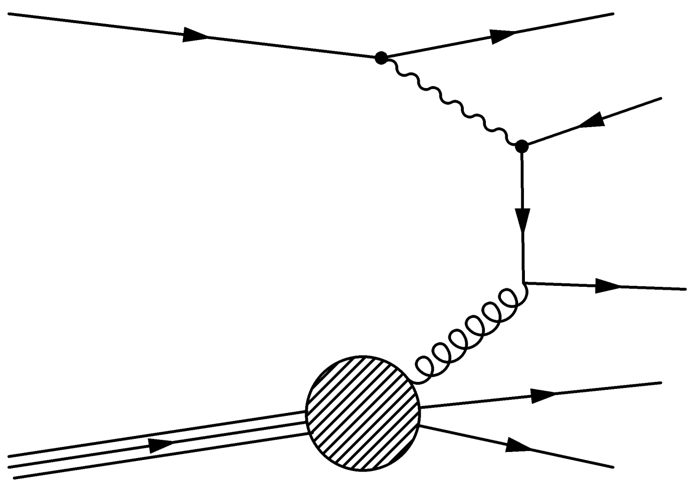

Figure 3.6: Photon-gluon fusion (PGF) process.

The spin helicity asymmetry for the photon interacting with a gluon from the nucleon, via quark exchange, is given by the ratio of the helicity dependent to the independent spin cross section asymmetries of the PGF process. Both cross sections may also be expressed as the convolution of the elementary photon-gluon fusion cross sections, $\Delta\hat{\sigma}$ and $\hat{\sigma}$ with the gluon distributions ΔG and G, as follows

$$A^{\gamma g\to q\bar{q}} = \frac{\Delta\sigma^{\gamma g\to q\bar{q}}}{\sigma^{\gamma g\to q\bar{q}}} = \frac{\int \Delta\hat{\sigma}(\hat{s})\Delta G(x_g,\hat{s})\,d\hat{s}}{\int \hat{\sigma}(\hat{s})G(x_g,\hat{s})\,d\hat{s}}\,, \tag{3.19}$$

$$= \frac{\int a_{\mathrm{LL}}\frac{\Delta G}{G}\hat{\sigma}(\hat{s})G(x_g,\hat{s})\,d\hat{s}}{\int \hat{\sigma}(\hat{s})G(x_g,\hat{s})\,d\hat{s}}\,, \tag{3.20}$$

$$= \left\langle a_{\mathrm{LL}}\frac{\Delta G}{G}\right\rangle . \tag{3.21}$$

In equations (3.20) and (3.21), the introduced term

$$a_{\mathrm{LL}} = \frac{\Delta\hat{\sigma}}{\hat{\sigma}} \tag{3.22}$$

represents the double longitudinal partonic spin asymmetry, also known as analysing power.

Another interesting quantity can be defined: the fraction of the nucleon momentum carried by the gluon, x_g. Using the Mandelstam variable $\hat{s} = (q + x_g P)^2 = -Q^2 + 2x_g Pq$, x_g may be derived as

$$x_g = \frac{\hat{s} + Q^2}{2Pq}\,, \tag{3.23}$$

where q and P are the photon and the nucleon momenta, respectively.

Nevertheless it is not possible to access experimentally the partonic variables, thus not possible to measure these quantities, a_{LL} and x_g, for each collected event. To estimate it, Monte Carlo simulation techniques that include kinematic information from data samples are used. Gluon polarisation measurements in DIS are extracted in a narrow range of x_g, due to the limited experimental coverage in x and Q^2 kinematic variables.

The PGF process is of the order of strong coupling constant α_s, thus this process has a reduced contribution by α_s with respect to the leading order photo-absorption process. This is equivalent to say that the probability of occurrence is low. Therefore due to this fact, the measurement of the gluon polarisation becomes a major challenge. Two analytical methods are used to select PGF events. The first one is based on the selection of high p_T hadron pair events, in which the PGF produces light $q\bar{q}$ quark pairs. The second one is the selection of events with open charm mesons, in this case the PGF process produces a $c\bar{c}$ pair. Both methods are described bellow.

Open-Charm Production

The open charm analysis is based on events containing D^0 mesons in the final state. The charm content in the D^0 mesons come from the $c\bar{c}$ quark pair production by the PGF process, since the intrinsic charm in the nucleon is widely known as negligible. On top of this, its production from light quark fragmentation is strongly suppressed. Therefore, DIS events with charmed mesons are PGF events, thus no physical background is present. These events are selected from the D^0 decaying products, *i.e.* $K\pi$ pairs.

To achieve an optimum selection of PGF events, a good particle identification is required. Applying a set of kinematic cuts, the combinatorial background originated from processes in which the virtual photon strikes a parton inside the nucleon is reduced. Additionally, the background is suppressed by studying the $D^\star \to D^0\pi_{slow}$ channel. In this way, the following $D^\star$ tagged channels are included in the analysis: $D^0 \to K\pi$, $D^0 \to K\pi\pi^0$ and $D^0 \to K\pi\pi\pi$.

The number of events containing D^0 particles is related with the helicity asymmetries as shown by the following expression:

$$N_t = \alpha(S+B)\left[1+\beta\left(a_{\mathrm{LL}}\frac{S}{S+B}\frac{\Delta G}{G}+D\frac{B}{S+B}A^{\mathrm{bg}}\right)\right]. \qquad (3.24)$$

The subscript t on the number of events corresponds to the possible muon target spin configurations. The α factor contains the acceptance, muon flux and number of nucleons and β the beam and target polarisations and the dilution factor. S and B represent the number of signal and background events taken under the invariant mass spectrum peak. The signal (background) significance is giben by $\frac{S(B)}{S+B}$. The asymmetry A^{bg} is related to the background events. To solve this system of equations, the partonic asymmetry a_{LL} and the signal significance $\frac{S}{S+B}$ must be estimated for every event. To compute the partonic asymmetry a_{LL} a dedicated MC simulation is used.

A NLO QCD analysis was also performed. Into the analysing power NLO QCD virtual and gluon bremstrahlung corrections were included to the PGF process, as well as background processes. Details about this analysis can be found in [47].

High p_T Hadron Pairs

The PGF process can also be selected using events containing high p_T hadron pairs. In this case the spin helicity asymmetry is calculated by selecting events containing high p_T hadron pairs, respectively for the highest and the second highest p_T hadron with respect the virtual photon direction. Two other processes compete with the PGF process in LO QCD approximation, namely the virtual photo-absorption leading order process (LP) and the gluon radiation (QCD Compton) process, illustrated in figure 3.7.

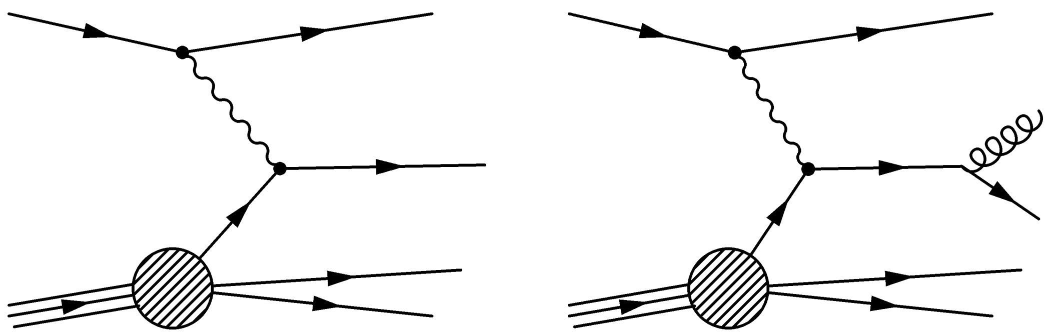

Figure 3.7: Virtual photo-absorption (left) and gluon radiation – QCD Compton (right) processes.

This analysis is divided in two Q^2 regimes: $Q^2 > 1$ and $Q^2 < 1$ $(\mathrm{GeV}/c)^2$. The first regime is defined by a cut on $Q^2 > 1$ $(\mathrm{GeV}/c)^2$, defining also the DIS event selection. The spin helicity asymmetry for the high p_T hadron pair data sample, in this Q^2 regime, can be thus schematically written as (see section 8):

$$A_{\mathrm{LL}}^{2h}(x_{Bj}) = R_{\mathrm{PGF}}\,\langle a_{\mathrm{LL}}^{\mathrm{PGF}}\rangle \frac{\Delta G}{G}(\overline{x}_G) + R_{\mathrm{QCDC}}\,\langle a_{\mathrm{LL}}^{\mathrm{QCDC}}\rangle A_1^{\mathrm{LP}}(\overline{x}_C) + R_{\mathrm{LP}}\,\langle a_{\mathrm{LL}}^{\mathrm{LP}}\rangle A_1^{\mathrm{LP}}(\overline{x}_{Bj})\,. \tag{3.25}$$

The process fractions are represented by R_i, i referring to the different processes. a_{LL}^i are the partonic cross section asymmetries. The depolarisation factor D represents the fraction of the muon beam polarisation transferred to the virtual photon. The final formula to extract the gluon polarisation has the following form:

$$\frac{\Delta G}{G}(x_g^{av}) = \frac{A_{\mathrm{LL}}^{2h}(x_{Bj}) + A^{\mathrm{corr}}}{\lambda}\,. \tag{3.26}$$

This formula corresponds to the spin helicity asymmetry A_{LL}^{2h}, measured directly from data, plus a correcting asymmetry A^{corr} involving mainly the virtual photo-absorption and the gluon radiation processes. The λ factor relates the partonic asymmetries and the fractions of the involving processes.

In the high p_T analysis the partonic asymmetries and the process fractions need to be estimated using a dedicated and well tuned Monte Carlo (MC) simulation. This analytical approach is used in the present work. All the details about this approach can be found in section 8.1.

A similar analysis was performed for the $Q^2 < 1$ $(\mathrm{GeV}/c)^2$ data, which contains $\sim 90\%$ of the whole Q^2 range. This separation is due to the physical processes contained in the two Q^2 regimes. The $Q^2 < 1$ $(\mathrm{GeV}/c)^2$ regime represents the quasi-real photon, which in such conditions may exhibit some inner structure. Therefore besides the already mentioned three intervening processes, the inclusion of photon structure processes in the MC simulation needs to be accomplished. Details of this analysis can be found in [48].

3.3 Direct Measurement of the Gluon Polarisation in $p-p$ Collisions

Along with the measurements in DIS, the gluon polarisation can also be extracted using $p-p$ collisions. In this case, the involved processes in the $\Delta G/G$ determination in the lowest order of QCD are depicted in figure 3.8.

The double spin helicity asymmetry A^i_{LL} for a particular reaction among the already mentioned processes is given by the expression

$$A^i_{\mathrm{LL}} = a^i_{\mathrm{LL}} \cdot \frac{\Delta f^i_1}{f^i_1} \frac{\Delta f^i_2}{f^i_2} \,. \tag{3.27}$$

The partonic cross section asymmetry a^i_{LL} for each process is calculated in perturbative QCD. $\Delta f^i / f^i$ are the spin dependent to spin averaged parton density function ratios. According to the processes in 3.8 one of these parton density function ratios equals to $\Delta G/G$. Nevertheless extracting the gluon polarisation $\Delta G/G$ from these sums becomes a major complex task. In this way an alternative method is given: the results of the longitudinal double spin asymmetry are presented and compared to different scenarios for the spin dependent parton distribution ΔG.

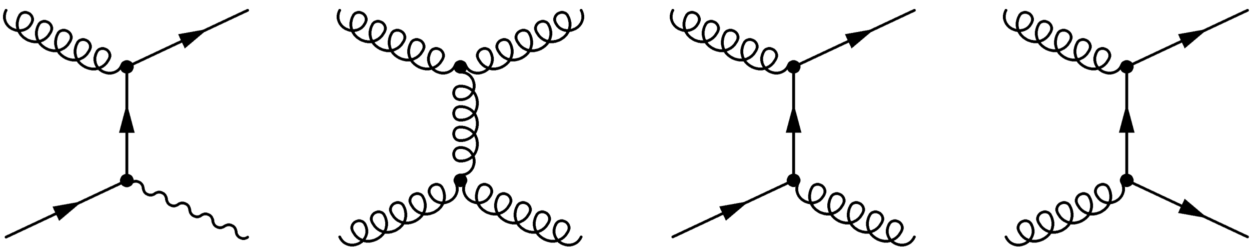

Figure 3.8: Processes involved in the gluon polarisation measurement in $p - p$ collisions.

The concerned processes are briefly described below:

Prompt Photon Production

In this process, a quark from one proton scatters with a gluon exchanging a quark and producing a photon and a quark. Photon production can be achieved by the $qg \to \gamma q$, figure 3.8, and $q\bar{q} \to \gamma g$ channels. Yet, for $p - p$ collisions, the former process is favoured, since the proton quark densities are larger than the antiquarks ones. Events produced by this process have a very clean signature: one isolated photon cluster without any jet debris nearby [49] .

Jet Production

The jet production is done by the $gg \to gg$ and $gq \to qg$ channels. At high energy collisions ($\sqrt{s}$ = 500 GeV/c), clearly structured jets are copiously produced by the originally created quark and gluon. A high p_T analysis can be performed for the leading hadrons in this case.

Heavy Flavour Production

The heavy flavour production in hadronic collisions is dominated by the $gg \to Q\bar{Q}$ reaction, the so called *gluon gluon fusion* process, where $Q\bar{Q}$ are a heavy quark (t and b) and antiquark pair. As stated in the prompt photon production, the $q\bar{q} \to Q\bar{Q}$ is strongly suppressed.

Part II

Experimental Framework

CHAPTER 4

THE COMPASS EXPERIMENT

In this chapter the COMPASS experiment described in detail. The experimental apparatus is briefly described in section 4.1. The polarised beam and target are presented in sections 4.2 and 4.3. The trigger system is described in section 4.4. And, finally, the last section of this chapter (sec. 4.5) is dedicated to the COMPASS data acquisition system.

4.1 The COMPASS Spectrometer

COMPASS is a deep inelastic scattering experiment located in the Super Proton Synchrotron (SPS) accelerator at CERN. It is dedicated to the spin structure of the nucleon and to hadron spectroscopy physics. The experiment consists of three main components: a polarised muon beam, a polarised target and a two-stage spectrometer. The COMPASS spectrometer, illustrated in figure 4.1, covers a large kinematic region (10^{-4} (GeV/c)$^2 < Q^2 < 60$ (GeV/c)^2, $10^{-5} < x_{Bj} < 0.5$). Each stage spectrometer is composed by a magnet, tracking chambers and trigger devices. The first spectrometer is located downstream from the polarised target; it covers an acceptance of ±180 mrad and its magnet (SM1) has a bending power of 1 Tm. Therefore, this spectrometer is mainly devoted to low momentum particles, being also known as large angle spectrometer (LAS). The next spectrometer is the small angle spectrometer (SAS) and is devoted to high momentum particles; it covers an acceptance of ±30 mrad, and its magnet (SM2) has a bending power of 4.4 Tm. The tracking system is distributed in both stage spectrometers and it can be divided into three main zones: very small area trackers (VSAT): the set of tracking planes between the solenoid magnet and the LAS magnet; the small area trackers (SAT): the set of tracking planes between the LAS and SAS magnets; and large area trackers (LAT): the set of planes after the SAS magnet.

For a more complete description about the experimental apparatus the reader is addressed to [50].

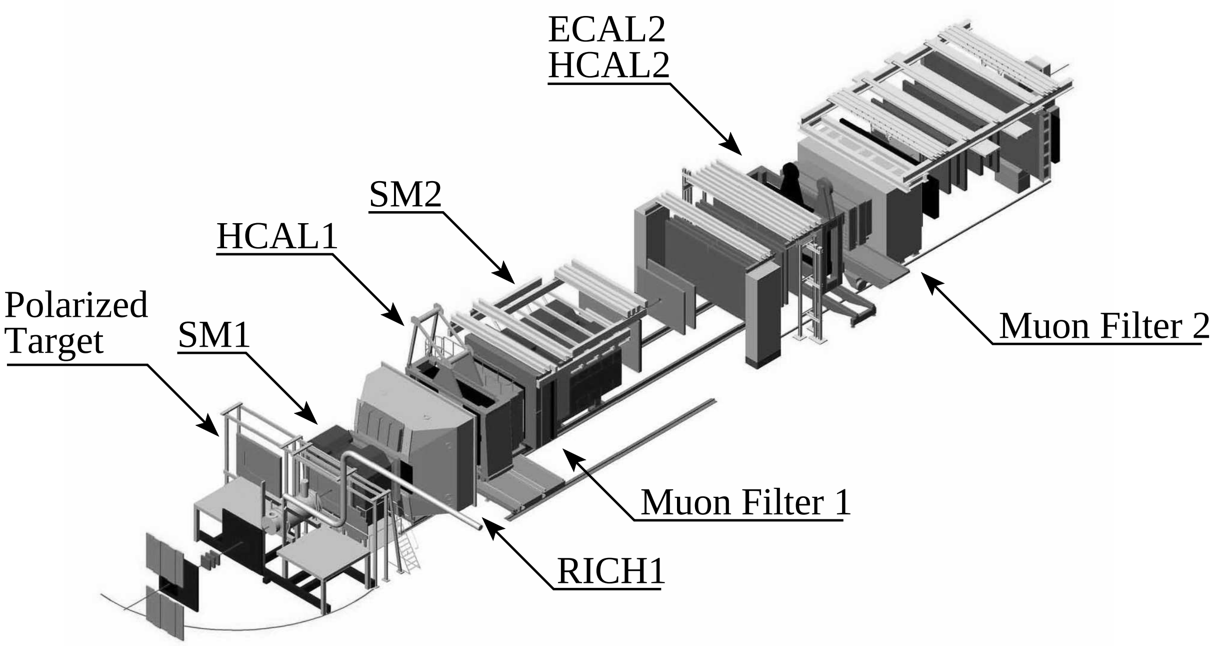

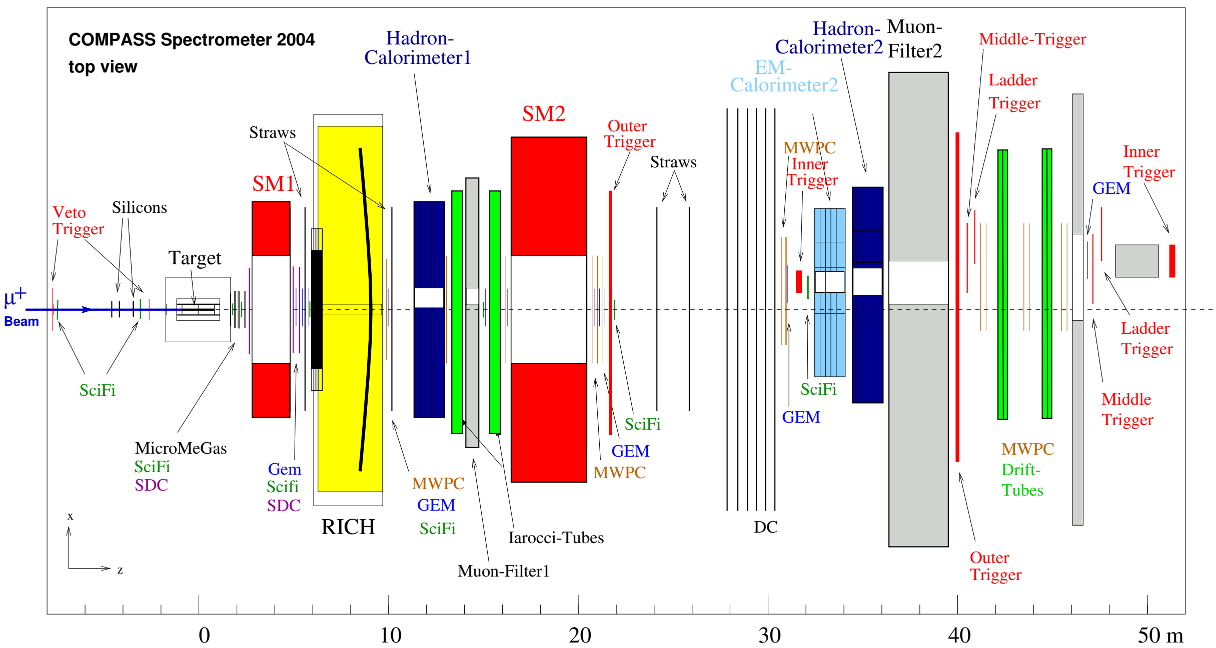

Figure 4.1: Compass 2004 muon setup (top) artistic view, (bottom) top view (for detector names, see text).

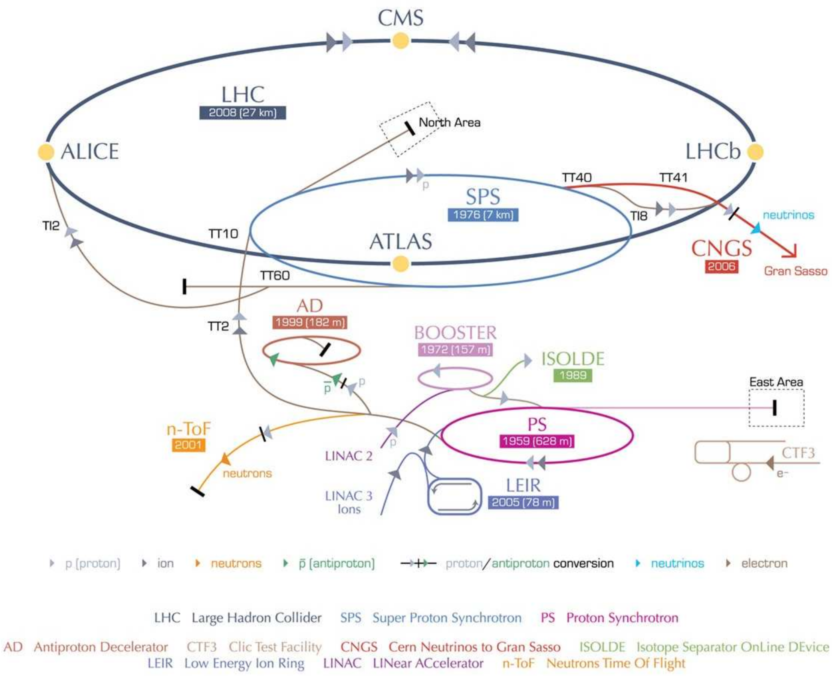

Figure 4.2: Schematic drawing of the CERN accelerator complex.

4.2 The Polarised Beam

The data used in the present work was produced with a naturally polarised lepton beam composed by positive muons. In figure 4.2, a scheme of the CERN accelerator complex is shown. Initially protons (H^+ ions) are extracted from a hydrogen plasma [51], then injected into the proton synchrotron (PS), passing through the linear accelerator LINAC2 and the proton synchrotron booster (PSB). These protons are then transferred to the super proton synchrotron (SPS). The total cycle time of the SPS machine, *i.e.* the duty cycle time from the first injection of the protons into the SPS until the end of the extraction time, was 16.8 s.

Figure 4.3 shows the behaviour of the proton beam intensity in a SPS duty cycle as a function of time. Initially, the protons are injected in two bunches; this can be seen by the sharp increase of the intensity in two steps; then, the acceleration phase occurs, in which protons are accelerated up to 400 GeV/c. During the extraction phase the proton beam is released, with an intensity of the order of 10^{13} particles. It then collides with a 50 cm thickness beryllium target, the so called T6 target, producing pions and kaons with an energy around 172 GeV/c. The beam is delivered onto the T6 target within a time period window of 4.8 s; this period is called *spill* time.

To produce the muon beam in the COMPASS experimental hall, these hadrons are allowed to travel through the 600 m long channel of the M2 beam line [52], leading to around 5 % of the pions to decay into muon and neutrino. The transport of all the particle ensembles, muons, parent and remain hadrons, along the 600 m long decaying channel involves a very accurate optics of several magnets regularly spaced and alternately placed focusing and defocusing (diverting) (FODO) quadrupole system. The unwanted hadrons are stopped by a 9.9 m long beryllium absorber. The beam arrives at the experimental area accompanied by a halo composed essentially by muons which are out of the beam core, the so called spot size of the target ($\sigma_x \times \sigma_y = 8 \times 8$ mm^2). This halo is due to the fact that the magnet optics of the FODO

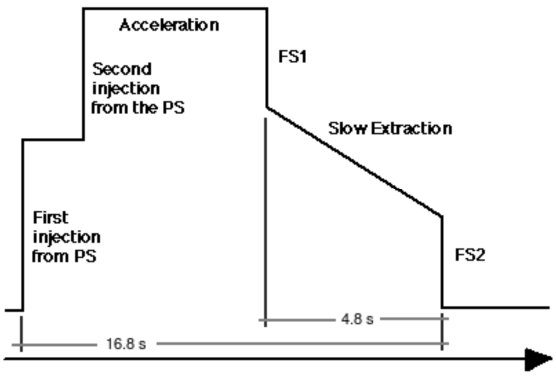

Figure 4.3: Behaviour of the proton beam intensity in a SPS duty cycle as a function of time.

region focuses the beam core, but this has the side effect of diverting the outer muons of the beam profile distribution.

Due to the parity violation in weak decays, these newly produced muons are naturally polarised. The polarisation of a naturally decayed positive muon, from a pion or a kaon, in the laboratory frame, can be calculated using the muon and its parent hadron kinematics [7]:

$$P_\mu = -\frac{m^2_{\pi,\,K} + (1 - 2E_{\pi,\,K}/E_\mu)m^2_\mu}{m^2_{\pi,\,K} - m^2_\mu} \,. \tag{4.1}$$

In the last equation, E_μ, $E_{\pi,\,K}$, m_μ and $m_{\pi,\,K}$ are the muon and its parents hadron energies and masses.

The beam momentum has a large spread; in some cases it can reach 5 %, due to the high intensity flux used. For an accurate measurement of the beam momentum, each muon momentum is measured by the beam momentum station (BMS). The BMS is composed by three consecutive dipole magnets (B6), these dipoles are surrounded by four quadrupole systems (Q29-Q32) and six hodoscopes (BM01-BM06). In figure 4.4 the BMS is illustrated. Hodoscopes BM01-BM04 are composed by 64 scintillating strips each, horizontally aligned. In the central region of the hodoscopes the strips are divided into several elements to ensure that each one is not exposed to a particle flux higher than $1 \times 10^7\ s^{-1}$. The readout is done by fast photomultiplier tubes, with a time resolution of 0.3 ns. In order to improve the beam detection efficiency, two scintillating fibre hodoscopes were included in between of each existing hodoscope pair. These scintillating fibre hodoscopes consist of eight layers of scintillating fibre, each layer being composed by cylindrical fibres with 2mm of diameter adjacently aligned as illustrated in figure 4.5. The BM05 plane has 64 readout channels, two columns per layer pair, to form a channel. For BM06 the channels are formed individually one per layer, thus in this case this plane has 128 channels.

The dependence of the beam momentum upon the track coordinates was parametrised using a dedicated MC simulation. The purpose of this parametrisation is to determine the muon track momentum to a precision of less than 1 %.

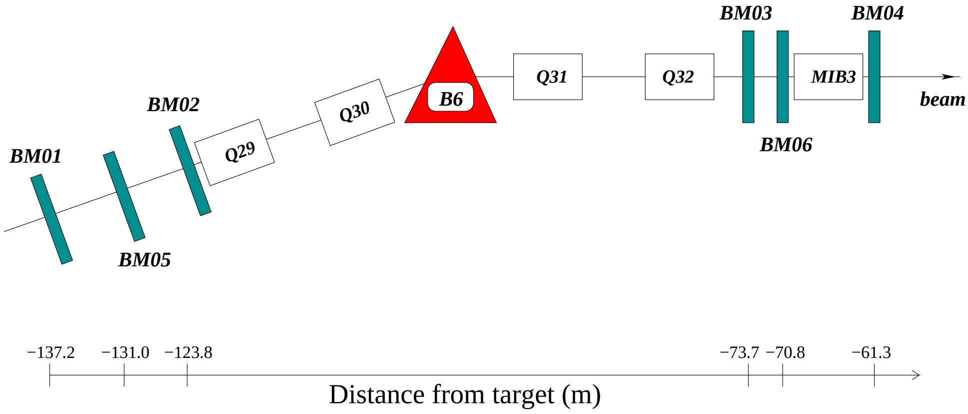

Figure 4.4: Layout of the Beam Momentum Station for the COMPASS muon beam.

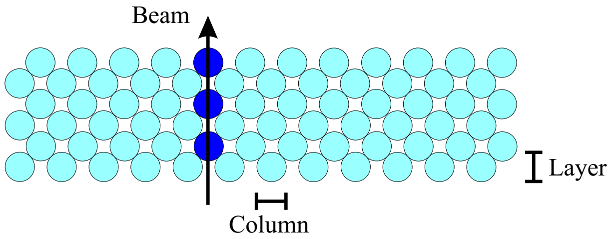

Figure 4.5: The BMS hodoscopes BM05 and BM06 have four stacks of two layers. In this figure three double layers are represented.

4.3 The Polarised Target

The purpose of the polarised target is to provide polarised deuterons, *i.e.* deuterons with a specific spin orientation. It is possible to polarise the deuterons by transferring the electron spin to the nucleons applying a microwave field with an appropriate frequency to the target material. This method is called dynamic nuclear polarisation (DNP) technique [53]. Therefore, it is required to polarise electrons by simply using a strong magnetic field at very low temperature: in these conditions, unpaired electrons become paramagnetic centres, with a polarisation of ~ 0.998, whilst the nucleons have ~ 0.001. Using solid-state deuterated lithium, ^{6}LiD as target material, a high degree of deuteron polarisation, above 40%, may be reached.

The deuterated lithium target material is produced by synthesising highly enriched ^{6}Li and pure deuterium gas via the following reaction $2\mathrm{Li} + \mathrm{D}_2 \rightarrow 2\mathrm{LiD}$, performed in a specially designed furnace at temperatures between 700 and 1000 K. After a slow cool down, small ^{6}LiD crystals of 2-4 mm size are produced [54]. These ^{6}LiD crystals are enclosed in cells and filled with a ^{3}He/^{4}He cooling liquid mixture. In the years 2002 to 2004, the polarised target was composed by two cylindrical target cells. Each cell was 60 cm long and had a radius of 3 cm. The target cells are placed longitudinally one after the other with a gap of 10 cm, having then the up and down-stream target cells. For 2006, instead of two, three longitudinally placed target cells were used; the most up and down-stream target cells are 30 cm long, the central one is 60 cm long, the gaps between central cells and the up and down-stream is 5 cm each.

In figures 4.6 and 4.7, the polarised target apparatus used in years 2002–2004 and 2006, respectively, are depicted. The 2002-2004 apparatus incorporates most of the elements used in the SMC (NA 47) experiment [55]. The polarised target apparatus consists in a ^{3}He/^{4}He dilution refrigerator system which keeps the target material at a low temperature of between

55 and 95 mK, a superconducting solenoid in a vessel with a highly homogeneous magnetic field of 2.5 T along the longitudinal (beam) direction, and also a dipole coil magnet with a 0.42 T magnetic field. A microwave cavity inside the solenoid surrounds the target material. The solenoid vessel had an angular aperture of ~ 70 mrad up to 2004. In 2006, the major change on the target apparatus was on its solenoid angular aperture, ~ 180 mrad. As a consequence, the solenoid, dipole magnets and also the microwave cavity needed to be adapted to this new design.

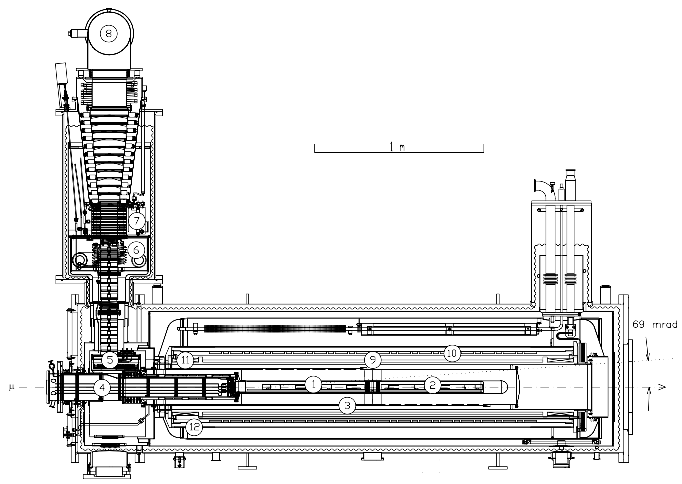

Figure 4.6: Side view of the 2002–2004 COMPASS polarised target: (1) upstream target cell and (2) downstream target cell inside mixing chamber, (3) microwave cavity, (4) target holder, (5) still (^{3}He evaporator), (6) ^{4}He evaporator, (7) ^{4}He liquid/gas phase separator, (8) ^{3}He pumping port, (9) solenoid coil, (10) correction coils, (11) end compensation coil, (12) dipole coil. The muon beam enters from the left. The two halves of the microwave cavity are separated by a thin microwave stopper.

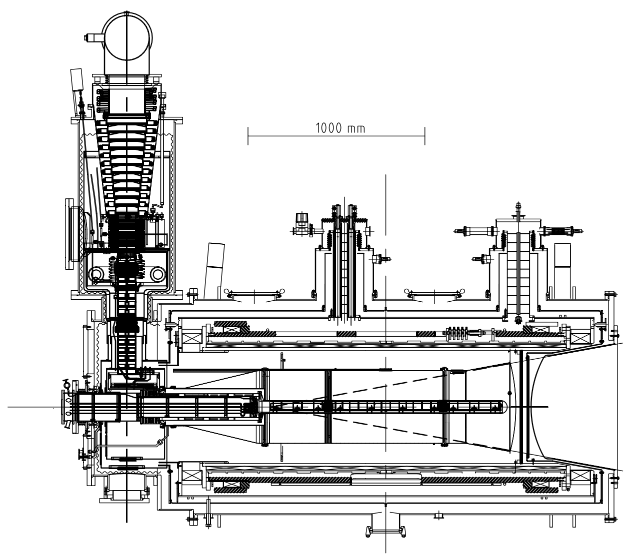

Figure 4.7: Side view of the 2006 COMPASS polarised target.

The target cells can be independently polarised using the DNP technique since the cell are separated by a microwave stopper. Therefore, irradiating each cell with an appropriate Larmor frequency leads to a controlled cell polarisation. The microwave frequency depends on the spin configuration of the electron-deuteron (e-d) system. The spin configurations are achieved by setting the frequency to $|\omega_e - \omega_D|$, which will flip the spins of the aligned e-d system, from this configuration ($\downarrow\Downarrow$) to this one ($\uparrow\Uparrow$). Using the frequency $|\omega_e + \omega_D|$ will flip the spin anti-aligned e-p system, from ($\downarrow\Uparrow$) to ($\uparrow\Downarrow$). The frequencies ω_e and ω_D are the Larmor frequencies of the electron and deuteron, respectively. In both cases the e-d system is in a high energy state. After flipping the spins of the e-d system, the electron spin will relax to a lower energy state within milliseconds due to its high magnetic moment. This process is illustrated in figure 4.8. On the other hand the small magnetic moment determines a low probability for the nucleon spin flip. In this way, the target cell polarisation is built. Nuclear magnetic resonance (NMR) coils made of a cupronickel (CuNi) alloy, with teflon coating containing carbon and fluor, are located around the target cells and are used to measure and monitor the cell polarisation.

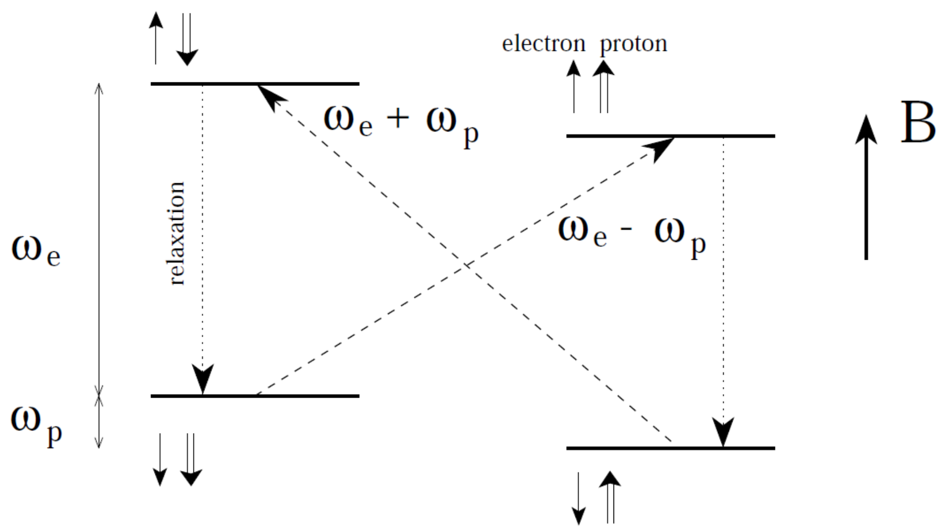

Figure 4.8: Scheme of the energy levels for the e-d state in a strong magnetic field B. The arrows indicate direction of the electron $\uparrow$ and deuteron $\Uparrow$ spins; ω_e and ω_D are Larmor frequencies of the electron and deuteron, respectively. The figure comes from Ref. [56]

4.4 The Trigger System

The main purpose of the trigger system is to decide, in a very high event rate environment, within a very short time period ($\sim$ 500 ns) and minimum dead time, if an event is interesting for physics analysis. In this sense, a trigger system to detect the scattered muons was conceived [57]. The trigger system also provides the time reference for the events to trigger the readout system of the detector and front-end electronics.

The trigger system is composed by a set of scintillator hodoscopes projected to detect the scattered muon angle. In a general way, taking into account equation (2.1), the scattering muon angle increases with Q^2. Thus, this system takes into account the event kinematics. For this reason, the trigger system is optimised to select two kinds of events: *quasi-real photon*

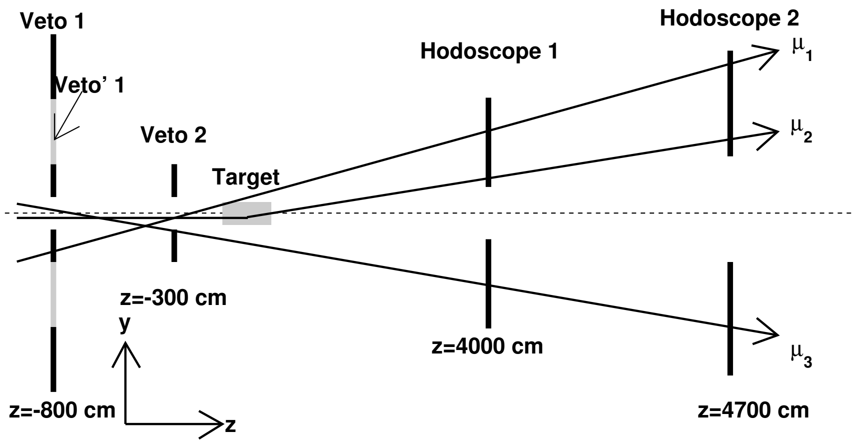

Figure 4.9: Schematic layout of the veto system. The tracks μ_1 and μ_3 are vetoed, whereas the track μ_2 fulfils the inclusive trigger condition.

and *DIS* events. To cope with the kinematic requirements, four different hodoscope sets were designed. For the quasi-real photon kinematic region (low Q^2):

- Inner Trigger hodoscopes: dedicated to events for which the scattering muon has very small angles leading to a range in energy loss y obeying $0.1 < y < 0.5$.
- Ladder Trigger hodoscopes: for photo-production events with a large scattering muon energy loss y, $0.5 < y < 0.9$.

And for the DIS region (high Q^2):

- Middle Trigger hodoscopes: focused on the detection of DIS events with small to moderate Q^2.
- Outer Trigger hodoscopes: for DIS events with high Q^2.

Each trigger hodoscope is composed by two planes, which allow to validate the trigger detection by a coincidence matrix. This matrix correlates the coincidence time between hits in the slabs of the pair of planes of the corresponding trigger. A tight time window allows to reject any potential spurious coincidence.

Two additional systems were included to improve the purities on the trigger detection. The first system is a set of scintillating veto detectors located upstream the polarised target. The scintillators have holes in the centre that allow the beam particles to pass without any interaction, only the halo particles are expected to hit them, provoking a veto signal. In such cases, if one scattered muon candidate is triggered, the event is rejected. In figure 4.9, the veto system is presented. The second system is the association of the hadronic calorimeters signal to the trigger. The energy deposit on the hadronic calorimeters of an event above a certain threshold rejects background events from muon-electron elastic scattering, radiative events and also events originated from the beam halo.The global idea of the COMPASS trigger system is shown in figures 4.10 and 4.11.

The COMPASS kinematic acceptance is limited in Q^2 by the SM2. In 2003, a pure Calorimetric Trigger was introduced, which signals events with deposit on the hadronic calorimeter

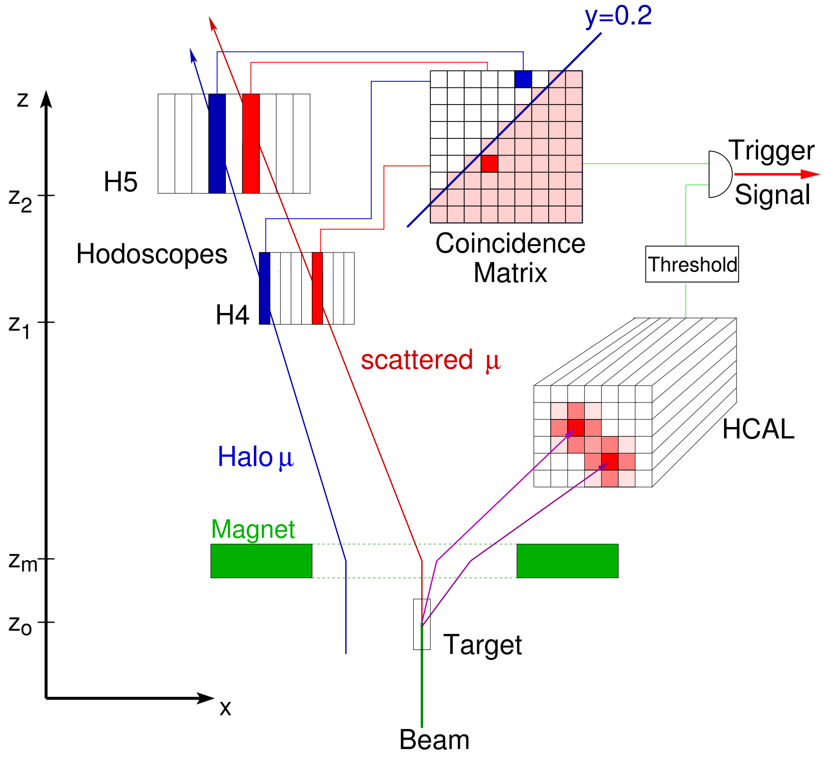

Figure 4.10: Concept of the trigger for quasi-real photoproduction with high energy loss. The scattered muon leads to a coincidence in the activated area of the coincidence matrix while the halo muon fails to do so. In addition, a minimum hadron energy can be required in the calorimeter.

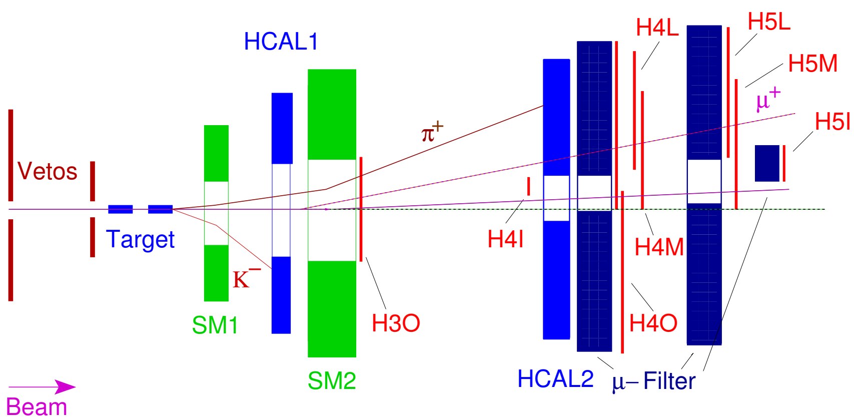

Figure 4.11: Location of the components relevant for the trigger (schematically).

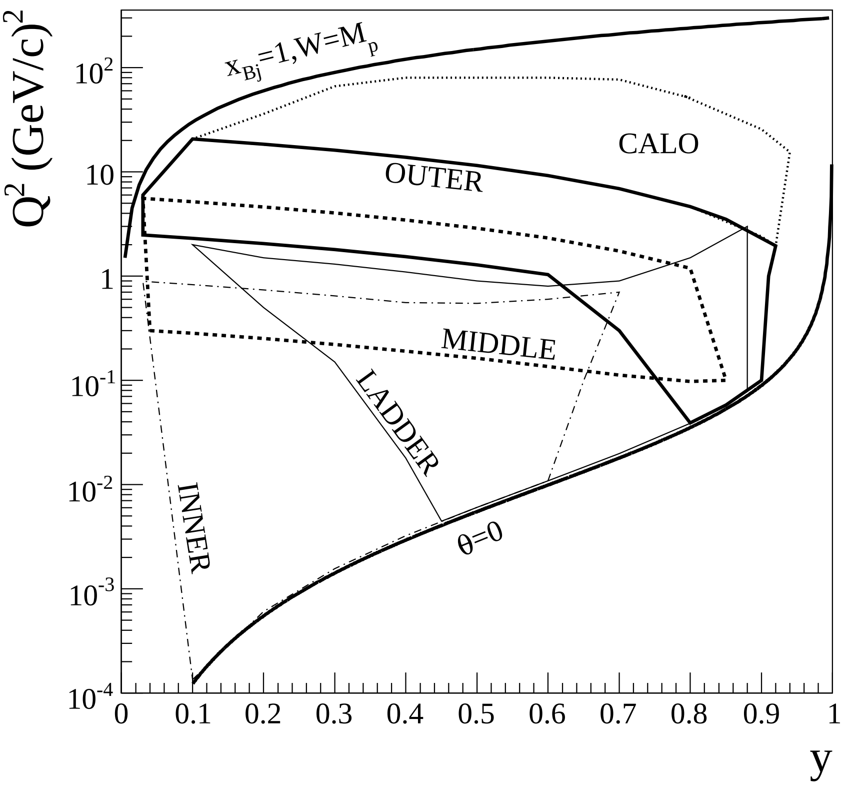

Figure 4.12: The kinematic coverage in y and Q^2 for the four hodoscope trigger subsystems and the standalone calorimetric trigger. The two lines, $x_{\mathrm{Bj}} = 1, W = M_{\mathrm{p}}$ and $\theta = 0$ show the kinematic limits of elastic scattering and forward scattering, respectively.

above the so called calorimetric high threshold. This trigger increased the COMPASS kinematic acceptance. In figure 4.12 the kinematic coverage of the triggers is presented. It shows the range in y and Q^2 for the four hodoscope trigger subsystems and the standalone calorimeter trigger.

With the information about the hadronic energy deposits the triggers may have a new classification:

- Inclusive Triggers: these triggers require only hits on the hodoscopes. This is the case of the Outer and Inclusive Middle Triggers.
- Semi-inclusive Triggers: these triggers require hits on the hodoscopes **and** energy deposit on the hadronic calorimeters. This is the case of the Inner, Ladder and Middle Triggers.
- pure Calorimetric Triggers: these triggers require energy deposit on the hadronic calorimeters above the high calorimetric threshold.

4.5 The Data Acquisition System

The purpose of the Data Acquisition (DAQ) system is to ensure that, during the data taking periods, data is collected and safely recorded. In this section, the architecture and the data

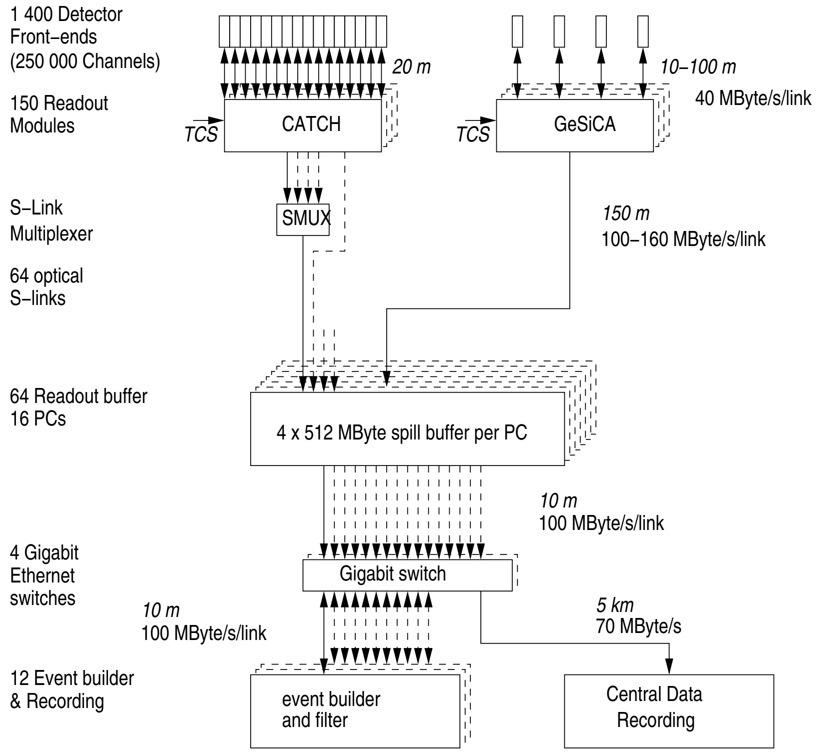

Figure 4.13: General architecture of the DAQ system. Digitised data from the detector front-ends are combined on the readout modules named CATCH and GeSiCA close to the detectors. The storage of the data during the spill and the event building is performed locally. The data are stored at the CERN computer centre.

flow will be explained. The COMPASS spectrometer has more that 250k channels from all its detectors. After digitising all these channels on the front-end boards, the signals are guided to the readout drivers using Ethernet or optical fibres. COMPASS uses two systems of readout drivers [50]: the COMPASS Accumulate, Transfer Control Hardware (CATCH) and the GEM Silicon Control and Acquisition (GeSiCA). Then data is transferred to the spill buffers that are located in the ReadOut Buffer (ROB) computers. Data is sent to event builder (EVB) computers; at this point the raw events are being assembled. The complete events are transferred to the Central Data Recording (CDR) at CERN and stored into tapes for long term storage. In figure 4.13 a scheme is presented showing the data acquisition process flow and the intervening systems.

The DAQ and detectors performance must be monitored during the whole period of data taking. To serve this purpose some tools are designed:

- Murphy/TV: allows to monitor the readout errors returned by the readout drivers.
- COOOL (COMPASS Object Oriented On Line): provides a quick monitoring of the detectors performances by comparison with reference histograms.
- DCS (Detector Control System): monitors all available parameters of various spectrometer elements, *e.g.* temperatures, currents, voltages, gas flows, *etc.* The control is done by pre-established alarm and threshold sets indicating any abnormal behaviour.

CHAPTER 5

UPGRADE OF THE RICH-1 DETECTION SYSTEM

For the data taking from 2006 on, an important upgrade of the COMPASS apparatus is implemented, in particular for the Ring Imaging CHerenkov (RICH-1) . The purpose of this chapter is to describe the upgrade in the COMPASS RICH-1 detector with respect to the simulation. The RICH detector and simulation systems and also its upgrade are described in the next two sections (5.1 and 5.2). Finally the characterisation procedure and results of the multianode photomultiplier, used in the upgrade, are presented.

5.1 The RICH Detector and Its Upgrade

The COMPASS RICH-1 [58] is a large-size Ring Imaging Cherenkov detector which performs hadron identification in the momentum domain between 5 GeV/c and 43 GeV/c. It has large transverse dimensions (it covers the whole angular acceptance of the COMPASS LAS, i.e. ± 250 mrad in the horizontal plane and ± 180 mrad in the vertical plane), high-rate capability and introduces minimum material in the region of the spectrometer acceptance. Its large-volume vessel (see Fig. 5.1) is filled with C_4F_{10} radiator gas. Cherenkov photons emitted in the gas are reflected by two spherical mirror surfaces. The photons are converted to electrons by the CsI photocathodes of eight Multi-Wire Proportional Chambers (MWPCs), which amplify the single photoelectrons and detect them.

In 2005, the RICH-1 detector was upgraded, its central part was instrumented with a system based on Multi-Anode Photo-Multipliers (MAPMTs) for fast photon detection. The time resolution, of a few ns, allows an efficient rejection of the high background due to uncorrelated events. Each MAPMT is coupled to a telescope composed of a field lens and a concentrator lens. These new detectors replace the four central photocathodes of the CsI MWPCs, corresponding to 25% of the total active surface.

The approach to detect photons in RICH counters with MAPMTs and lenses is not new

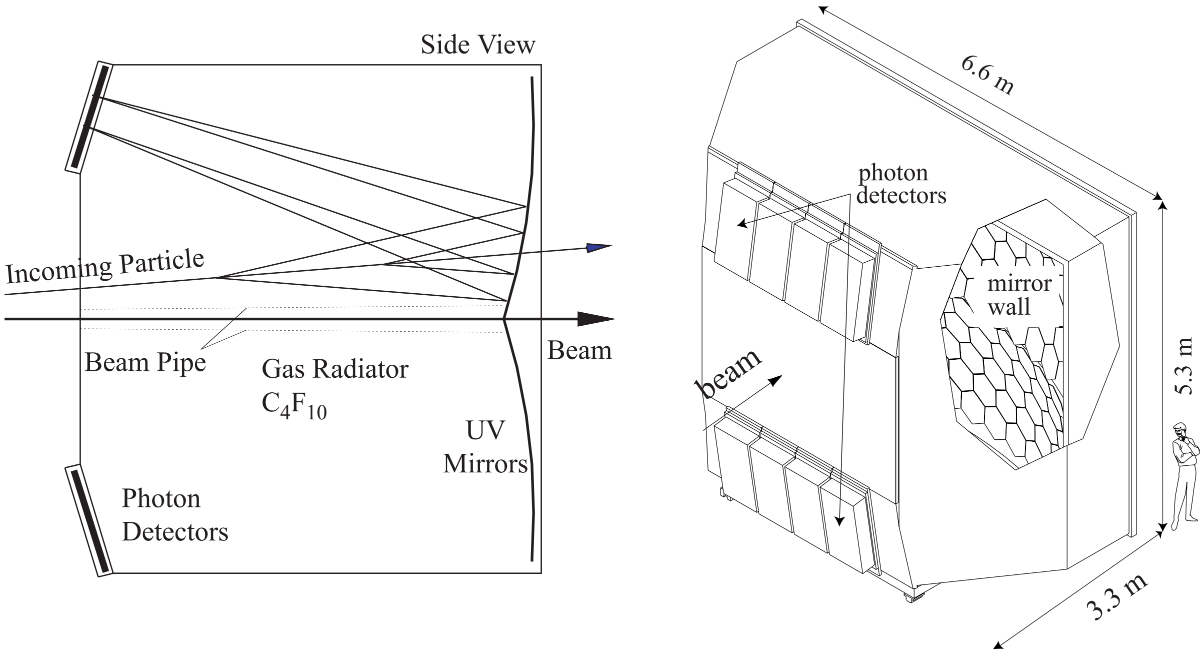

Figure 5.1: COMPASS RICH-1: principle and artistic view.

(HERA-B [59], studies for LHCb [60, 61]). In our design, two new elements are introduced: the detection of visible and UV photons and a largely increased ratio of the collection surface to the photocathode one. We extend the detected range of the Cherenkov light spectrum to the UV domain (down to $\sim$ 200 nm) by using UV extended MAPMTs and fused silica lenses.

The lens telescope has been designed in order to satisfy several important requirements. The image distortion has to be minimised, keeping the telescope length around 10 cm, in spite of the large image demagnification and the large angular acceptance. Simulations show that only about 10% of the photons are not detected in the corresponding MAPMT pixel, but in a nearby one. The telescope must have a large angular acceptance; the value achieved is about $\pm$165 mrad, resulting in an estimated ring loss below 5%. The dead zone should be as small as possible; an accurate mechanical design assures only 2% dead zone between field lenses.

5.2 The RICH-1 Simulation Upgrade

In this section, the main topics of the RICH-1 simulation are highlighted, in particular the RICH-1 simulation upgrade is emphasised. The RICH-1 detector was upgraded with the inclusion in the central region of four new panels in the central region, containing each 144 (12$\times$12) new MAPMTs, each MAPMT has a concentrator device composed by a lens telescope.

The RICH-1 simulation system is composed essentially by three modules, which are illustrated in figure 5.2:

- The RICH apparatus setup is described by the first module. This module is the Monte Carlo (MC) detector simulation software package COMGEANT.

- The photon propagation and digitisation is performed by the second module.

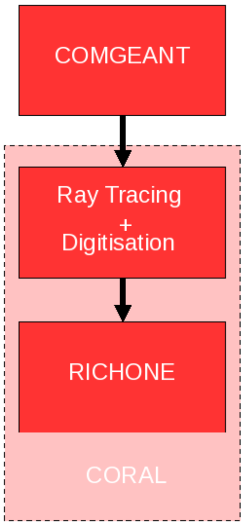

Figure 5.2: The RICH-1 simulation system.

- The rings reconstruction and particle identification is the purpose of the third and last module.

The surface of the first lens of the telescope –also known as field lens– needs to be simulated as a sensitive device, *i.e.* a sensible area to detect the Cherenkov photons.

Figure 5.3 shows the technical drawing of the grid which supports the 144 lenses with (left top figure) and without the lenses (left bottom figure), and also a picture of a machined grid panel (right bottom figure). Based on the parameter design and technical drawing of the panels and the lenses, a similar panel, containing a grid to house the 144 lens surfaces, was included in the RICH-1 detector description in the MC simulation, as depicted in figure 5.3 (centre and top right figures).

The specification of the technical details concerning the spherical lens parameters, namely the radius, (54.9 ± 0.4) mm, and exposure area $((44.8 \times 47.7) \pm 6.5)$ mm^2 [62], led to finally implementation in the MC detector simulation the *boxes* of the grid and the lens surface. In figure 5.4 the field lens as well as the lens telescope system and the MAPMT are illustrated (top left figure); the implementation of the lens in the MC detector simulation by the intersection of the *sphere* with the *box* (bottom right figure).

As mentioned in the beginning of this section, this upgrade was on the four central RICH-1 panel; these panels are named as Top-Jura, Top-Salève, Bottom-Jura and Bottom-Salève [1]. In figure 5.5, the hit distribution in the lens surfaces of the new RICH-1 detector implementation in the MC simulation is presented. On the top left plot, the hit distribution is on the x-y plane; the hit distribution can be seen in the 12 outer CsI panels and also in the four inner panels that contain the new geometry with the lens surfaces. On the top right plot, the hit distribution in the z-y plane is shown; in which the surface curvatures are seen.

In order to assess which lens surface and which panel a Cherenkov photon struck, a coding is defined. The coding is set by an identifier *id*: if $17 < id < 160$, the photon struck one of the 144 lens surfaces in the Top-Jura panel, if $161 < id < 304$, the photon struck one of the lens surfaces in the Top-Salève panel, if $305 < id < 448$, the photon struck one of the lens

[1] Jura and Salève are two mountains which *enclose* our experimental hall. They thus define our horizontal reference. Placing ourselves in the beamline with the beam *hitting* our back, Jura is on our left and Salève is on our right.

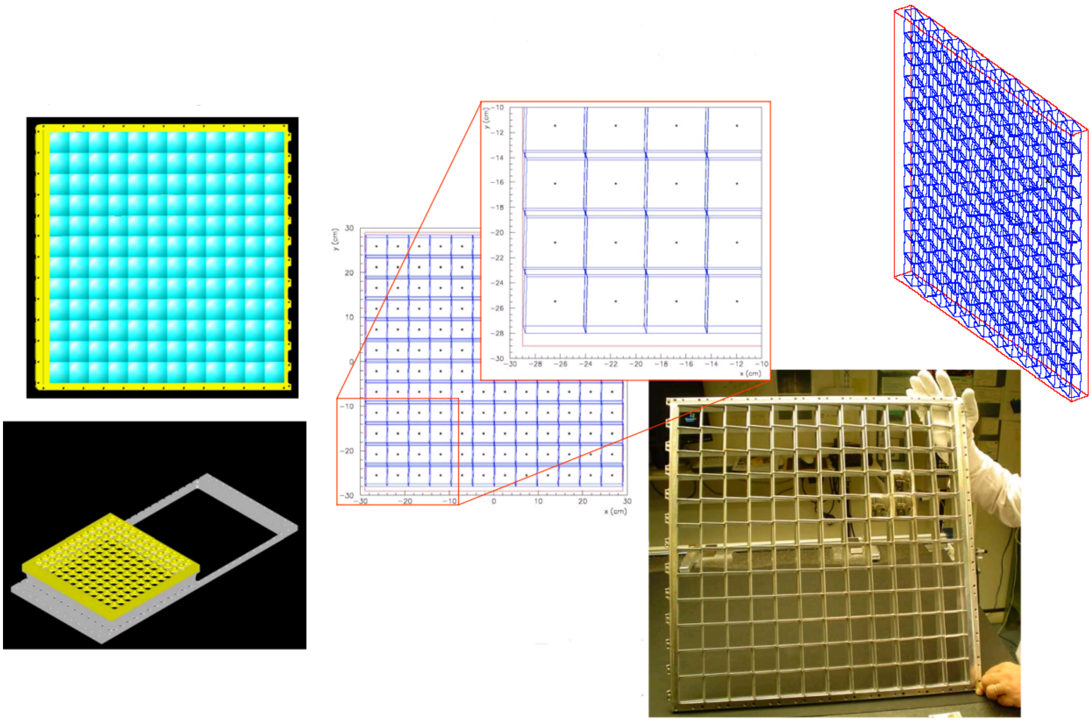

Figure 5.3: Technical drawing of the grid panel which supports the 144 lenses with (left top figure) and without the lenses (left bottom figure). Implementation in the detector MC simulation of the grid panel (centre and top right figure). Picture of a machined grid panel (right bottom figure).

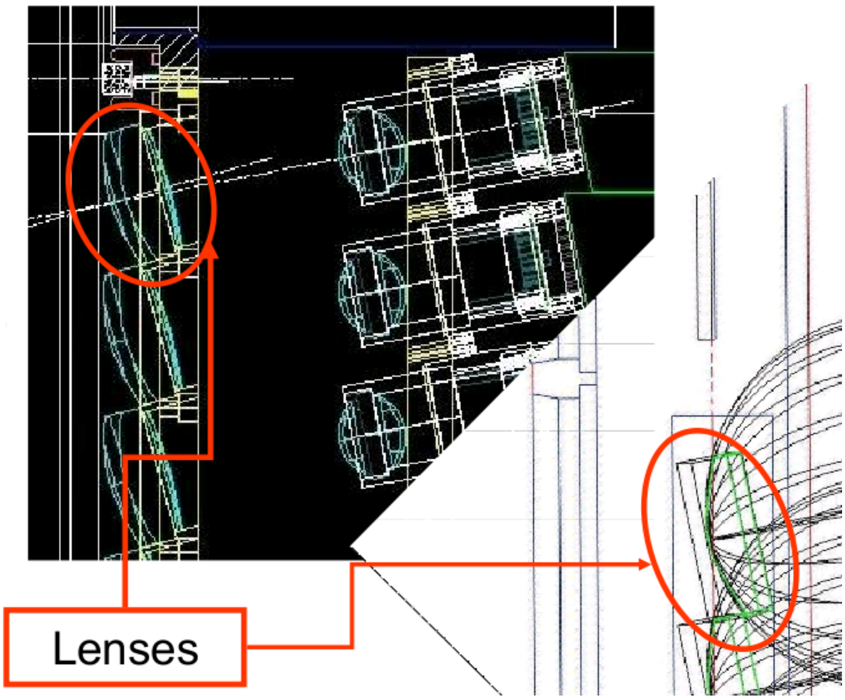

Figure 5.4: The field lens. The field lens and the telescope system (top left) and the field lens implemented in the MC detector simulation (bottom right).

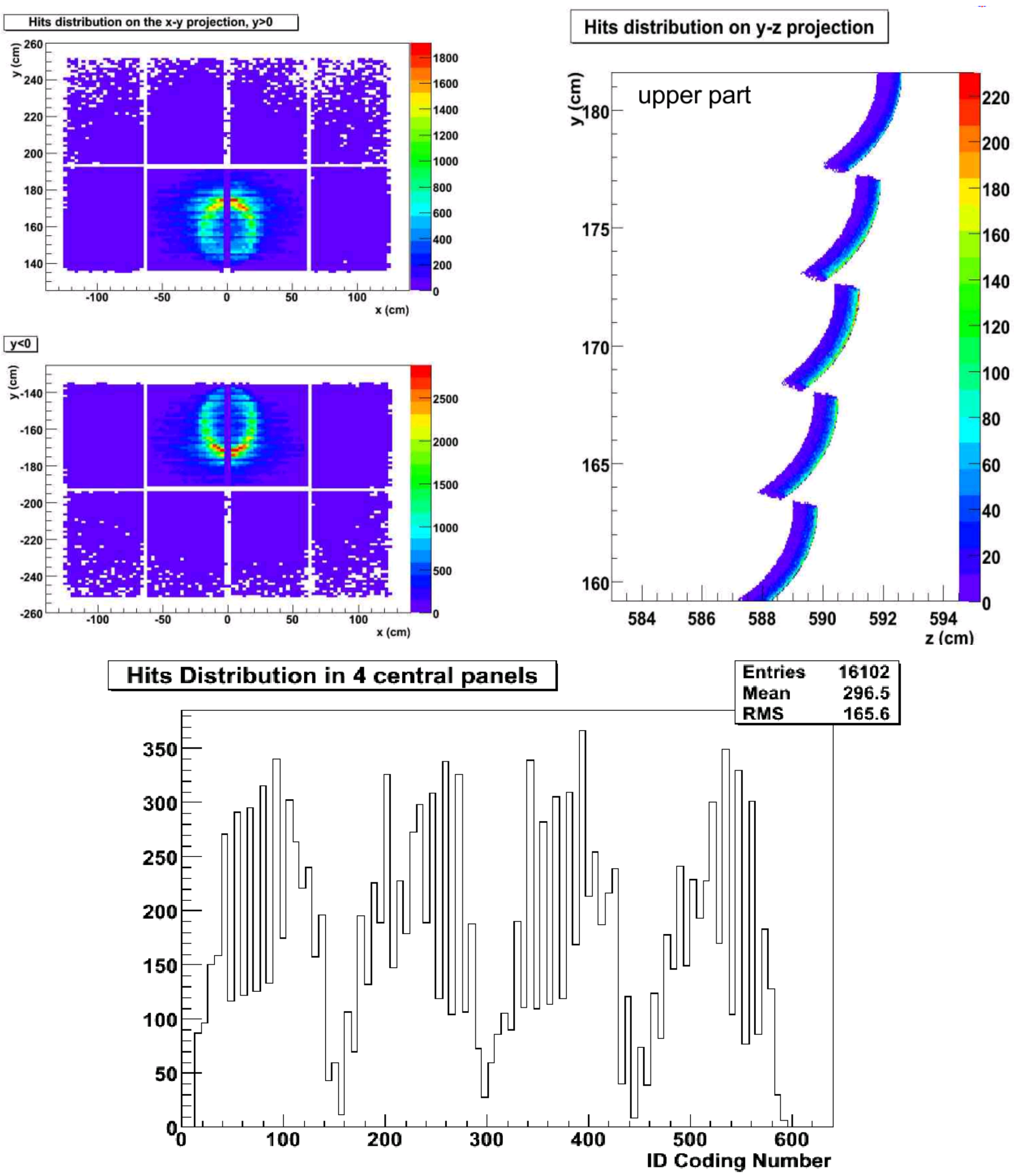

Figure 5.5: Hit distribution in the lens surfaces of the RICH-1 detector implementation in the MC simulation.

surfaces in the Bottom-Jura panel and finally if $449 < id < 592$, the photon struck one of the Bottom-Salève panel lenses. In figure 5.5 the coding distribution is shown (bottom plot).

At this stage, the information of the impact position, direction and energy of each photon for each lens of the telescope is transported to the second module of the RICH-1 simulation: the ray trace and the digitisation. Photons have to be traced through the telescope and the MAPMT pixel hit by the photon has to be determined. The pixel information has to be transformed into some pad (digit) information. The information related to the photon energy is used to calculated the refractive index n of the lens material. Using Snell's law, the photon is propagated to the next surface. The new impact point is computed and this process is repeated until the photon reaches the MAPMT; optionally, an energy dependent efficiency correction is applied.

The information of the digitised photons on the MAPMT pixel pads is used for RICHONE [63], the ring reconstruction software package, using the method described in [64]. In order to determine a PID likelihood, each photon angle is compared to the Cherenkov angle of the mass hypothesis computed using particle momentum and refractive index of the corresponding detector system. The photon angles are renormalised; this allows us to define sharp rings without any discontinuities in the radius.

Detector geometry validation

A sample of MC data containing 30 K events was generated. Some tests were performed to validate all components and its backward compatibility. In figure 5.6, the integrated distribution of ϕ_{photon} is shown (on the right side) and against $\theta_{photon} - \theta_{ring}$ (on the left side). Here θ_{photon} and ϕ_{photon} are the photon polar angles around the particle trajectory from the so called pseudo-pads for the MAPMT cathodes. The plot on the left side shows a very regular behaviour, with all the maxima of the point densities along a straight line well centered at zero; any misalignment in the geometry will result in evident distorsions of the distributions. The distributions on the right side allow a first order evaluation of the single photon resolution; from this plot, the direct conclusion is that photon reconstruction and angular resolution are essentially good within the specifications.

In figure 5.7, the $\theta_{ring} - \theta_{mass}$ distribution (plot at the left top), where θ_{mass} is the Cherenkov angle for a particle assuming the pion mass hypothesis, has been divided in 6 bins of θ_{mass} as indicated, (centre and bottom plots) showing that it is rather well centered at zero, as expected. The top right plot corresponds to the distribution of mean values of the binned $\theta_{ring} - \theta_{mass}$ distributions; the full dots are related to the proposed refractive index, $n = 1.001357$, for the MAPMTs, the open dots are related to the values with the refractive index ($n = 1.001364$) normally used in the ring reconstruction for the CsI outer panels. As expected, the two detecting systems in the RICH-1 detector need two different refractive indices.

Figure 5.8, shows the MC PID (particle identification) efficiencies; the PID is done using the likelihood method [63]. The table on the top shows the efficiency of identifying the particles, generated as indicated in the column label, as shown by the row label (note that we do not ask the RICH-1 to distinguish pions from muons or electrons). On the bottom part of the figure, the distribution of the MC PID efficiency for pions (stars), kaons (open dots) and protons (full dots) as a function of the particle momentum, from 2.5 up to 50 GeV/c, are shown.

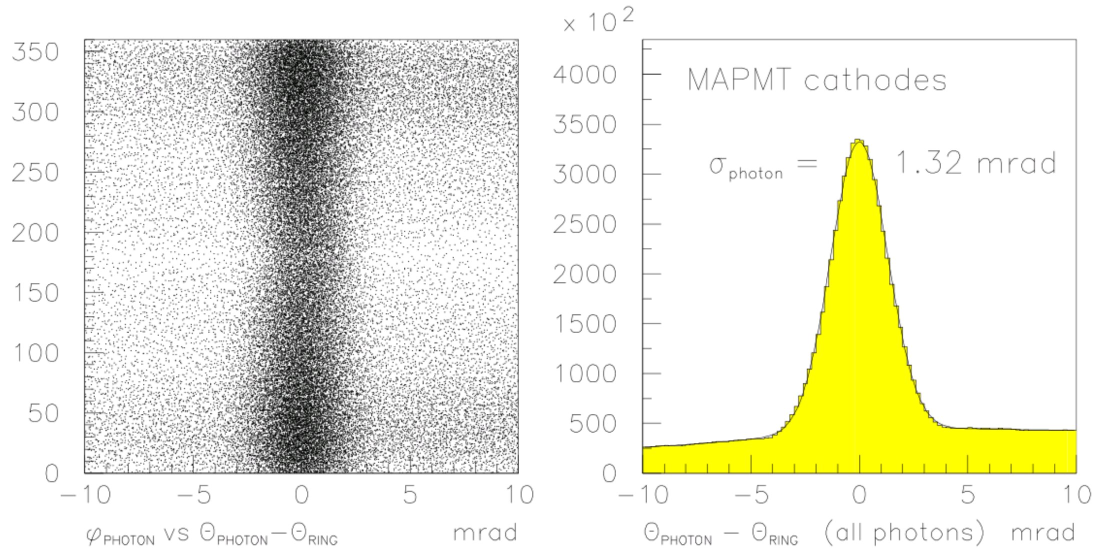

Figure 5.6: ϕ_{photon} against $\theta_{photon} - \theta_{ring}$ (left side) and the integrated distribution of $\theta_{photon} - \theta_{ring}$, where θ_{photon} and ϕ_{photon} are the photon polar angles around the particle trajectory from pseudo-pads for the MAPMT cathodes.

Conclusion

The new implemented geometry in the detector simulation to cope with the upgrade for the central part of the RICH-1 detecting system is able to handle the information of the photons for every single detecting system (576 lens telescopes + MAPMTs). This information is accordingly transported from the simulation to the digitisation and to the reconstruction sytems. This geometry was successfully validated with respect to the reconstruction of the Cherenkov rings.

5.3 Characterisation of the Multianode Photomultiplier Tubes

In order to detect single photons with high efficiency at high beam intensities and trigger rates, the photon sensor should have a rate independent response up to more than 1 MHz per pixel, provide a quantum efficiency of more than 20%, gain factors of about 10^7 and exhibit low dark current.

The Multianode Photomultiplier tubes

For the RICH-1 upgrade, the MAPMT type R7600-03-M16 by Hamamatsu has been chosen. It provides a common bialkali photocathode with 18×18 mm^2 active surface, followed by 16 independent channels, arranged in a 4×4 pixel matrix with 4×4 mm^2 size each, while the gap between two adjacent pixels is 0.5 mm.

The photocathode itself is obtained from vapour deposited on an UV-extended glass window, allowing a spectral sensitivity from 200 to 750 nm. The relative signal amplitude vari-

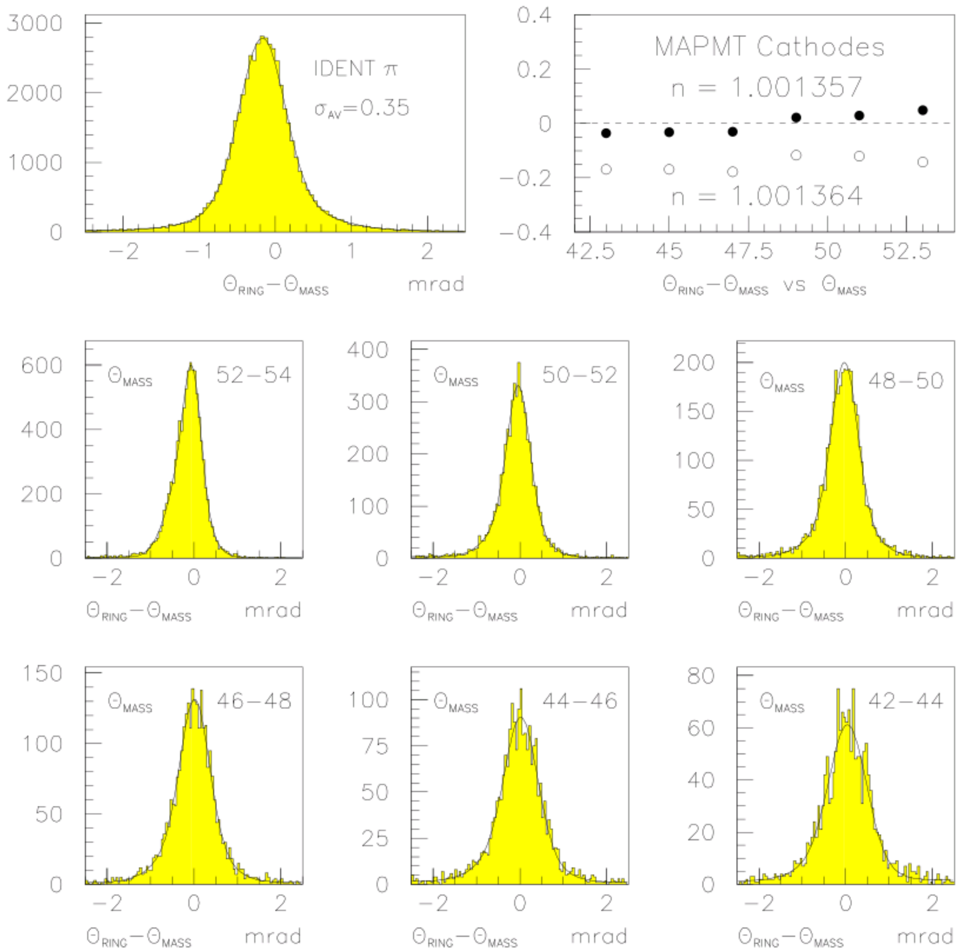

Figure 5.7: $\theta_{ring} - \theta_{mass}$ distribution (top left plot) and the same distribution in bins of θ_{mass} (centre and bottom plots). The distribution of the mean values of $\theta_{ring} - \theta_{mass}$ as a function of θ_{mass} is plotted on the top right side. θ_{mass} is the Cherenkov angle for a particle assuming the pion mass hypothesis.

ations (uniformity) of all 16 channels are specified better to be than 1:3, for the selected MAPMTs, and the cross-talk between neighbouring channels obtained with the RICH-1 readout chain has been measured to be less than 1% [65]. The electron multiplication is done with a 12-stage metal-channel type dynode structure, resulting in a typical gain of 6×106 at 850 V (maximum voltage: 1000 V). Using the MAPMT equipped with the standard voltage divider circuit proposed by Hamamatsu, it was shown that no significant gain reduction occurs even at single photon rates above 5 MHz per channel [65]. An outstanding parameter of this device is the dark current, which is specified to be less than 2 nA per channel.

Experimental Procedure and Setup

To guarantee that the complete set of 576 MAPMTs used in the upgraded RICH-1 detector fulfills all specified parameters and that all the 9216 channels are operated at the optimum working point, an experimental method was designed and implemented with an automated test setup. The experimental setup is schematically illustrated in figure 5.9.

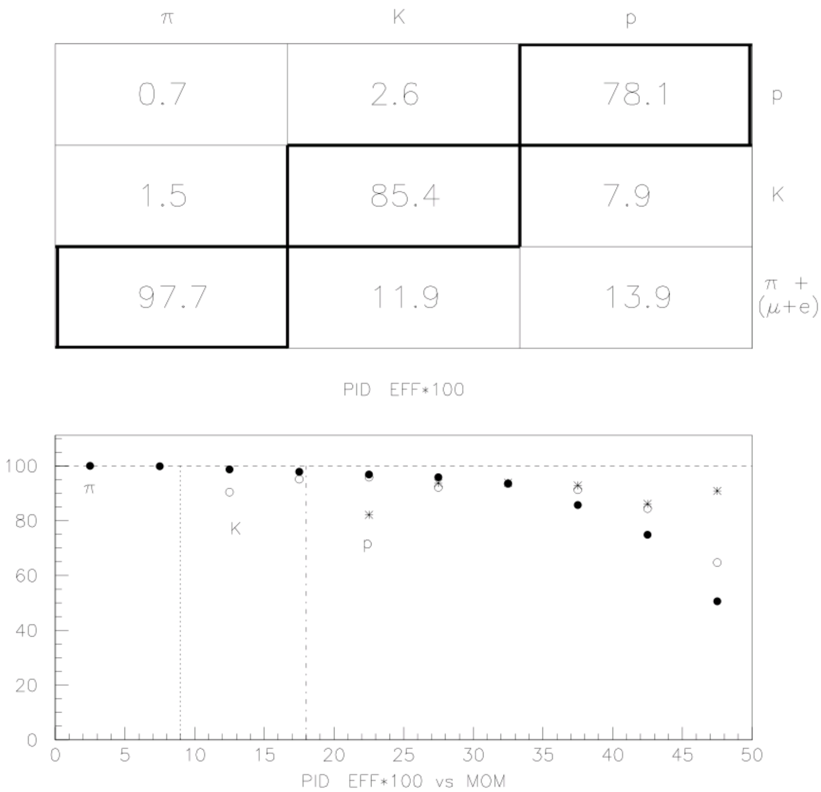

Figure 5.8: On the top part, the table shows the efficiency of identifying the particles, which are divided into pions, kaons and protons, in columns, according to the MC truth information. The values of the efficiencies for the protons, kaons and pions (together with muons and electrons) are given in rows. On the bottom part of the figure, the distribution of the MC PID efficiency for pions (stars), kaons (open dots) and protons (full dots) as a function of the particle momentum.

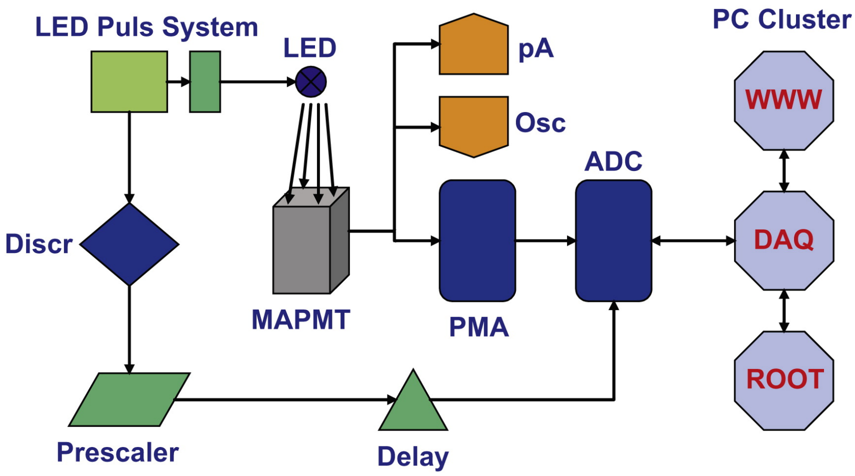

Figure 5.9: Scheme of the test setup showing analog-to-digital converter (ADC), dark current measurement (pA), oscilloscope analysis (osc), data acquisition (DAQ), online monitoring and analysis system based on ROOT [66] (ROOT), data storage and web hosting (WWW).

A pulsing LED system illuminates homogeneously the photocathode of the MAPMT and concurrently generates a trigger signal as gate for the analog-to-digital converter (ADC). The frequency of the LED pulses can be adjusted from 1 Hz up to 2 MHz. To study the single photon response, polarisation filters placed directly in front of the LED are used. The MAPMT output signals are amplified by a factor of 10 by LeCroy PMA 612A modules and then digitised by CAMAC charge sensitive ADCs of type LeCroy 2249A (10 bit, 0.25 pC per bin). The data acquisition system is based on CAMAC (CC16 by Wiener). Due to basic limitations of the CAMAC ISA controller, the trigger signal is prescaled and therefore the read-out reduced to 1 kHz. The high voltage for the MAPMT is provided and monitored by a four channel HV power supply by WENZEL. Dark current measurements by a Keithley picoamperemeter model 6485, and signal inspection at the scope are performed upstream of the PMA stage and a 16-fold relay circuit allows to switch among different channels and measurements. The complete system is fully controlled via a Debian Linux system based on kernel 2.6×.

The measurement protocol of each MAPMT lasts 2 h and it includes: the visual inspection of the cathode surface, the recording of ADC spectra at five different high voltage values (from 850 to 970 V in steps of 30 V) for two different wavelength values each (360 and 480 nm), recording of oscilloscope images, and the analysis of the amplitude spectra of all the channels at maximum high voltage level. Right before and after data recording, the dark current of all 16 channels is measured. During each test, no significant ambient room temperature changes occurred. The measurement procedure is immediately followed by data analysis, determining uniformity, relative quantum efficiency and gain. The raw data as well as the results of the analysis are stored in a mirrored RAID5 server platform. In addition, all data are hosted on a webserver and are accessible via a graphical user interface based on the state-of-the-art, object oriented RubyOnRails technology [67]. More than 600 MAPMTs (576 plus spares) were characterised in terms of all relevant parameters. During the complete period of the measurements, more than 120 days, 12 h a day, the automated test setup collected data continuously without failures.

Results and Conclusions

Of all tested photomultiplier tubes, only 20 units did not fulfill all test criteria, since the conditions of dark current limit smaller than 2 nA for each individual channel was not respected. For the rest of the photomultiplier tubes, the parameters are significantly better than the allowed values. In general, the dark current registered at the end of the 2 h measurement protocol is an order of magnitude less than specified, as show in figure 5.10. The uniformity behaviour turned out to be excellent, with amplitude variations of only 20–30%.

Figure 5.11 shows one of the typical single photon ADC distributions obtained. Besides the ADC pedestal, two main components are visible. The main peak includes the signals of the photoelectrons subjected to the full 12-step amplification chain, whereas the smaller amplitude peak is due to those photoelectrons for which at least an amplification stage is missed. For the foreseen usage in RICH-1, both contributions are equally important. Mean value and standard deviation of each contributing peak is determined by a double Gaussian fit. The uniformity of each MAPMT and the gain behaviour of each individual channel are extracted from these parameters, depicted in figure 5.12.

The ideal high voltage setting for each MAPMT is the minimum value which guarantees at least 95% efficiency for all the MAPMT channels coupled to the front-end read-out chain, based on the MAD4 discriminator boards [65]: 1.7 pC (gain $\sim 10^7$). The HV setting is

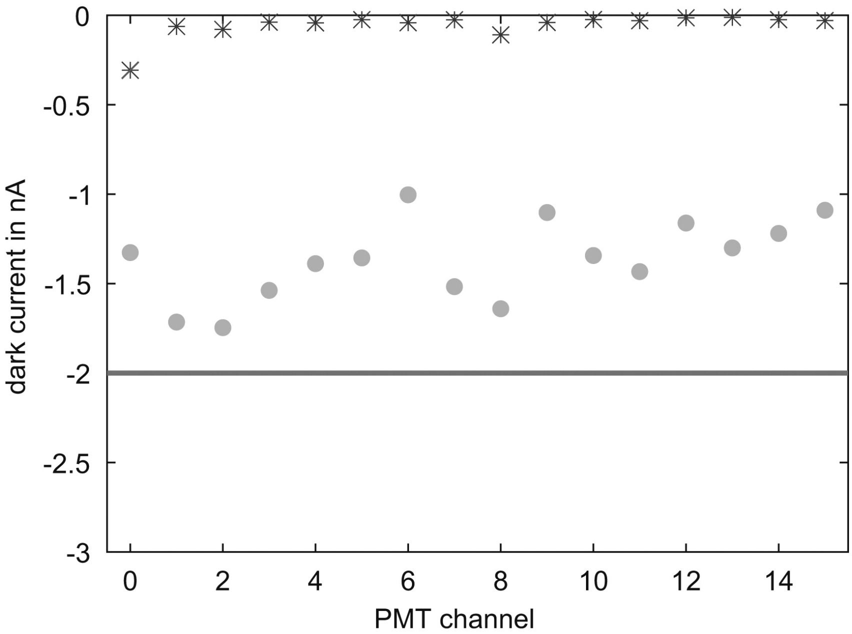

Figure 5.10: Dark current values for the 16 channels of a MAPMT before (circles) and after (stars) the measurement procedure. The line marks the specification limit.

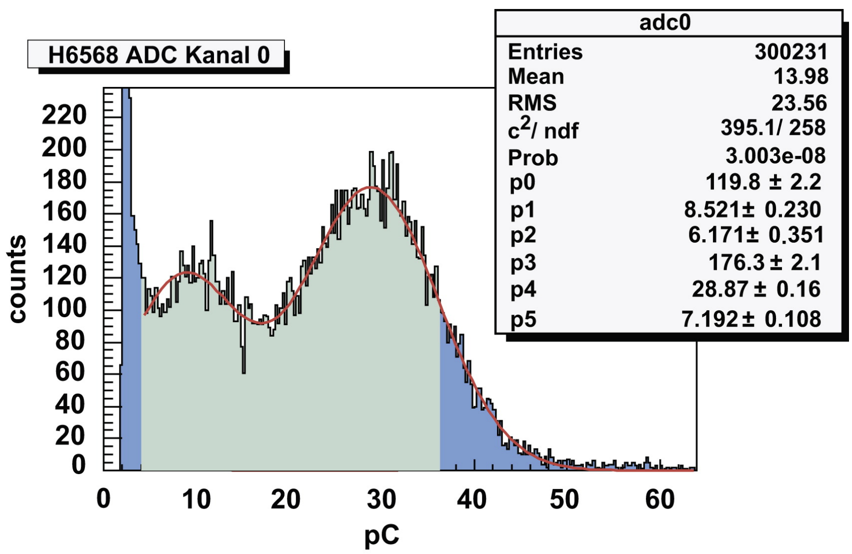

Figure 5.11: Typical single photoelectron response measured at 970 V using 360 nm photons. The shaded area shows the $\pm 1\sigma$ region of each of the two contributing peaks.

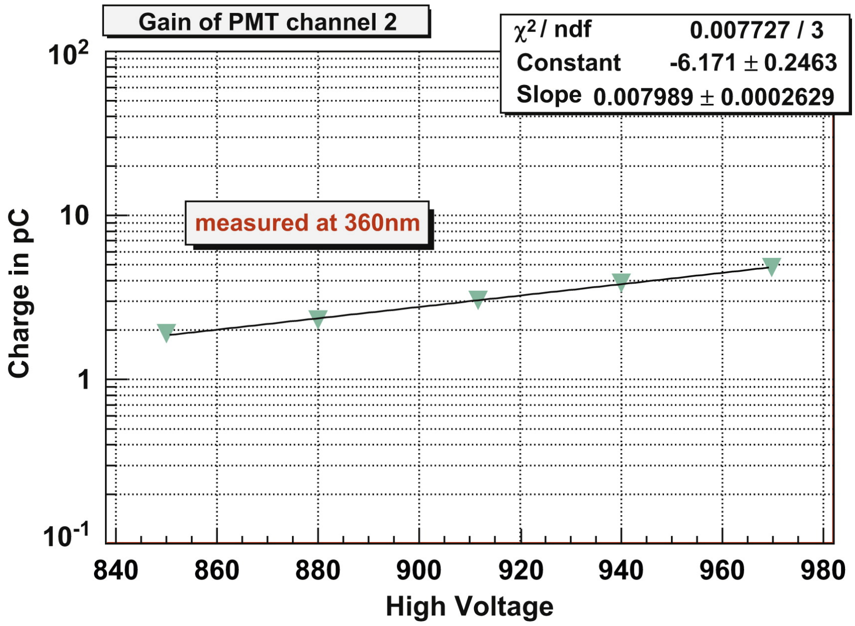

Figure 5.12: Gain values measured at 360 nm wavelength for a channel of a MAPMT. The curve is the exponentially fitted function.

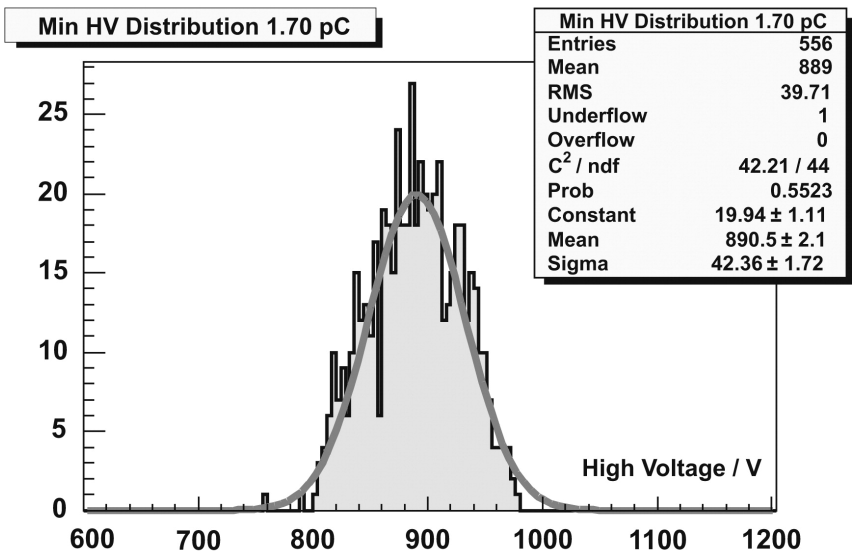

Figure 5.13: Distribution of the high voltage value needed to get a minimum output charge of 1.7 pC for a sample of 556 MAPMTs.

deduced from an exponential fit to the measured gain data. Figure 5.13 shows the calculated high voltages for a subsample of 556 MAPMTs. These values are Gaussian distributed around 890 V with a standard deviation of $\sim$ 40 V. The central value corresponds pretty well to the typical value given by Hamamatsu ($\sim$ 910 V for an amplification of $\sim 10^7$).

In conclusion, more than 600 MAPMTs with 16 individual channels each have been tested in terms of uniformity, gain, dark current and relative quantum efficiency in a fully automated test-stand, developed for this purpose. From the analysis of these data, the ideal working point for each individual photomultiplier tube has been extracted. Since 2006, the RICH-1 upgraded detector is taking data successfully in the COMPASS environment with excellent performance, exhibiting a resolution of the measured Cherenkov angle of $\sigma_{ring} = 0.3$ mrad (before $\sigma_{ring} = 0.6$ mrad) and a number of photons per ring of ~ 56 (before ~ 14).

Part III

Analysis Framework

CHAPTER 6

ANALYSIS METHOD: A PRELUDE

All methods are sacred if they are internally necessary. All methods are sins if they are not justified by internal necessity.

Wassily Kandinsky.

The methodology used in the analysis is explained in this section. In chapter 3, the main guidelines about the gluon in the QCD improved quark parton model were drawn. In particular, in section 3.2, a brief description focusing on the main attributes of the high p_T hadron pair analysis is presented. The gluon polarisation measurement is not given by a single and direct observable, but rather by an observable defined by the difference of two states of the nucleon *spin*, a very specific property for nuclear particles. Therefore, it requires a dedicated method and well suited analytical techniques to produce the most reliable measurement. For this, several important steps must be defined and accomplished in an articulated way. In the following sections, a brief overview of all the intervenient players in the analysis are given. In section 6.1, the extraction procedure of the gluon polarisation is elaborated. The main ideas of data selection method are explained in section 6.2. The simulation is generally described in section 6.3. In section ?? the neural network approach is drawn. Finally, the systematic uncertainties issues are specified in section 6.4.

6.1 From Asymmetries to Gluon Polarisation

In section 3.2, it was explained that the gluon polarisation measurement, ideally containing only PGF processes, is related to the spin helicity asymmetry by the following expression:

$$A_{\mathrm{LL}}^{\mathrm{PGF}} = a_{\mathrm{LL}}^{\mathrm{PGF}} \frac{\Delta G}{G} . \tag{6.1}$$

Here the spin helicity asymmetry for PGF events $A_{\rm LL}^{\rm PGF}$ is given by the partonic asymmetry $a_{\rm LL}^{\rm PGF}$ times the gluon polarisation $\frac{\Delta G}{G}$. The spin helicity asymmetry is evaluated using the number of events collected with two different muon and target spin configurations. This method is described in detail in chapter 7.

In principle, equation (6.1) would be sufficient to determine the gluon polarisation, apart one experimental constrain: it is not possible to distinguish the PGF processes in an event sample using data analysis criteria, because it is impossible to access the partonic information for an event. This constrain has a huge impact on the analysis approach. Therefore the gluon polarisation extraction is performed using a data sample with events containing high p_T hadrons in the final state [68]. As already explained in section 3.2 this sample is composed by two other processes at LO in QCD in addition to the PGF (eq. (3.25)): the virtual photo-absorption process and the QCD Compton. The extraction of the gluon polarisation is fully described in chapter 8.

6.2 The Data

As discussed in the previous section, it is not possible to select in an isolated way the PGF events. Therefore, one way to yield a feasible and considerable amount of events of a PGF sample is to select events with high p_T hadrons in the final state. In particular, to select events with high p_T hadron pairs, respectively the highest and the second highest p_T hadron with respect to the virtual photon direction, denoted leading and subleading hadrons, respectively. These high p_T hadrons are very likely to contain the $q\bar{q}$ pair produced in the PGF process, each quark hadronising into a high p_T hadron. Therefore, a set of cuts is applied to the data to select DIS events with high p_T hadrons.

The present analysis uses data taken with the COMPASS spectrometer with longitudinal muon and target polarisations from the years 2002 to 2006. The data collection process ends when the raw data files are created from the DAQ system and stored into the Central Data Recording at CERN, as discussed in section 4.5. Then the data reconstruction process starts; at the end prepared files containing all needed information are available for analysis.

The whole process involving data collection, starting from the event reconstruction from raw data using information of the detector calibration up to the analysis criteria applied to data is covered in chapter 9.

6.3 Monte Carlo Simulation and Neural Network

In equations (3.25) and (3.26) there are several terms that can not be extracted from the data, since this information refers to the partonic level. The only way to estimate these important partonic quantities is using a Monte Carlo (MC) simulation in order to extract the gluon polarisation. Therefore, the MC simulation must describe and reproduce correctly experimental data. An extensive campaign was undertaken in order to improve the agreement between the data and the simulation. The simulation is also used to understand how an event sample, containing high p_T hadrons, is constituted. The MC simulation description is detailed chapter 10.

In previous analyses of high p_T events [69, 70] only mean values of R_i and $a_{\rm LL}^i$ for the three processes were used. Furthermore, in order to minimize the statistical uncertainty of

$\Delta G/G$, cuts on the transverse momenta of hadrons were optimised. Unfortunately, these requirements lead to a severe loss of statistics, since only hadrons with high transverse momenta were selected. This approach allows the use of loose p_T cuts by dealing simultaneously with the three processes. The neural networks, trained on a MC sample, assigns to each event a probability to originate from one of these processes, which is then included in the weight. Events more likely originating from processes other than PGF are kept with a small weight, using the statistics in an optimal way. For a given event, different neural networks provide not only the probabilities to originate from a particular process but also the corresponding analysing powers and the momentum fractions x_C and x_G. This approach makes optimal use the data and avoids biases which may arise from correlations between analysing power and kinematic quantities used to evaluate the asymmetries. The statistical uncertainty of $\Delta G/G$ is reduced by a factor of two comparing with the method used in [69, 70].

6.4 Systematic Uncertainty Studies

The last but not, of course, the least subject about the analysis procedure are the systematic uncertainty studies. As mentioned in the beginning of this chapter the gluon polarisation is determined by an observable measured by the difference of two states defined by the muon and target spin. Thus it is not a very sensible observable. As described along in this chapter, the analysis method is composed by several parts, each of them carrying an intrinsic systematic uncertainty, which contribute to the whole systematic uncertainty of the gluon polarisation measurement. The systematic uncertainty studies are presented and extensively discussed in chapter 11.

CHAPTER 7

ASYMMETRY CALCULATION

The subtlety of nature is greater many times over than the subtlety of the senses and understanding.

Sir Francis Bacon.

In nature, to assess very small differences or to investigate a very slight bias in a particular occurrence, a tool which is sensible enough to measure these tiny effects needs to be defined. This tool is the asymmetry calculation. In section 2.3, the spin asymmetries were briefly introduced, in the context of the nucleon spin structure (chapter 2, part I). The spin asymmetries were presented in two approaches: in the first one the asymmetry is defined from the cross sections (*i.e.* number of events) taken with two opposite spin configurations, which experimentalists are more familiar with; in the second, the asymmetry is defined by the nucleon photon absorption. Both definitions are related by the depolarisation factor. The computation of the asymmetry and the definition of the interaction counting rates are discussed in section 7.1 and 7.2. In section 7.3 the so called first order method for asymmetry extraction is explained. In the same way the second order method is explained in section 7.4.

7.1 Interaction Counting Rates

The number of observed interactions N integrated over a certain set of conditions is given by

$$N = \int \frac{d^2\sigma}{dx\, dQ^2} \mathscr{L}\, d\vec{\xi}\ . \tag{7.1}$$

For simplicity and to allow an easy reading of the expressions the differential cross section $d^2\sigma/dx\, dQ^2$ will be simplified to σ. The vector $\vec{\xi}$ contains the integration variables which vary for each interaction: x, Q^2, the vertex interaction position $\vec{r}$, time t, *etc.* The luminosity $\mathscr{L}$ given by a particle flux ϕ colliding on a fixed target with nucleon density n and experimental acceptance a is just the product of these quantities. Thus equation (7.1) reads

$$N = \int a\phi n\sigma \, d\vec{\xi} \, . \tag{7.2}$$

Now let us assume that the calculations are done in small intervals of x and Q^2 variables; as a, n and σ depend essentially on these kinematic variables, equation (7.2) can be written as

$$N(x,Q^2) = a(x,Q^2)n(x,Q^2)\sigma(x,Q^2)\int \phi \, d\vec{\xi}' = an\sigma\Phi \, , \tag{7.3}$$

where the integrated flux is defined as

$$\Phi = \int \phi \, d\vec{\xi}' \, .$$

The number of interactions can be related with the spin projections of the beam and target. In our experimental procedure the deuteron target has three projections, which are represented symbolically as: $\leftarrow$, 0 and $\rightarrow$, while for the beam there are two: $\leftarrow$ and $\rightarrow$, with respect to a considered reference axis. In this way equation (7.2) may be rewritten as

$$N = a\Big[(\Phi^{\rightarrow}n^{\leftarrow} + \Phi^{\leftarrow}n^{\rightarrow})\sigma^{\rightleftarrows} + (\Phi^{\rightarrow}n^{\rightarrow} + \Phi^{\leftarrow}n^{\leftarrow})\sigma^{\rightrightarrows} + (\Phi^{\rightarrow} + \Phi^{\leftarrow})n^{0}\sigma^{\overset{\rightarrow}{0}} + (\Phi^{\rightarrow} + \Phi^{\leftarrow})\sum_i n_i\overline{\sigma}_i\Big] \, . \tag{7.4}$$

The first term is related to the interaction in which the beam and the target have their spin projections aligned in anti-parallel; the probability of such kind of interaction is given by the cross section $\sigma^{\rightleftarrows}$. In the second term, the beam and target spin projections are paralleled aligned; the corresponding cross section is $\sigma^{\rightrightarrows}$. The third term concerns the interaction in which the target spin projection is 0, regardless of the beam spin projection; the cross section for this case is $\sigma^{\overset{\rightarrow}{0}}$. The last term is related to the beam interactions on material other than the deuteron target material; since most of this material is not polarised, the spin average cross section $\overline{\sigma} = \left(\sigma^{\rightleftarrows} + \sigma^{\leftleftarrows}\right)/2$ is used.

Let us define the beam and target polarisations, P_b and P_t respectively as

$$P_b = \frac{\Phi^{\leftarrow} - \Phi^{\rightarrow}}{\Phi}, \quad \text{where} \quad \Phi = \Phi^{\leftarrow} + \Phi^{\rightarrow} \, , \tag{7.5}$$

$$P_t = \frac{n^{\leftarrow} - n^{\rightarrow}}{n_t}, \quad \text{where} \quad n_t = n^{\leftarrow} + n^{\rightarrow} + n^{0} \, . \tag{7.6}$$

In order to express the total number of interactions N in a more convenient way, a few concepts must be introduced. The cross sections can be gathered, as shown in equation (2.26), in which the double longitudinal cross section asymmetry A of the interactions is defined. The concept of the dilution factor f is now introduced, which is explained in section 7.2. Finally using equations (2.26), (7.5), (7.6) and (7.9) into equation (7.3) this expression reads

$$N = a\Phi n\sigma\left(1 - fDP_bP_tA\right) \, . \tag{7.7}$$

Equation (7.7) relates the number of interactions in a target volume to the cross section asymmetry A.

In the next section (7.2) the inputs used in the asymmetry extraction are described. In sections 7.3 and 7.4 the asymmetry extraction is implemented in two methods using a practical approach taking into account the last derived equation (7.7).

7.2 Inputs to the Asymmetry

As mentioned in the previous section, the number of interactions in the target volume taking into account the spin asymmetry and the cross section is represented in equation 7.7. The parameters related to the beam and target, dilution factor f, depolarisation factor D, and beam and target polarisation, P_b and P_t, are explained and defined in this section. This explanation is important to understand some physical and experimental issues relevant for the analysis.

Dilution Factor f

In the expression 7.7 the dilution factor f appeared in an *ad hoc* way. In this section the dilution factor is explained. Generically the dilution factor f is defined as the quantity of polarisable material over the total bulk. This means

$$f = \frac{\text{nb. of polarisable nucleons}}{\text{nb. of total nucleons}} \ . \tag{7.8}$$

The target material used in all data taking periods is ^{6}LiD. The ^{6}Li nucleus can be regarded approximately as a loose bound of an α particle plus a deuteron, thus the ^{6}LiD molecule can be regarded as one unpolarisable α particle and two polarisable deuterium nuclei [71]. Taking into account this picture the naive expectation of the dilution factor is, as already mentioned, the number of polarisable nucleons over the total number of nucleons available in the molecule, *i.e.* $4/8 = 0.5$. Nevertheless there are materials other than the ^{6}LiD molecules in the target, namely He, C, F, Ni and Cu. The He element is used in a ^{3}He/^{4}He liquid cooling mixture. The packing factor of the ^{6}LiD molecule is ~ 0.5; this means that nearly half of the target is filled with this cooling mixture. The Ni and Cu elements are used in the NMR coils (see section 4.3).

The dilution factor can be defined more precisely by quantifying expression 7.8 using the cross section information. The dilution factor can then read

$$f = \frac{n_d \sigma_d}{n_d \sigma_d + \sum_A n_A \sigma_A} \ . \tag{7.9}$$

The number of nuclei of type i inside the target is represented by n_i, and the muon-deuteron and muon-nucleus scattering cross sections are represented by σ_d and σ_A, respectively.

Equation 7.9 can be rewritten as

$$f = \frac{n_d}{n_d + \sum_A n_A \frac{\sigma_A}{\sigma_d}} \ . \tag{7.10}$$

In the calculation of the dilution factor, the ratio σ_A/σ_d is proportional to the ratio of the unpolarised structure functions F_2^A/F_2^d. These data were measured by the NMC and EMC experiments, and then parametrised. In this way, the dilution factor f is computed using this result. The average value of the dilution factor, of the whole data used in this analysis, is 0.39 .

Further more, this dilution factor needs to be corrected. The effective dilution factor is then written as

$$f_{\text{eff}} = \rho C f \ . \tag{7.11}$$

The factor ρ takes into account the unpolarised radiative corrections calculated using the TERAD [72] program. In the already mentioned approximation of the ^{6}LiD molecule to an unpolarisable α particle and two polarisable deuterons, the factor C includes the probability of how much time the quasi-free proton and the neutron, representing the deuteron, in the ^{6}Li material, are aligned with the nuclear spin. Another correction is included to take into account the probability of the nucleon spins to be parallel with respect to the deuteron in the D-state. The purity of the ^{6}LiD target material during the production process is also taken into account in the factor C.

Depolarisation Factor

The amount of polarisation transferred from the incoming muon to the virtual photon in the scattering process is defined as the depolarisation factor D. This factor strongly depends on the kinematics and is given by

$$D = \frac{y\frac{-m^2y^2}{Q^2(1-xy)} + y - 2}{\left((1-y)^2 - \frac{-2m^2y^2}{Q^2} + 1\right)\sqrt{1 - \frac{4m^2(1-x)xy^2}{Q^2(1-xy)^2}}} \,. \tag{7.12}$$

From the last expression, it is clear that the depolarisation factor D depends essentially on the energy loss of the scattering muon, y.

Beam and Target Polarisation

The beam polarisation in our case can not be directly measured by applying equation (4.1) from section 4.2, due to lack of knowledge regarding the muon's parent hadron kinematics. Therefore a dedicated Monte Carlo simulation was designed to estimate the beam polarisation by parametrising the muon polarisation beam as a function of the muon and hadron momentum taking into account the transport of the particles along the FODO channel [52]. The results obtained using the simulation were found to be in agreement with performed measurements [52,73,74]. The average of the beam polarisation is given by the interaction of all individual muon helicitiy states over a phase space defined by the beam optics.

To optimise the statistical factor of merit of the COMPASS experiment a compromise between three main parameters of the beam, namely the intensity of the muon flux, the average polarisation and the momentum has to be found; the average polarisation should be taken into account in order to be as high as possible. In this case, the optimal values are a polarisation around -80 %, with a flux of 2×10^8 muons per spill, for an energy in the range of 80 to 160 GeV/c. This is shown in figure 7.1, where the muon flux is measured as a function of the muon momentum; the parametrisation is also drawn.

The target polarisation P_t is measured directly several times per run, using the NMR coils, described in section 4.3.

The relative uncertainty associated to the measurements used for the beam and target polarisation, δP_b and δP_t is 5 % for each measurement.

Deuteron D state Probability Correction

The asymmetry is usually given in terms of the average *nucleon N*. Since the deuteron is

The deuteron has no shell structure, so its total angular momentum is formed by orbital angular momenta and the spin (L-S) coupling. That is, $L = l_p + l_n$ and $S = s_p + s_n$. The

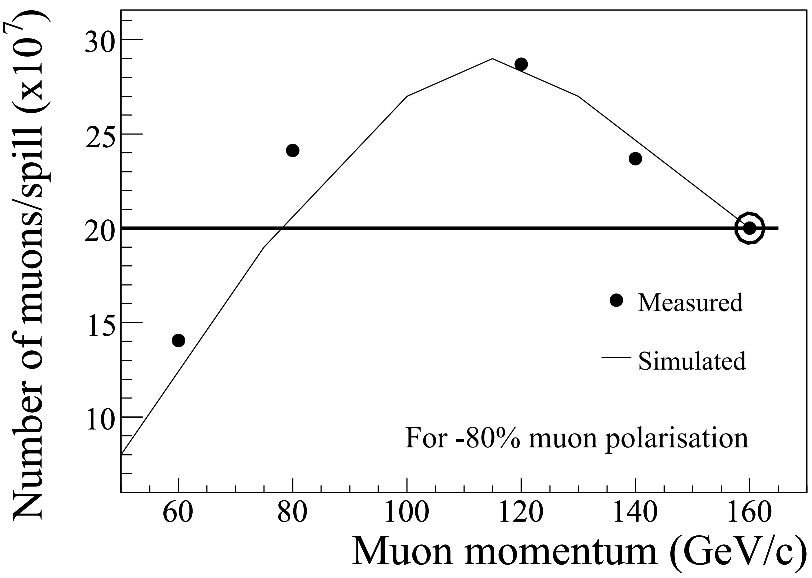

Figure 7.1: Polarisation and flux of the muon beam as a function of the muon momentum.

deuteron has a virtual D state that is occupied by the nucleons some fraction of the time. Since the orbital angular momentum of this state is $L = 2\hbar$, it affects the polarisation of the nucleons with respect to the nucleus. In the S state $L = 0$, so the nucleons add up their $1/2\hbar$ spins to $I = 1$, parallel to the deuteron spin. In the D state, $L = 2$, so $I = 1$ is formed from L.

The probability of the nucleons being in the D state is calculated using the Clebsh-Gordan coeficients [71], resulting in 50% of the nucleons in the D state have polarisations anti-parallel with respect to the deuteron; meaning that the total number of nucleons in the deuteron with spins parallel to the deuteron is

$$N_{||} = N_S - \frac{1}{2}N_D = N - \frac{3}{2}N_D \,, \tag{7.13}$$

where $N = N_S + N_D$ is the total number of nucleons in the S and D states.

Therefore, equation (7.13) can be applied to the measured asymmetries, giving

$$A^d_{||} = A^N_{||}\left(1 - \frac{3}{2}\omega_D\right) \,, \tag{7.14}$$

and the gluon polarisation $\Delta G/G$ is corrected accordingly

$$\left(\frac{\Delta G}{G}\right)^d_{||} = \left(\frac{\Delta G}{G}\right)^N_{||}\left(1 - \frac{3}{2}\omega_D\right) \,. \tag{7.15}$$

The coeficient ω_D is the so called probability of the D state, it has been variously estimated using the different models and the average is 5% [71].

7.3 1st Order Method

Let us proceed with the simple exercise of computing the raw spin asymmetry of several interactions, in order to introduce the 1st order method to extract the spin helicity asymmetry.

The COMPASS polarised target, described in the section 4.3, has the possibility to have two cells longitudinally polarised in opposite directions, denoted $\Rightarrow$ and $\Leftarrow$. The muon beam is longitudinally polarised in one direction, in a natural way, as described in section 4.2; let us define the direction of incoming muon polarisation as $\leftarrow$. Assuming the spin projection of the incoming muon is oppositely aligned with the target cell polarisation, the number of events collected in such conditions is denoted as $N^{\overset{\leftarrow}{\Rightarrow}}$; and the number of events in which the muon and the target spin projections are aligned, with respect the same direction, is $N^{\overset{\leftarrow}{\Leftarrow}}$.

The raw asymmetry can be simply defined as

$$A_{\text{raw}} = \frac{N^{\overset{\leftarrow}{\Leftarrow}} - N^{\overset{\leftarrow}{\Rightarrow}}}{N^{\overset{\leftarrow}{\Leftarrow}} + N^{\overset{\leftarrow}{\Rightarrow}}} \tag{7.16}$$

Equation (7.7) applied for N_u and N_d target cells reads

$$N_u = a_u \Phi n_u \sigma \left(1 - f D P_b P_{t,u} A\right), \tag{7.17}$$
$$N_d = a_d \Phi n_d \sigma \left(1 - f D P_b P_{t,d} A\right). \tag{7.18}$$

Some remarks about the physical conditions during data taking need to be made. Looking at equations (7.17) and (7.18) the flux, for which the incoming beam muon track involved in the interaction is extrapolated through the nominal volume of both target cells, the interaction cross section σ, the dilution factor f, the depolarisation factor D and the beam polarisation P_b are assumed to be the same for both target cells. Using these equations in eq. (7.16) one obtains

$$A_{\text{raw}} = \frac{r - 1 - wA(rP_u - P_d)}{r + 1 - wA(rP_u + P_d)}, \tag{7.19}$$

where

$$r = \frac{a_u n_u}{a_d n_d} \quad \text{and} \quad w = f D P_b .$$

In equation (7.19) the polarisation P_t was replaced by the polarisations P_u and P_d, related to the upstream and downstream target cell polarisations. Normally $r \neq 1$; therefore, this quantity may introduce a bias. It is easy to understand why: r involves the event acceptance a. This acceptance depends strongly on the interaction position along the target cells. In particular, the acceptance is different with respect to events occurring in the upstream and in the downstream cell. Therefore, to eliminate this potential bias, the spin projections of the target cells are reverted. So, in this case, the projections of the spin polarisation of both cells point outwards. In this case the number of interactions inside the upstream cell are accounted to $N'^{\overset{\leftarrow}{\Leftarrow}}$, while the interactions inside the downstream cell account to $N'^{\overset{\rightarrow}{\Leftarrow}}$.

Applying equations (7.17) and (7.18) for the case where the target cells are reverted, the number of interactions in the upstream and downstream cells are

$$N'_u = a'_u \Phi' n'_u \sigma \left(1 - f D P_b P'_u A\right), \tag{7.20}$$
$$N'_d = a'_d \Phi' n'_d \sigma \left(1 - f D P_b P'_d A\right). \tag{7.21}$$

And the raw asymmetry for data taken in this case is

$$\begin{aligned} A'_{\text{raw}} &= \frac{N'^{\rightleftarrows} - N'^{\leftleftarrows}}{N'^{\rightleftarrows} + N'^{\leftleftarrows}} = \frac{N'_d - N'_u}{N'_d + N'_u}, && (7.22)\\ &= -\frac{N'_u - N'_d}{N'_u + N'_d}, && (7.23)\\ &= -\frac{r' - 1 - wA(r'P'_u - P'_d)}{r' + 1 - wA(r'P'_u + P'_d)}, && (7.24) \end{aligned}$$

The main idea is to extract the asymmetry A from the raw asymmetries defined aboved. Let us merge equations (7.19) and (7.24):

$$\frac{A_{\text{raw}} + A'_{\text{raw}}}{2} = \frac{1}{2}\left[\frac{r - 1 - wA(rP_u - P_d)}{r + 1 - wA(rP_u + P_d)} - \frac{r' - 1 - wA(r'P'_u - P'_d)}{r' + 1 - wA(r'P'_u + P'_d)}\right]. \quad (7.25)$$

Some remarks related to expression (7.25). The ratio r can be nearly the same for both cases, *i.e.* $r \approx r'$, and the product $wA \ll 1$. Also concerning the target cell polarisations, $P_u - P'_u \ll 1$ and $P_d - P'_d \ll 1$. This leads to a simplification of equation (7.25).

$$\frac{A_{\text{raw}} + A'_{\text{raw}}}{2} = \frac{1}{2}\frac{4r}{(r+1)^2}\left[\frac{r-1}{r+1} - \frac{r'-1}{r'+1} + wA\left(\frac{P_u + P_d + P'_u + P'_d}{4}\right)\right]. \quad (7.26)$$

Extracting the asymmetry A in this expression one obtains:

$$\begin{aligned} A &= \left(\frac{1}{1-\gamma^2}\right)\frac{1}{wP_T}\frac{A_{\text{raw}} + A'_{\text{raw}}}{2} - A_{\text{false}},\\ &= \left(\frac{1}{1-\gamma^2}\right)\frac{1}{wP_T}\frac{1}{2}\left[\frac{N_u - N_d}{N_u + N_d} - \frac{N'_u - N'_d}{N'_u + N'_d}\right] - A_{\text{false}}, && (7.27) \end{aligned}$$

where the terms $1-\gamma^2$, P_T and A_{false} are defined below

$$\begin{aligned} P_T &= \frac{1}{4}(P_u + P_d + P'_u + P'_d), && (7.28)\\ 1-\gamma^2 &= \frac{4r}{(r+1)^2}, && (7.29)\\ A_{\text{false}} &= \left(\frac{1}{1-\gamma^2}\right)\frac{1}{2wP_T}\left(\frac{r-1}{r+1} - \frac{r'-1}{r'+1}\right). && (7.30) \end{aligned}$$

The term A_{false} concerns to the so called *false asymmetries*. This asymmetry is related to changes of the spectrometer acceptance; it takes into account changes of density in the target material exposed to the beam. Its effect will be taken into account in the systematics studies (chap. 11).

The statistical error of this asymmetry is given by

$$\delta A = \frac{1}{2wP_T\sqrt{1-\gamma^2}}\sqrt{\frac{1}{N_u + N_d} + \frac{1}{N'_u + N'_d}} \quad (7.31)$$

The details of the assumptions used in the derivation of formulae (7.27) to (7.31) are in [75].

The quantity w is computed using the product of the mean values of f, D and P_b, *i.e.* $\langle w\rangle = \langle f\rangle\langle D\rangle\langle P_b\rangle$. The statistical uncertainty in this case is not an optimal one. To optimise the statistical uncertainty, the solution is to use a statistical method which gives the smallest variance. This method is the weighted method. Applying a weight w in an event-by-event basis instead of using the number of events, the asymmetry and its statistical error formulae become

$$A = \left(\frac{1}{1-\gamma^2}\right)\frac{1}{wP_T}\frac{1}{2}\left[\frac{\sum_u w_u - \sum_d w_d}{\sum_u w_u^2 + \sum_d w_d^2} - \frac{\sum'_u w'_u - \sum'_d w'_d}{\sum'_u w'^2_u + \sum'_d w'^2_d}\right] - A_{\text{false}}\,, \tag{7.32}$$

$$\delta A = \frac{1}{2wP_T\sqrt{1-\gamma^2}}\sqrt{\frac{1}{\sum_u w_u^2 + \sum_d w_d^2} + \frac{1}{\sum'_u w'^2_u + \sum'_d w'^2_d}}\,. \tag{7.33}$$

This weighting improves the statistical accuracy. It is noteworthy to mention that the weight w, in this case, can also include the target polarisation, *i.e.* $w = fDP_bP_t$, since all involved variables in the average $\langle w\rangle$ are computed in an event-by-event basis.

An important remark with respect to the ratio r: as mentioned before, it may introduce a bias. This can be well illustrated by the term $(r-1)/(r+1)$, also called the apparatus asymmetry, which is present in the A_{false} term and also by the correction factor $1-\gamma^2$ which is defined upon the r ratio.

It is known that $r \approx 1$; this means that $\gamma \approx 0$ and $A_{\text{false}} \approx 0$. The expressions of the asymmetry extraction and its errors, assuming $r \approx 1$ and weighted event-by-event, are

$$A = \frac{1}{wP_T}\frac{1}{2}\left[\frac{\sum_u w_u - \sum_d w_d}{\sum_u w_u^2 + \sum_d w_d^2} - \frac{\sum'_u w'_u - \sum'_d w'_d}{\sum'_u w'^2_u + \sum'_d w'^2_d}\right]\,, \tag{7.34}$$

$$\delta A = \frac{1}{2wP_T}\sqrt{\frac{1}{\sum_u w_u^2 + \sum_d w_d^2} + \frac{1}{\sum'_u w'^2_u + \sum'_d w'^2_d}}\,. \tag{7.35}$$

In practise, the ratio r is not measured, since the acceptances are not measured. Assuming $r \approx 1$ this neglects the false asymmetry term A_{false}, *i.e.* it is not possible to measure this false asymmetry; this effect is considered in the systematic uncertainty.

7.4 2$^{\text{nd}}$ Order Method

The starting point is equation (7.7), which will be written as $N = N(\vec{\xi})$, *i.e.* N depending on the vector $\vec{\xi}$

$$N = \langle a\rangle(1-\langle\beta\rangle A)\int \Phi n\sigma\, d\vec{\xi}\,, \tag{7.36}$$

with the averages $\langle a\rangle$ and $\langle\beta\rangle$ defined as

$$\langle a\rangle = \frac{\int a\phi n\sigma\, d\vec{\xi}}{\int \phi n\sigma\, d\vec{\xi}} \quad \text{and} \quad \langle\beta\rangle = \frac{\int \beta a\phi n\sigma\, d\vec{\xi}}{\int a\phi n\sigma\, d\vec{\xi}} \overset{N\ \text{large}}{\approx} \frac{\sum_i^N \beta^i}{N}\,, \tag{7.37}$$

where $\beta = fDP_bP_t$.

Equations (7.17) to (7.21) then read

$$
\begin{aligned}
N_u &= \langle a_u \rangle (1 - \langle \beta_u \rangle A) \int \phi n_u \sigma \, d\vec{\xi} \,, && (7.38)\\
N_d &= \langle a_d \rangle (1 - \langle \beta_d \rangle A) \int \phi n_d \sigma \, d\vec{\xi} \,, && (7.39)\\
N'_u &= \langle a'_u \rangle (1 - \langle \beta'_u \rangle A) \int \phi n'_u \sigma \, d\vec{\xi} \,, && (7.40)\\
N'_d &= \langle a'_d \rangle (1 - \langle \beta'_d \rangle A) \int \phi n'_d \sigma \, d\vec{\xi} \,. && (7.41)
\end{aligned}
$$

In this case, an interesting variable is defined, the so called double ratio of the counting rates, δ,

$$
\delta = \frac{N_u N'_d}{N_d N'_u} = \frac{\langle a_u \rangle \langle a'_d \rangle}{\langle a_d \rangle \langle a'_u \rangle} \frac{\int \phi n_u \sigma \, d\vec{\xi} \int \phi n'_d \sigma \, d\vec{\xi}}{\int \phi n_d \sigma \, d\vec{\xi} \int \phi n'_u \sigma \, d\vec{\xi}} \frac{(1 - \langle \beta_u \rangle A)(1 - \langle \beta'_d \rangle A)}{(1 - \langle \beta_d \rangle A)(1 - \langle \beta'_u \rangle A)} \,. \tag{7.42}
$$

Two assumptions are made: the ratio of the acceptances is equal to unity, *i.e.*

$$
\frac{\langle a_u \rangle \langle a'_d \rangle}{\langle a_d \rangle \langle a'_u \rangle} = 1 \,, \tag{7.43}
$$

and the target conditions are the same before and after the solenoid field reversal, *i.e.*

$$
\frac{\int \phi n_u \sigma \, d\vec{\xi} \int \phi n'_d \sigma \, d\vec{\xi}}{\int \phi n_d \sigma \, d\vec{\xi} \int \phi n'_u \sigma \, d\vec{\xi}} = 1 \,. \tag{7.44}
$$

Taking into account these assumptions equation (7.42) can be written in a second order form with respect to the asymmetry A

$$
aA^2 + bA + c = 0 \,, \tag{7.45}
$$

where

$$
\begin{aligned}
a &= \delta \langle \beta'_u \rangle \langle \beta_d \rangle - \langle \beta_u \rangle \langle \beta'_d \rangle, && (7.46)\\
b &= \delta \Big(\langle \beta'_u \rangle + \langle \beta_d \rangle \Big) - \Big(\langle \beta_u \rangle + \langle \beta'_d \rangle \Big), && (7.47)\\
c &= \delta - 1 \,. && (7.48)
\end{aligned}
$$

Thus, if $a \neq 0$, the asymmetry is given by the usual formula

$$
\begin{aligned}
A &= \frac{-b \pm \sqrt{b^2 - 4ac}}{2a} \,; && (7.49)\\
&\text{if } \quad a = 0 \quad \text{, then} \quad A = -\frac{c}{b} \,. && (7.50)
\end{aligned}
$$

The statistical error associated to asymmetry is

$$
\delta A = \frac{1}{\langle \beta \rangle \sqrt{N_{\mathrm{Tot}}}} \,. \tag{7.51}
$$

In this formula, two assumptions were made: the interaction counting rates of both target cells before and after the solenoid field reversal are assumed to be the same; thus $N_{\mathrm{Tot}}/4 = N_u \approx N_d \approx N'_u \approx N'_d$, where N_{Tot} is the total number of interactions; also the average β in each situation is $\langle\beta\rangle = \langle\beta_u\rangle \approx \langle\beta'_d\rangle \approx -\langle\beta'_u\rangle \approx -\langle\beta_d\rangle$.

In this case it is also possible to apply a weighted method. Let us define p_i as

$$p_i = \int w N_i \, d\vec{\xi} = \langle a\rangle_w (1 - \langle\beta_i\rangle_w A) \int \Phi n_i \sigma d\vec{\xi} \,. \tag{7.52}$$

Then,

$$\langle a_i\rangle_w = \frac{\int a_i w \phi n_i \sigma d\vec{\xi}}{\int w \phi n_i \sigma d\vec{\xi}} \quad \text{and} \quad \langle\beta_i\rangle_w = \frac{\int \beta_i w \phi n_i \sigma d\vec{\xi}}{\int w \phi n_i \sigma d\vec{\xi}} \overset{N_i \text{ large}}{\approx} \frac{\sum_{j=1}^{N_i} w_j \beta_i^j}{\sum_{j=1}^{N_i} w_j}\,, \tag{7.53}$$

here β_i^j represents β_i, *i.e.* in a particular case u, d, u', or d', for an event j. Thus, the double ratio δ is defined as

$$\delta = \frac{p_u p'_d}{p_d p'_u}\,, \tag{7.54}$$

and using the assumptions described in equations (7.43) and (7.44), an expression of the same form of equation (7.45) will be obtained. In this case the parameters a, b and c are

$$a = \delta\langle\beta'_u\rangle_w\langle\beta_d\rangle_w - \langle\beta_u\rangle_w\langle\beta'_d\rangle_w, \tag{7.55}$$

$$b = \delta\Big(\langle\beta'_u\rangle_w + \langle\beta_d\rangle_w\Big) - \Big(\langle\beta_u\rangle_w + \langle\beta'_d\rangle_w\Big), \tag{7.56}$$

$$c = \delta - 1\,. \tag{7.57}$$

The statistical uncertainty including the weight w is given by

$$\delta A = \sqrt{\frac{\langle w^2\rangle}{\langle w\beta\rangle^2 N_{\mathrm{Tot}}}}\,. \tag{7.58}$$

As the optimum weight is $w = \beta$ the last expression is rewritten as

$$\delta A = \sqrt{\frac{1}{\langle\beta^2\rangle N_{\mathrm{Tot}}}}\,. \tag{7.59}$$

One remark about the two solutions for equation (7.45). Only one has physical interpretation, the other solution is discarded since it gives $A \gg 1$.

CHAPTER 8

EXTRACTION OF THE GLUON POLARISATION

There is a strong relationship between the gluon polarisation $\Delta G/G$ and the nucleon spin helicity asymmetry. In the previous chapter (7), the spin asymmetry calculation was explained in detail. The spin asymmetry is the appropriate tool to extract the gluon polarisation. The measured spin asymmetry is sensitive to the spin, associated to the partons inside the nucleon. In particular, for the gluon, this effect represents the gluon contribution to nucleon spin. The measurement of $\Delta G/G$ depends primarily on the double spin asymmetry calculation. Therefore, in section 8.1, the gluon polarisation formula is derived from the starting point of the double spin helicity asymmetry. The methodology, as well as all involved steps used in the analysis, is explained in section 8.2.

The gluon polarisation is measured directly via the Photon-Gluon Fusion process (PGF); which allows to probe the gluon inside the nucleon. Two other processes compete with the PGF process in the leading order QCD approximation, namely the virtual photo-absorption leading process (LP) and the gluon radiation (QCD Compton) process. In Fig. 8.1, all contributing processes are depicted.

8.1 The Gluon Polarisation Formula

According to the known involved processes the double spin asymmetry can be written as follows:

$$A_{\mathrm{LL}}^{p_T} = \frac{\Delta\sigma^{\mathrm{PGF}} + \Delta\sigma^{\mathrm{QCDC}} + \Delta\sigma^{\mathrm{LP}}}{\sigma^{\mathrm{PGF}} + \sigma^{\mathrm{QCDC}} + \sigma^{\mathrm{LP}}} \tag{8.1}$$

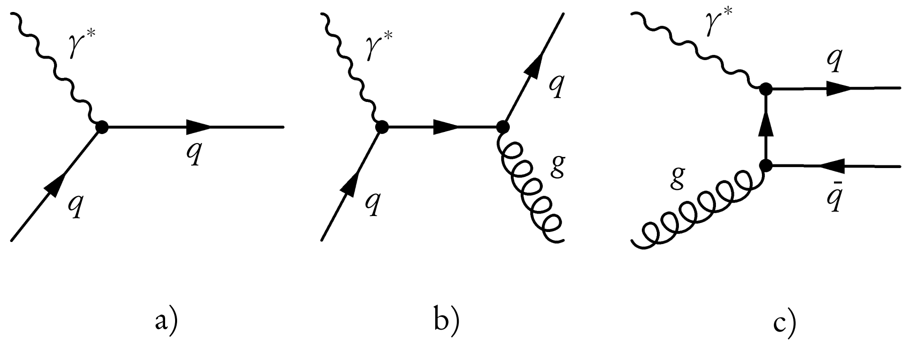

Figure 8.1: The contributing processes: a) DIS LO, b) QCD Compton and c) Photon-Gluon Fusion.

Applying the factorisation theorem, the unpolarised cross sections can be written as

$$\sigma^{\mathrm{LP}} = \sum_f e_f^2 q_f \otimes \hat{\sigma}^{\mathrm{LP}} \otimes H_F, \tag{8.2}$$

$$\sigma^{\mathrm{QCDC}} = \sum_f e_f^2 q_f \otimes \hat{\sigma}^{\mathrm{QCDC}} \otimes H_F, \tag{8.3}$$

$$\sigma^{\mathrm{PGF}} = G \otimes \hat{\sigma}^{\mathrm{PGF}} \otimes H_F, \tag{8.4}$$

and the polarised cross sections as

$$\Delta\sigma^{\mathrm{LP}} = \sum_f e_f^2 \Delta q_f \otimes \Delta\hat{\sigma}^{\mathrm{LP}} \otimes H_F, \tag{8.5}$$

$$\Delta\sigma^{\mathrm{QCDC}} = \sum_f e_f^2 \Delta q_f \otimes \Delta\hat{\sigma}^{\mathrm{QCDC}} \otimes H_F, \tag{8.6}$$

$$\Delta\sigma^{\mathrm{PGF}} = \Delta G \otimes \Delta\hat{\sigma}^{\mathrm{PGF}} \otimes H_F, \tag{8.7}$$

where the unpolarised parton distribution functions are represented by q_f and the polarised ones by Δq_f, where f runs over all contributing quarks and antiquarks. The hard scattering unpolarised partonic cross sections are described by the terms $\hat{\sigma}^i$ and the polarised ones by $\Delta\hat{\sigma}^i$, where i runs over the three processes, PGF, QCDC and LP; these terms give the cross section of the interaction between the virtual photon and the struck parton. And the fragmentation function is H_F, which is assumed to be spin independent. For sake of simplicity the dependence of the fragmentation function on the initial partonic state is not shown explicitly.

Equations (8.5)–(8.7) can be rewritten as

$$\begin{aligned}
\Delta\sigma^{\mathrm{LP}} &= \frac{\sum_f e_f^2 \Delta q_f \otimes \Delta\hat{\sigma}^{\mathrm{LP}} \otimes H_F}{\sum_f e_f^2 q_f \otimes \hat{\sigma}^{\mathrm{LP}} \otimes H_F} \cdot \sigma^{\mathrm{LP}} \\
&= \frac{\frac{\sum_f e_f^2 \Delta q_f}{\sum_f e_f^2 q_f} \sum_f e_f^2 q_f \otimes \frac{\Delta\hat{\sigma}^{\mathrm{LP}}}{\hat{\sigma}^{\mathrm{LP}}} \hat{\sigma}^{\mathrm{LP}} \otimes H_F}{\sum_f e_f^2 q_f \otimes \hat{\sigma}^{\mathrm{LP}} \otimes H_F} \cdot \sigma^{\mathrm{LP}} \\
&= \frac{A_1^{\mathrm{LP}}(x) \sum_f e_f^2 q_f \otimes a_{\mathrm{LL}}^{\mathrm{LP}} \hat{\sigma}^{\mathrm{LP}} \otimes H_F}{\sum_f e_f^2 q_f \otimes \hat{\sigma}^{\mathrm{LP}} \otimes H_F} \cdot \sigma^{\mathrm{LP}} ,
\end{aligned} \tag{8.8}$$

$$
\begin{aligned}
\Delta\sigma^{\mathrm{QCDC}} &= \frac{\sum_f e_f^2 \Delta q_f \otimes \Delta\hat{\sigma}^{\mathrm{QCDC}} \otimes H_F}{\sum_f e_f^2 q_f \otimes \hat{\sigma}^{\mathrm{QCDC}} \otimes H_F} \cdot \sigma^{\mathrm{QCDC}} \\
&= \frac{\frac{\sum_f e_f^2 \Delta q_f}{\sum_f e_f^2 q_f} \sum_f e_f^2 q_f \otimes \frac{\Delta\hat{\sigma}^{\mathrm{QCDC}}}{\hat{\sigma}^{\mathrm{QCDC}}} \hat{\sigma}^{\mathrm{QCDC}} \otimes H_F}{\sum_f e_f^2 q_f \otimes \hat{\sigma}^{\mathrm{QCDC}} \otimes H_F} \cdot \sigma^{\mathrm{QCDC}} \\
&= \frac{A_1^{\mathrm{QCDC}}(x_C) \sum_f e_f^2 q_f \otimes a_{\mathrm{LL}}^{\mathrm{QCDC}} \hat{\sigma}^{\mathrm{QCDC}} \otimes H_F}{\sum_f e_f^2 q_f \otimes \hat{\sigma}^{\mathrm{QCDC}} \otimes H_F} \cdot \sigma^{\mathrm{QCDC}} ,
\end{aligned}
\tag{8.9}
$$

$$
\begin{aligned}
\Delta\sigma^{\mathrm{PGF}} &= \frac{\Delta G \otimes \Delta\hat{\sigma}^{\mathrm{PGF}} \otimes H_F}{G \otimes \hat{\sigma}^{\mathrm{PGF}} \otimes H_F} \cdot \sigma^{\mathrm{PGF}} \\
&= \frac{\frac{\Delta G}{G} G \otimes \frac{\Delta\hat{\sigma}^{\mathrm{PGF}}}{\hat{\sigma}^{\mathrm{PGF}}} \hat{\sigma}^{\mathrm{PGF}} \otimes H_F}{G \otimes \hat{\sigma}^{\mathrm{PGF}} \otimes H_F} \cdot \sigma^{\mathrm{PGF}} \\
&= \frac{\frac{\Delta G}{G} G \otimes a_{\mathrm{LL}}^{\mathrm{PGF}} \hat{\sigma}^{\mathrm{PGF}} \otimes H_F}{G \otimes \hat{\sigma}^{\mathrm{PGF}} \otimes H_F} \cdot \sigma^{\mathrm{PGF}} .
\end{aligned}
\tag{8.10}
$$

And taking into account that the following averages can be defined within the sample of the three processes:

$$
\begin{aligned}
\langle X \rangle_{\mathrm{LP}} &= \frac{\int_{sample} X(x) \sum_f e_f^2 q_f(x) \hat{\sigma}^{\mathrm{LP}}(x,z) H(z) dx dz}{\int_{sample} \sum_f e_f^2 q_f(x) \hat{\sigma}^{\mathrm{LP}}(x,z) H(z) dx dz} , \\
\langle Y \rangle_{\mathrm{QCDC}} &= \frac{\int_{sample} Y(x) \sum_f e_f^2 q_f(x) \hat{\sigma}^{\mathrm{QCDC}}(x,z) H(z) dx dz}{\int_{sample} \sum_f e_f^2 q_f(x) \hat{\sigma}^{\mathrm{QCDC}}(x,z) H(z) dx dz} , \\
\langle Z \rangle_{\mathrm{PGF}} &= \frac{\int_{sample} Z(x) G(x) \hat{\sigma}^{\mathrm{PGF}}(x,z) H(z) dx dz}{\int_{sample} G(x) \hat{\sigma}^{\mathrm{PGF}}(x,z) H(z) dx dz} ,
\end{aligned}
\tag{8.11}
$$

equations (8.8)–(8.10) can be further rewritten as

$$\Delta\sigma^{\mathrm{LP}} = \left\langle A_1^{\mathrm{LP}}(x) a_{\mathrm{LL}}^{\mathrm{LP}} \right\rangle \sigma^{\mathrm{LP}} , \tag{8.12}$$

$$\Delta\sigma^{\mathrm{QCDC}} = \left\langle A_1^{\mathrm{LP}}(x_{\mathrm{C}}) a_{\mathrm{LL}}^{\mathrm{QCDC}} \right\rangle \sigma^{\mathrm{QCDC}} , \tag{8.13}$$

$$\Delta\sigma^{\mathrm{PGF}} = \left\langle \frac{\Delta G}{G}(x) a_{\mathrm{LL}}^{\mathrm{PGF}} \right\rangle \sigma^{\mathrm{PGF}} , \tag{8.14}$$

where the virtual photon asymmetry A_1^{LP} is defined as

$$A_1^{\mathrm{LP}}(x) \equiv \frac{\sum_f e_f^2 \Delta q_f(x)}{\sum_f e_f^2 q_f(x)} , \tag{8.15}$$

and the a_{LL}^i represent the partonic cross section asymmetries,

$$a_{\mathrm{LL}}^i = \frac{\Delta\hat{\sigma}^i}{\hat{\sigma}^i} \tag{8.16}$$

for the process i; a_{LL} is also known as the analysing power. The average products can be decomposed into the product of the averages, namely

$$\left\langle A_1^{\mathrm{LP}}(x) a_{\mathrm{LL}}^{\mathrm{LP}} \right\rangle = \left\langle A_1^{\mathrm{LP}}(x) \right\rangle_{a_{\mathrm{LL}}} \left\langle a_{\mathrm{LL}}^{\mathrm{LP}} \right\rangle , \tag{8.17}$$

$$\left\langle A_1^{\mathrm{LP}}(x_{\mathrm{C}}) a_{\mathrm{LL}}^{\mathrm{QCDC}} \right\rangle = \left\langle A_1^{\mathrm{LP}}(x_{\mathrm{C}}) \right\rangle_{a_{\mathrm{LL}}} \left\langle a_{\mathrm{LL}}^{\mathrm{QCDC}} \right\rangle , \tag{8.18}$$

$$\left\langle \frac{\Delta G}{G}(x) a_{\mathrm{LL}}^{\mathrm{PGF}} \right\rangle = \left\langle \frac{\Delta G}{G}(x) \right\rangle_{a\mathrm{LL}} \left\langle a_{\mathrm{LL}}^{\mathrm{PGF}} \right\rangle . \tag{8.19}$$

An assumption of the linear dependence of $\Delta G/G$ with respect to x is made. The reason for such assumption is due to the fact that within the narrow x range of the measurement, the linear behaviour is very consistent with what the QCD fits show. In figure 12.2, the NLO QCD fit curves from LSS [76] and DSSV [27,77] groups illustrate such linear dependence.

The averages of the parton distribution helicity, shown in the left side of equations (8.18)-(8.19), may be approximated to the parton distribution helicity averaged in its respective x region. Therefore, the spin dependent cross sections in equations (8.13)-(8.14) become

$$\Delta\sigma^{\mathrm{LP}} \approx A_1^{\mathrm{LP}}(\overline{x}) \left\langle a_{\mathrm{LL}}^{\mathrm{LP}} \right\rangle \sigma^{\mathrm{LP}} , \tag{8.20}$$

$$\Delta\sigma^{\mathrm{QCDC}} \approx A_1^{\mathrm{LP}}(\overline{x}_{\mathrm{C}}) \left\langle a_{\mathrm{LL}}^{\mathrm{QCDC}} \right\rangle \sigma^{\mathrm{QCDC}} , \tag{8.21}$$

$$\Delta\sigma^{\mathrm{PGF}} \approx \frac{\Delta G}{G}(\overline{x}_{\mathrm{G}}) \left\langle a_{\mathrm{LL}}^{\mathrm{PGF}} \right\rangle \sigma^{\mathrm{PGF}} . \tag{8.22}$$

The helicity asymmetry for the high p_T hadron pairs in the high Q^2 regime can be written as:

$$A_{\mathrm{LL}}^{2h}(x) = R_{\mathrm{PGF}} \langle a_{\mathrm{LL}}^{\mathrm{PGF}} \rangle \frac{\Delta G}{G}(\overline{x}_G) + R_{\mathrm{QCDC}} \langle a_{\mathrm{LL}}^{\mathrm{QCDC}} \rangle A_1^{\mathrm{LP}}(\overline{x}_C) + R_{\mathrm{LP}} \langle a_{\mathrm{LL}}^{\mathrm{LP}} \rangle A_1^{\mathrm{LP}}(\overline{x}_{Bj}) . \tag{8.23}$$

The $R_i = \frac{\sigma^i}{\sigma}$ are the fractions of each process, which are estimated using a Monte Carlo simulation. The calculation of the partonic cross section asymmetries is done at leding order (LO) of perturbative QCD, using also the Monte Carlo technique. The virtual photon asymmetry A_1^{LP} is estimated using a parametrisation based on the inclusive A_1 asymmetry data [78]; an alternative method using parton distribution function models could be applied; yet, this relies on assumptions related to the shape of the $\Delta G(x)$ and $G(x)$ functions which might introduce a bias in the extraction

From equations (2.47), (2.54) and (2.56), one obtains

$$A_1(x) \approx \frac{\sum_f e_f^2 \Delta q_f(x)}{\sum_f e_f^2 q_f(x)} \equiv A_1^{\mathrm{LP}}(x) . \tag{8.24}$$

Thus equation (8.23) reads

$$A_{\mathrm{LL}}^{2h}(x) \approx R_{\mathrm{PGF}} \langle a_{\mathrm{LL}}^{\mathrm{PGF}} \rangle \frac{\Delta G}{G}(\overline{x}_G) + R_{\mathrm{QCDC}} \langle a_{\mathrm{LL}}^{\mathrm{QCDC}} \rangle A_1(\overline{x}_C) + R_{\mathrm{LP}} \langle a_{\mathrm{LL}}^{\mathrm{LP}} \rangle A_1(\overline{x}_{Bj}) . \tag{8.25}$$

The inclusive asymmetry A_{LL}^{incl} contains more than the LO photo-absorption DIS process. In this formulation, the contributions from QCD Compton and PGF are also included.

Therefore, the form of $A_{\rm LL}^{incl}$ will look similar to equation (8.23) and thus it can be rewritten as

$$A_1(x)D \approx A_{\rm LL}^{incl}(x) = R_{\rm PGF}^{incl}\langle a_{\rm LL}^{incl,{\rm PGF}}\rangle \frac{\Delta G}{G}(\overline{x}_G) + R_{\rm LP}^{incl}\langle a_{\rm LL}^{incl,{\rm LP}}\rangle A_1^{\rm LP}(\overline{x}) + R_{\rm QCDC}^{incl}\langle a_{\rm LL}^{incl,{\rm QCDC}}\rangle A_1^{\rm LP}(\overline{x}_C)\,. \tag{8.26}$$

It is important to point out the difference of kinematic phase-space between the inclusive and high p_T samples, since the y, D, x, x_G and x_C distributions can be different for the two samples. Nevertheless, it was checked using a Monte Carlo simulation that the averages of the x_i distributions for the three processes are very similar for the high p_T and the inclusive samples. In particular, a new equation can be written form the inclusive sample (equation (8.26)), using the average of the x_C distribution, *i.e.* $\overline{x} = \overline{x}_C$

$$A_1(x) = R_{\rm LP}^{incl} A_1^{\rm LP}(\overline{x}) + R_{\rm QCDC}^{incl} \frac{\langle a_{\rm LL}^{incl,{\rm QCDC}}\rangle}{D} A_1^{\rm LP}(\overline{x}_C) + R_{\rm PGF}^{incl} \frac{\langle a_{\rm LL}^{incl,{\rm PGF}}\rangle}{D} \frac{\Delta G}{G}(\overline{x}_G)\,, \tag{8.27}$$

$$A_1(x_C) = R_{\rm LP}^{incl} A_1^{\rm LP}(\overline{x}_C) + R_{\rm QCDC}^{incl} \frac{\langle a_{\rm LL}^{incl,{\rm QCDC}}\rangle}{D} A_1^{\rm LP}(\overline{x}'_C) + R_{\rm PGF}^{incl} \frac{\langle a_{\rm LL}^{incl,{\rm PGF}}\rangle}{D} \frac{\Delta G}{G}(\overline{x}'_G)\,. \tag{8.28}$$

The averages $\overline{x}'_C$ and $\overline{x}'_G$ are related to the fraction of the nucleon momentum carried by the struck quark for the sample averaged at $\overline{x} = \overline{x}_C$.

To extract the gluon polarisation, a set defined by equations (8.23), (8.27) and (8.28) is used. Combining these equations and neglecting the small terms as in this case the fractions $R_{\rm PGF}$ and $R_{\rm QCDC}$ are smaller for the inclusive than for the high p_T sample. The spin helicity asymmetry for the sample of events with high p_T hadron pair reads

$$\begin{aligned} A_{\rm LL}^{2h}(x) &= R_{\rm PGF}\langle a_{\rm LL}^{\rm PGF}\rangle \frac{\Delta G}{G}(\overline{x}_G) \\ &+ \frac{R_{\rm QCDC}}{R_{\rm LP}^{incl}}\langle a_{\rm LL}^{\rm QCDC}\rangle \left[A_1(x_C) - A_1^{\rm LP}(\overline{x}'_C)\frac{R_{\rm QCDC}^{incl}}{R_{\rm LP}^{incl}}\frac{\langle a_{\rm LL}^{incl,{\rm QCDC}}\rangle}{D} + R_{\rm PGF}^{incl}\frac{\langle a_{\rm LL}^{incl,{\rm PGF}}\rangle}{D}\frac{\Delta G}{G}(\overline{x}'_G)\right] \\ &+ \frac{R_{\rm LP}}{R_{\rm LP}^{incl}} D \left[A_1(x) - A_1^{\rm LP}(\overline{x}_C)\frac{R_{\rm QCDC}^{incl}}{R_{\rm LP}^{incl}}\frac{\langle a_{\rm LL}^{incl,{\rm QCDC}}\rangle}{D} - R_{\rm PGF}^{incl}\frac{\langle a_{\rm LL}^{incl,{\rm PGF}}\rangle}{D}\frac{\Delta G}{G}(\overline{x}_G)\right]\,. \end{aligned} \tag{8.29}$$

Rearranging equation (8.29) the final expression to extract the gluon polarisation $\Delta G/G$ reads

$$\frac{\Delta G}{G}(x_G^{av}) = \frac{A_{\rm LL}^{2h}(\overline{x}) + A^{\rm corr}}{\lambda}\,, \tag{8.30}$$

$$\begin{aligned} A^{\rm corr} &= -A_1(\overline{x})D\frac{R_{\rm LP}}{R_{\rm LP}^{incl}} - A_1(\overline{x}_C)\frac{1}{R_{\rm LP}^{incl}}\left[\langle a_{\rm LL}^{\rm QCDC}\rangle R_{\rm QCDC} - \langle a_{\rm LL}^{incl,{\rm QCDC}}\rangle R_{\rm QCDC}^{incl}\frac{R_{\rm LP}}{R_{\rm LP}^{incl}}\right] \\ &+ A_1(\overline{x}'_C)\langle a_{\rm LL}^{incl,{\rm QCDC}}\rangle \frac{R_{\rm QCDC}^{incl}}{R_{\rm LP}^{incl}}\frac{R_{\rm QCDC}}{R_{\rm LP}^{incl}}\frac{\langle a_{\rm LL}^{\rm QCDC}\rangle}{D}\,. \end{aligned} \tag{8.31}$$

In equation (8.29) $\Delta G/G$ is probed at two different x_G values, namely x_G and x'_G. Thus the extraction of $\Delta G/G$ requires a definition of the averaged x_G at which the measurement is performed

$$x_G^{av} = \frac{\lambda_1 x_G - \lambda_2 x'_G}{\lambda}\,, \tag{8.32}$$

where

$$\begin{aligned}
\lambda_1 &= a_{\rm LL}^{\rm PGF} R_{\rm PGF} - a_{\rm LL}^{incl,{\rm PGF}} R_{\rm LP} \frac{R_{\rm PGF}^{incl}}{R_{\rm LP}^{incl}} , & (8.33)\\
\lambda_2 &= a_{\rm LL}^{incl,{\rm PGF}} R_{\rm QCDC} \frac{R_{\rm PGF}^{incl}}{R_{\rm LP}^{incl}} \frac{a_{\rm LL}^{\rm QCDC}}{D} , & (8.34)\\
\lambda &= \lambda_1 - \lambda_2 . & (8.35)
\end{aligned}$$

The term $A^{\rm corr}$ contains the correction due to the other two processes; namely the photo-absorption and the QCD Compton processes.

The gluon polarisation is extracted in an event-by-event basis applying a weight estimator, which reduces the statistical uncertainties. The input variables $a_{\rm LL}^i$ and R are estimated using Monte Carlo simulation and afterwards parametrised in the COMPASS kinematic phase space.

8.2 Gluon Polarisation Measurement using the 2nd Order Method

The gluon polarisation $\Delta G/G$ is extracted using the weighted 2nd order method, as described in section 7.4 for the spin helicity asymmetry. In this particular case, instead of a simple asymmetry, the spin helicity asymmetry through events with high p_T hadron pairs is used and, according to eq. (8.30), this asymmetry reads

$$A_{\rm LL}^{2h} = \lambda \frac{\Delta G}{G} - A^{\rm corr} . \qquad (8.36)$$

Thus the number of events for each target cell and spin configuration, given by equations (7.38) to (7.41), are in this case summarised by

$$\begin{aligned}
N_i &= \langle a_i \rangle \left[1 - \langle \beta_i \rangle \left(\lambda \frac{\Delta G}{G} - A^{\rm corr} \right) \right] \int \phi n_i \sigma \, d\vec{\xi} , & (8.37)\\
&= \langle a_i \rangle \left[\langle C_i \rangle - \langle \beta_i \rangle \frac{\Delta G}{G} \right] \int \phi n_i \sigma \, d\vec{\xi} . & (8.38)
\end{aligned}$$

Here, i represents the possible spin configuration (u, d, u', d'), and a_i and β_i are defined according to section 7.4. The averages $\langle \beta_i \rangle_w$ and $\langle C_i \rangle_w$ are redefined in this case as

$$\langle \beta_i \rangle_w = \frac{\sum_j^N w_i^j \beta_i^j}{\sum_j^N w_i^j} \qquad (8.39)$$

and

$$\langle C_i \rangle_w = 1 + \frac{\sum_j^N w_i^j C_i^j}{\sum_j^N w_i^j} . \qquad (8.40)$$

Using the double ratio procedure, described in section 7.4, the variable p_i, defined in equation (7.52), for the 2nd order weighted method can be redefined as

$$p_i = \int wN_i \, d\vec{\xi} = \langle a \rangle_w \left(\langle C_i \rangle_w - \langle \beta_i \rangle_w \frac{\Delta G}{G} \right) \int \Phi n_i \sigma d\vec{\xi} \,. \tag{8.41}$$

Then the gluon polarisation is extracted from an analogous formula to (7.45)

$$a \left(\frac{\Delta G}{G} \right)^2 + b \left(\frac{\Delta G}{G} \right) + c = 0 \,. \tag{8.42}$$

In this case a is given by the same expression (7.46), whereas b and c are given by

$$b = -\delta \left(\langle C_d \rangle \langle \beta'_u \rangle + \langle C'_u \rangle \langle \beta_d \rangle \right) + \left(\langle C'_d \rangle \langle \beta_u \rangle + \langle C_u \rangle \langle \beta'_d \rangle \right) \tag{8.43}$$

and

$$c = \delta \langle C'_u \rangle \langle C_d \rangle - \langle C'_d \rangle \langle C_u \rangle \,. \tag{8.44}$$

The solution for equation (8.42) is given by a similar expression to (7.49),

$$\frac{\Delta G}{G} = \frac{-b \pm \sqrt{b^2 - 4ac}}{2a} \,; \tag{8.45}$$

$$\text{if} \quad a = 0 \quad \text{, then} \quad \frac{\Delta G}{G} = -\frac{c}{b} \,. \tag{8.46}$$

In this method the gluon polarisation, $\Delta G/G$ is extracted directly without any prior calculation of the asymmetry. Thus, the desired quantity to be extracted is redefined according to equation (8.36), taking into account the corrections from the other processes in the term A^{corr}. The optimal weight w in equations (8.39) to (8.41) is defined according to the statistical and systematic errors, which in the case of the COMPASS experiment leads to $w = f D P_b \lambda$.

CHAPTER 9

DATA ANALYSIS

– Senator, you have the vote of every thinking person!
– That's not enough, madam, we need a majority!

Adlai Stevenson commenting to a lady while running on the U.S. presidential elections.

Data is the information contained in the events. An event, in a philosophical sense, is an occurrence in a particular location at a specific time (or time period) with an additional requirement: this occurrence has to be special, so it has to carry some special information, thus it has to carry data. In this sense, the main idea of an event in High Energy Physics (HEP) embodies also this philosophical concept.

In this chapter data analysis is fully explained, starting by the event reconstruction described in section 9.2. The beam and target inputs data parameters to the analysis are presented in section 9.1. The quality procedure applied to the data is described in section 9.3. The way the data is associated is explained in section 9.4. In section 9.5 the data selection criteria is discussed.

9.1 Beam and Target Inputs into the Analysis

In section 7.2 the input data used in the spin asymmetry calculation was introduced. The purpose of this section is to show and describe with detail the beam and target parameters used in the current analysis to extract the gluon polarisation, namely the dilution factor f, the depolarisation factor D, and the beam and target polarisations, P_b and P_t.

Dilution Factor f

The cross sections σ_d and σ_A, in equations (7.9) and (7.10), depend on the event kinematics (x, Q^2). Therefore, some dependence on the kinematics is also expected on the dilution factor f. This is illustrated in figure 9.1, in which a dependence on the x_{Bj} variable is observed.

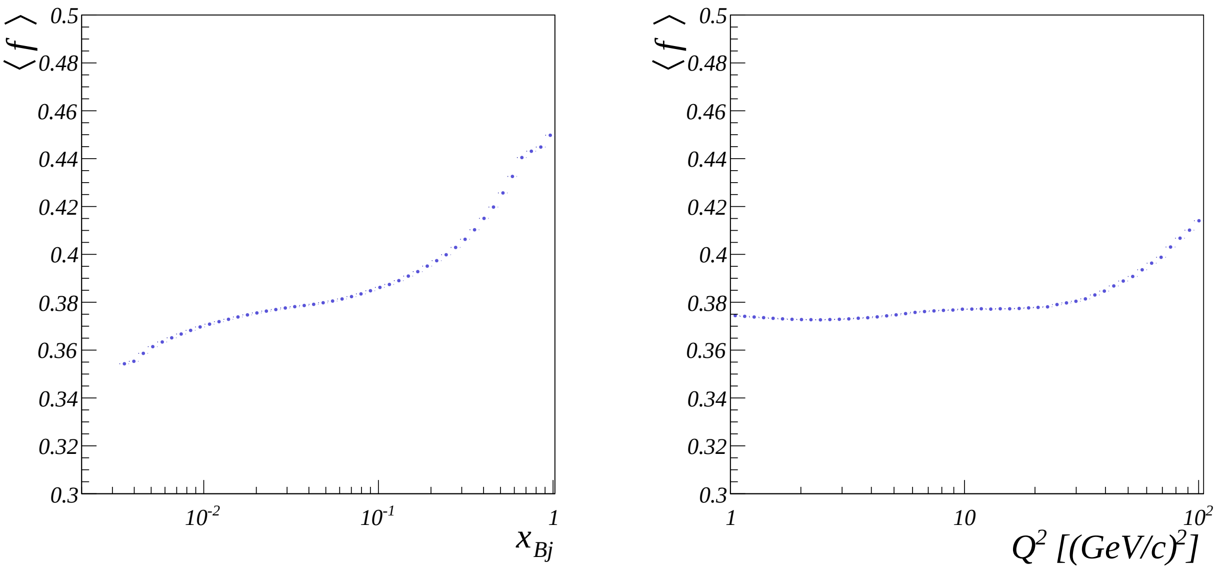

Figure 9.1: The average value of the effective dilution factor as a function of x_{Bj} (on the left) and Q^2 (on the right).

Depolarisation Factor D

The depolarisation factor D is determined by equation (2.49). The dependence of the depolarisation factor on the three kinematic variables is depicted in figure 9.2.

Beam and Target Polarisation

The beam polarisation strongly depends on the ratio between muon and hadron momenta. In figure 9.3, this dependence is well illustrated, where the parametrised polarisation of the muon beam is shown as a function of the central muon beam momentum. Before starting the 2004 data taking campaign, it was found out that the parametrisation of the beam polarisation could be improved leading to a lower intensity in the beam, yet gaining on the beam polarisation and consequently improving the figure of merit of the asymmetries.

The target cells are polarised by setting the microwave field, as described in section 4.3. However, this polarisation technique takes not less than one day, with an associated risk of losing completely the polarisation. Therefore a quicker and safer way of reverting the target cell polarisations is used. In this sense, the target cell polarisation is manipulated using the solenoid magnetic field direction.

In figure 9.4 all possible muon and target cells polarisation configurations are shown. The

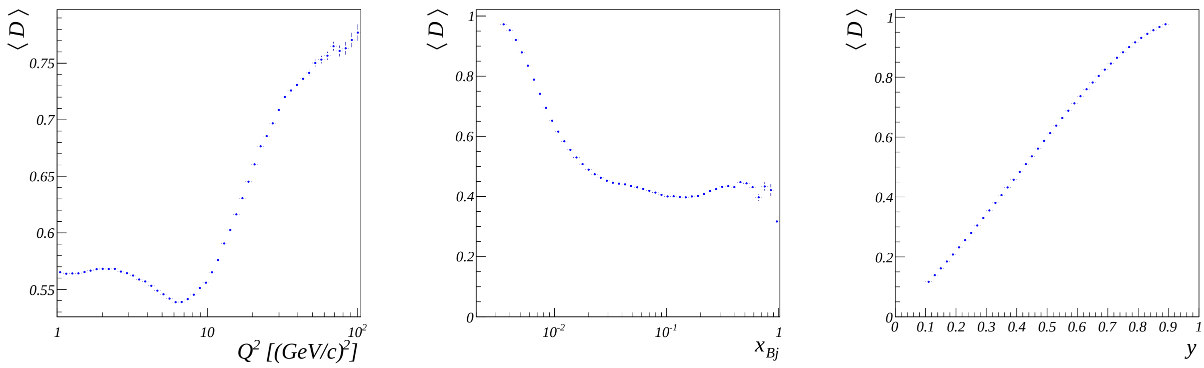

Figure 9.2: The average value of the effective depolarisation factor as a function of Q^2 (left side), x_{Bj} (centre) and y (right side).

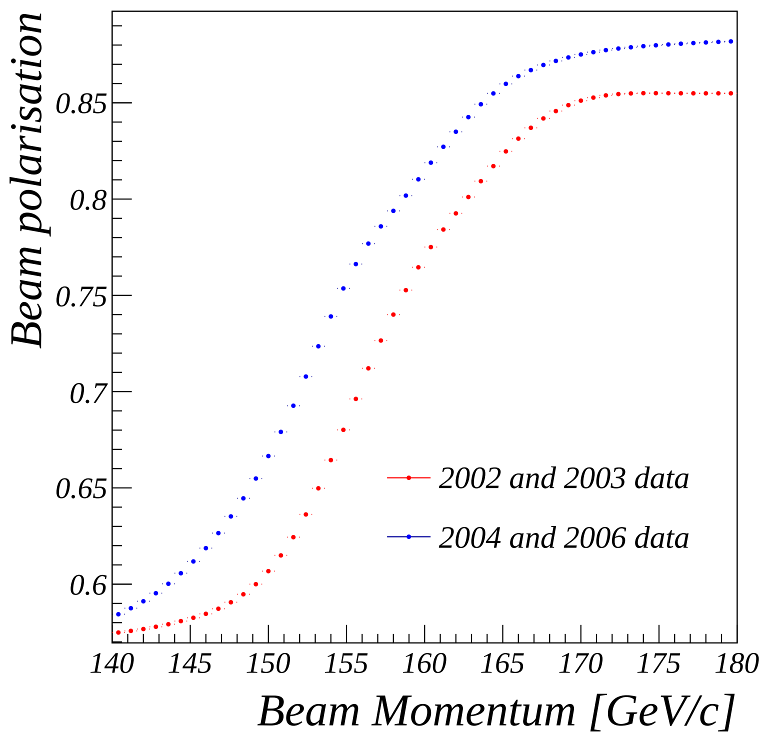

Figure 9.3: Polarisation as a function of the muon momentum.

muon polarisation is fixed, represented by the thick arrow next to the label, while the long thin arrow represents its trajectory direction. The arrows inside the target cells represent their polarisation states. There are in total 4 configurations: a) The interaction vertex for an event occurred in the first cell (from left to right), so the number of events is given by $N_{u}^{\overset{\leftarrow}{\Rightarrow}}$ [1] and events for which the interaction vertex is inside the second cell, the number of events is given

[1] The upper arrow is related to the muon polarisation. The lower arrow represents the polarisation of the deuteron in the respective target cell

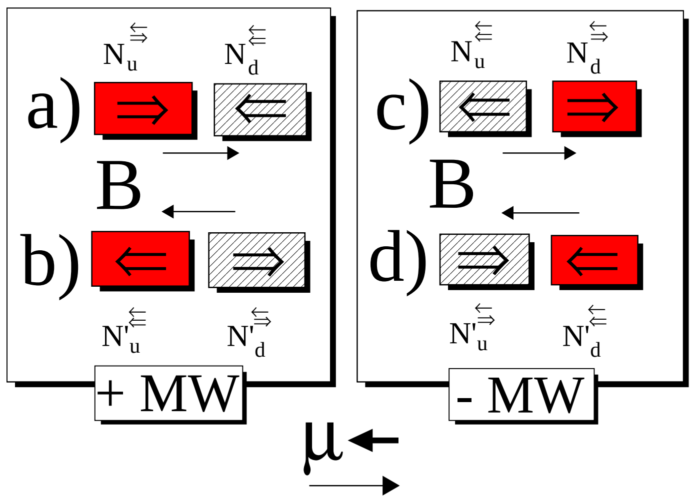

Figure 9.4: Illustration of the muon target spin configurations. Details in the text.

by $N_d^{\overleftarrow{\Leftarrow}}$. b) After reverting the direction of the solenoid magnetic field, the polarisations are also reverted. And, therefore, the events with interaction vertex in the first cell are accounted as $N'^{\overleftarrow{\Leftarrow}}_u$ and the events with the interaction vertex inside second cell are accounted as $N'^{\overleftarrow{\Rightarrow}}_d$. The situation for configurations c) and d) are analogous, apart the fact that in c) the first cell accounts for the $N_u^{\overleftarrow{\Leftarrow}}$ and the second for $N_d^{\overleftarrow{\Rightarrow}}$. And after the solenoid magnetic field reversal, the first cell accounts for $N'^{\overleftarrow{\Rightarrow}}_u$ and the second for $N'^{\overleftarrow{\Leftarrow}}_d$.

Thus, using the sign of the solenoid magnetic field the muon and target configurations can be switched rather quickly from a) to b), or from c) to d). This operation was done three times per day, *i.e.* once per data taking shift. From 200 on, there was the decision to perform this rotation field once per day, the reason being related to technical issues: reducing this procedure minimises the probabilities of technical problems on the polarised target, which might compromise the data taking.

Configurations a) and b), are named as positive (+) microwave configurations, because the sign of the solenoid magnetic field and first polarised target cell are the same. Configuration c) and d) are named negative (−) microwave configuration, in this case the sign of the solenoid magnetic field and first polarised target cell are the opposite. Figure 9.5 shows the typical target polarisations for several periods.

9.2 Event Reconstruction

In section 4.5 the raw data processed and collected by the DAQ system was explained in detail. This data contains essentially hits information.

The event reconstruction begins with the decoding process. The information about hits from fired channels (wire, pad or cell, depending on the kind of detector) needs to be extracted from the raw data. For MC data, the decoding process is replaced by digitisation, which simulates the detector response, producing hits.

Regardless the data origin (MC or real), the hits are clustered. The main idea of the clustering process is to gather the hits belonging to the same particle. In this process information

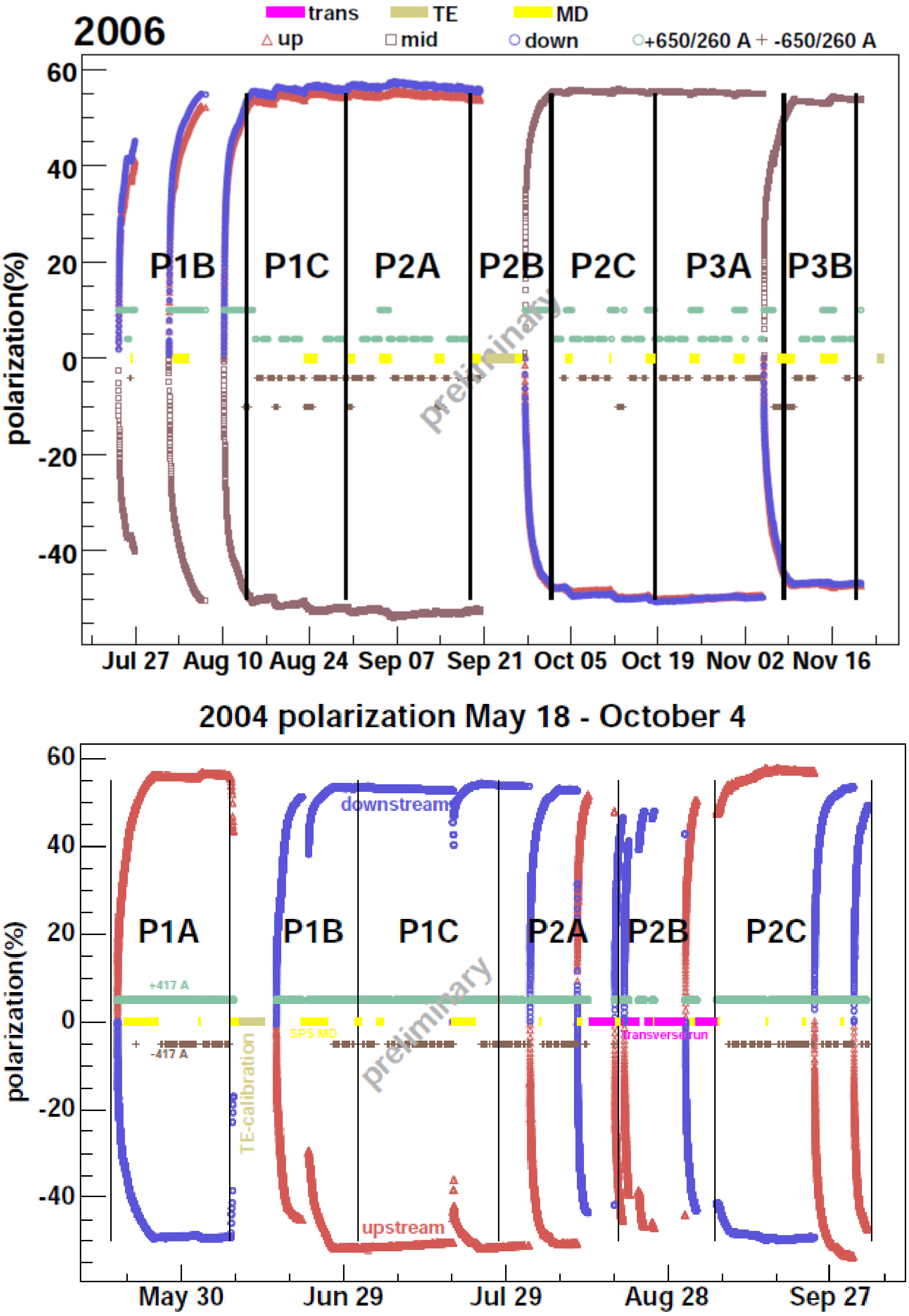

Figure 9.5: Target polarisation for 2006 (top) and for 2004 (bottom). These distributions are plotted against the data taking time period.

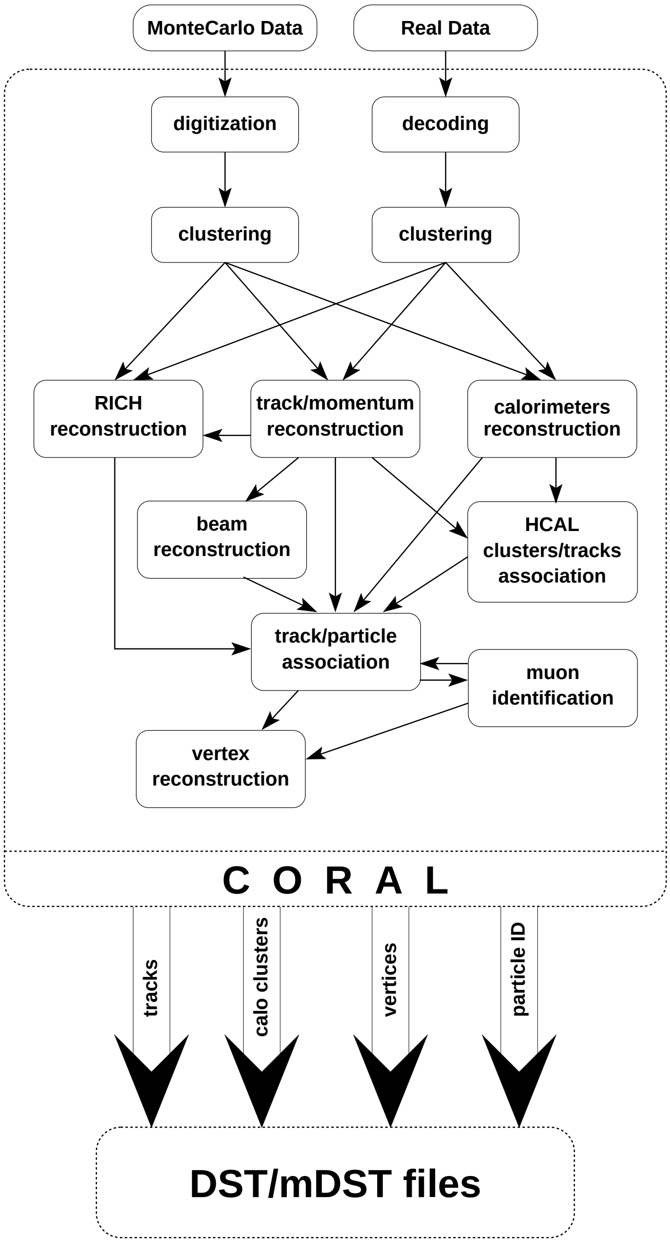

Figure 9.6: Schematic representation of the COMPASS reconstruction software.

about the hits and detector position is used to compute the final cluster position in the spectrometer main reference frame.

The clusters are used in the reconstruction process. This process is divided in several modules according to the type of reconstruction. Information from tracking detectors is used to reconstruct and determine, with help of the magnets, the momentum of a charged particle. From calorimeter clusters, muon and hadrons are separated, also energy and impact point coordinates of photons and electrons are determined. Particle identification (PID) is performed in the RICH, as explained in section 5.1. The association of a particle to a given track is made by combining information from the RICH, the tracking and the calorimeter reconstruction. The vertex reconstruction procedure is performed to all reconstructed charged tracks, in order to find the primary interaction point and subsequent ones; also during this process, particles are associated to event reconstructed vertices. All these tasks are performed by the COMPASS reconstruction algorithm (CORAL) [79] program. The reconstruction procedure is accomplished at CERN by the data production team [80].

At this point, the data is prepared to be used for analysis. The main philosophy is to make available all the needed and useful information to the analysis users in a practical and flexible way. All the information about tracks, vertex and calorimeter parameters is associated to the event together with the PID probabilities from the RICH detector and also hits and clusters from all the detectors. This information is compiled, in order to know the relations between the different elements. Also information related to the event identification, *i.e.* run, event and spill numbers, is assigned. Finally all information is stored in mini Data Summary Tape (mDST) structures in ROOT [66] files, which are available at CERN and also distributed to several computing centres to facilitate the analysis for several groups. These mDST files can be analysed with the physics analysis software Ttools (PHAST) [81]. The spectrometer condition within a period is assumed to be stable enough, therefore data within a period is reconstructed in one block. It is also common to use the term *production* to refer a data period reconstruction.

Figure 9.6 depicts the general flow diagram of the COMPASS reconstruction software.

9.3 Data Quality

The data quality procedure has the purpose to indicate which of the reconstructed data can be used for physics analysis. This procedure is initially based on event general criteria, *i.e.* number of spills per run, number of detector planes signalled by the shift crew as having problems, etc. This information is registered in an electronic logbook. After this first filter, data is analysed, the behaviour of some observables, known as macro variables [2], are checked for stability against the spill number. As an example the distributions of some of these macro variables are presented in figure 9.7. The distributions are related to the week 42 of the 2006 data period. Data plotted in red is signalled as *good* to be used for analysis, the black one is signalled as *bad*. The rejection criteria are based on the statistical significance of the projected distributions.

For each data production a list containing the spills to be discarded from the analysis is produced. This list is also known as the *bad spill list* and is used, normally for all the analyses in COMPASS, to exclude bad quality data.

[2] http://wwwcompass.cern.ch/compass/software/offline/input/stab/macro.html

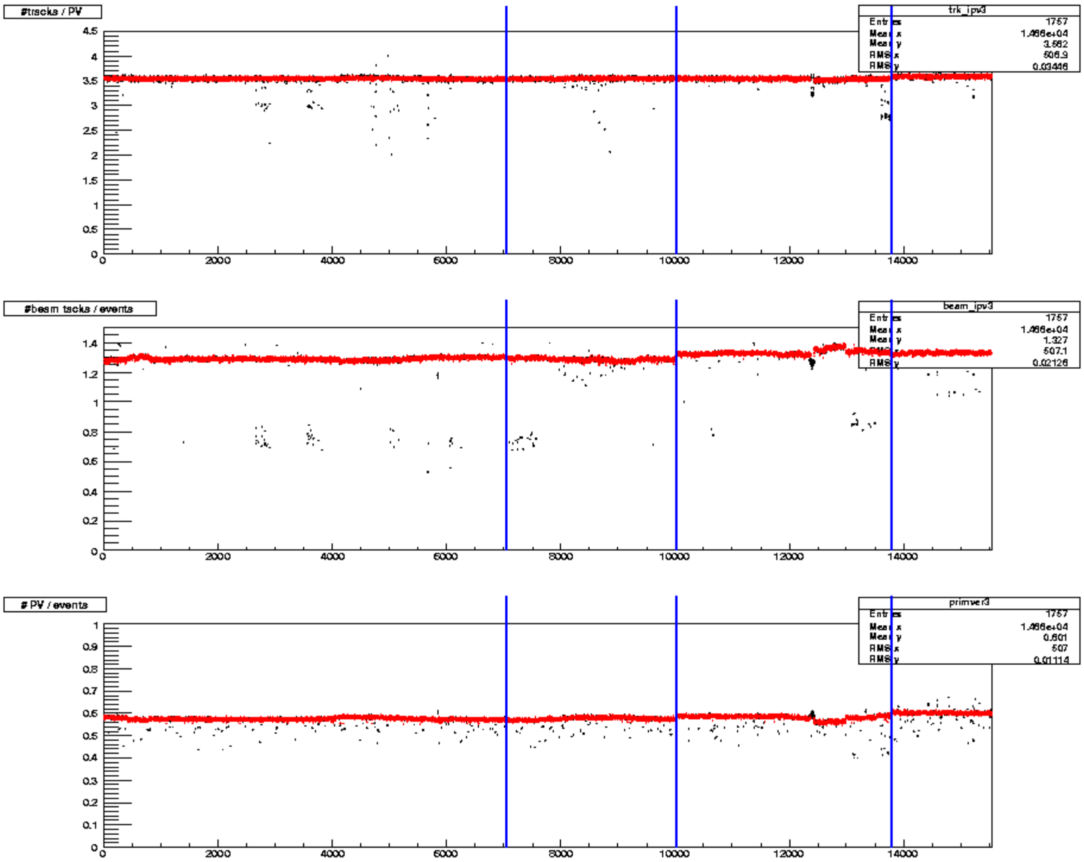

Figure 9.7: Macro variable distributions. Number of primary vertices (top), number of beam tracks per event (middle), number of primary vertices per event (bottom). All these variables are plotted against the spill number.

9.4 Data Grouping

To calculate the gluon polarisation according to section 8.2, the number of events are taken by using, sequentially, two possible muon and target spin configurations, namely $N^{\overleftarrow{\Rightarrow}}$ and $N^{\overleftarrow{\Leftarrow}}$.

During data taking the SPS accelerator undergoes maintenance periods called *Machine Development* periods. These periods occur in a weekly basis, lasting in average 8 hours. During the machine development time some maintenance works may be performed on the COMPASS spectrometer. Therefore, between two consecutive machine development periods, the spectrometer conditions remain stable. In this way, systematic effects due to spectrometer conditions are avoided. Moreover, these time periods between machine development are called formally *data taking periods*. Within a data taking period, the polarisation target cells are reverted every 8 (24) hours for the data taking periods in 2002–2004 (2006–).

Within a data taking period, data are grouped in two possible ways or configurations (fig. 9.8):

- **Global:** The whole period is taken as a group (fig. 9.8 left side).
- **Consecutive:** The period is split in data groups of runs. The group corresponds to the set of runs taken with one solenoid field direction and the set of runs taken with the immediate opposite one. And, on top of this, for each set the spectrometer conditions

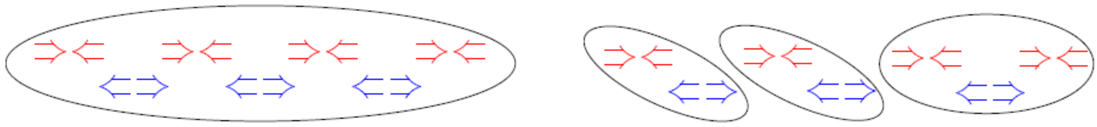

Figure 9.8: Possible data grouping: Global (left) and Consecutive (right).

must be very similar. On the right side of figure 9.8 an illustration representing the scheme of this grouping is shown.

The clear advantage of consecutive over global configurations is that the analysis on such data group is less affected by systematic uncertainties due to differences in spectrometer situations.

The usage of consecutive configuration has its price, especially for the 2006 data. In this year, in which there was only one field rotation per day, about 30% of the events that did not have a partner with opposite field direction.

9.5 Data Selection

The data sample used in this analysis includes data from the years 2002, 2003, 2004 and 2006. The selected events have a primary vertex containing an incoming muon beam, a scattered outgoing muon and at least two outgoing hadrons with high transverse momentum. The purpose of the described criteria is to ensure a correct event topology.

As it was already referred, the goal of the data selection in this analysis is to increase the yield of PGF events. From simulations, it was learnt that the fraction of LP events is significantly higher compared to the QCD Compton and PGF event fractions (see section 10.2). In this section, the data selection cuts and criteria are discussed and explained.

Target geometry

The incoming muon, μ, is required to cross all target cells, to ensure that each target cell has the same muon beam flux. Another requirement is that the primary vertex should to be inside an homogeneous target volume for which its characteristics remain stable. These conditions are ensured with a radius $r < 1.3$ cm and vertex coordinate $y < 1.0$ cm; both criteria are applied to each target cell.

Selection on inclusive kinematic variables

In order to define the high Q^2 region, the following kinematic cut is applied: $Q^2 > 1\,(\mathrm{GeV}/c)^2$. This ensures the high virtuality character of the photon in the DIS photo absorption process.

Upper and lower limits are applied to the variable y, the fraction of the energy lost by the incoming muon: $0.1 < y < 0.9$. Events with $y < 0.1$ are rejected because the depolarisation factor related to this data is rather low, leading to a yield of events which might produce an intrinsic low gluon polarisation and a possible source of uncertainty. Events with $y > 0.9$ are rejected because they are strongly affected by radiative effects, which are difficult to evaluate in this analysis. The distributions of the kinematic variables Q^2, y, x_{Bj} are shown in Fig. 9.9.

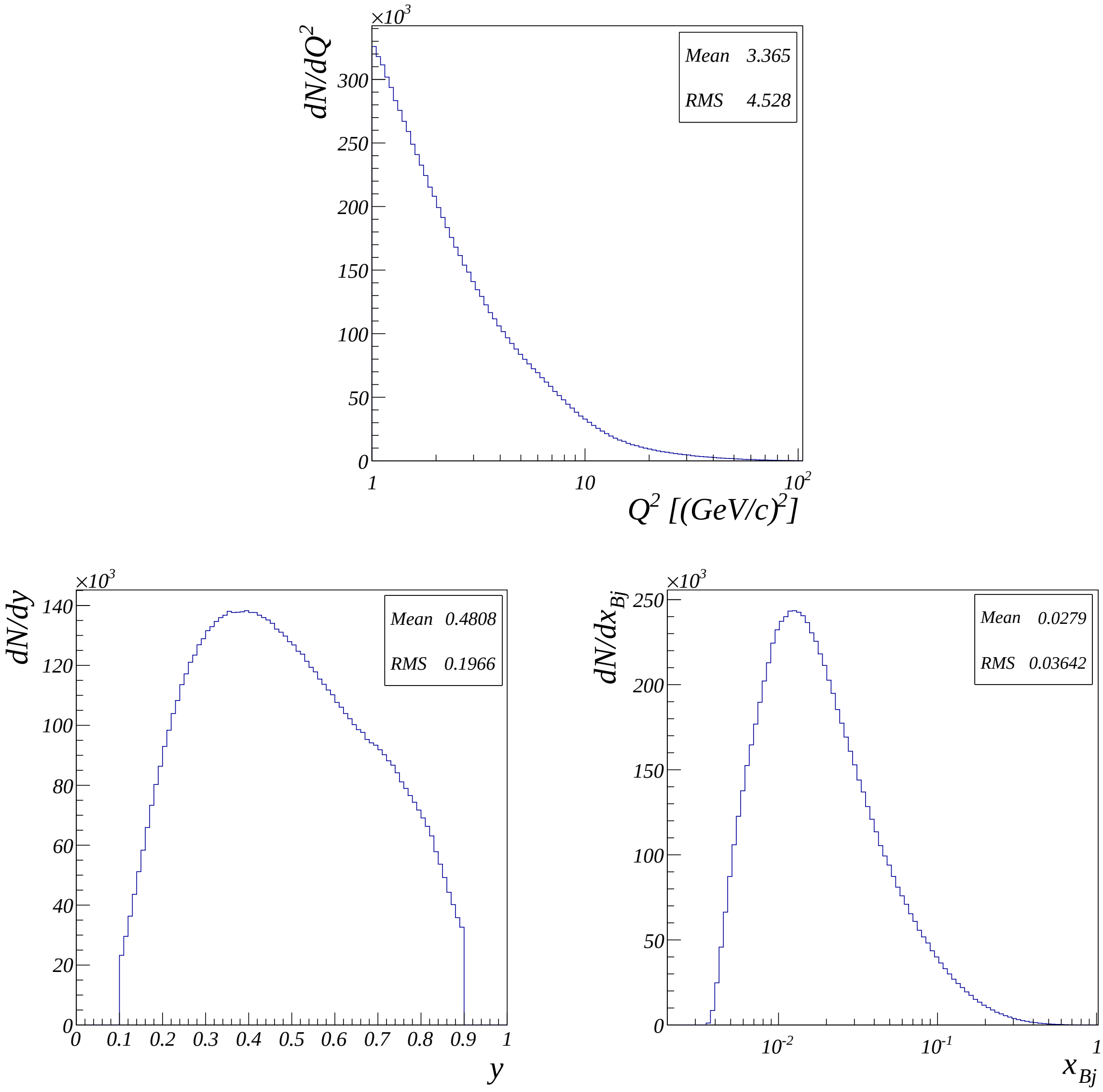

Figure 9.9: Q^2, y and x distributions after all cuts applied.

The kinematic phase-space in a 2-dimensional plot of Q^2 versus y is shown in figure 9.10. The same plot is shown for the relevant triggers (*cf.* sec. 4.4) in figure 9.11. It is worthy to point out that the most significant triggers to this analysis are the Calorimetric, Middle and Outer triggers.

Figure 9.12 presents the distribution of the events for all these triggers.

Particle identification

In order to improve the muon identification, it is also required that the scattered muon μ' track has an associated cluster in both hodoscope planes of the trigger that was fired (as discussed in the trigger section). In case of mixed triggers, it is required that this condition is met at least for one of them. In case of semi-inclusive triggers, one requires that at least one hadron track in the primary vertex.

Two particles with the highest transverse momentum p_T associated with the primary

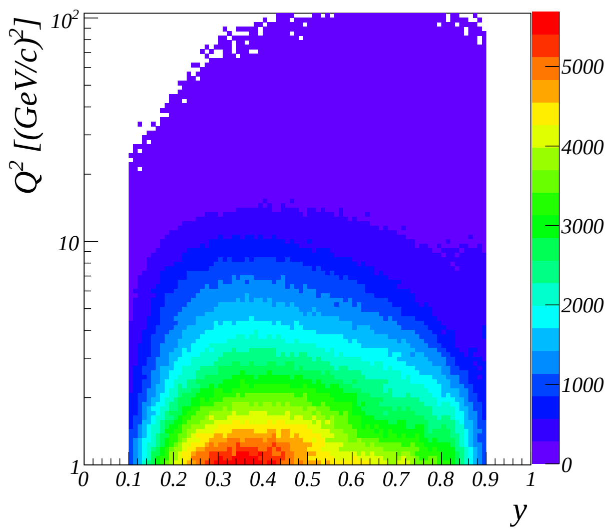

Figure 9.10: Q^2 vs y distribution.

vertex besides the incoming and scattered muons μ and μ' are considered as *hadron candidates*. They must fulfil the following requirements:

- The hadron candidates should not be muons. There is indeed a small probability of a pile-up muon to be included in the primary vertex and therefore being considered as a hadron candidate. The hadron candidate is rejected if it goes through the Muon Filter 2 (position of the last cluster $z > 40$ m) or if it travels through too much material, having a radiation with a total length of $X/X_0 > 30$.

- The track reconstruction quality should be good. To achieve the desired quality level first a criterium imposing $\chi^2/ndf < 20$ is applied. Then, it is verified that the track was not reconstructed only within the fringe field of SM1 by requiring the last cluster to be located downstream from SM1.

- Hadrons do not go through the solenoid. The hadron tracks are extrapolated to the entrance of the solenoid and then the distance between the track and the z axis should be less than the radius of the solenoid aperture.

Cuts on hadronic variables

The following cuts are applied to the leading (highest transverse momentum) and sub-leading hadrons:

- For the leading hadron, the transverse momentum cut is $p_{T_1} > 0.4$ GeV/c and for the sub-leading hadron the cut is $p_{T_2} > 0.7$ GeV/c. This requirement constitutes the high p_T cut. The main purpose of this cut is to enhance the event yield coming from the PGF processes.

- $x_F > 0$, $z > 0$ and $z_1 + z_2 < 0.95$. The first cut ensures that the hadron comes from the current fragmentation region (see fig. 2.4). The last cut is meant to reject events from exclusive production heavier than pions.

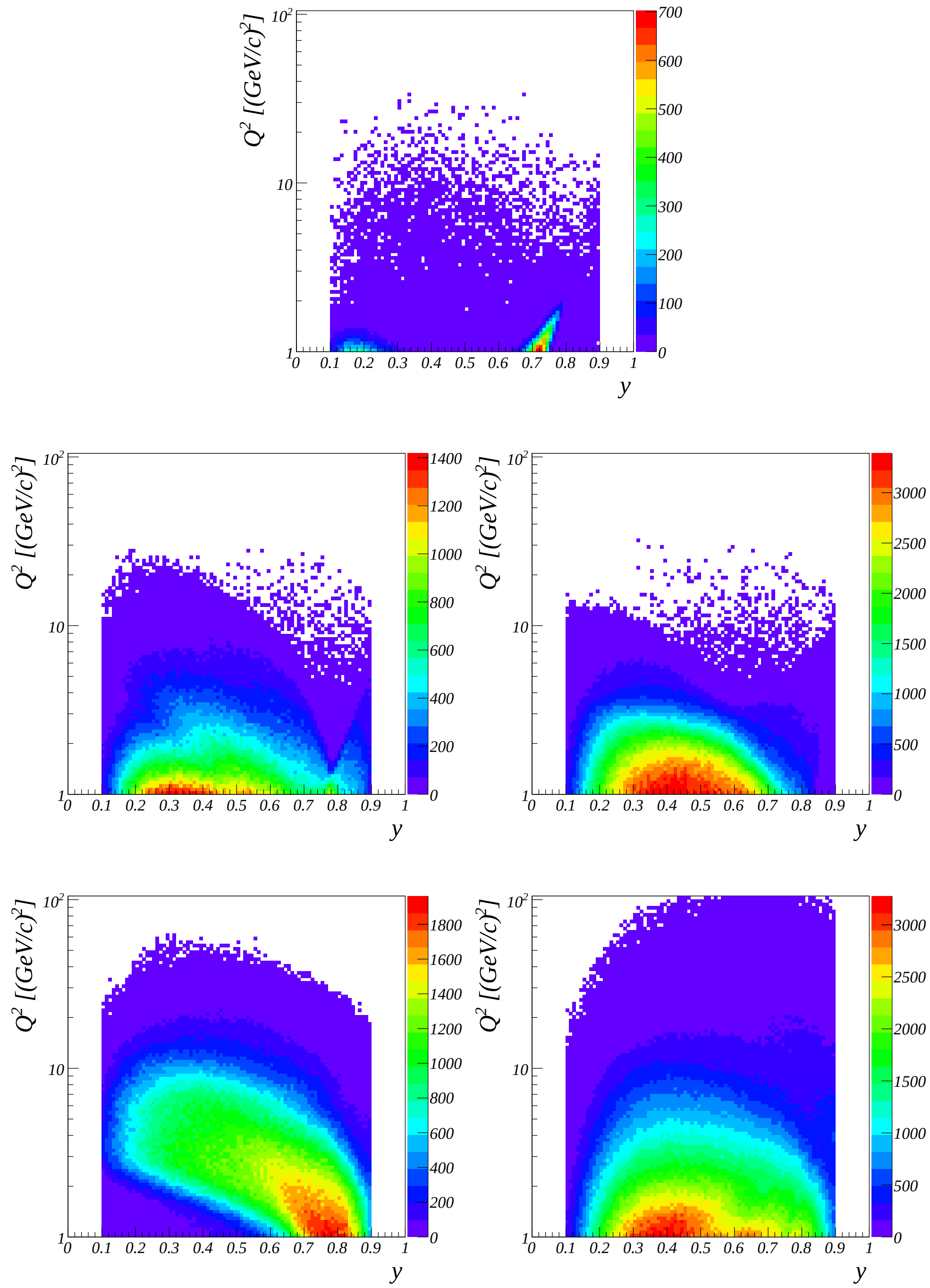

Figure 9.11: Q^2 vs y per trigger. Inner (top plot), Ladder (centre left plot), Middle (centre right plot), Outer (bottom left plot) and Calorimetric (bottom right plot) triggers.

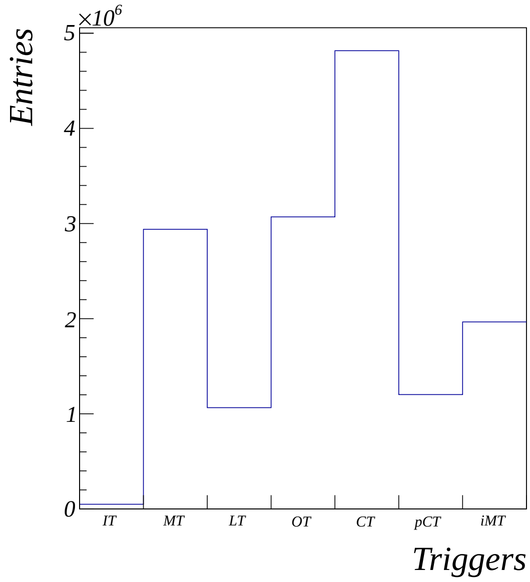

Figure 9.12: Trigger distribution.

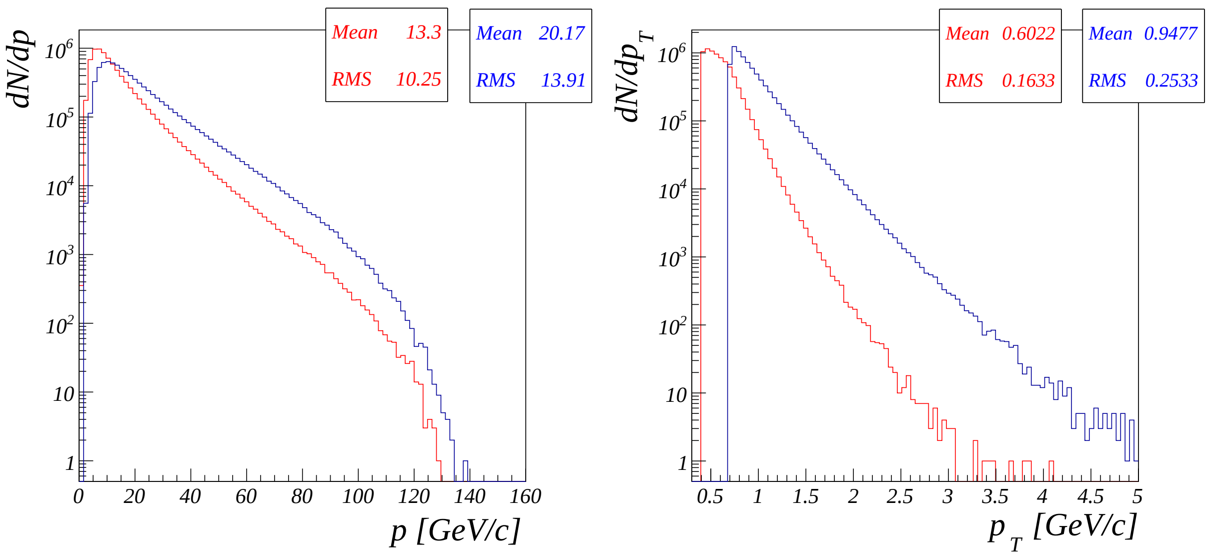

Figure 9.13: p and p_T distributions for leading (in blue) and sub-leading (in red) hadrons.

The number of events and the percentage that survives each cut are displayed in table 9.1. In this table, the *candidate* events are those which pass all kinematic and high p_T cuts. "Hadron ID" refer to events which pass the first cut of *hadron candidates*, while hadron quality refers to the second cut.

The distributions of p and p_T variables are presented in figure 9.13. In figure 9.14 the distributions for the z, x_F and θ are shown. In both figures, the whole data sample, namely from 2004 to 2006, is used in the distributions.

An interesting issue is to compare data with respect to the increased geometrical acceptance brought by the new solenoid aperture for 2006 data. In figure 9.15, the distributions of Q^2, x_{Bj}, y and θ for the leading high p_T are shown, the difference in the inclusive variables

Cuts	2002		2003		2004		2006		All years	
	# Events	%	# Events	%	# Events	%	# Events	%	# Events	%
micro DST	9146075	100.00	19002305	100.00	38253588	100.00	36697956	100.00	103099924	100.00
≥ 4 particles in event	7606575	83.17	16640796	87.57	35031752	91.58	34531980	94.10	93811103	90.99
Ineffective region of MT	7606575	83.17	16640796	87.57	35031752	91.58	33801539	92.11	93080662	90.28
Target cuts	4730494	51.72	10640710	56.00	23080442	60.34	21718149	59.18	60169795	58.36
$Q^2 > 1$ GeV/c^2	3364874	36.79	7921287	41.69	17193086	44.95	16419888	44.74	44899135	43.55
$0.1 < y < 0.9$	3133251	34.26	7289299	38.36	15624721	40.85	14794021	40.31	40841292	39.61
≥ 2 outgoing hadrons	2179813	23.83	5188411	27.30	10470930	27.37	12561232	34.23	30400386	29.49
p_T cut	685527	7.50	1672704	8.80	3374947	8.82	4654945	12.68	10388123	10.08
Hadron χ^2 cut	685523	7.50	1672695	8.80	3374872	8.82	4654340	12.68	10387430	10.08
Solenoid aperture cut	604283	6.61	1470687	7.74	2956183	7.73	4620795	12.59	9651948	9.36
Grouping cut	470268	5.14	1431545	7.53	2902851	7.59	3962690	10.80	8767354	8.50
Solenoid > 100 A	470268	5.14	1431545	7.53	2896501	7.57	3934698	10.72	8733012	8.47
Hadron ID	468404	5.12	1425748	7.50	2884986	7.54	3925816	10.70	8704954	8.44
$x_F > 0$	462642	5.06	1402413	7.38	2841504	7.43	2868271	7.82	7574830	7.35
$z_1 + z_2 < 0.95$	455612	4.98	1385086	7.29	2805543	7.33	2834678	7.72	7480919	7.26
SM1 fringe field	450134	4.92	1363630	7.18	2770995	7.24	2776831	7.57	7361590	7.14
Empty configurations	450134	4.92	1363630	7.18	2770995	7.24	2722176	7.42	7306935	7.09

Table 9.1: Table summarising cuts. The lines correspond to relevant cuts applied sequentially and the number (fraction) of events that survived until the cut.

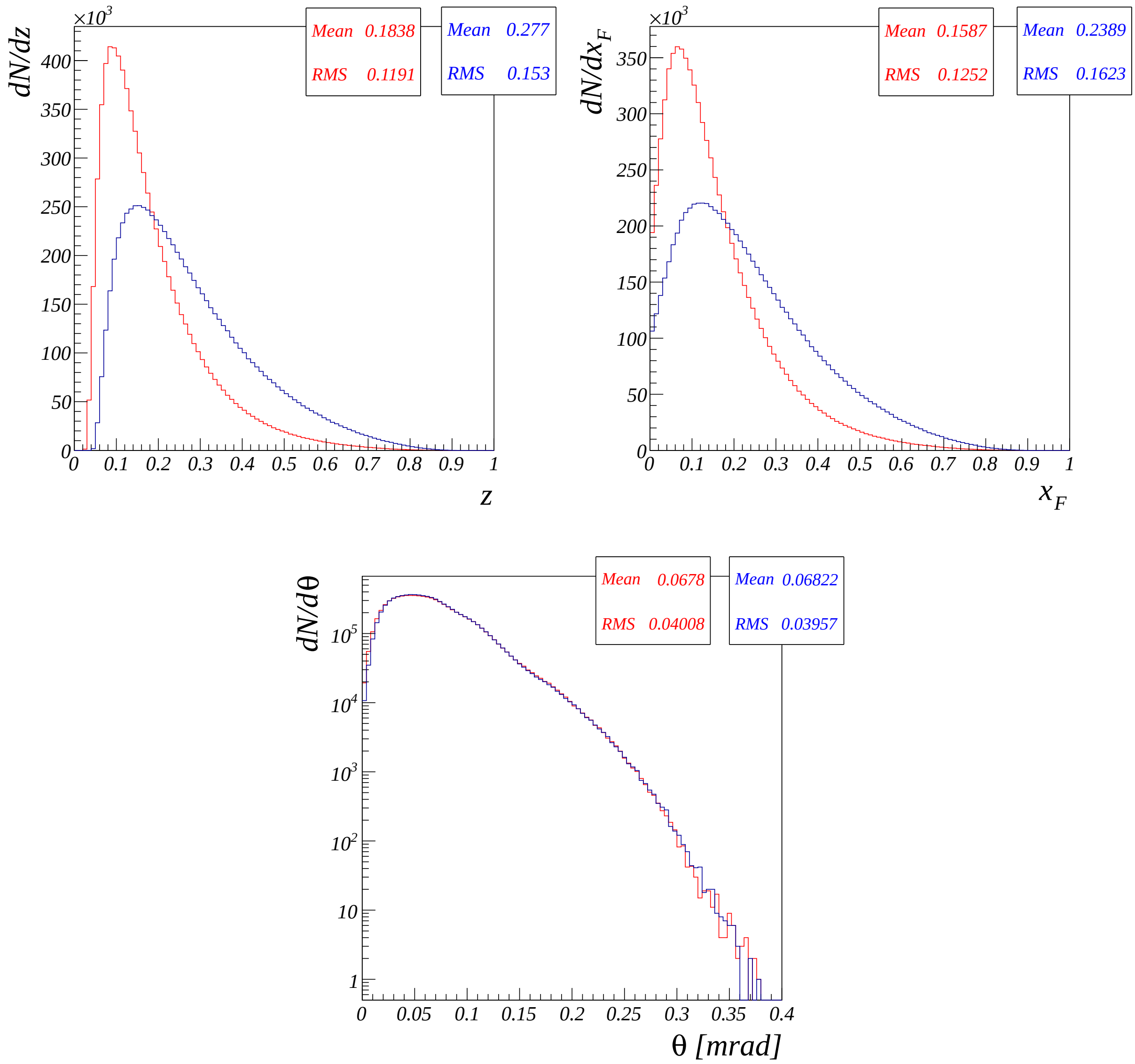

Figure 9.14: z, x_F and θ distributions for the leading (in blue) and sub-leading (in red) hadrons.

being only clearly noticed in the fraction of energy loss with respect to scattered muon.

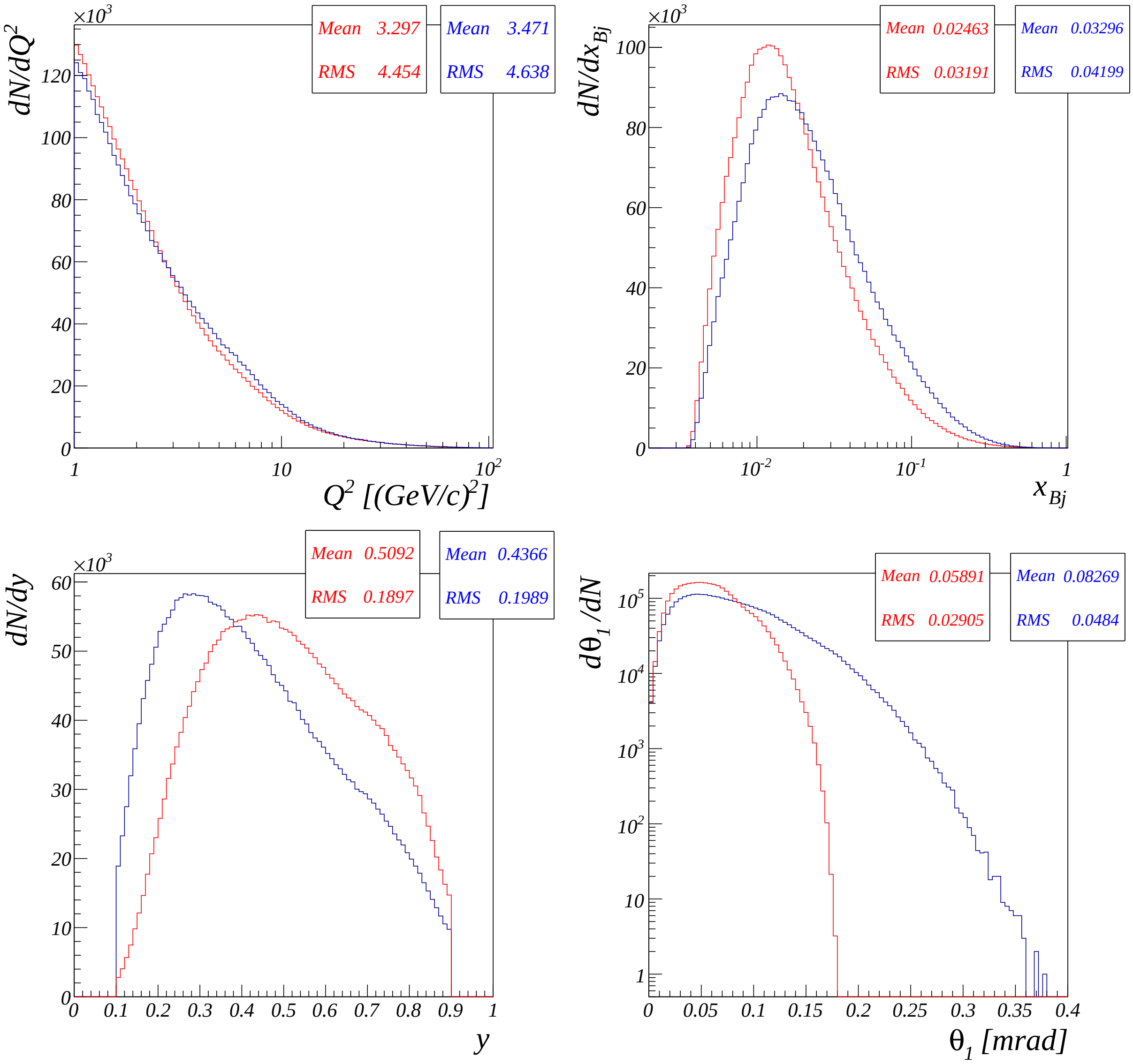

Figure 9.15: Q^2 (top left plot), x_{Bj} (top right plot), y (bottom left plot) and θ for the leading high p_T (bottom right plot) distributions for 2002-2004 (in red) and 2006 (in blue) data.

CHAPTER 10

MONTE CARLO SIMULATIONS

Trust is the highest form of human motivation. It brings out the very best of people. But it takes time and patience.

Stephen Covey.

In god we trust, all others pay cash.

Jean Shepherd.

Simulation is a very special topic in physics. Generally, the main goal of a simulation is to reproduce, as close as possible, a specific process or effect in nature, *i.e.* in real life. Many problems in physics are only solved thanks to a simulation process, *e.g.* in meteorology, most of the models of weather forecasts are based on simulations. In high energy physics, this is an issue of major importance and in particular for this analysis, in which some information, obtained from simulations, is used to extract the gluon polarisation.

Since the simulation is intended to reproduce reality and its final purpose is to extract reliable information, then it should be trustworthy. In section 10.1 the reasons to use this kind of simulation is presented.

It is impossible to reproduce reality as it is. The reason is simple: in real life, the amount of parameters which need to be controlled is huge (in practically infinity). The description of the whole simulation as a system composed of several kinds of parameters to be controlled, which can be grouped into different modules, is given in section 10.2. The modules and their respective functionalities are described in the following sections: the event generator in section 10.3, the simulation of the spectrometer apparatus in section 10.4

As already mentioned, to trust, *i.e.* have confidence, on the information given by the simulation, it needs to reproduce, as close as possible, nature: in this case, the DIS events. For this, adjustments and fine tuning need to be taken into account. This is discussed in detail in the next sections. The parton distribution functions, longitudinal structure functions and gluon radiation are discussed in section 10.5. In section 10.6, a tuning in order to describe properly the hadronic variables is applied; the tune concerns the intrinsic momenta of the produced hadrons and also the hadronisation model. Science can not be built upon statements with a simple and blind belief. To trust, some evidence is demanded to verify if the simulated data indeed is close enough, for our purpose, to real data. In section 10.7, the comparison of data with the simulation is shown. The result of this comparison is a remarkable agreement between simulation and data. In section **??** other used MC simulation samples are presented.

The MC simulation samples are used to parametrise partonic variables needed for the gluon polarisation extraction. In section 10.8, the tool to parametrise these quantities, the neural network, is described.

10.1 Why a Monte Carlo Simulation?

As mentioned in the beginning of this chapter, the main reason to use a simulation in this analysis is because some information is lacking and needs to be estimated. In section 8.1, the general form of the expression to extract the gluon polarisation $\Delta G/G$ is stated in equation (8.30). Looking more closely to all the terms enclosed in this formula, it turns out that the information needed to evaluate it can not be completely extracted from real data. The reason, as explained in the beginning of chapter 8, is the fact that, from all the processes in DIS, the only one from which the spin information of the gluon is accessed directly is the PGF process (in figure 8.1). There is no possibility via analytical selection on the data to select unequivocally this process. Usually, analytical techniques are used to enrich the yield of PGF events.

10.2 MC Simulation

Many sample characteristics essential for the extraction of the gluon polarisation have to be obtained from the Monte Carlo simulations. In order to be available on event-by-event basis they are parametrised using neural networks (NN) (section 10.8). This is the reason why a good description of the experimental data by MC is crucial for the analysis. The contributions to the hadrons transverse momentum p_T for the LP process come from two sources: i) the intrinsic transverse momentum k_T of the quarks in the nucleon and ii) the fragmentation process. From both sources, the resulting p_T is small. The opposite situation occurs for the case of the QCDC and PGF processes, in which the gluon introduces an additional k_T. Moreover having the possibility of extra gluon radiation, the k_T yield may increases during the process. Therefore, at the end of the fragmentation, the final hadrons acquire high p_T.

A strong effort was made to achieve a simulation very close to the real data. The MC production comprises three steps: first the events are generated, then the particles pass through a simulated spectrometer using a program based on GEANT (version 3.4) [82] and finally the events are reconstructed using the same procedure applied to real data.

10.3 Event Generator

The LEPTO 6.5 [83] DIS event generator is used in all the simulations in this analysis. The generation is done at two levels: the simulation of the hard scattering processes and the fragmentation and hadronisation model.

Hard scattering

In the hard scattering, LEPTO generates leading order and first order QCD parton level processes. For simplicity, they are designated as leading process (LP), $\gamma^\star q \to q$, QCD Compton process (QCDC), $\gamma^\star q \to qg$, corresponding to a gluon radiation, and photon-gluon fusion process (PGF), $\gamma^\star g \to q\overline{q}$, respectively.

These first order QCD processes are included in the transition matrix elements, thus they are taken into account for the cross section evaluation. The matrix elements have soft and collinear divergences, which can be partially cancelled, by virtual corrections, and partially absorbed in the PDF's. The partonic cross section of the QCDC and PGF processes diverge as

$$\hat{\sigma}_{qg} \sim \frac{1}{(1-x_p)(1-z_q)}, \tag{10.1}$$

$$\hat{\sigma}_{q\bar{q}} \sim \frac{1}{z_q(1-z_q)}, \tag{10.2}$$

where $x_p = x_{Bj}/\xi$ is the scaling variable associated to the parton, ξ is the the fraction of energy of the parton with respect to the virtual photon, $z_q = p.p_q/p.q$, where the 4-momenta of the proton, final quark and photon are given by p, p_q and q, respectively.

To avoid any singularity due to the above divergences in the MC calculation, a cut-off scheme is used, in particular the so called $z\hat{s}$ scheme. In this scheme, z_q and the invariant mass of the hard system, $\hat{s}$, are cut to minimum safe values, z_q^{min} and $\hat{s}^{min}$: $z_q^{min} < z_q < 1 - z_q^{min}$ and $\hat{s}^{min} < \hat{s}$.

The probability of the LP process depends on the probabilities on the QCD processes in this way: $P_{LP} = 1 - P_{QCDC} - P_{PGF}$, where P_{QCDC} and P_{PGF} are the QCD Compton and PGF process probabilities respectively. The probability of the QCD processes is calculated using the first order matrix elements and the overall differential cross section.

The description of the interactions requires the choice of a factorisation scale, which is related with the parton densities, and the renormalisation scale, which appears in expressions depending on the strong coupling α_s. In this analysis, the Q^2 scale is used in both cases.

Fragmentation

The fragmentation is based on the Lund string model [84, 85] implemented in the JETSET program [86]. In this model, the probability that a fraction z of the available energy will be carried by a newly created hadron is expressed by the Lund string symmetric function

$$f(z) \propto \frac{1}{z}(1-z)^a \exp\left(-\frac{b \cdot m_T^2}{z}\right), \tag{10.3}$$

with $m_T^2 = m^2 + p_T^2$. The mass of the produced quark (or anti-quark) is described by m. The a and b parameters of the fragmentation function are represented, respectively, by the PARJ(41) and PARJ(42) parameters in JETSET.

In the string breaking mechanism, there are two interesting facts worthy to be mentioned: classically the two newly created quarks of the $q_i\bar{q}_i$ pair must be produced at a certain distance, so that the field energy between them can be used to produce the mass. Quantum mechanically, the quarks may be created at the same point with local flavour conservation and then tunnelled out to the classically allowed region. For $q_i\bar{q}_i$ pairs generated in a tunnelling process, the production probability is

$$exp\left(-\frac{\pi m_T^2}{\varkappa}\right) = exp\left(-\frac{\pi m^2}{\varkappa}\right) exp\left(-\frac{\pi p_T^2}{\varkappa}\right) ,$$

where again m is the quark mass of the $q_i\bar{q}_i$ pair and k_T is their intrinsic transverse momentum, relatively to the string. $\varkappa$ is the string constant, representing the energy per unit length of the colour tube. Originally, the string is assumed to have no transverse excitations. Thus the k_T is locally compensated between the q_i and $\bar{q}_i$ quarks. The model implemented in JETSET to describe the transverse momentum of the newly created hadrons is performed by a convolution of two gaussian distributions. PARJ(21) is the width of the narrower gaussian, PARJ(23) and PARJ(24) are, respectively, the factors to apply to the amplitude and to the width for the broader gaussian. The default values of PARJ(21), PARJ(23) and PARJ(24) are 0.36 $(\mathrm{GeV}/c)^2$, 0.01 and 2.0, respectively. Some studies [69,70,87] indicate that the parameters related to the transverse behaviour of the hadrons need a better description of the experimental data. In the present analysis this study was also carried out as explained in section 10.6.

10.4 Spectrometer Description in the Simulation

The description and simulation of the experimental apparatus is performed by the software package GEANT. In this section, these issues will be discussed. The description of the geometry of each detector component, namely its position, dimension and material is taken into account, as well as the relevant processes of the particles interacting with the materials. The output of the simulated data has the same format as the real (raw) data. Therefore, it is reconstructed in the same way, as real data, by the reconstruction program.

In order to compute the weights needed for the extraction of $\Delta G/G$, we need information from two samples: the selected "high p_T" sample and the inclusive one. Both samples should be restricted to the DIS region of the phase-space, defined here by $Q^2 > 1\,(\mathrm{GeV/c})^2$ and $y > 1$ cuts. All events surviving the two above cuts are kept for the inclusive sample, and for the high p_T MC sample the same cuts are applied as in the analysis of the experimental data.

In principle, both samples should be generated in several sets each prepared to describe one year of data taking. In practise only two sets are used: one produced taking into account the spectrometer setup information for the year 2004 and the second using the information for 2006. The 2004 data represent the majority of the data sample collected in the 2002-2004 period. In addition, this data sample is the most complete from the phase-space point of view for the considered period and it was shown [88] that 2004 MC gives a satisfactory description of the 2003 inclusive data sample. Thus a neural network prepared to be used for the 2002-2004 data sample was trained on 2004 MC. In the 2006 data sample, the angular acceptance of the spectrometer is larger and the performance of the hadron calorimeters differs significantly as compared to 2004. Thus, for proper description of the 2006 data sample, a dedicated MC was needed.

The 2006 data sample is the broadest from the phase-space point of view among all considered years. This allows the neural network trained on this sample to be the most general. Indeed, as shown in section 11.7, the results obtained on the 2004 data sample with a neural network trained on the 2006 MC are almost the same as the ones obtained with the 2004 neural network. Therefore, the 2006 neural network was used for $\Delta G/G$ extraction for all years.

In order to obtain a good description of the data, a proper simulation of the apparatus was examined. For this purpose, mainly the agreement for muon variables in the inclusive sample was considered. Incoming beam particles that are considered in the generator were extracted from the data. To properly describe the beam halo, a sophisticated procedure was developed. It was shown that variations of the beam profile have negligible effect on the description of the inclusive kinematic variables for other triggers than the Inner Trigger. As the Inner Trigger contributes marginally to the selected data sample it was decided to use a beam description based on 2004 for all MC samples. In order to properly simulate the background from pile-up beam particles, a dedicated minimum bias MC sample was merged with the generated MC samples.

Two important issues about the spectrometer have been found to be crucial for the proper description of the 2006 data sample. The first issue is related to the energy thresholds for the simulated calorimeter component of the trigger. The best values of the energy thresholds were selected by comparing the description of the MC data sample for the Inclusive Middle Trigger with the one obtained for the Middle Trigger. The only difference between these two triggers is that the Middle Trigger case requires a calorimeter signal. To properly set the thresholds for the calorimeters, the MC sample for the two triggers should provide an identical description of the data. There are two categories of thresholds for the calorimeters: the normal thresholds, also known as low thresholds, for the Inner, Ladder and Middle Triggers, and the high thresholds, used for the Calorimeter Trigger. For the high thresholds used in the Calorimeter Trigger, the Inclusive Middle Trigger sample was compared with a sample where both Inclusive Middle and Calorimeter triggers fired. The obtained values for the thresholds are presented in table 10.1.

	HCAL1 (GeV)		HCAL2 (GeV)	
Data year	Low thres.	High thres.	Low thres.	High thres.
2002 to 2004	6.0	8.0	8.0	9.0
2006	7.0	8.5	7.5	10.0

Table 10.1: Thresholds for the calorimeters used in semi-inclusive and calorimetric triggers. See text for details.

The second crucial component for proper description of the data is the efficiencies of the trigger hodoscope planes. For the 2004 MC sample, they were estimated and included into the simulation. The effect for this sample is considered to be small [88]. This is not the case for the 2006 data sample, where a significant region of lower efficiency was found for the Middle Trigger. For this sample, it was decided to remove the problematic region by using a geometrical cut instead of extracting the efficiencies. The decision was based on the fact that the efficiencies varied considerably from period to period.

10.5 Parton Distribution Functions (PDFs), Longitudinal Structure Function, F_L and Parton Shower

After correcting all issues related with the description of the spectrometer and having enough confidence that the apparatus is described to the best of our knowledge, now the focus is turned on to the physics simulation. Some of these physical aspects of the simulation are described in the PDFs, in the structure function F_L and in the parton shower and are importa to the MC tuning. These issues are discussed in the following section.

The essential *a priori* requirement is that the PDF covers the same kinematic region as the data. Among the most recent analytical developments on the PDFs, MSTW 2008 is found to have the following kinematic validity region : $10^{-6} < x < 1$ and $1(\mathrm{GeV/c})^2 < Q^2 < 10^9\,(\mathrm{GeV/c})^2$ which is very suitable for the COMPASS phase space. Another requirement is that the parametrisation of the F_2 structure function and the measurement obtained by the NMC experiment agree fairly well. This requirement is usually met without difficulty since most of the fits used in the extraction of PDFs already include these data. Finally, the PDF set has to be consistent with the LO approximation in our formula. Therefore, in the present analysis the selected set is the MSTW2008LO [89]. As a tool to access the parametrisation, the PDF software library LHAPDF [90] is used.

Previously, in some high p_T analyses, as in ref. [70], the longitudinal to transverse cross section ratio, R, was neglected. In this analysis, this contribution is taken into account using the longitudinal structure function F_L. The LEPTO built-in parametrisation of F_L was used (LST(11)=122). This addition mainly affects kinematics in the low-x region.

The $R(x,Q^2)$ function changes globally the cross section. On the other hand, the F_L function changes the process fractions R_{LP}, R_{QCDC} and R_{PGF}.

In order to improve the description of the hadrons transverse momentum, the *parton shower* mechanism in LEPTO has to be enabled. This mechanism allows gluon radiation from the initial and/or final parton state. In this way, higher orders in α_s, although not complete, are taken into account in the MC generation. The inclusion of the parton shower mechanism improves substantially the simulation of the hadronic distributions [88]. This poses a problem as with parton shower we simulate higher order effects while the formula for $\Delta G/G$ is derived in LO. Impact of this fact is taken into account in the estimate of the systematic uncertainty. On the other hand, as we include part of higher order effects into the MC, the argument that by restricting ourselves to the QCD LO approximation we neglect important effects is less valid.

10.6 MC Tuning

In order to match the hadron production in the same way as is done in real data some parameters need to be tuned. As mentioned in section 10.3, the transverse description of the hadrons given by the default JETSET parameters is in clear disagreement with the data, as it will be shown. In this section, the features concerning the tuning of these parameters are deeply explained. As this analysis relies very much on information extracted from the MC simulations to have confidence in our measurement it is mandatory that the simulation describes our data as close as possible. In practise, we assess this by comparing several distributions of physical observables for the data and the MC. All relevant observables related to inclusive variables, namely the kinematical variables Q^2, x_{Bj} and y; and also to the hadronic variables, namely the multiplicity, the total and transverse momenta, p and p_T (respectively), the energy fraction of the virtual photon carried by the hadron, z, the Feynman x, x_F (these last variables are defined in sec. 2.7) and the polar angle θ. The tuning of the generator parameters is performed in an iterative procedure where by adjusting several parameters in small steps one seeks the best possible agreement between the data an the simulation. The tuning of the MC generator parameters was done for the 2006 sample only; this reason is a practical one. The physics used in the simulations should be year independent. Using the 2006 sample, we take advantage from all the *know-how* about the spectrometer gathered since the first data acquisition. In addition, the 2006 sample is the broadest from the phase space point of view.

Comparing data with a MC sample produced using the LEPTO default tuning (see table 10.2) results in a very poor agreement for the inclusive kinematic variables and for the longitudinal momenta of the two leading hadrons. For the transverse momenta distributions the comparison is even more catastrophic (see Figs. 10.4). It is interesting to note the data - MC comparison for another variable that is sometimes omitted, the final hadron multiplicity: it is also bad, which further points that the fragmentation is not correctly described in the simulation (Fig. 10.9). All these points clearly to the fact that the LEPTO default tuning does not describe the physics of our data.

As mentioned in section 10.3, the interesting parameters governing the fragmentation in LEPTO can be divided into two sets. The first consists of JETSET parameters PARJ(41) and PARJ(42) which are related to the parameters a and b of the Lund string fragmentation function. The second set consists in the PARJ(21), PARJ(23) and PARJ(24) parameters, which are used to simulate the transverse momenta, p_T, of the newly created hadrons.

Conveniently, the two sets of JETSET parameters can be tuned separately with a minimal correlation between them. The tuning is a two step procedure: first, the fragmentation set is tuned; then, after obtaining the best agreement, the tuning of the intrinsic transverse momenta performed.

To tune the fragmentation parameters a and b, the minimisation of a Kolmogorov distance test was performed, in which the difference between data and MC for the kinematic variables x and y is evaluated. The MC sample used in this test is an inclusive sample without full MC chain, but acceptance corrected. The test showed that the x and y kinematic variables are largely unaffected, only for $b < 0.1\,(\mathrm{GeV})^{-2}$ there is some space for improving. Also the test shows that one obtains correct the multiplicity for $a \sim b$. Taking into account the information obtained from the test and using several sets of fragmentation parameters for full chain MC simulations, the set which gives the best agreement for the kinematic variables is $a = 0.025$ and $b = 0.075\,(\mathrm{GeV})^{-2}$. Both tunings, the LEPTO default and the new COMPASS one, are illustrated in figure 10.1.

Concerning the tuning of the transverse momenta component of the outgoing hadrons, an interesting problem arises: three parameters are used to tune essentially two physical observables, p_{T_1} and p_{T_2}, the transverse momenta components of the leading and sub-leading hadrons. Therefore, we need to understand how these three parameters act on the p_T distributions. The PARJ(21) parameter has a direct impact on the low p_T region of the hadrons transverse momenta distributions, particularly on the leading hadron. The data - MC ratio distributions for the hadron transverse momentum change dramatically, within the momentum range 0.4 to $0.8\,(\mathrm{GeV}/c)^2$, as PARJ(21) increases, while keeping PARJ(23) and PARJ(24) values fixed. This fact is illustrated in figure 10.2.

A reasonably flat slope for the data - MC ratio of p_T distributions was found for PARJ(21) $= 0.34\,(\mathrm{GeV}/c)$. A grid is made of several values of PARJ(23) and PARJ(24) between 0.01 to 0.06 and 1.6 to 3.5, respectively. After producing full chain MC simulations for all points

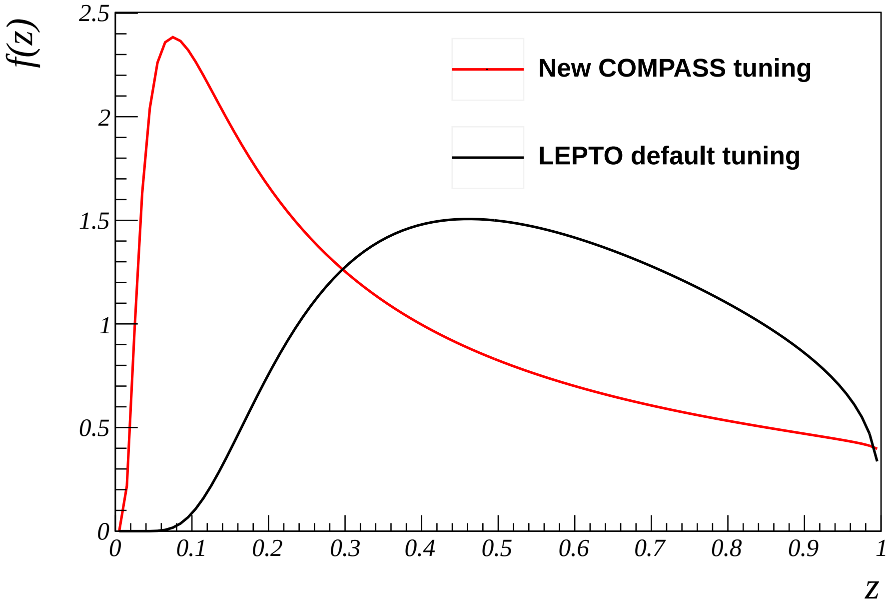

Figure 10.1: The Lund symmetric string fragmentation function is depicted for two different sets of a (PARJ(41)) and b (PARJ(42)), namely the LEPTO default set ($a = 0.3$ and $b = 0.58\,(\mathrm{GeV})^{-2}$) and the new COMPASS tuning ($a = 0.025$ and $b = 0.075\,(\mathrm{GeV})^{-2}$).

of the grid and analysing the data - MC agreement for p_T distributions, the best values for parameters PARJ(21), PARJ(23) and PARJ(24) are $0.34\,(\mathrm{GeV}/c)$, 0.04 and 2.8, respectively. Table 10.2 summarises the values of JETSET parameters for LEPTO default and the new COMPASS tuning.

	PARJ 21	PARJ 23	PARJ 24	PARJ 41	PARJ 42
Default	0.36	0.01	2.0	0.300	0.580
COMPASS	0.34	0.04	2.8	0.025	0.075

Table 10.2: LEPTO parameters values used for the default and new COMPASS tuning.

To be self-consistent, the analysis should be done using the option parton shower OFF; unfortunately, it was not possible to achieve a satisfactory description of the data by a MC using PS OFF.

The last two years in this analysis were spent basically on understanding and improving the 2006 MC. At the end the data/MC agreement is very good as shown in the section 10.7. As for the 2004 MC, there is some room for improvements. The biggest difference between the 2004 and 2006 data is the hadron acceptance change due to the new target magnet.

10.7 Comparison of the MC Simulation with Data

A lot of information to be used in the $\Delta G/G$ calculation is obtained from Monte Carlo simulation, therefore this analysis is very model dependent. That is the main reason why a

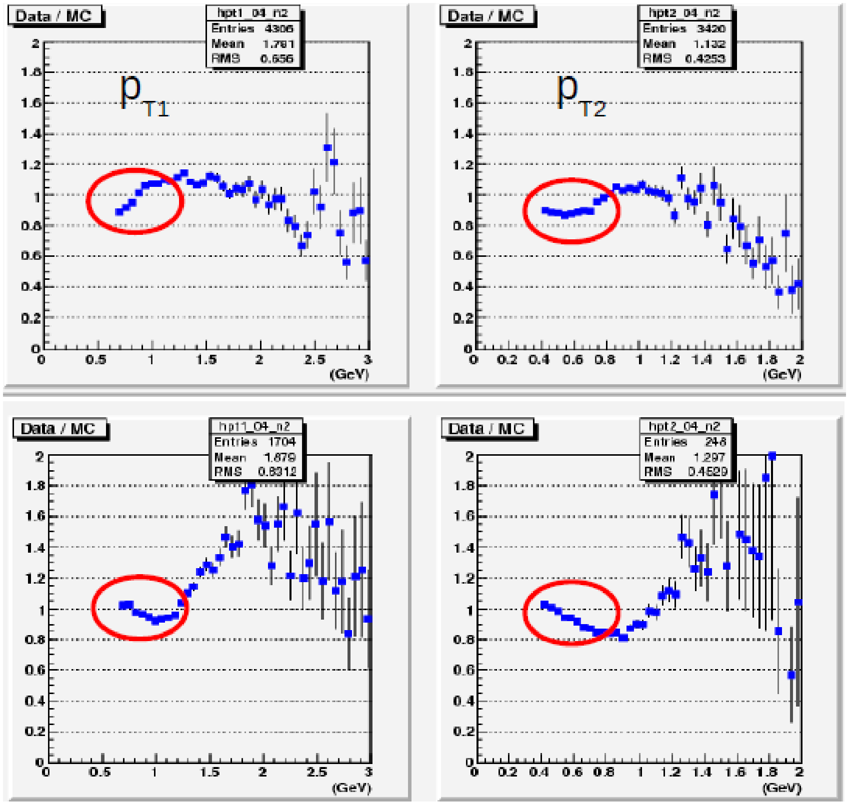

Figure 10.2: Transverse momentum distributions for the leading and sub-leading hadrons. The top plots show the distributions for the case $PARJ(21) = 0.30\,\mathrm{GeV}/c$. The bottom plots show the same distributions for the case $PARJ(21) = 0.42\,\mathrm{GeV}/c$. The region of interest is enclosed by the red ellipse. See text for details.

good description of the experimental data by MC is fundamental in this analysis. Two MC samples were produced to account for the estimation of the weights: one uses the high p_T event selection cuts explained in the previous section (sec. 9.5) and the other uses an inclusive selection based only on the cuts on the DIS kinematic variables (Q^2 and y).

The comparison between MC and data for the high p_T sample is shown in figure 10.3 for the kinematic variables and in figures 10.4 to 10.9 for the hadronic variables, namely p_T, p, z, x_F, θ and hadron multiplicities.

The agreement between MC and data using the new tuning is, in general, better than the default one; in particular, the big improvement is related to the transverse momentum of the hadrons.

Figures 10.10 to 10.30 show the same comparison for the Calorimetric, Outer and Middle trigger events.

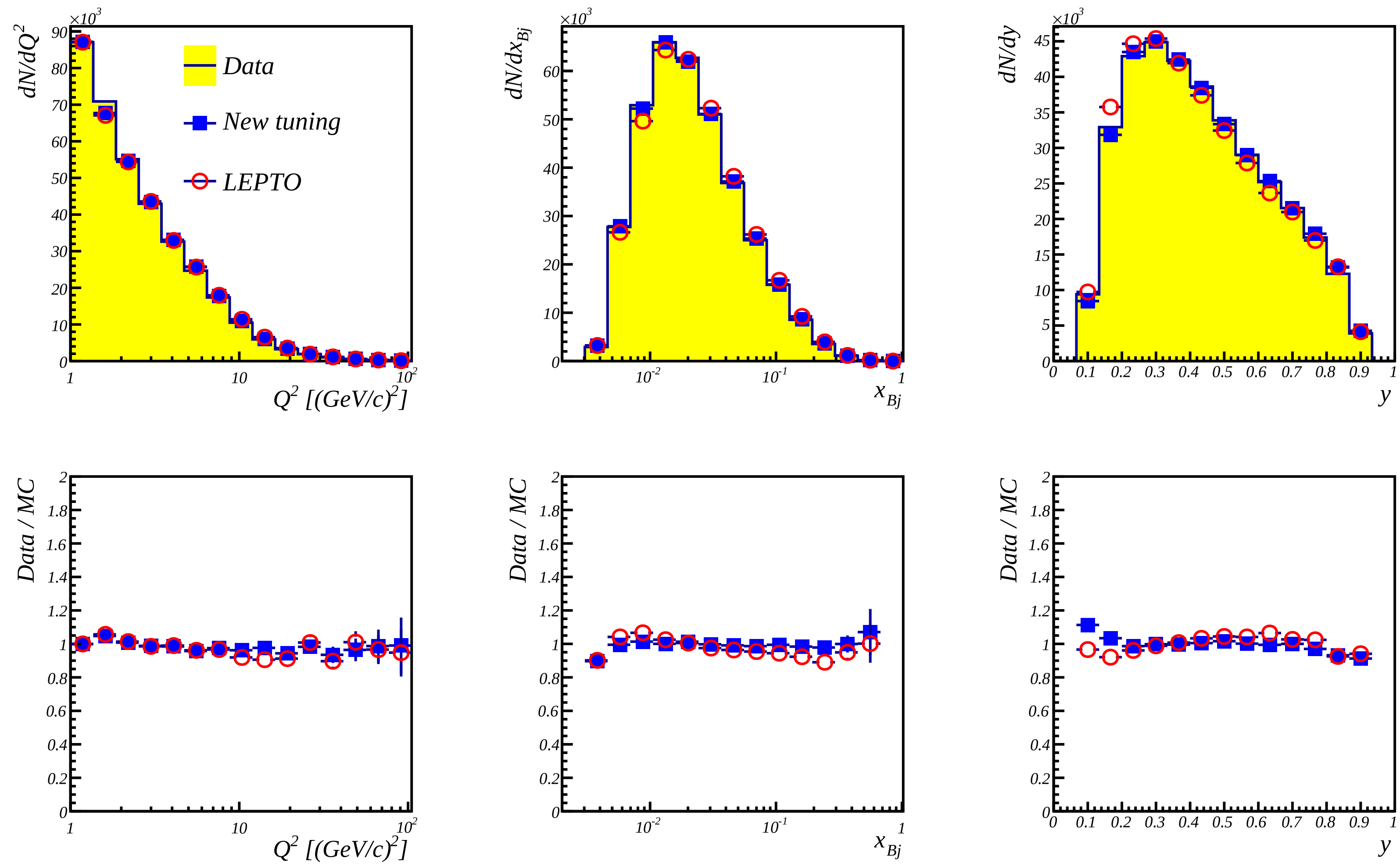

Figure 10.3: Comparison between data and MC simulation: distributions (top) and ratios Data/MC (bottom) for the inclusive variables: x_{Bj}, Q^2 and y are shown.

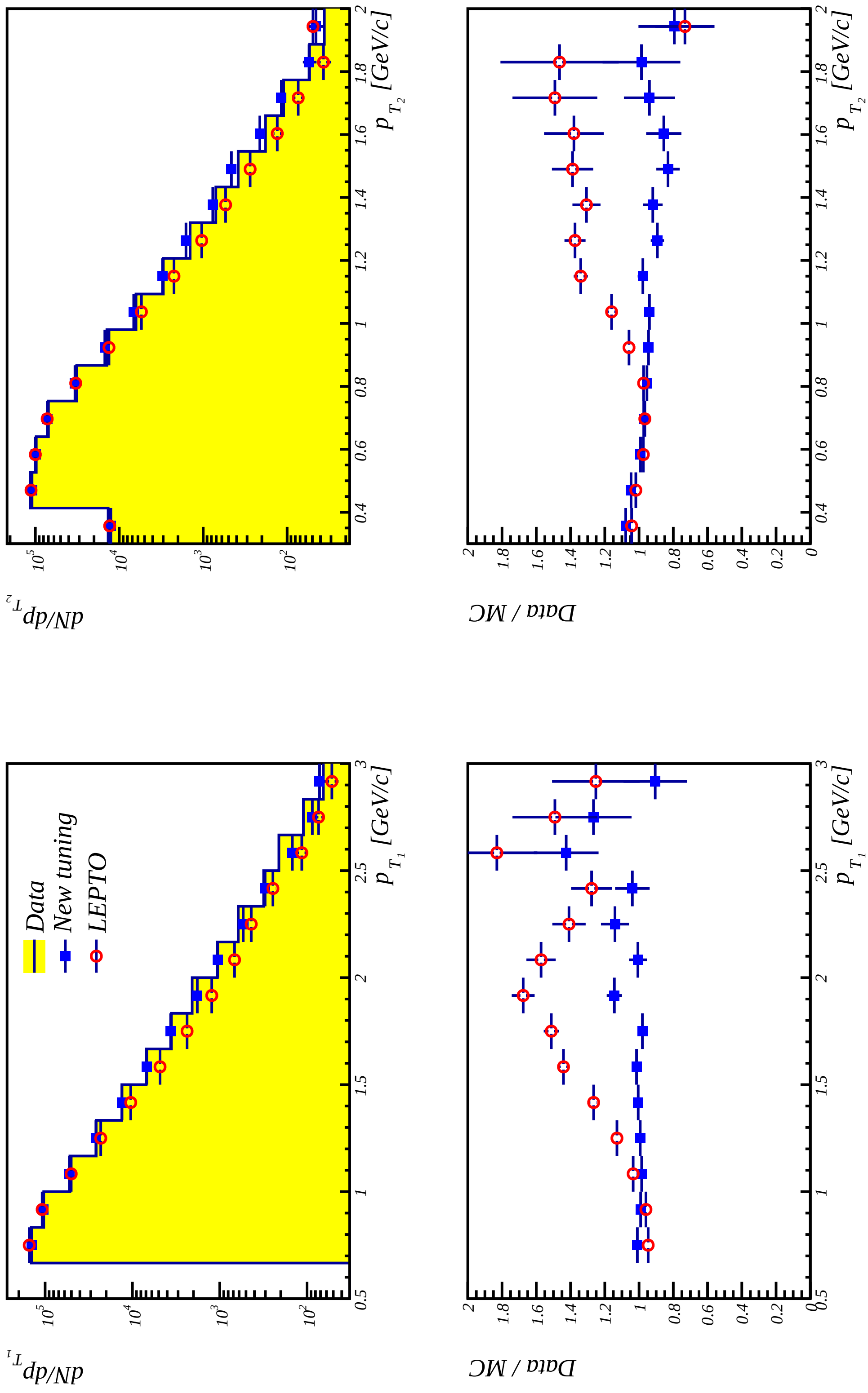

Figure 10.4: Comparison between data and MC simulation: distributions (top) and also Data/MC ratios (bottom) for the leading (p_{T_1}) and sub-leading (p_{T_2}) hadron transverse momenta.

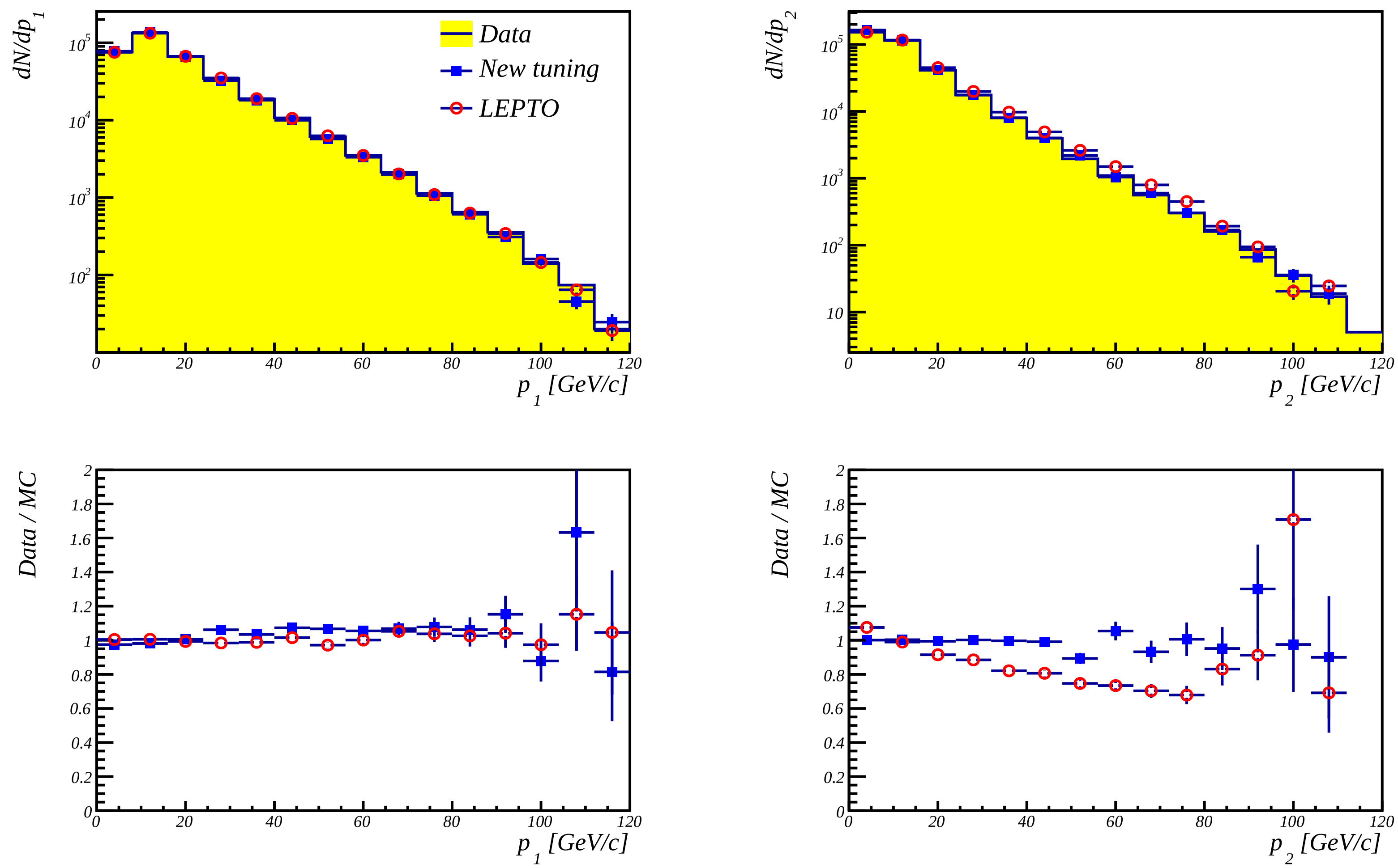

Figure 10.5: Comparison between data and MC simulation: distributions (top) and also Data/MC ratios (bottom) for the leading (p_1) and sub-leading (p_2) hadron momenta.

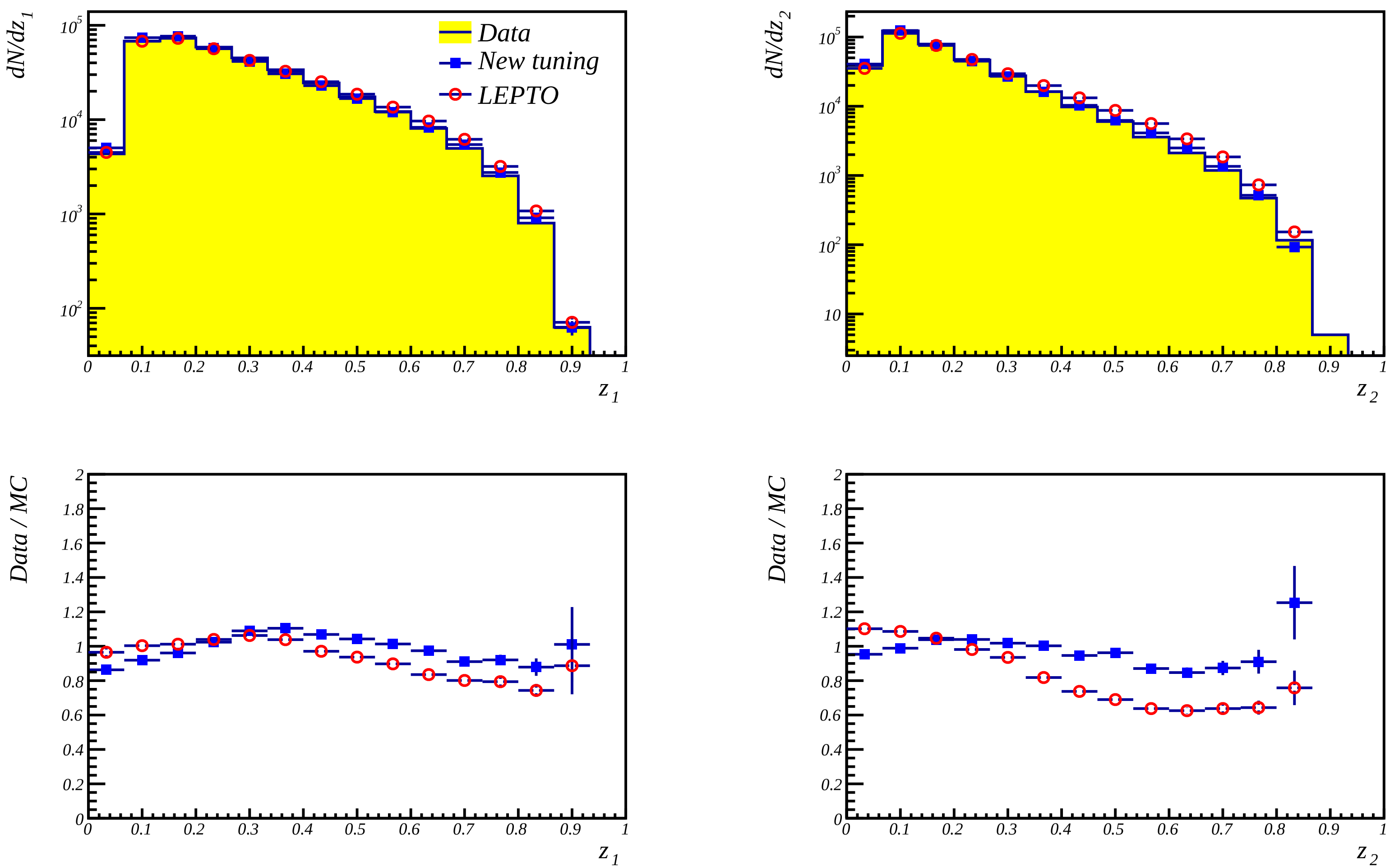

Figure 10.6: Comparison between data and MC simulation: distributions (top) and also Data/MC ratios (bottom) for the energy fraction of the virtual photon carried by the leading (z_1) and sub-leading (z_2) hadrons.

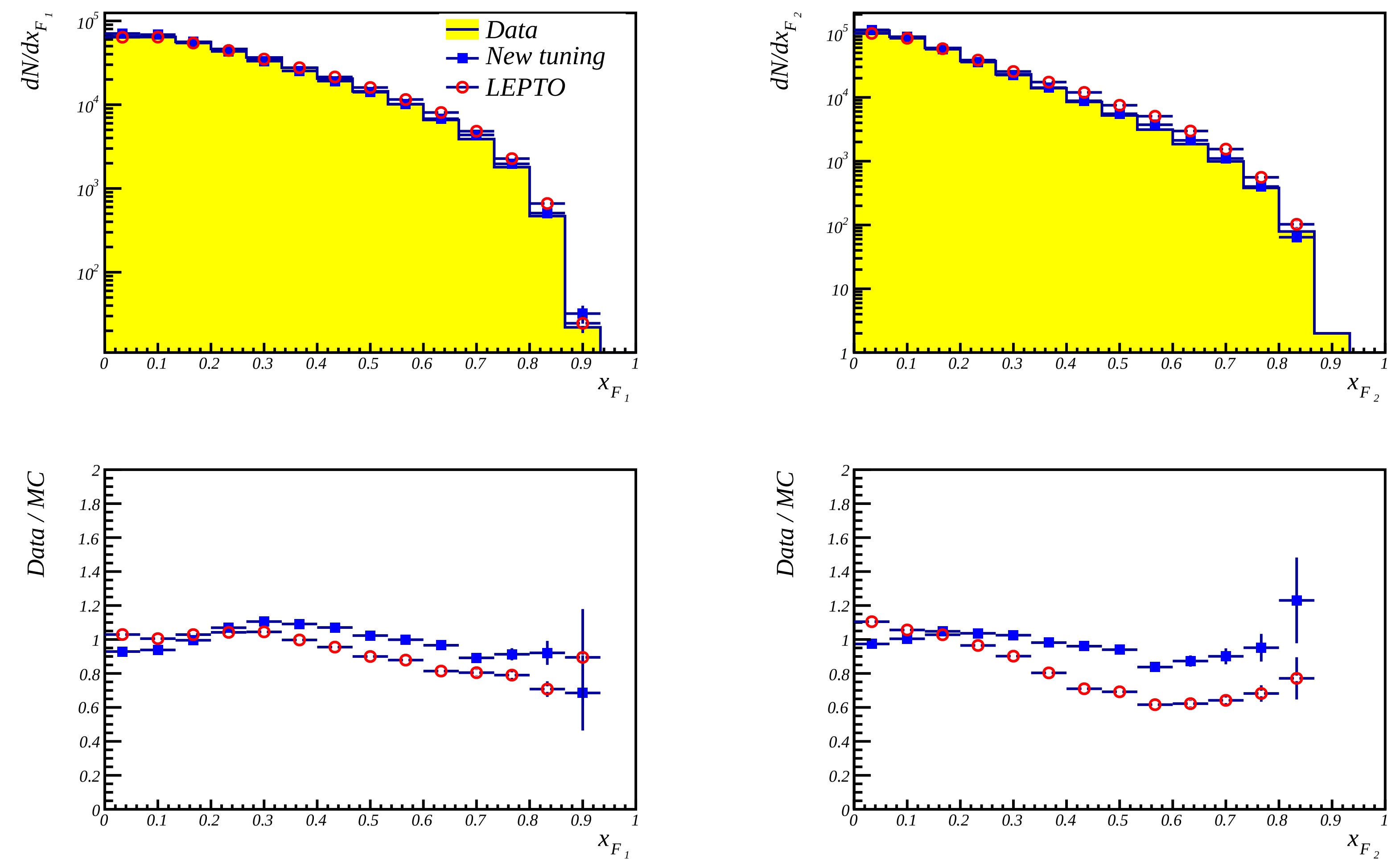

Figure 10.7: Comparison between data and MC simulation: distributions (top) and also Data/MC ratios (bottom) for the Feynman x variable for the leading (x_{F_1}) and sub-leading (x_{F_2}) hadrons.

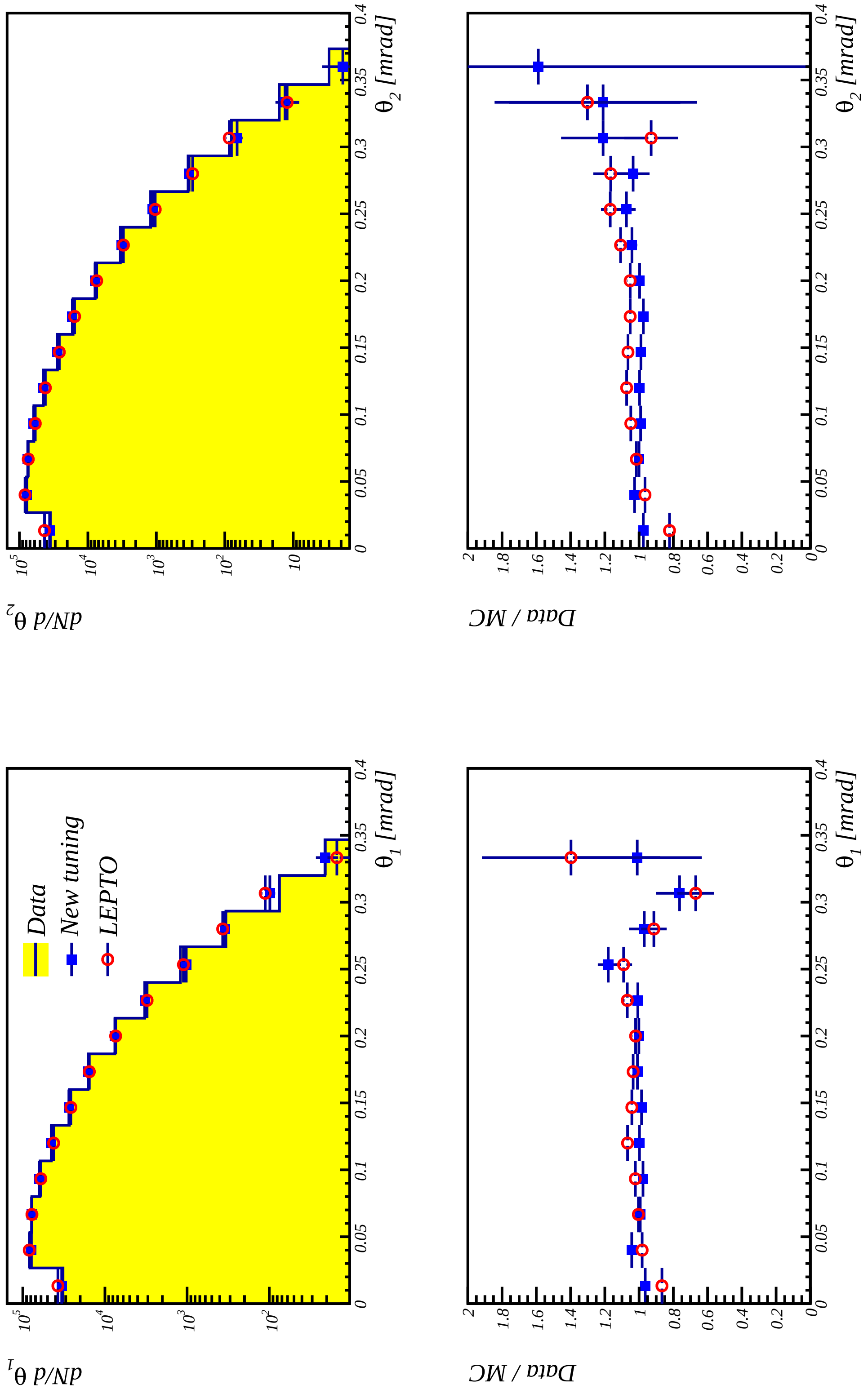

Figure 10.8: Comparison between data and MC simulation: distributions (top) and also Data/MC ratios (bottom) of the azimuthal angle with respect to the z coordinate for the leading (θ_1) and sub-leading (θ_2) hadrons.

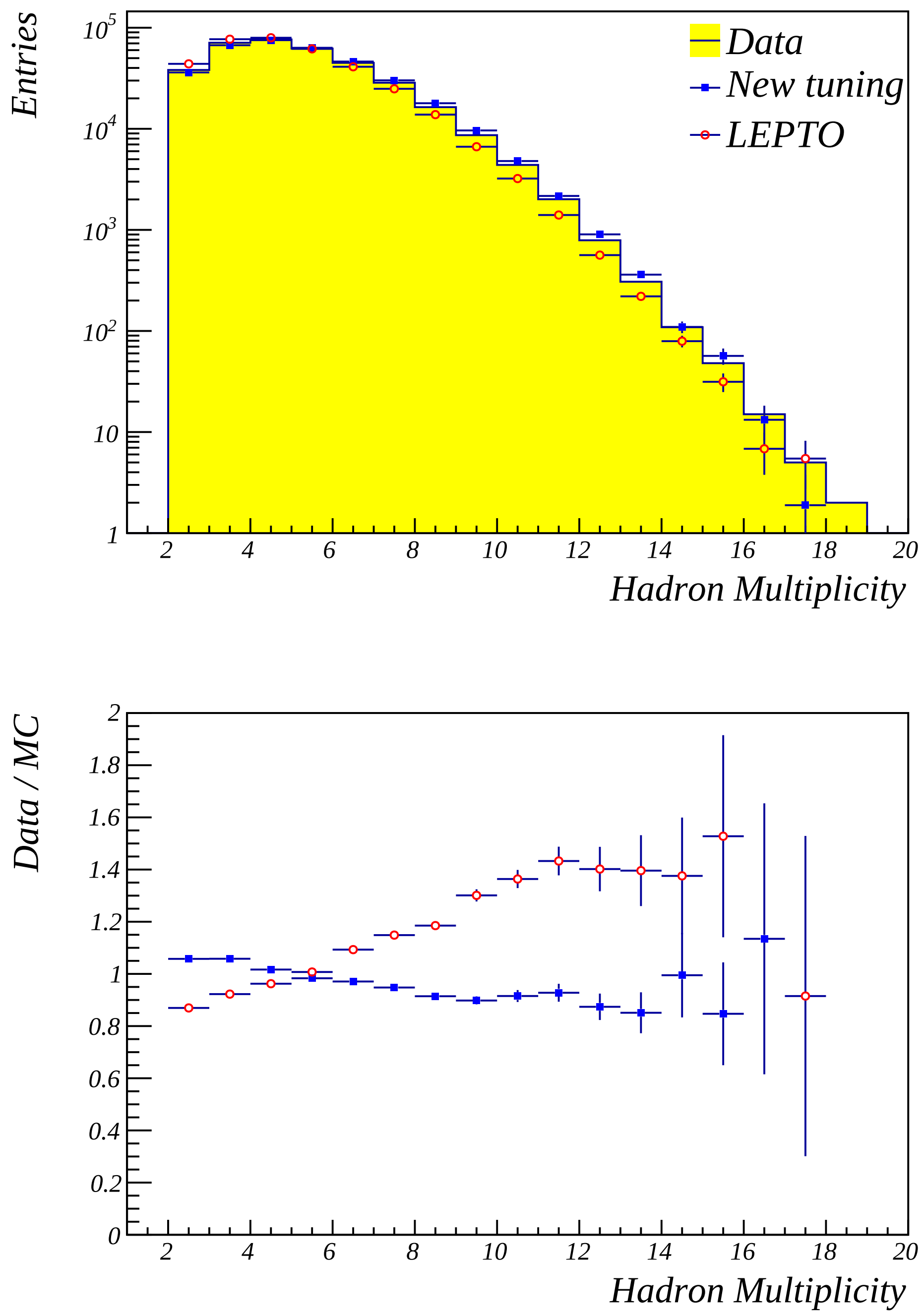

Figure 10.9: Comparison between data and MC simulation: distributions (top) and also Data/MC ratios (bottom) of the hadron multiplicities for the leading and sub-leading hadrons.

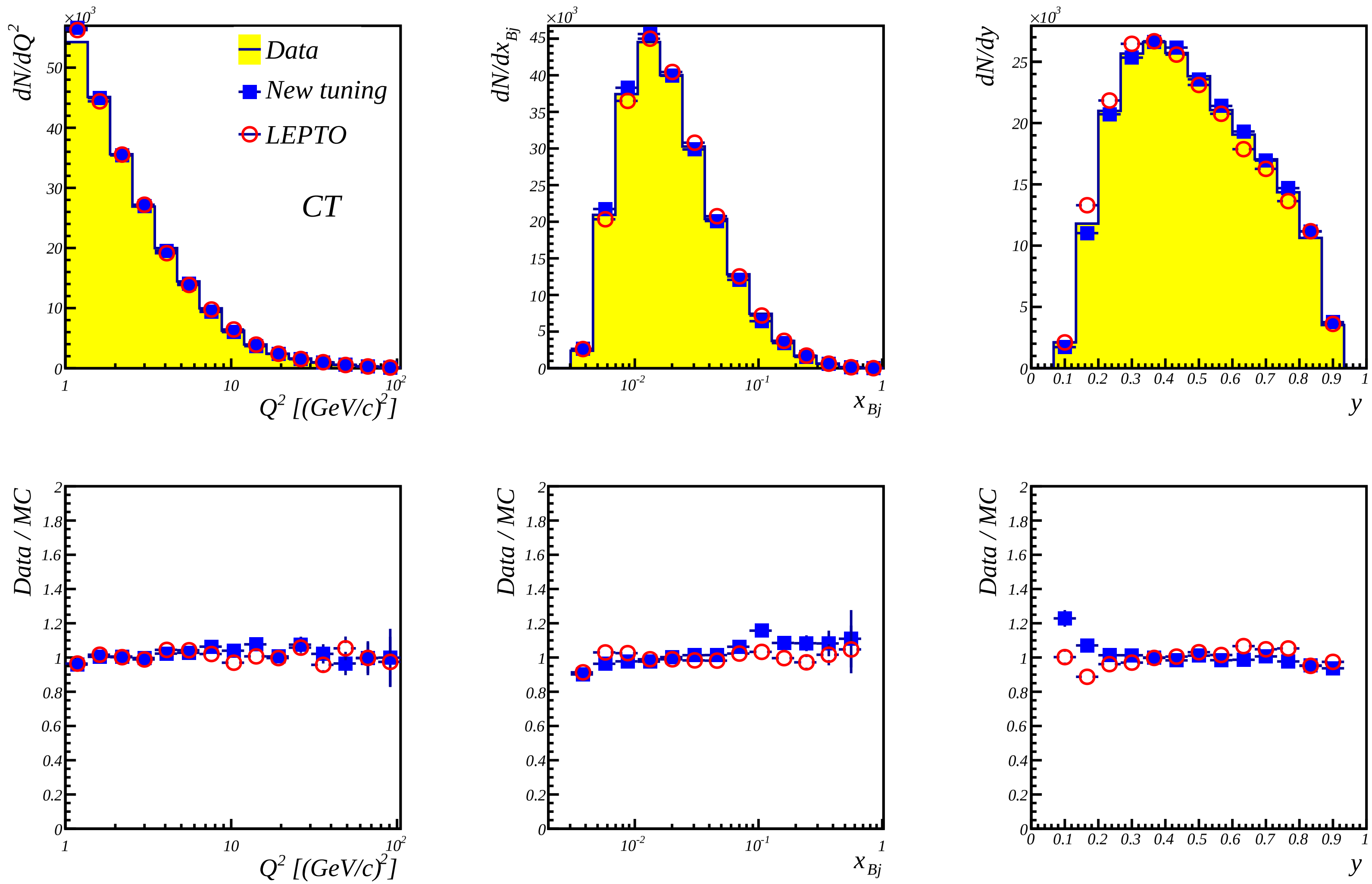

Figure 10.10: Comparison between data and MC simulation for Calorimetric triggers events: distributions (top) and ratios Data/MC (botom) for the inclusive variables: x_{Bj}, Q^2 and y are shown.

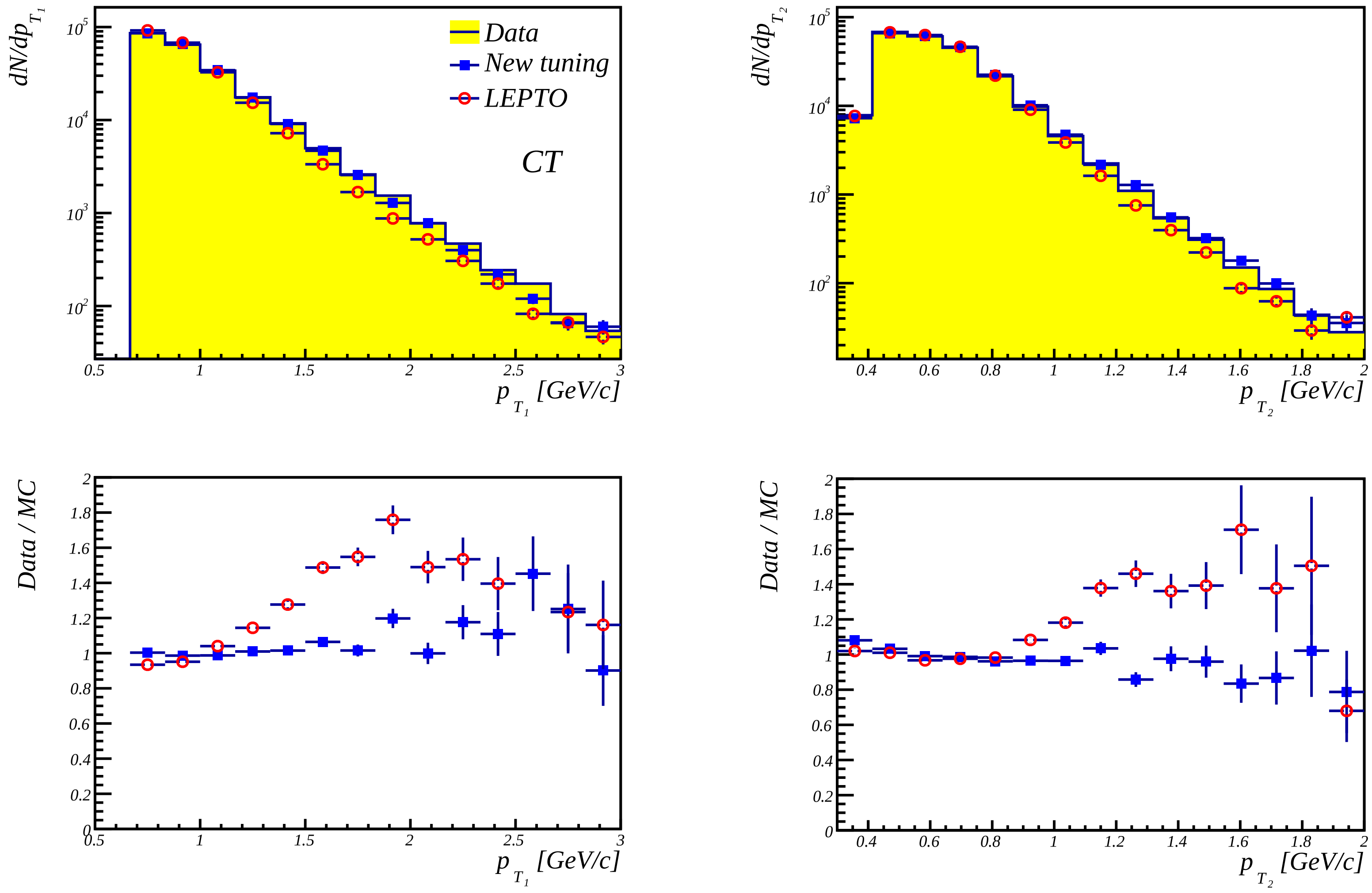

Figure 10.11: Comparison between data and MC simulation for Calorimetric triggers events: distributions (top) and also Data/MC ratios (bottom) for the leading (p_{T_1}) and sub-leading (p_{T_2}) hadron transverse momenta.

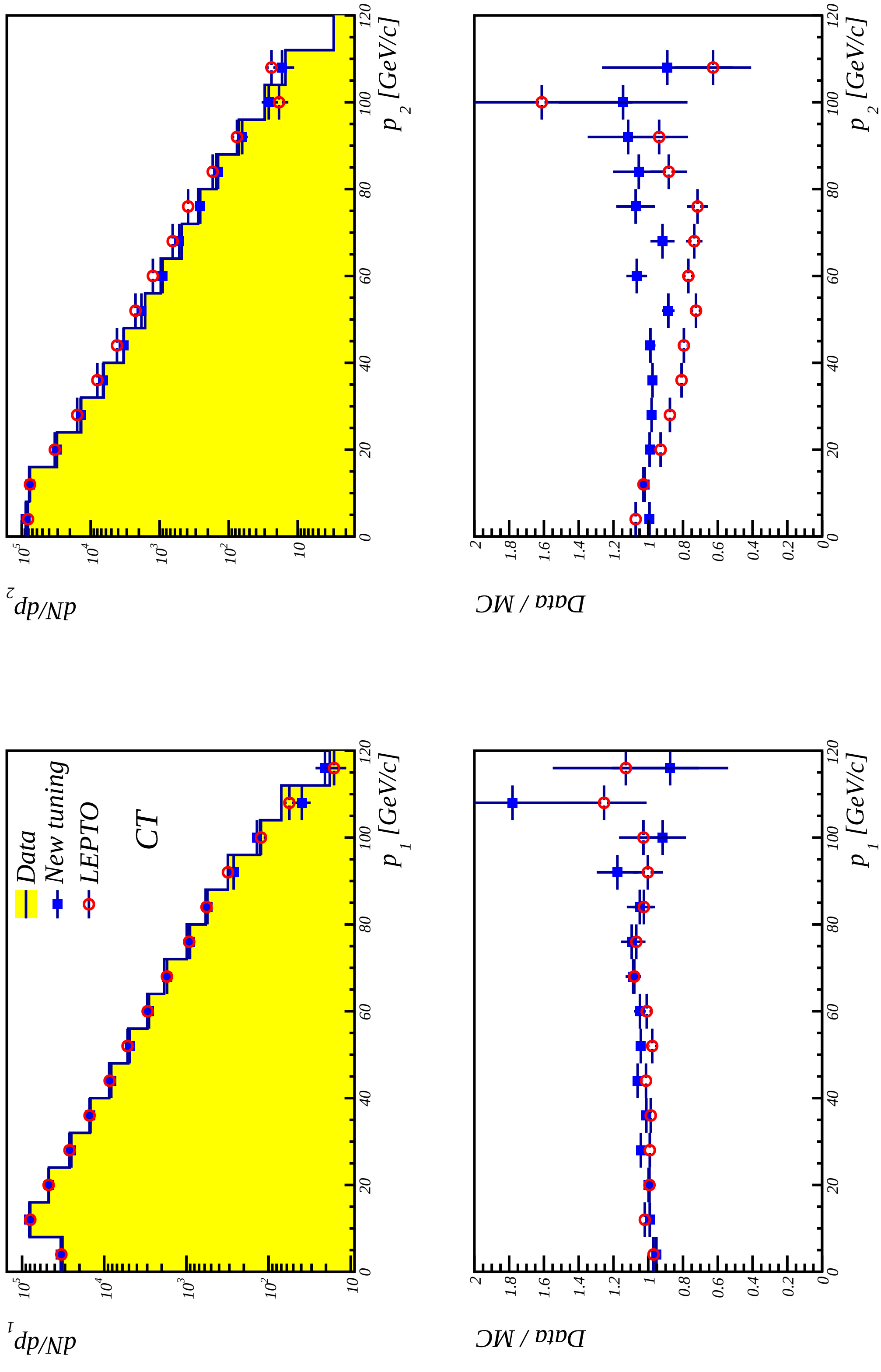

Figure 10.12: Comparison between data and MC simulation for Calorimetric triggers events: distributions (top) and also Data/MC ratios (bottom) for the leading (p_1) and sub-leading (p_2) hadron momenta.

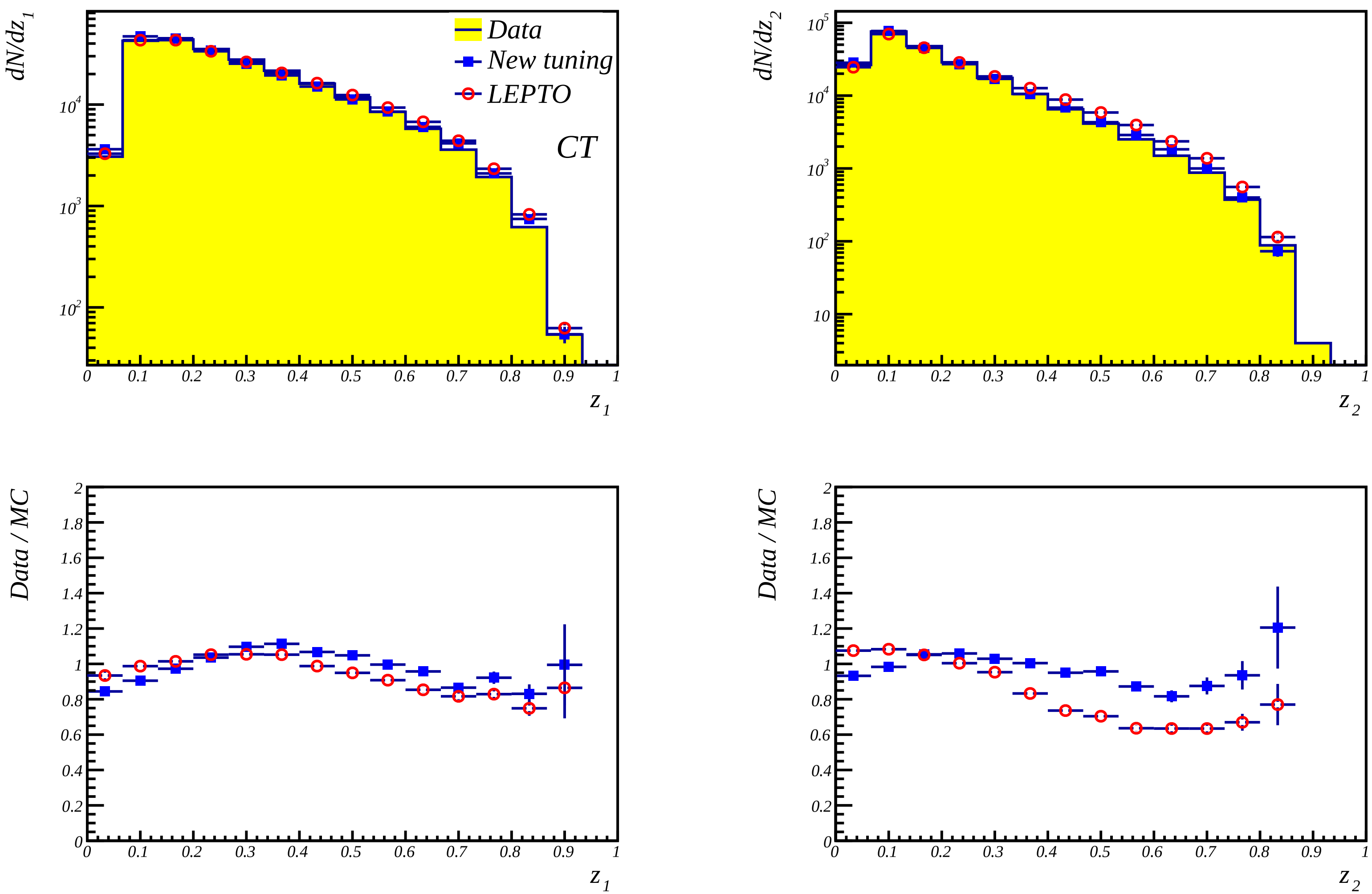

Figure 10.13: Comparison between data and MC simulation for Calorimetric triggers events: distributions (top) and also Data/MC ratios (bottom) for the energy fraction of the virtual photon carried by the leading (z_1) and sub-leading (z_2) hadrons.

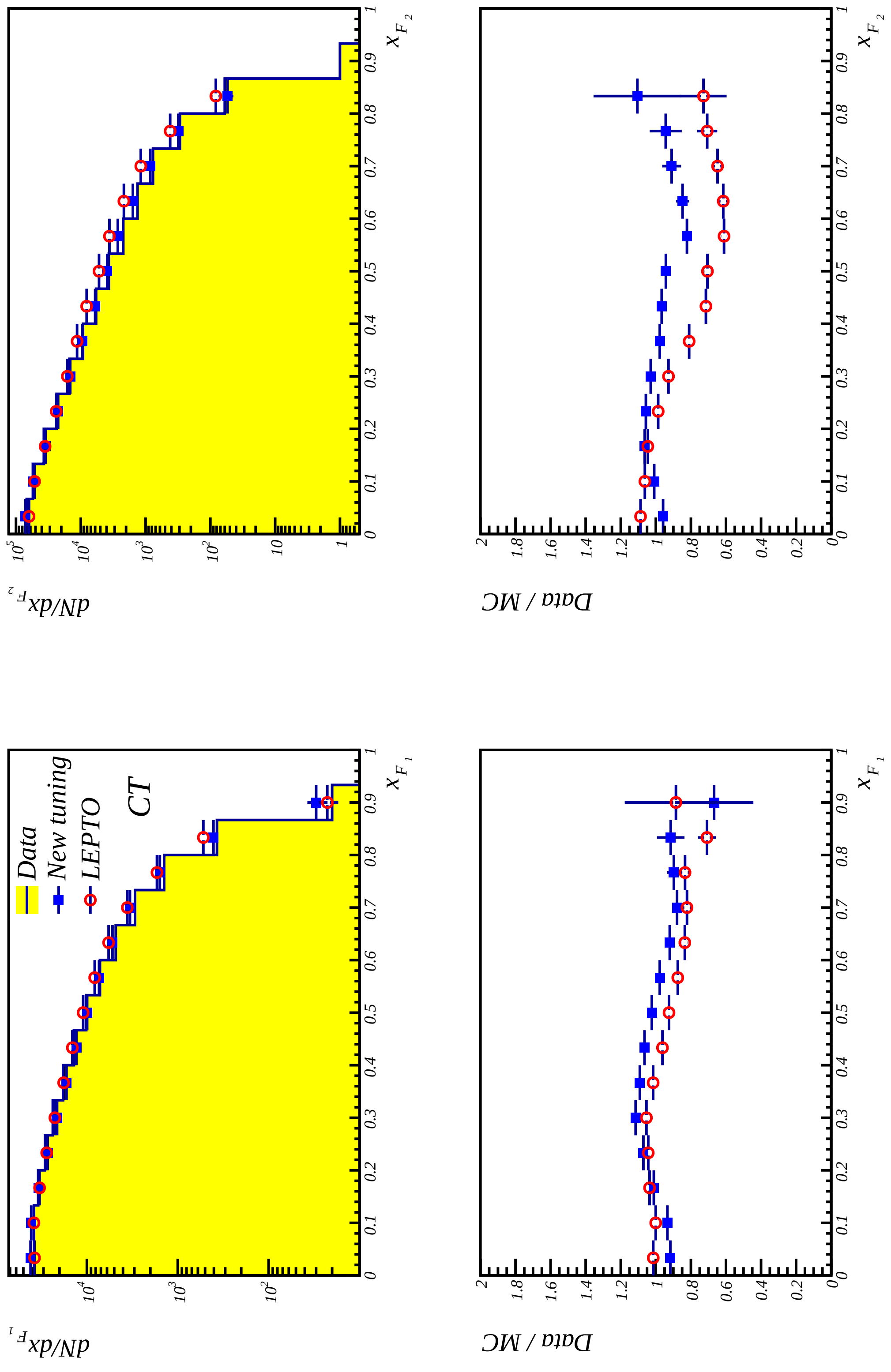

Figure 10.14: Comparison between data and MC simulation for Calorimetric triggers events: distributions (top) and also Data/MC ratios (bottom) for the Feynman x variable for the leading (x_{F_1}) and sub-leading (x_{F_2}) hadrons.

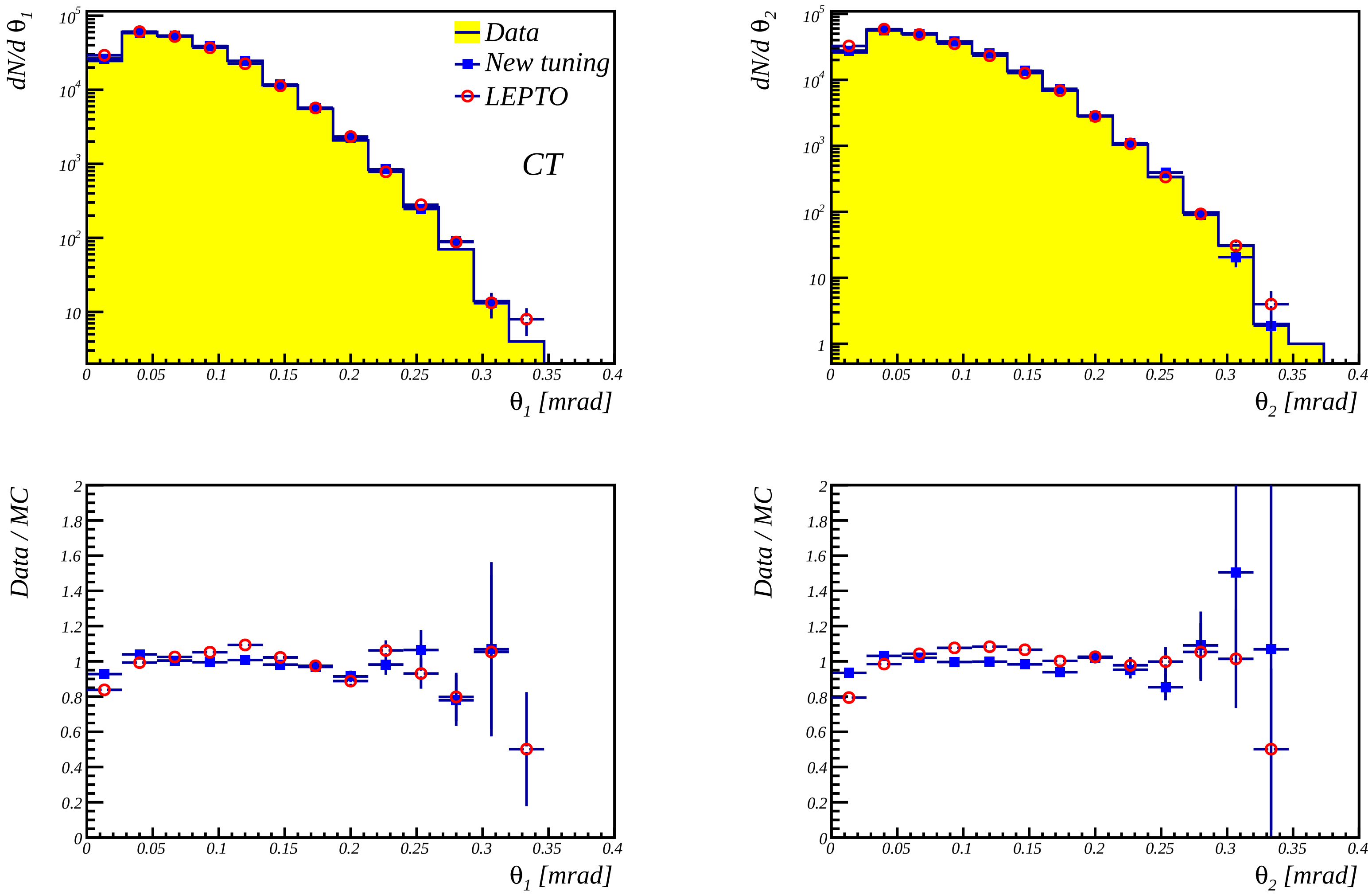

Figure 10.15: Comparison between data and MC simulation for Calorimetric triggers events: distributions (top) and also Data/MC ratios (bottom) of the azimuthal angle with respect to the z coordinate for the leading (θ_1) and sub-leading (θ_2) hadrons.

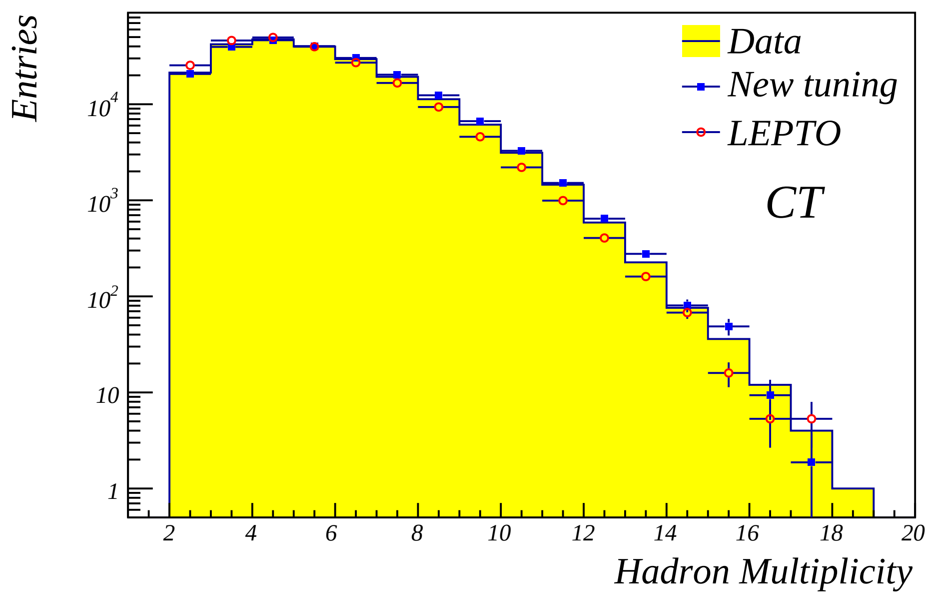

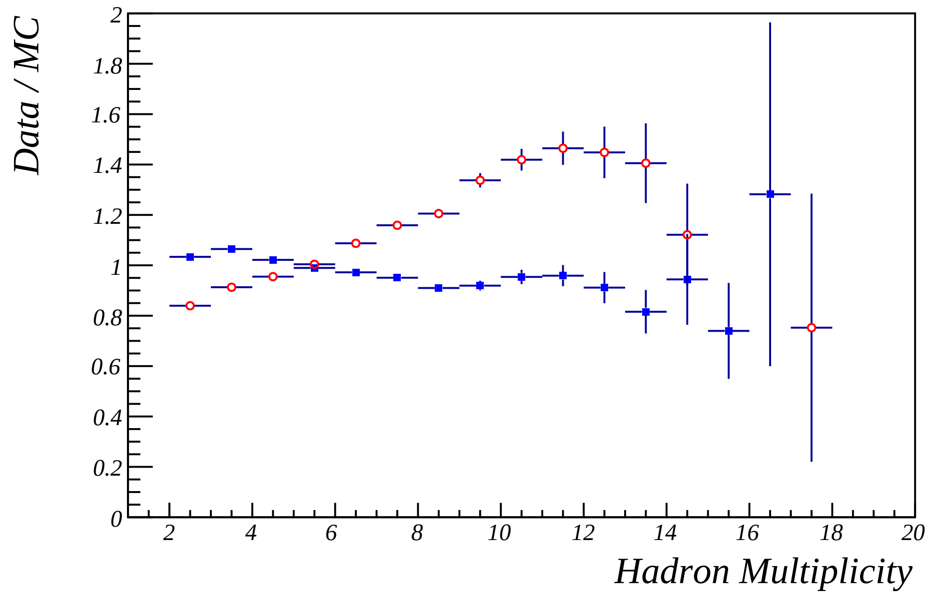

Figure 10.16: Comparison between data and MC simulation for Calorimetric triggers events: distributions (top) and also Data/MC ratios (bottom) of the hadron multiplicities for the leading and sub-leading hadrons.

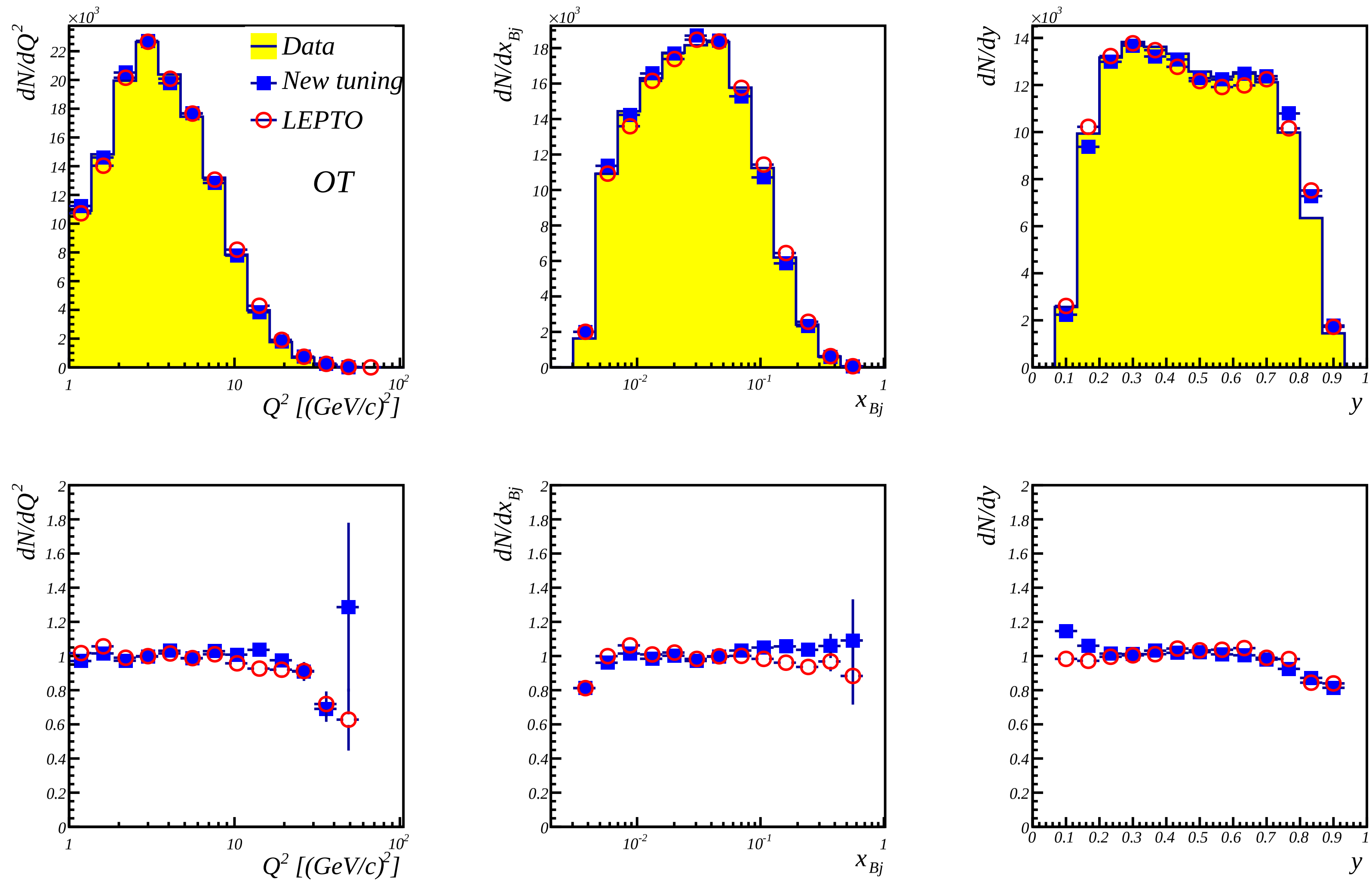

Figure 10.17: Comparison between data and MC simulation for Outer triggers events: distributions (top) and ratios Data/MC (bottom) for the inclusive variables are shown: x_{Bj}, Q^2, y.

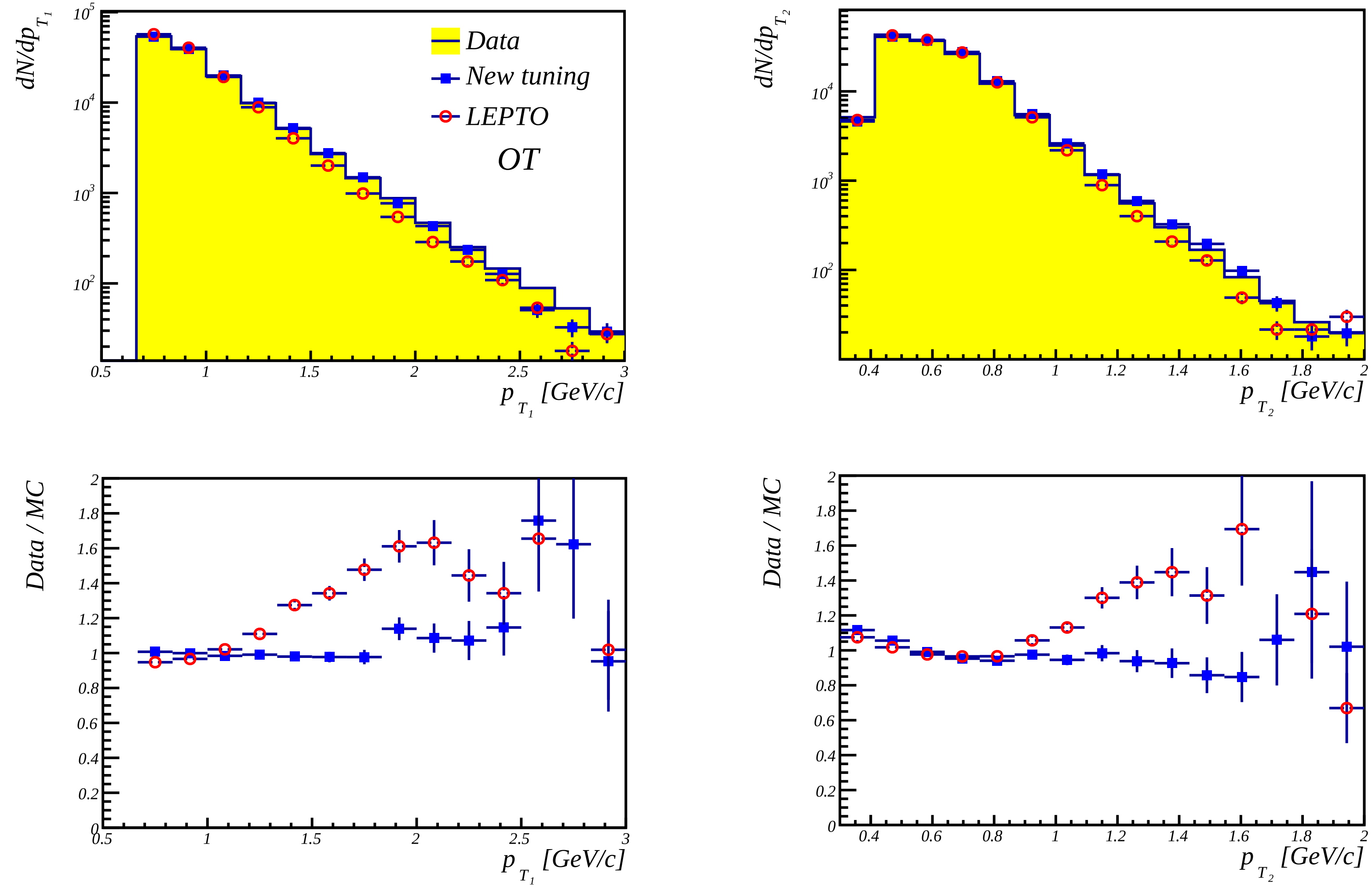

Figure 10.18: Comparison between data and MC simulation for Outer triggers events: distributions (top) and also Data/MC ratios (bottom) for the leading (p_{T_1}) and sub-leading (p_{T_2}) hadron transverse momenta.

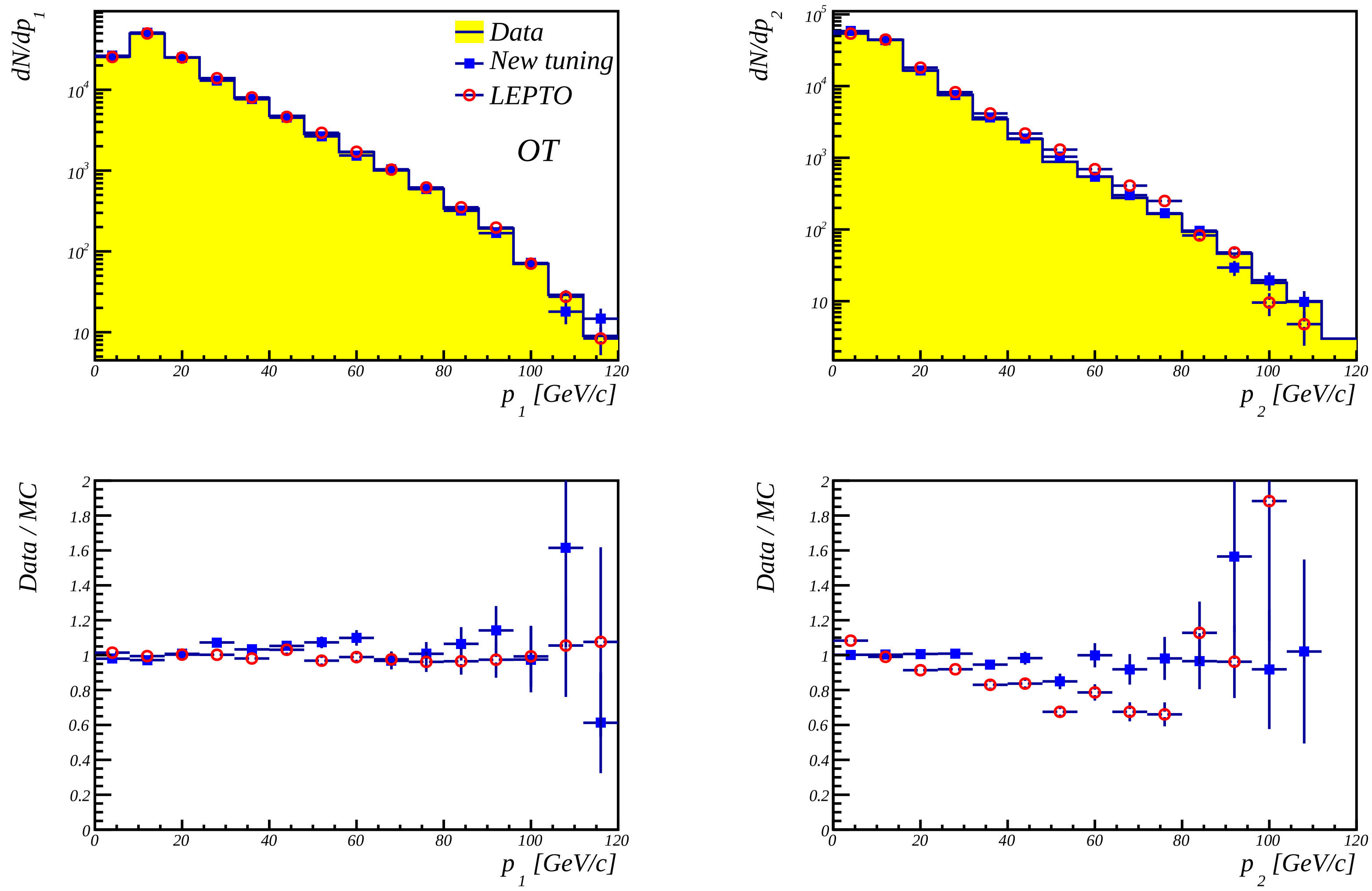

Figure 10.19: Comparison between data and MC simulation for Outer triggers events: distributions (top) and also Data/MC ratios (bottom) for the leading (p_1) and sub-leading (p_2) hadron momenta.

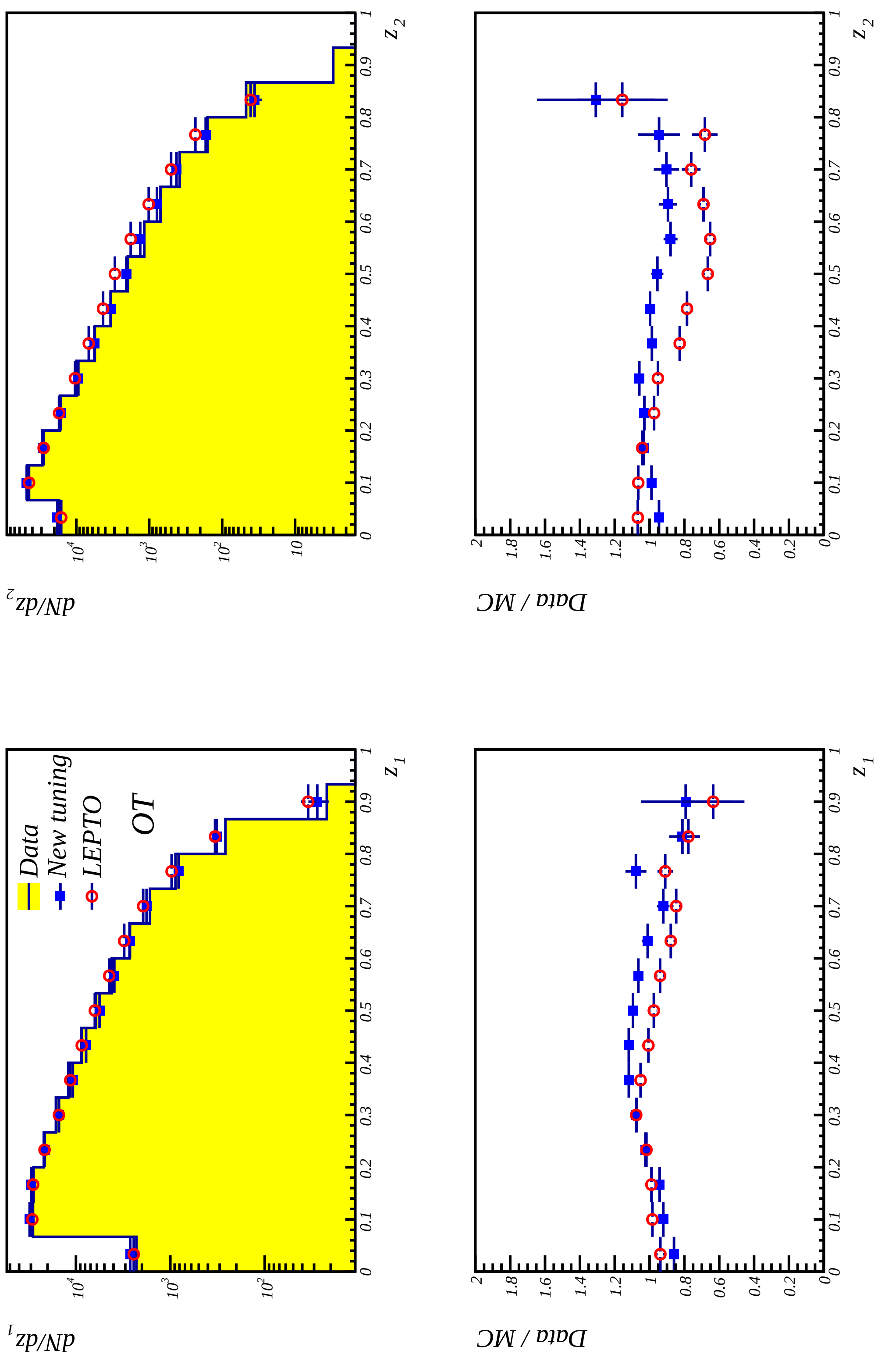

Figure 10.20: Comparison between data and MC simulation for Outer triggers events: distributions (top) and also Data/MC ratios (bottom) for the energy fraction of the virtual photon carried by the leading (z_1) and sub-leading (z_2) hadrons.

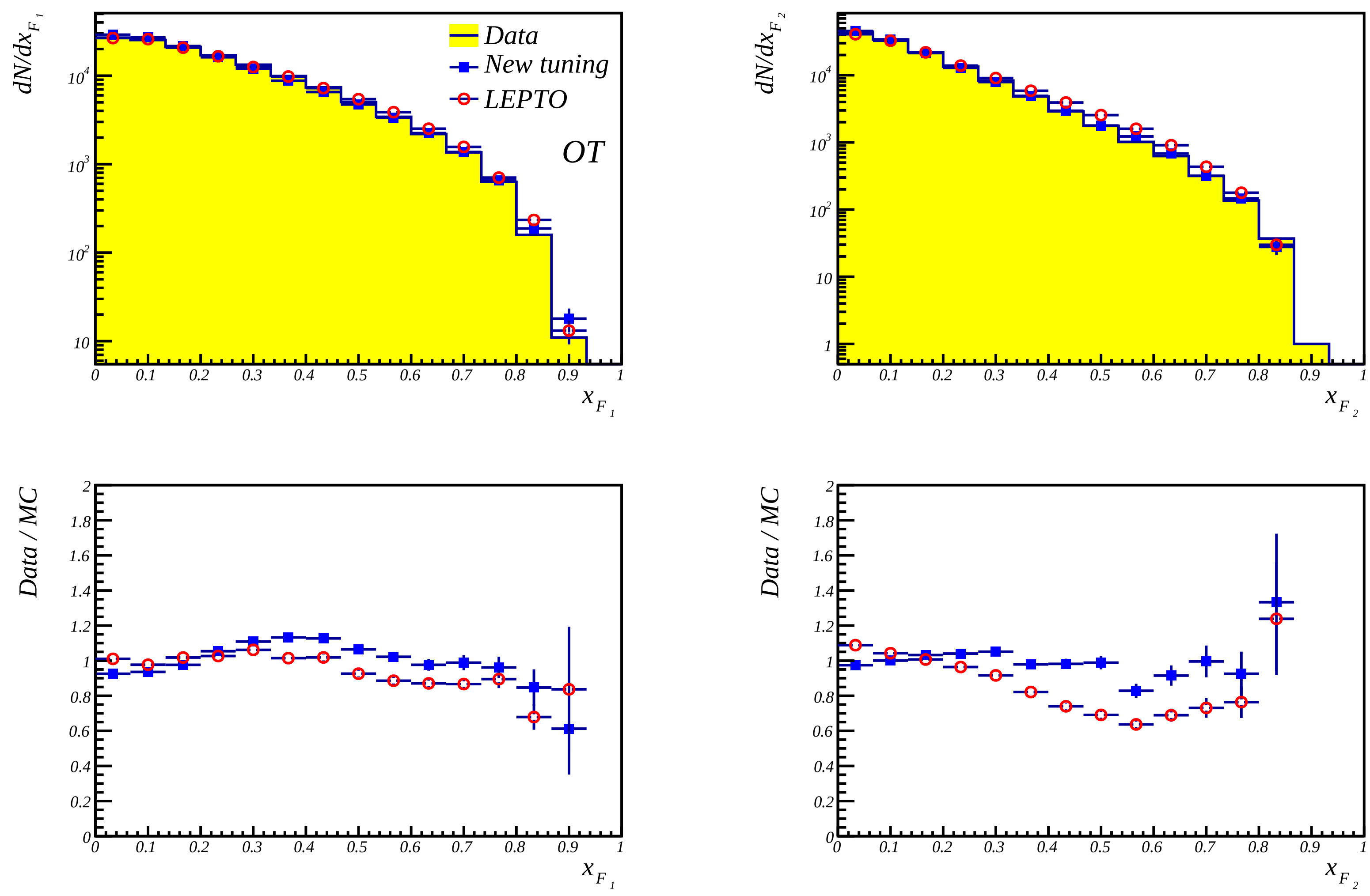

Figure 10.21: Comparison between data and MC simulation for Outer triggers events: distributions (top) and also Data/MC ratios (bottom) for the Feynman x variable for the leading (x_{F_1}) and sub-leading (x_{F_2}) hadrons.

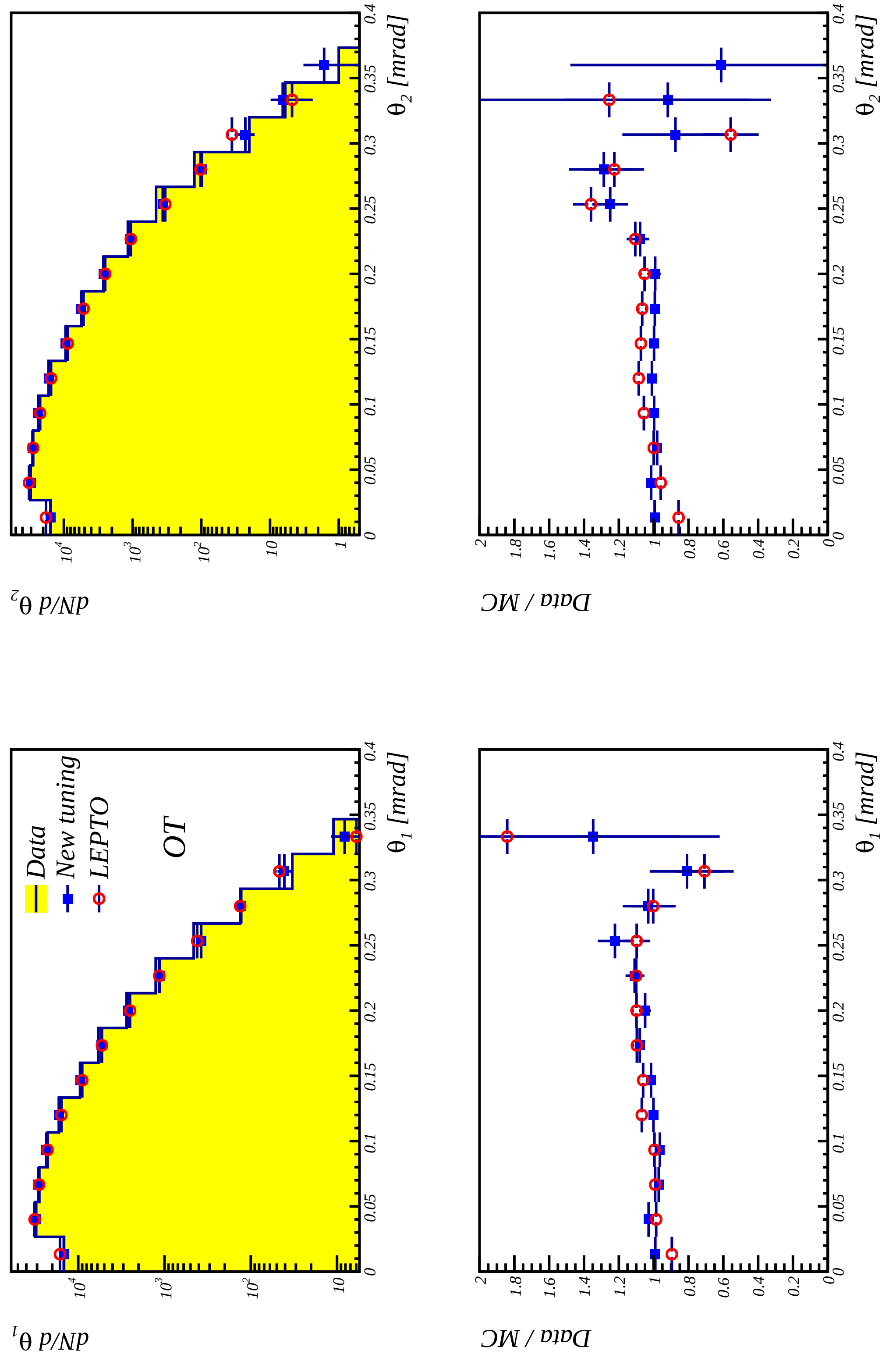

Figure 10.22: Comparison between data and MC simulation for Outer triggers events: distributions (top) and also Data/MC ratios (bottom) of the azimuthal angle with respect to the z coordinate for the leading (θ_1) and sub-leading (θ_2) hadrons.

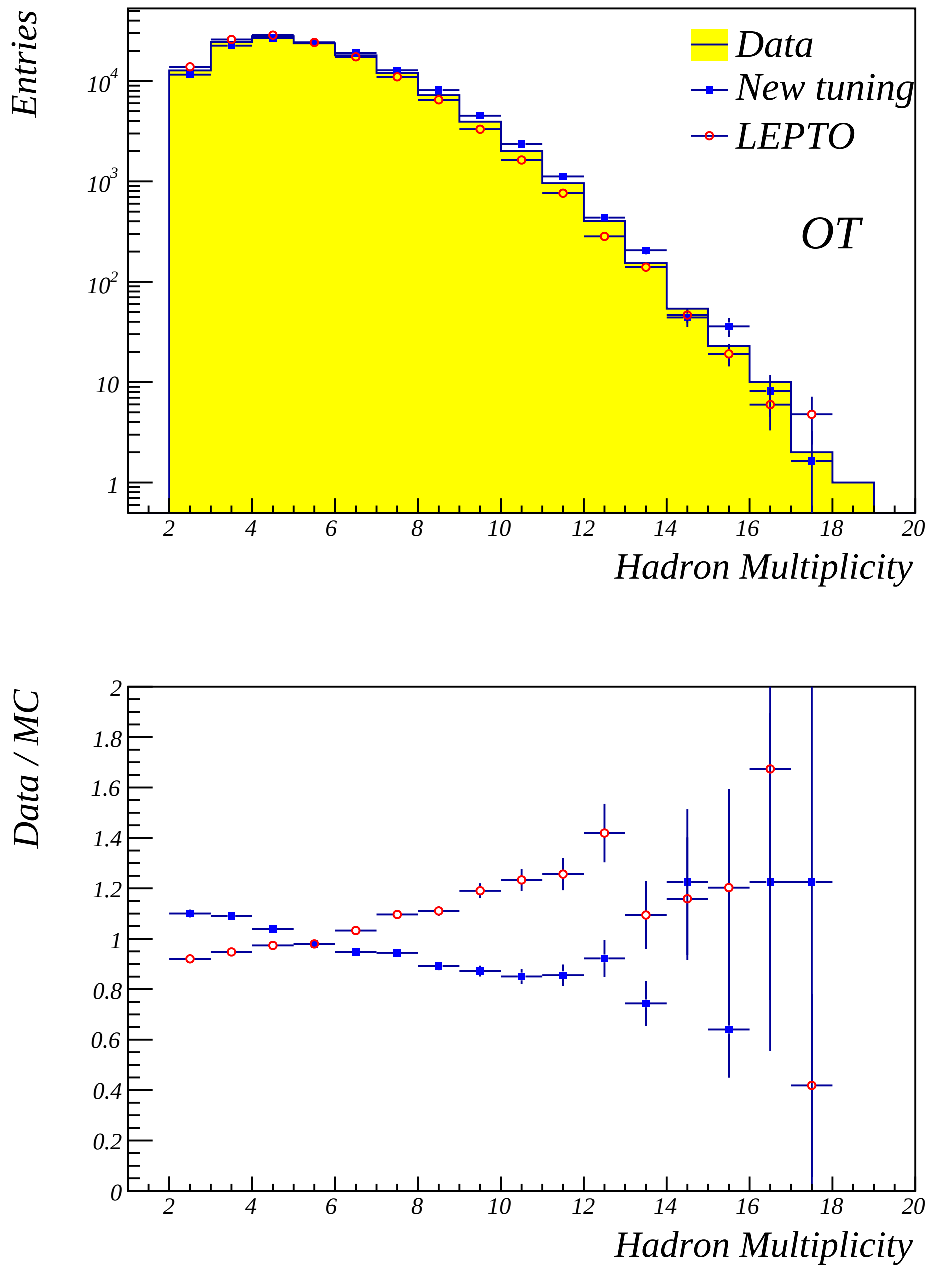

Figure 10.23: Comparison between data and MC simulation for Outer triggers events: distributions (top) and also Data/MC ratios (bottom) of the hadron multiplicities for the leading and sub-leading hadrons.

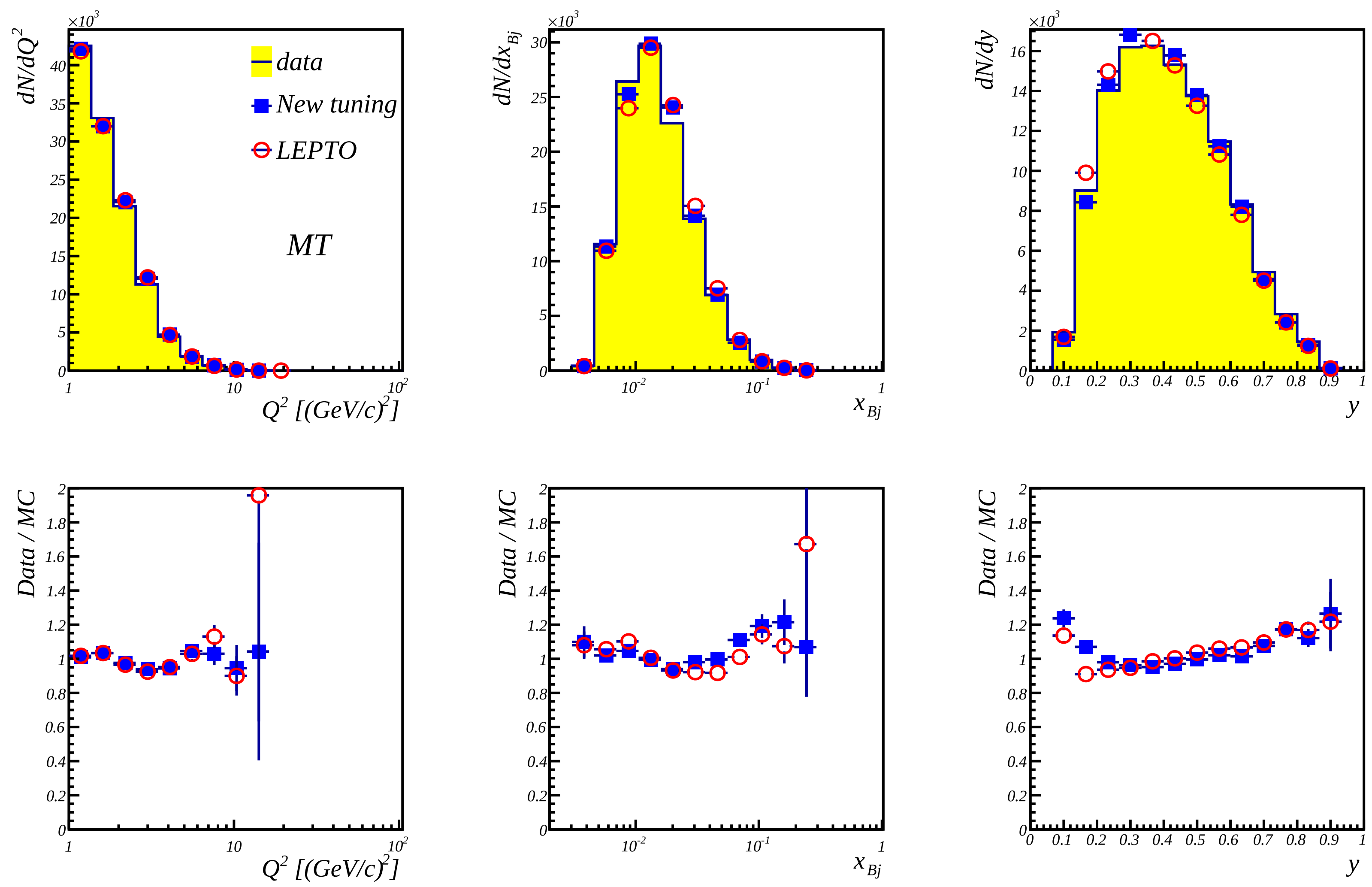

Figure 10.24: Comparison between data and MC simulation for Middle triggers events: distributions (top) and ratios Data/MC (bottom) for the inclusive variables: x_{Bj}, Q^2 and y are shown.

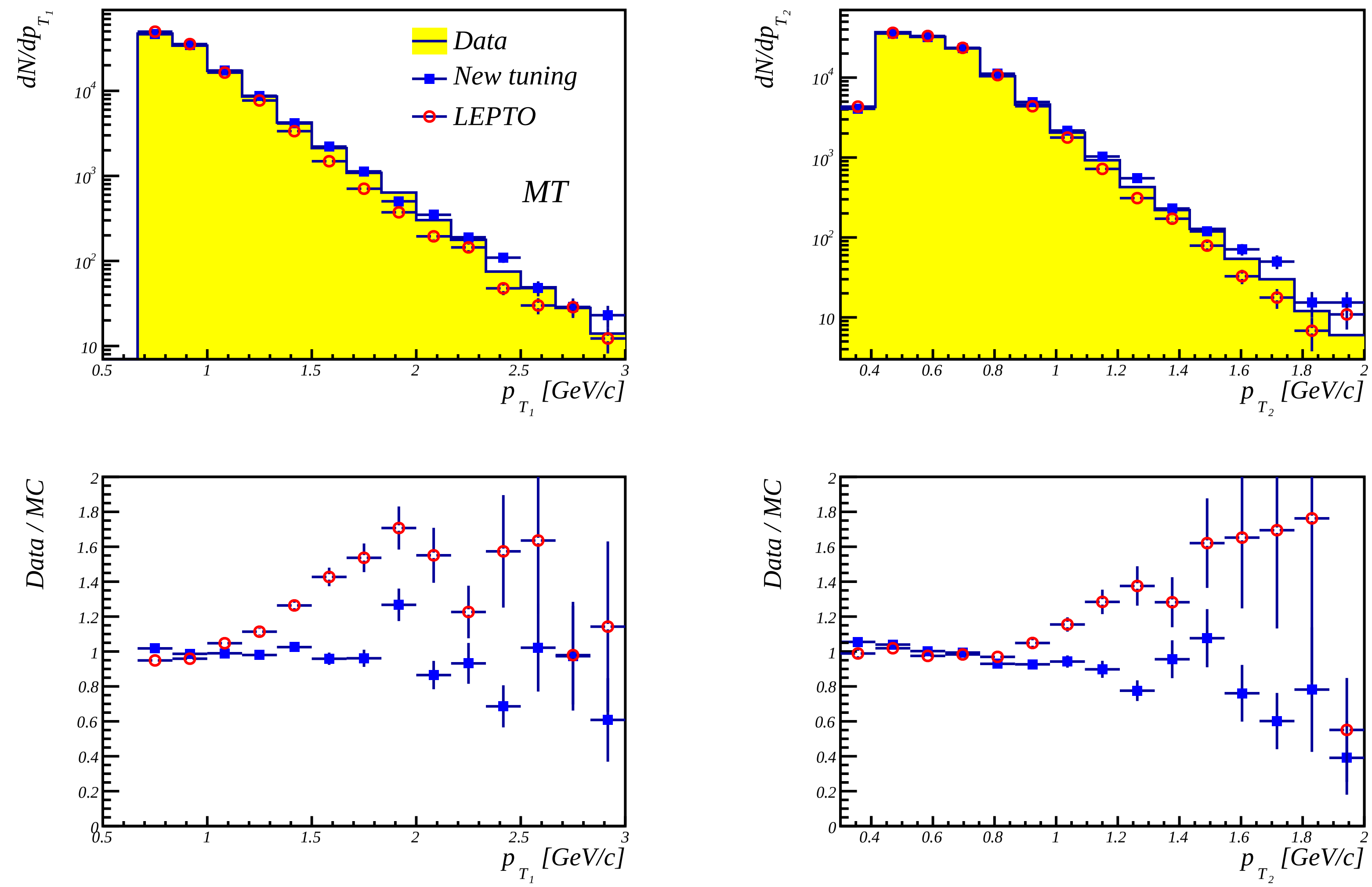

Figure 10.25: Comparison between data and MC simulation for Middle triggers events: distributions (top) and also Data/MC ratios (bottom row) for the leading (p_{T_1}) and sub-leading (p_{T_2}) hadron transverse momenta.

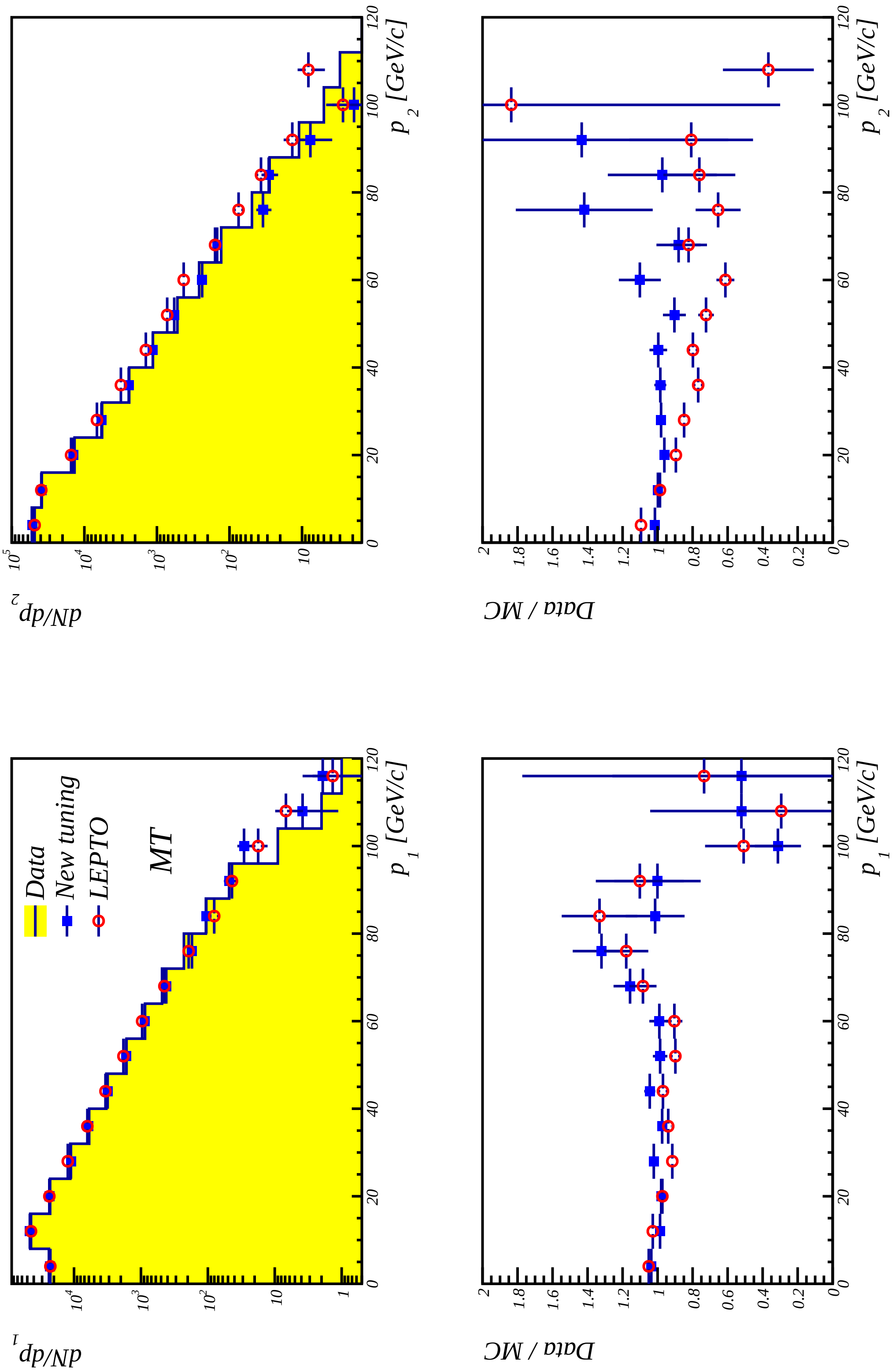

Figure 10.26: Comparison between data and MC simulation for Middle triggers events: distributions (top) and also Data/MC ratios (bottom) for the leading (p_1) and sub-leading (p_2) hadron momenta.

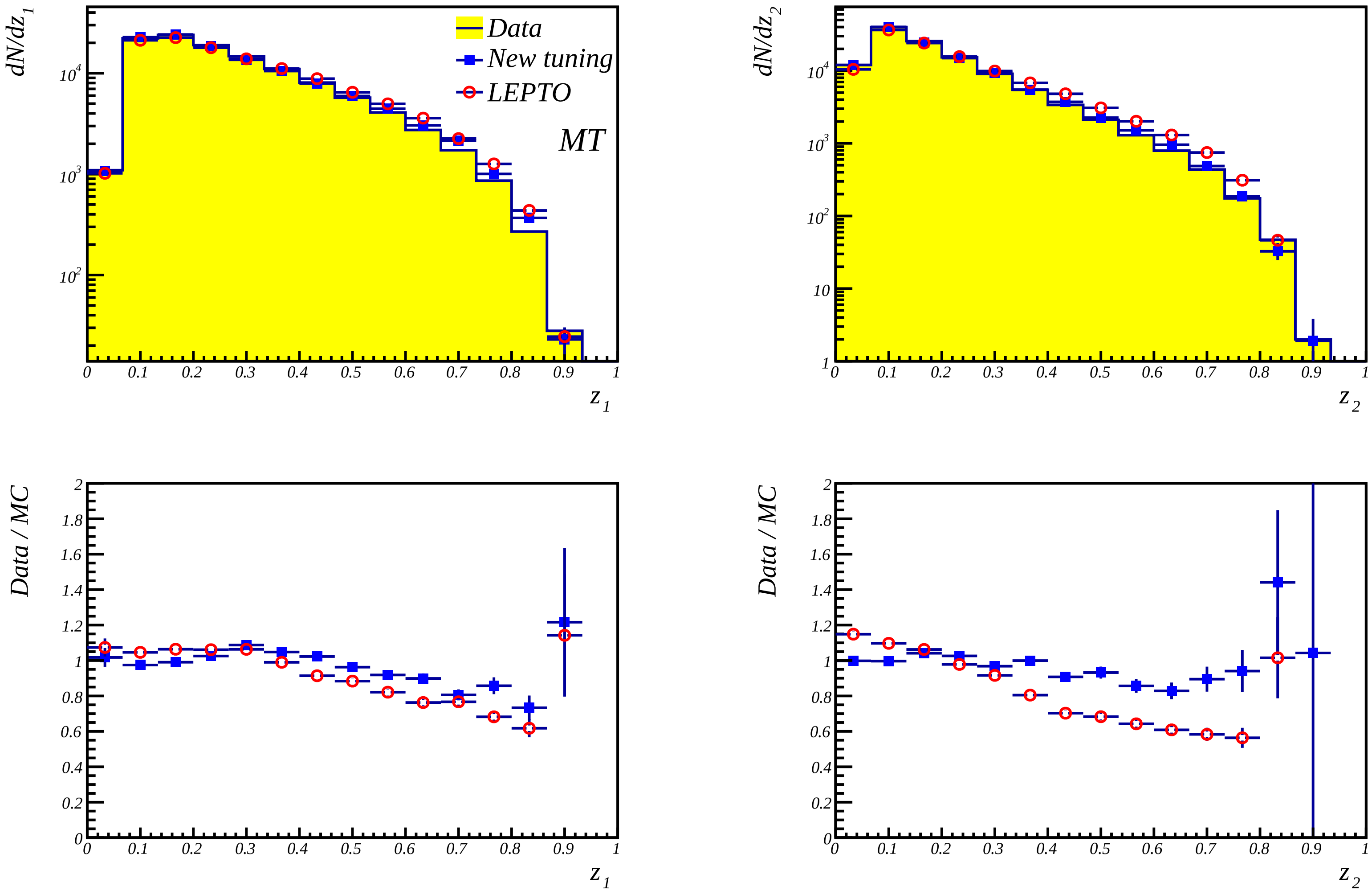

Figure 10.27: Comparison between data and MC simulation for Middle triggers events: distributions (top) and also Data/MC ratios (bottom) for the energy fraction of the virtual photon carried by the leading (z_1) and sub-leading (z_2) hadrons.

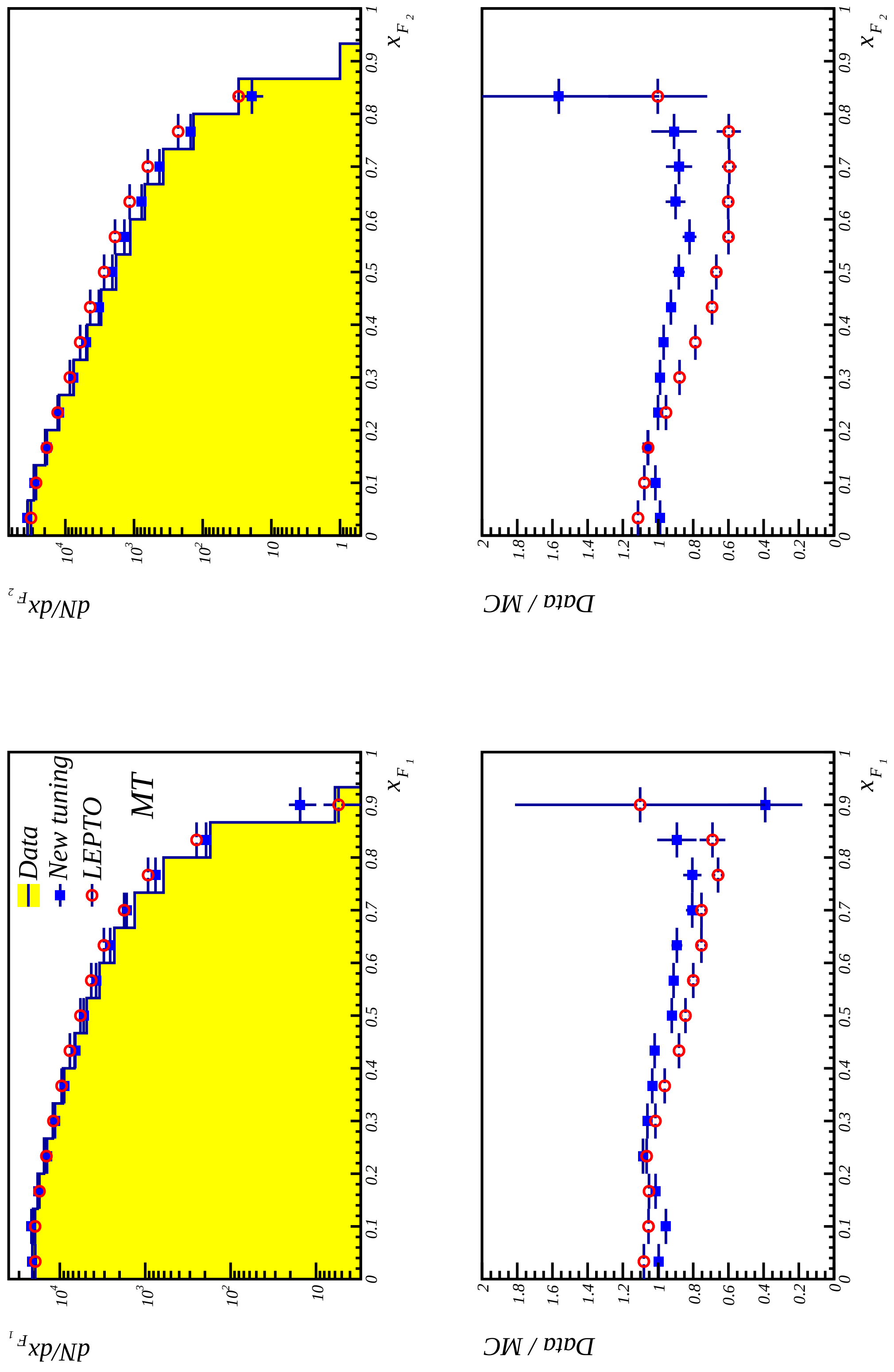

Figure 10.28: Comparison between data and MC simulation for Middle triggers events: distributions (top) and also Data/MC ratios (bottom) for the Feynman x variable for the leading (x_{F_1}) and sub-leading (x_{F_2}) hadrons.

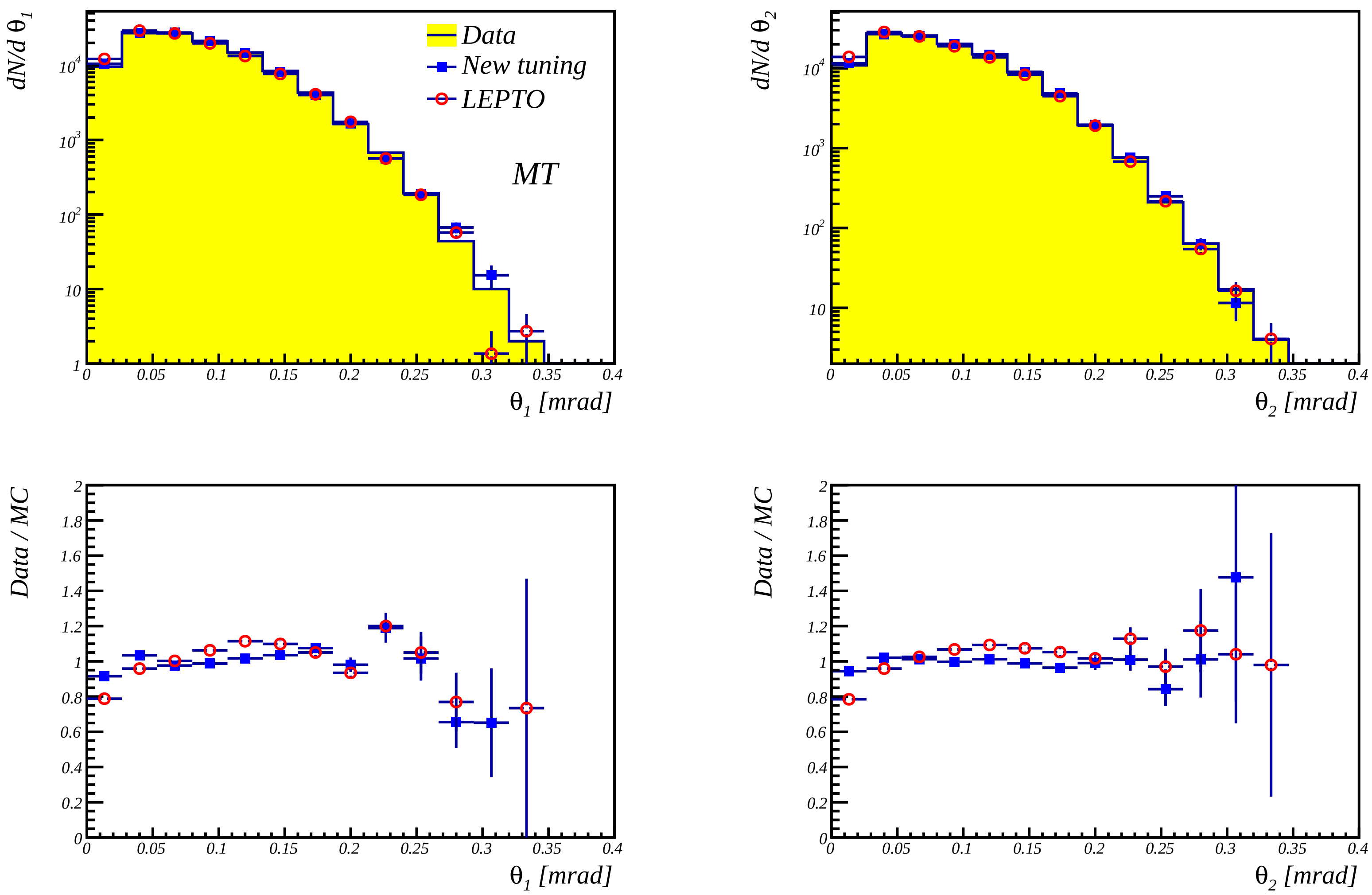

Figure 10.29: Comparison between data and MC simulation for Middle triggers events: distributions (top) and also Data/MC ratios (bottom) of the azimuthal angle with respect to the z coordinate for the leading (θ_1) and sub-leading (θ_2) hadrons.

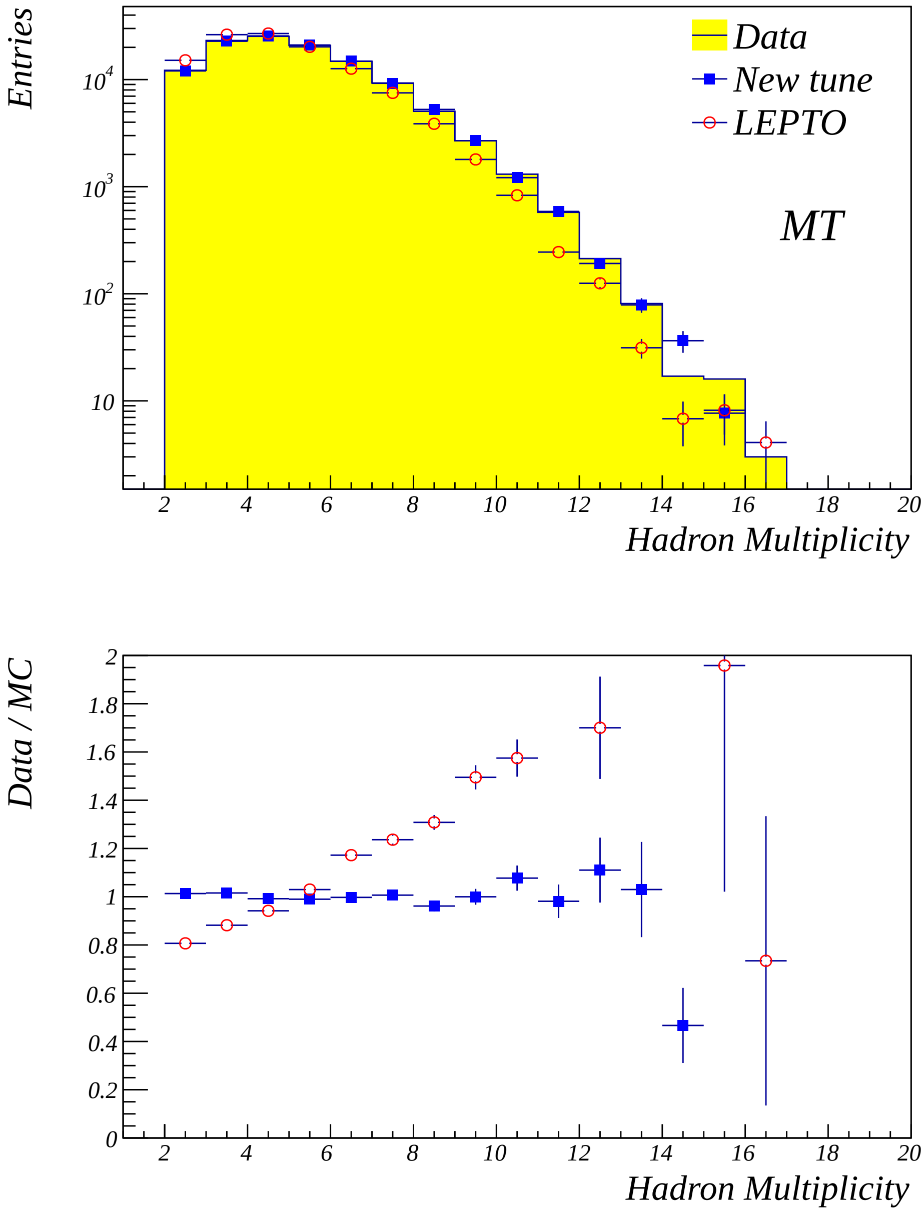

Figure 10.30: Comparison between data and MC simulation for Middle triggers events: distributions (top) and also Data/MC ratios (bottom) of the hadron multiplicities for the leading and sub-leading hadrons.

The improvement achieved by the new tuning is also present in these relevant triggers.

The gluon radiation generation is compared in figures 10.31 and 10.32. The tuning describes better the data using the PS ON mode. This is particularly apparent in the very high Q^2 region, where the hadrons p_T is also high.

In figure 10.33, the comparison of the kinematic variables are shown for the inclusive variables Q^2, x_{Bj} and y.

In conclusion, the MC comparisons with the data showed that the physics is described by the simulation in a satisfactory way. The purpose of the simulation being to extract the partonic information to be used in the gluon polarisation measurement, this information is used

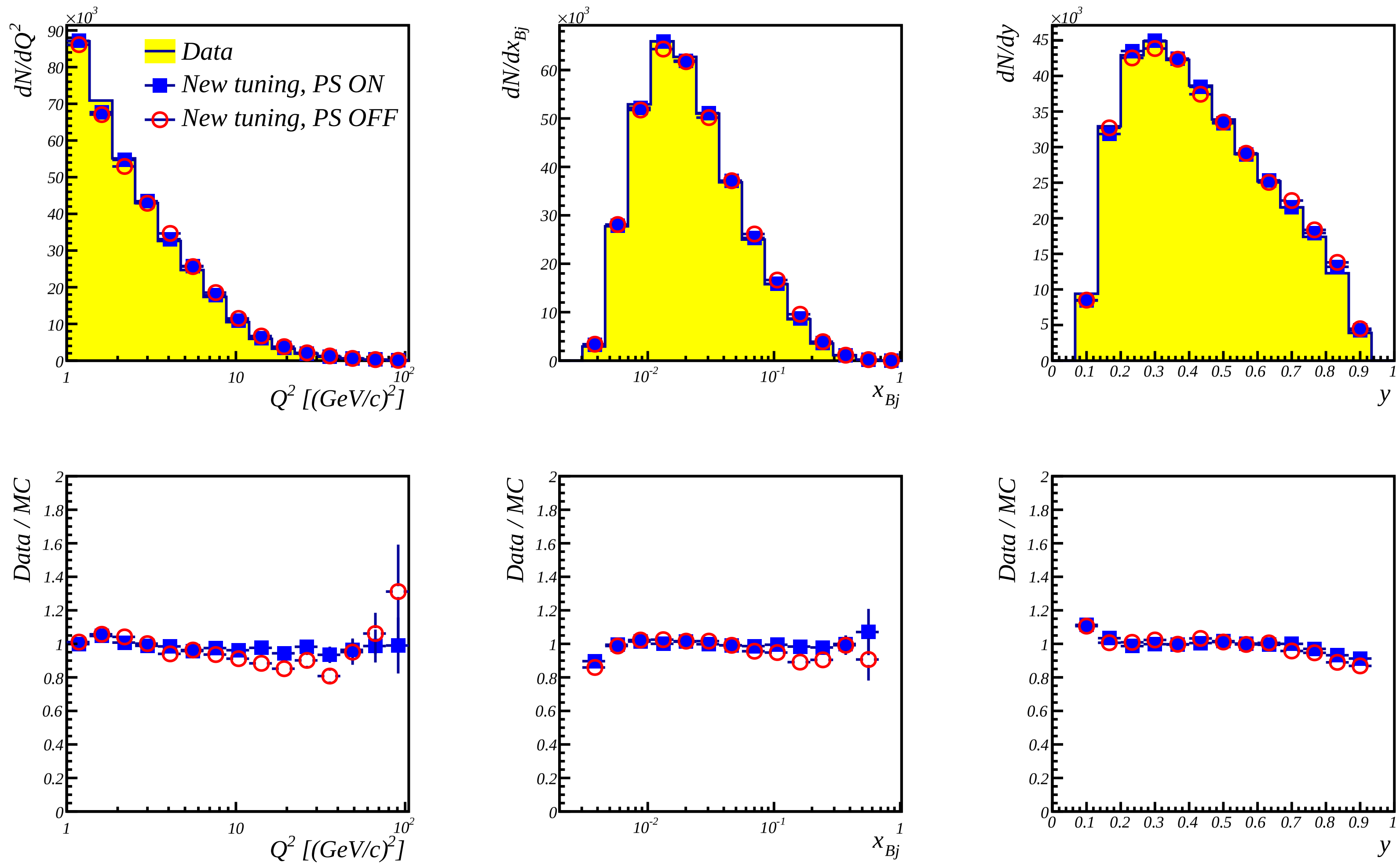

Figure 10.31: Comparison between data and MC simulation with and without gluon radiation: distributions (top) and ratios Data/MC (bottom) for the inclusive variables: x_{Bj}, Q^2 and y are shown.

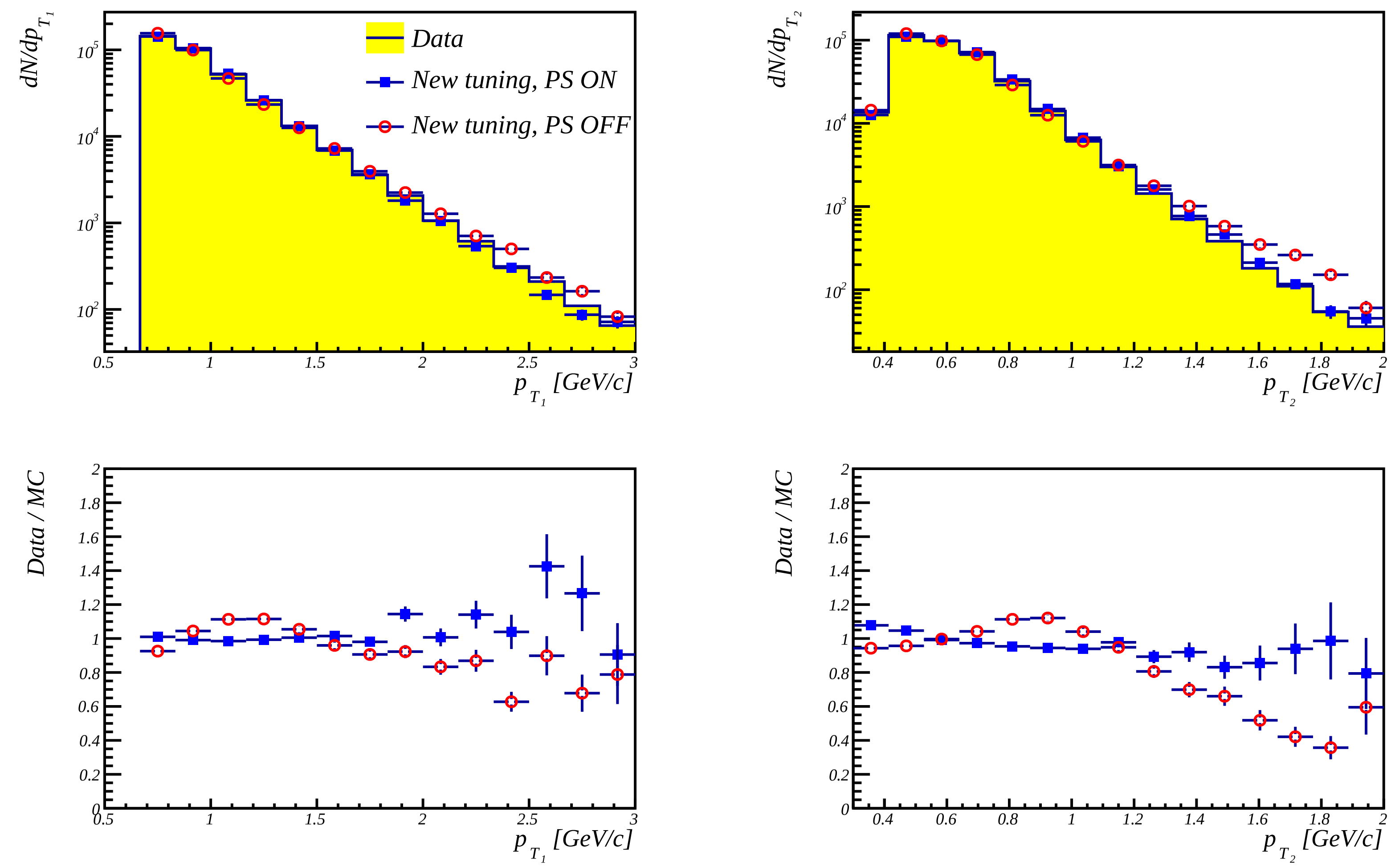

Figure 10.32: Comparison between data and MC simulation with and without gluon radiation: distributions (top) and also Data/MC ratios (bottom) for the leading (p_{T_1}) and sub-leading (p_{T_2}) hadron transverse momenta.

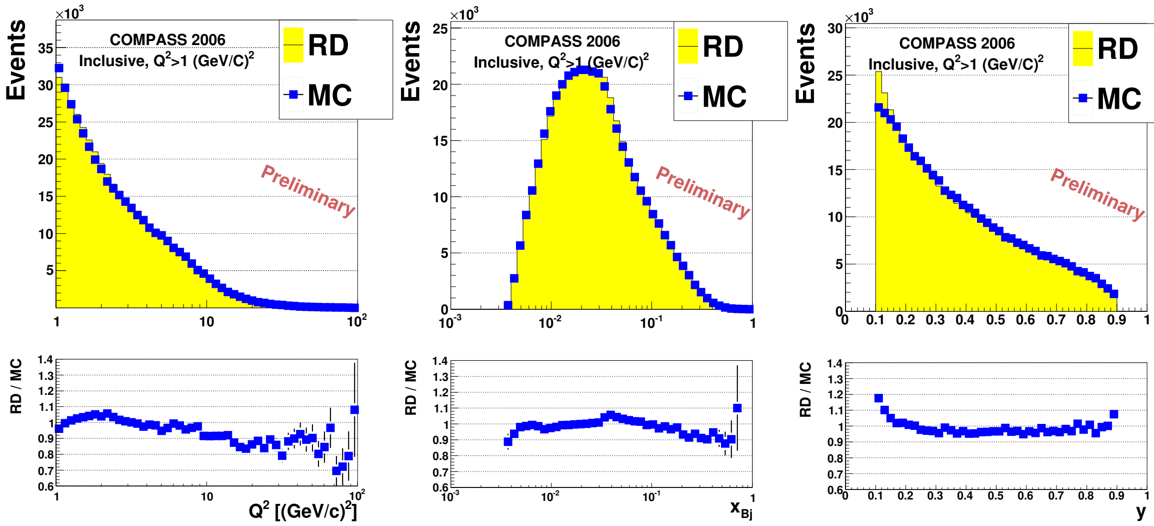

Figure 10.33: Comparison between data and MC simulation: On plots distributions (top) and ratios Data/MC (bottom) for the inclusive sample: Q^2, x_{Bj} and y are shown.

with a high degree of confidence taking into account the good description of the simulation.

10.8 Neural Network

In the presented analysis method (chap. 8) of the gluon polarisation extraction, the knowledge of the process fractions (R_{LP}, R_{QCDC}, R_{PGF}, R^{inc}_{LP}, R^{inc}_{QCDC} and R^{inc}_{PGF}) of the partonic spin asymmetries (a^{PGF}_{LL}, a^{QCDC}_{LL}, $a^{inc,PGF}_{\mathrm{LL}}$ and $a^{inc,QCDC}_{\mathrm{LL}}$), and also the momentum fractions carried by the struck parton in the QCDC and PGF processes (x_C, x^{inc}_C, x_G and x^{inc}_G) is required for each event. Therefore a parametrisation is built to obtain such quantities. A bayesian neural network is the tool used to parametrise these partonic variables, which are experimentally inaccessible. Several neural networks are used, since the x_C and x_G (also x^{inc}_C and x^{inc}_G) variables are parametrised independently. To parametrise them, the process fractions two neural networks are used: one for the inclusive and another for the high p_T sample. Figure 10.34 shows the distributions of the parametrised variables used in the $\Delta G/G$ determination.

The neural networks are trained in a mode in which their output has the interpretation of the expectation value X of the parametrised quantities as a function of the input parameters. The set of input parameters for the inclusive sample the input parameter phase space is given by the x_{Bj} and Q^2 variables, while for the high p_T sample in addittion to the previous variables, the transverse and longitudinal momenta of the leading and sub-leading hadrons (p_{T_1}, p_{T_2}, p_{L1}, and p_{L2}) and partonic information (originating process, a_{LL} and x_p) are used. In all cases MC simulation data is used to train the neural network. Details about the neural network are found in [88, 91].

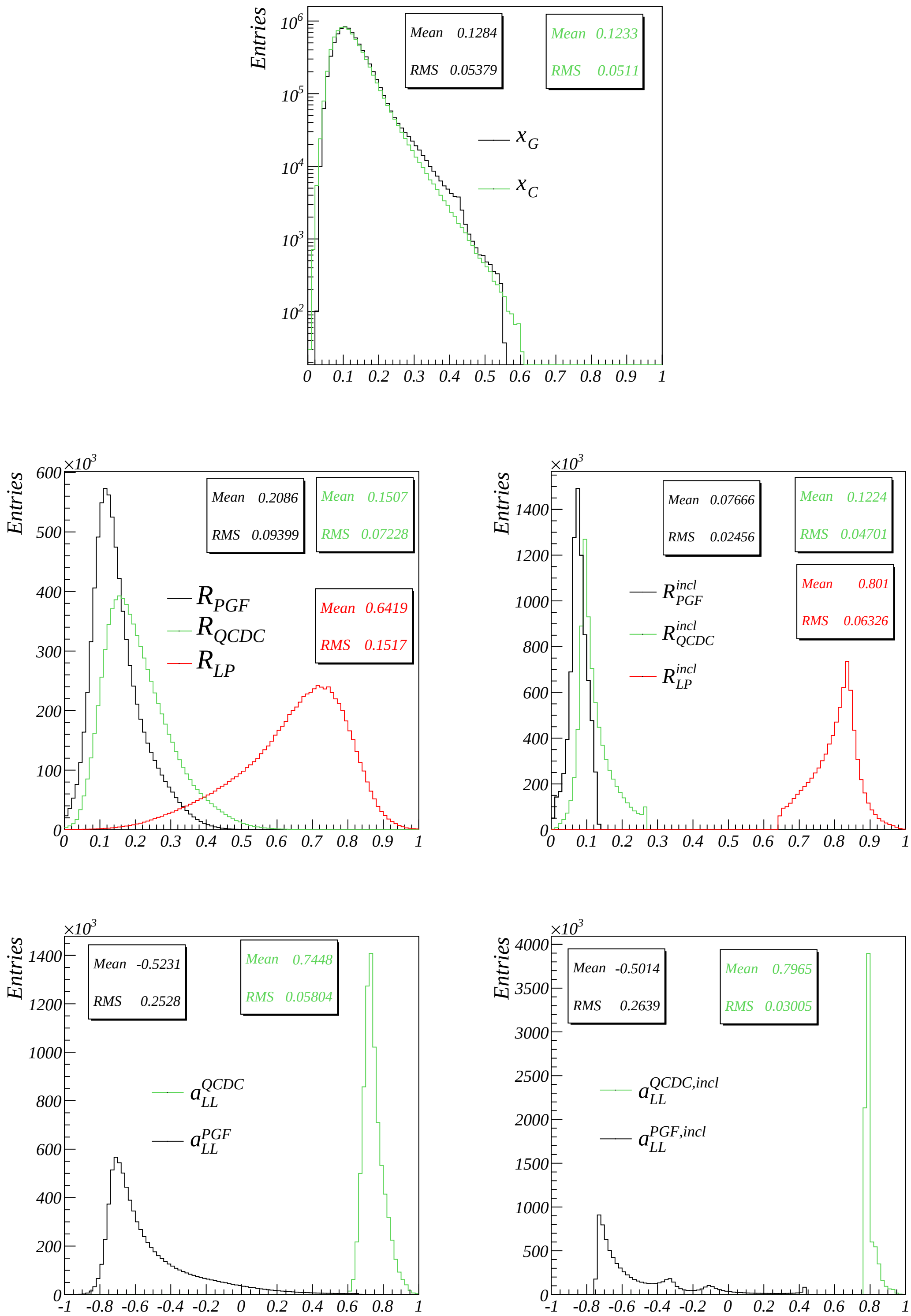

Figure 10.34: Distributions of the parametrised variables used in the $\Delta G/G$ determination. On top, the parton momentum fraction distributions, x_C and x_G, for the QCDC and PGF processes respectively. The middle plots, the process fractions, for the high p_T (left) and inclusive (right) samples. On the bottom, the partonic asymmetries, for the high p_T (left) and inclusive (right) samples.

CHAPTER 11

THE SYSTEMATIC UNCERTAINTIES

In this world nothing can be said to be certain, except death and taxes.

Benjamin Franklin.

The systematic uncertainties associated with this measurement are related to several sources. In this section, the systematic studies performed on data and MC are presented and discussed. In some studies, the knowledge from previous analyses is used [11, 70, 88, 92, 93], as well as results and ideas discussed in the so called COMPASS high-p_T group and also presented in the COMPASS analysis meetings.

11.1 Sources of Systematic Uncertainties

In this study, the following systematic uncertainty sources are discussed:

1. False asymmetries;
2. Neural network;
3. Monte Carlo simulation;
4. Target and beam parameters;
5. A_1^d parametrisation;
6. Radiative corrections;
7. Resolved photon contribution;
8. $\Delta G/G$ formula simplification.

11.2 Samples and Tools used in the Systematic Uncertainty Studies

In this section, the several samples used for the systematic studies are presented as follows:

1. The "standard" high-p_T sample from which the final $\Delta G/G$ value is extracted;
2. The sample with looser cuts on p_T and Q^2, namely $p_{T_{1,2}} > 0.35$ GeV/c and $Q^2 > 0.7$ (GeV/c)^2;
3. An all-p_T sample for which no cut is applied on the transverse momenta of hadrons.

Samples (2) and (3) have higher statistics than sample (1). In order to enable relevant systematic studies of the high p_T sample, the events in sample (2) and (3) should have a similar distribution in the spectrometer as the ones of sample (1). In the high p_T low Q^2 analysis, this condition can only be met when an appropriate cut on the hadrons polar angle θ is applied. In the present analysis, such a cut is not crucial due to the looser the cut in p_T selection. In addition, due to the moderate and high Q^2, all hadrons have some non-negligible transverse momentum with respect to the beam direction.

However, sample (2), whose phase-space is much closer to our final sample's one, shows larger instabilities than sample (3). Therefore, the final systematic error due to false asymmetries and stability of the spectrometer is estimated using sample (2), while sample (3) is used for additional tests.

Four asymmetries are used as tools to assess the contribution of each of the aforementioned sources:

1. $\Delta G/G$;
2. $\Delta G/G - A^{\mathrm{corr}}/\lambda$;
3. $A_1^{p_T}$;
4. A_1^{2h}.

The quantity $\Delta G/G - A^{\mathrm{corr}}/\lambda$ is the value for the $\Delta G/G$ obtained under the assumption that the correction of a non zero A_1^d for LP and QCDC processes can be neglected. Asymmetry $A_1^{p_T}$ is the A_1 asymmetry measured in the high p_T sample. Finally, A_1^{2h} is the A_1 asymmetry measured in samples (2) and (3). As a matter of fact, this asymmetry for sample (3) is very similar to the semi-inclusive A_1^d, since in COMPASS there are only a few events with only one hadron in the primary vertex (PV). Therefore a non-zero A_1^{2h}, at large x, is expected.

11.3 False Asymmetries

In chapter 7, some beam and target properties were assumed to be constant for the definition of the asymmetries in the calculation procedure. False asymmetries may arise from several sources, in particular, from changes in the spectrometer geometrical acceptance, or changes in the density of the target material exposed to the beam. In section 7.3, the false asymmetries are presented as a function of r, ratio of acceptance times the target material density between the up and down-stream polarised target cell, as shown in equation (7.30). False asymmetries are divided into two kinds:

- **Reproducible false asymmetries:** These asymmetries are related to known changes on the spectrometer performance, *e.g* acceptance. Some examples of asymmetries studied are:
  - *Microwave (MW) asymmetries:* In this case, the asymmetries are calculated using positive microwave (MW_+) and negative microwave (MW_-) separately and the reproducible asymmetry was estimated as $A_{rep} = \frac{1}{2}(MW_+ - MW_-)$;
  - *False asymmetries in data without physical asymmetry:* In order to quantify the effects due to non-physical asymmetries, the data is combined in such a way that the physical asymmetries do not contribute. The effect of asymmetries using the same muon target spin configuration was considered;
  - *False asymmetries in presence of physical asymmetry:* Some false asymmetries may average to zero when data is combined using the consecutive grouping (defined in section 9.4). Thus data is combined in several ways:
    * day-night;
    * trigger-by-trigger;
    * inner-outer (with respect to a defined polar angle);
    * left-right and top-bottom with respect to the scattered muon;
    * top-bottom with respect to the hadron.
- **Random false asymmetries:** These asymmetries are caused by random (unpredicted) changes in the spectrometer performance, *e.g.* if a set of detectors has a lower efficiency, this would affect in a different way the acceptance of the spectrometer for events coming from the two (three, in 2006 data) target cells.

All these false asymmetries were investigated and found to be lower than 2×10^{-3} [88, 93].

Estimation of the False Asymmetry Systematic Uncertainty

The estimate of the systematic error connected with false asymmetries is done on sample (2). The principle is to select a larger sample than the initial one and study the stability of the results.

Since all the false asymmetries were found to be very small, an additional test was performed to assess the contribution from false asymmetries. To estimate any possible impact of the false asymmetry into the $\Delta G/G$ measurement, the A_1^{2h} asymmetry is used, since it may contain some false asymmetry value. In this view a test of its stability as a function of the data taking periods has been performed using the following χ^2 definition

$$\sum_{i=0}^{Nperiod} \frac{(A_{1,i}^{2h} - \langle A_1^{2h} \rangle)^2}{\sigma_i^2 - \sigma_{\langle A_1^{2h} \rangle}^2}, \qquad (11.1)$$

where $A_{1,i}^{2h}$ is the asymmetry value obtained from consecutive configuration for a given period. For the 2002-2004 data, a value of $\chi^2/ndf = 32.8/27$ shows the consistency of the asymmetry

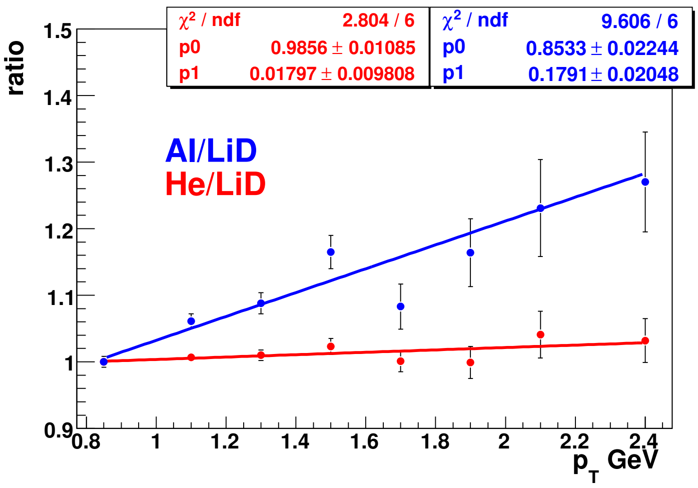

Figure 11.1: Ratios of the observed number of events for different nuclei as functions of the hadron p_T.

A_1^{2h}. On the other hand, for the 2006 data, the obtained results are $\chi^2/ndf = 26.8/12$; the probability of such occurrence is only 0.8%. Nevertheless, the results of A_1^{2h} between 2002-2004 and 2006 are in agreement and the contribution from the whole data will be used.

The contribution to the $\Delta G/G$ from any possible false asymmetry is estimated from the following formula related to statistical error:

$$\delta \Delta G/G_{false} = \delta A_1^{2h} \cdot \langle \beta_{A_1} \rangle_w / \langle \beta_{\Delta G/G} \rangle_w \,. \tag{11.2}$$

In this analysis $\langle \beta_{\Delta G/G} \rangle_w = \langle w^2 \rangle / \langle w \rangle = 0.0209$, $\langle \beta_{A_1} \rangle_w = \langle (FDP_b)^2 \rangle / \langle FDP_b \rangle = 0.189$ and $\delta A_1^{2h} = 0.002$; this value is related to the A_1^{2h} extracted from all data (2002-2004 and 2006), which also includes false asymmetries. The quatity w is the weight of the event used for the $\Delta G/G$ calculation. Finally, the systematic uncertainty related to the false asymmstry is $\delta \Delta G/G_{false} = 0.019$.

11.4 Systematic Uncertainty due to P_b, P_t and f variables.

The relative error of the beam and target polarisations, P_b and P_t, is taken as 5% and 2% for dilution factor f. The systematic error of these factors, $\delta(\Delta G/G)_{fP_bP_t}$, is assumed to be proportional to the errors given above. Therefore, the contribution to the systematic error of $\Delta G/G$ is estimated using the standard error propagation, giving $\delta(\Delta G/G_{fP_bP_t}) = 0.004$. The value is very small even if again a safety margin was used due to the fact that the measured $\Delta G/G - A^{\mathrm{corr}}/\lambda$ is close to zero.

With respect to the error of the dilution factor, the HERMES collaboration results [94] suggest that, for larger nuclei, it depends upon the hadron transverse momentum. Some tests were done and the results were presented in ref. [95]. The analysis is summarised in the figure 11.1. The ratio of the hadron p_T distributions produced in He and Al environment to the hadrons produced in the ^{6}LiD target is shown. Within statistical errors, the ratio He/LiD is flat. Therefore, a rather weak dependence of f on p_T for our LiD target was assumed.

Concerning the dependence of $f(p_T)$ the effect for the ratio Al/He is clearly seen and this means that with respect to data taken with the NH_3 target, namely the 2007 and 2011 data, further studies will be needed.

11.5 Systematic Uncertainty related to the A_1^d Parametrisation

In this section, the impact of different parametrisations of A_1^d asymmetry was studied. Four different A_1^d parametrisations are used to estimate the associated systematics, namely:

- v1[1]: using world data, all Q^2;
- v2: same as v1, but using data with $Q^2 > 1$ (GeV$/c$)^2;
- v3: using COMPASS data only, with $Q^2 > 1$ (GeV$/c$)^2;
- v4: using all data and the simple functional form $A_1^d(x) = x^\alpha$.

In the parametrisations v1 to v3, the following functional form, $A_1^d(x) = (x^\alpha - \gamma^\alpha)\left(1 - e^{-\beta x}\right)$ [78] was used.

The obtained results are presented in table 11.1. The rms value of these results is used as an estimate of the uncertainty related to the A_1^d parametrisation. The estimated error is $\delta(\Delta G/G)_{A1} = 0.015$.

Parametrisation	$\Delta G/G$
v1	0.125 ± 0.060
v2	0.128 ± 0.060
v3	0.156 ± 0.060
v4	0.149 ± 0.060

Table 11.1: Results for $\Delta G/G$ using various A_1^d parametrisations. The quoted uncertainty is related to statistics.

11.6 Systematic Uncertainty due to the Monte Carlo Simulations

The effect of the Monte Carlo simulation is taken into account in the following study. As mention in sec. ??, seven different MCs are used:

1. COMPASS tuning, parton shower ON, PDF=MSTW08;
2. COMPASS tuning, parton shower OFF, PDF=MSTW08;

[1]For the final $\Delta G/G$ result, the $v1$ parametrisation was used.

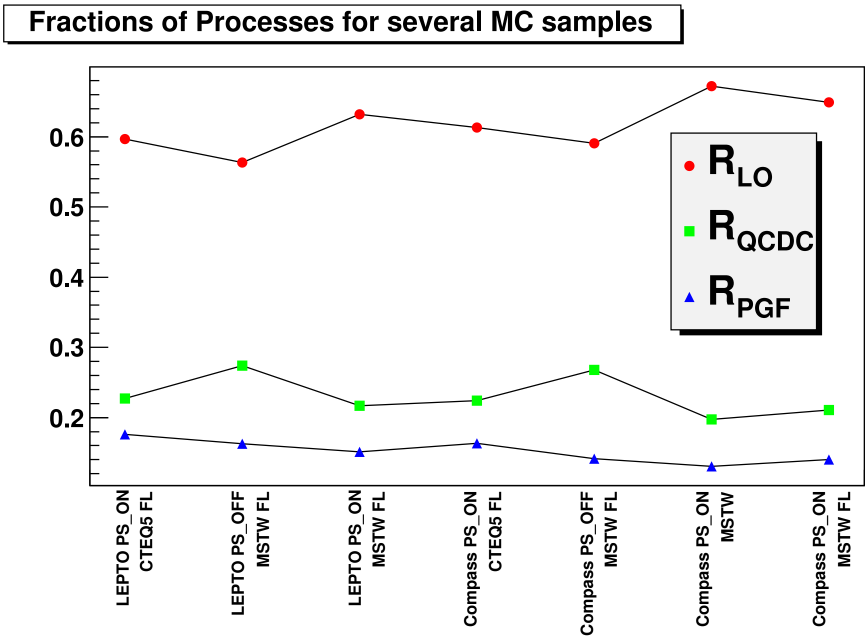

Figure 11.2: Fractions of processes, R, for several high p_T MC samples.

3. COMPASS tuning, parton shower ON, PDF=CTEQ5L;
4. COMPASS tuning, parton shower ON, PDF=MSW08, NO F_L;
5. LEPTO DEFAULT tuning, parton shower ON, PDF=MSTW08;
6. LEPTO DEFAULT tuning, parton shower OFF, PDF=MSTW08;
7. LEPTO DEFAULT tuning, parton shower ON, PDF=CTEQ5L.

All of them were used in the systematics studies except the first one, which was used to extract the parametrisation used in the analysis.

In figure 11.2 the fractions of processes, R, are compared for all MC samples. The analysing power, a_{LL}, are shown in figure 11.3 in the same way. In table 11.2 all these values are summarised.

Therefore seven values were extracted for $\Delta G/G$, which are summarised in table 11.3. In the first column, the kind of the MC sample is indicated. In the second and third columns, the values and the statistical errors for $\Delta G/G$ are given, respectively. The last column shows $\Delta G/G - A^{\text{corr}}/\lambda$, the value of $\Delta G/G$ obtained when the correction from A_1^d for LP and QCDC processes are neglected. The error on $\Delta G/G - A^{\text{corr}}/\lambda$ is the same as the error on $\Delta G/G$.

All the results presented in the table 11.3 are very close to each other. The rms value for $\Delta G/G$ was found to be small, 0.02.

However, the values of $\Delta G/G$ and $\Delta G/G - A^{\text{corr}}/\lambda$ are very close to zero. In such a case, even dramatic changes of the PGF process fraction would not change the final $\Delta G/G$ results. On the other hand, a large deviation of $\delta\Delta G/G$ for various tunings up to a factor of 1.75 (= 0.0716/0.0410) was observed. This fact needs to be taken into account in the systematic error.

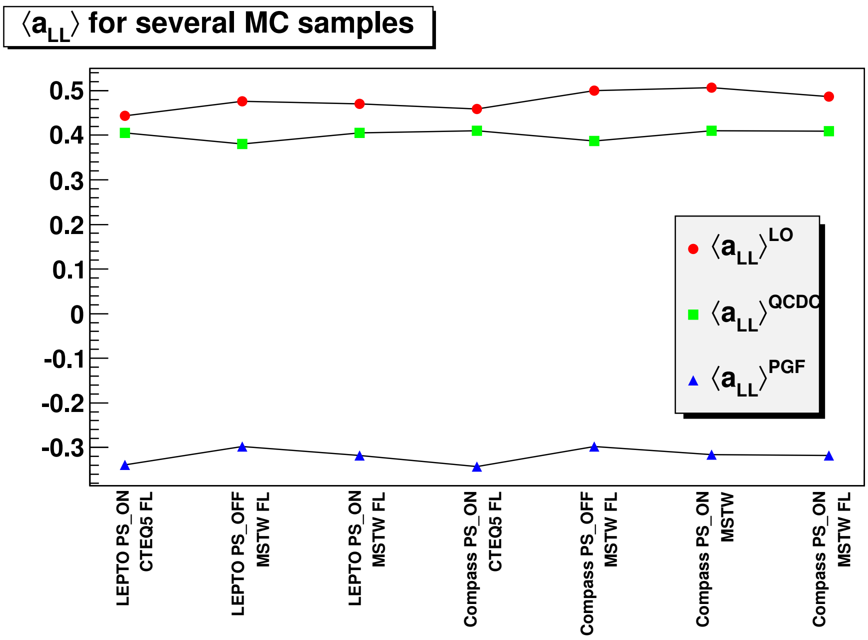

Figure 11.3: Analysing power *per* process, a_{LL}, for several high p_T MC samples.

Therefore, a method for the estimation of the systematic uncertainty based on the ratio of the errors for the extreme cases (*i.e.* 1.75) is proposed:

$$\delta(\Delta G/G)_{MC} = \mathrm{Max}(\delta(\Delta G/G), \Delta G/G - A^{\mathrm{corr}}/\lambda)_{\mathrm{case1}} \times \left(\frac{\mathrm{Max}(\delta(\Delta G/G))}{\mathrm{Min}(\delta(\Delta G/G))} - 1 \right) = 0.045\ .$$

The term $\mathrm{Max}(\delta(\Delta G/G), \Delta G/G - A^{\mathrm{corr}}/\lambda)_{\mathrm{case1}}$ is the maximum between the $\Delta G/G$ and $\Delta G/G - A^{\mathrm{corr}}/\lambda$ values for 'case 1.', *i.e.* COMPASS_ON_MS. The 'Max' and 'Min' values, in the following term, are related to the extreme $\delta(\Delta G/G)$ values considering all cases. In the present analysis, this is the biggest contribution to systematic error.

11.7 Neural Network Stability

In this section, the neural network tests used to assess the neural network stability are presented. First, the behaviour of the neural network is tested in order to check if the output is the expected one. The most crucial neural network of the whole analysis chain is the one that computes the probabilities for any given event to be of either PGF, QCDC or LP type. Moreover, its 2-dimensional output makes it more difficult to train than simpler, 1-dimensional, neural networks, like the one for a_{LL}^{PGF} estimation.

A MC data set used as testing sample, different from the learning sample used in neural network training, is divided in bins of R_{PGF}, R_{QCDC} and R_{LP} values. In each bin and for each process p, the fraction R_p is computed according to neural network and MC truth bank. The results are presented in figure 11.4. In the top part, the fractions according to MC and neural network are compared and in the bottom part, the difference between neural network and MC as a function of neural network output are presented. The results are in a reasonable agreement.

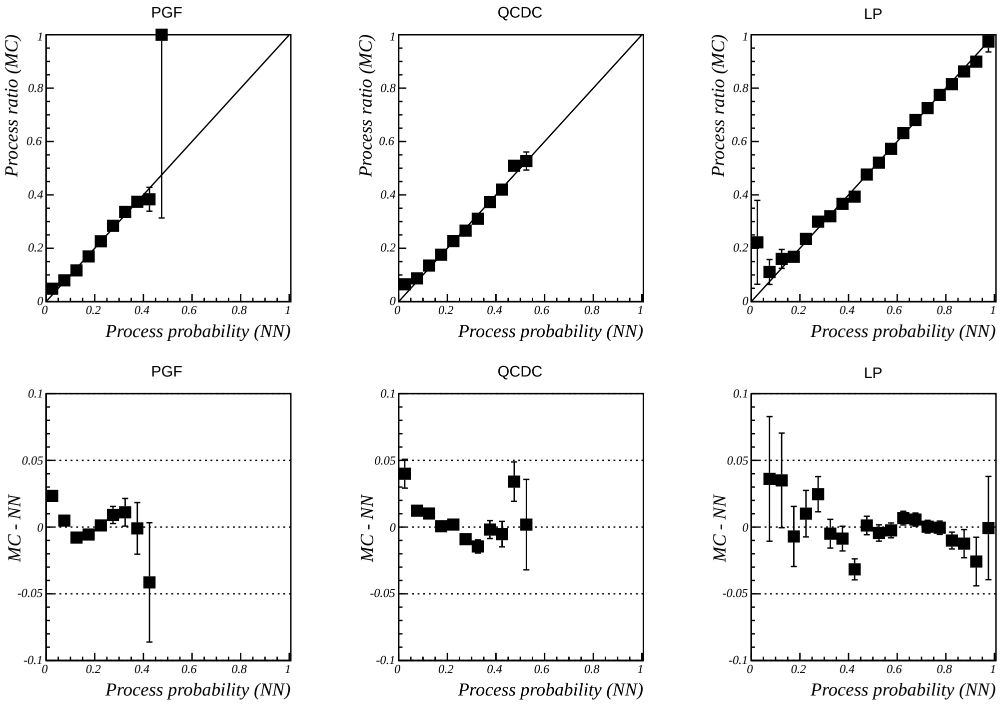

Figure 11.4: Neural network and MC comparison for R_{PGF}, R_{QCDC} and R_{LP} as function of the neural network output.

At very low QCDC and PGF fractions some bias may be indeed observed. Such bias occurs at the edges of the phase space and it is due to *e.g.* some events (around 4 %) that the neural network parametrised with negative values Rs. Nevertheless the observed bias has negligible effect on the final results. For example, removing from the sample events with R_{PGF} and $R_{QCDC} < 0$ changes the final $\Delta G/G$ by about 0.002.

In figures 11.5 to 11.7, a comparison of neural network and MC as a function of Q^2, x and the sum of the p_T^2 of the two hadrons is presented. The neural network output corresponds to the mean value of the given variable in MC. The results from neural network and MC are in agreement.

In previous analyses [70, 96], in which the high p_T cuts used for the leading and subleading hadrons were $p_{T1(2)} > 0.7\,\mathrm{GeV}/c$, the error of $\Delta G/G_{NN}$ was estimated to be 0.006. In the present analysis only limited tests were done. The feeling is that the stability of the neural network is worse than before. The main reason for this behaviour is related to the cuts performed in the aforementioned analysis; the cuts were released as compared to the ones performed in present work; the neural network has to describe a larger phase space *e.g.* comparing current and previous sample. The relative number of events for $\sum p_T^2 > 2.5\,(\mathrm{GeV}/c)^2$ (a slightly tighter cut than $p_{T1(2)} > 0.7\,\mathrm{GeV}/c$) decreased by a factor of 10. The proposed $\Delta G/G_{NN}$ is 0.010 . The result is an educated guess rather than a strictly obtained number.

2004 vs 2006 MC Samples with respect to the Neural Network procedure

Let us consider what is expected if a neural network trained on the 2006 MC is used for the 2004 data. The input parameters for the neural network contain p_T and p_L, in this sense the

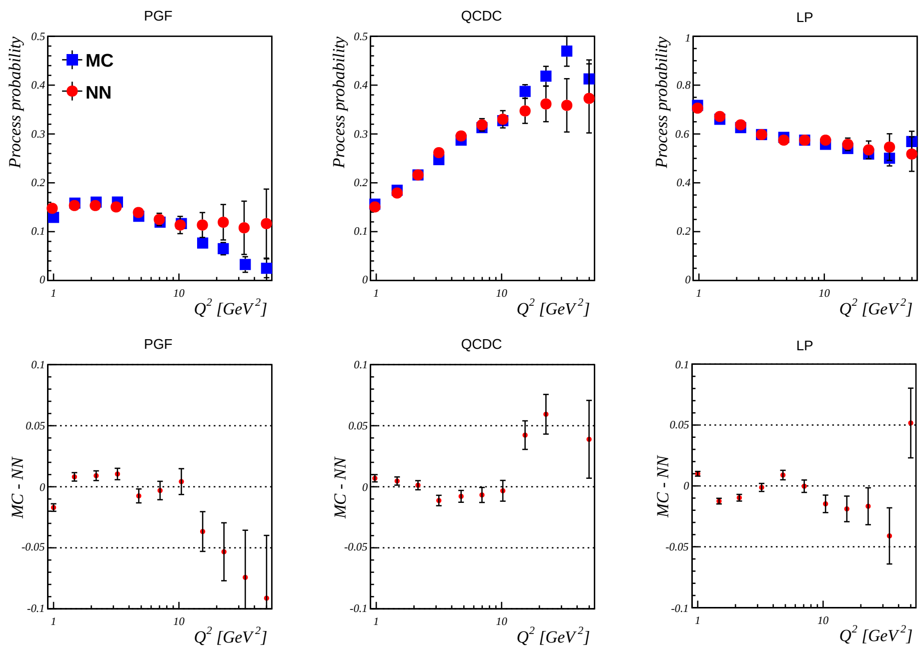

Figure 11.5: Neural network and MC comparison for R_{PGF}, R_{QCDC} and R_{LP} as functions of Q^2. The average of the probability given by the MC (blue squares) and the neural network (red circles) in bins of Q^2 for the three processes is shown in the top row. The differences between the MC and the neural network probabilities are shown in the bottom row.

information about the angle of the hadron with respect to virtual photon γ^*, θ^*, was taken into account during the neural network training. The neural network returns an average value of the output variable in the given phase space point of the input parameters.

Taking this information altogether one would expect that a neural network trained on the 2006 MC and a neural network trained on 2004 MC should give similar results in a narrower phase-space sample, such as the 2002-2004 real data sample.

Therefore, the 2004 MC was used to train a neural network and $\Delta G/G$ was extracted for the 2002-2004 data. Accordingly, the 2006 MC was used to train a neural network and used to extract the $\Delta G/G$ for the 2002-2004 data. The results are the following:

- $\Delta G/G_{NN_{2004}} = 0.108 \pm 0.075$;
- $\Delta G/G_{NN_{2006}} = 0.105 \pm 0.074$.

Both results are compatible as expected.

Performing the same study for the whole data sample, *i.e.* 2002-2006 data, the difference given by the two neural networks would be marginal, of the order of 3% of the statistical error. For the sake of simplicity and faster analysis progress it was decided to use the neural network parametrisation trained on 2006 MC for the whole data set.

11.8 Radiative Corrections

Radiative corrections are properly treated for the data in the dilution factor calculation. However the inclusion of the longitudinal structure function F_L to the cross section parametrisation used by the MC generator requires a proper treatment of radiative corrections for the

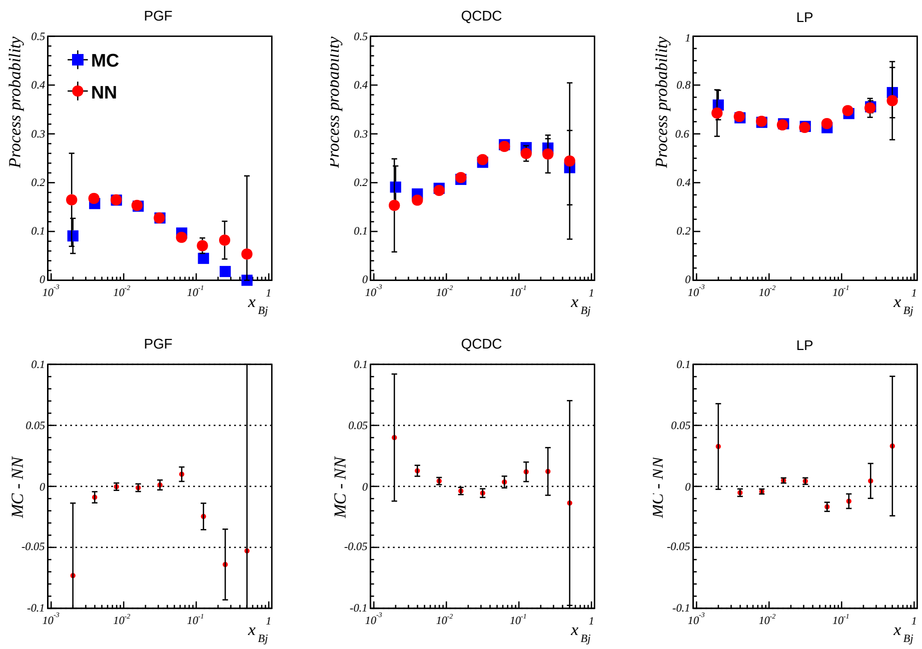

Figure 11.6: Neural network and MC comparison for R_{PGF}, R_{QCDC} and R_{LP} as functions of x_{Bj}. The average of the probability given by the MC (blue squares) and the neural network (red circles) in bins of x_{Bj} for the three processes is shown in the top row. The differences between the MC and the neural network probabilities are shown in the bottom row.

inclusive MC sample. The two effects cancel out to a high degree and cannot be applied separately as this would lead to large discrepancy with the real data. Radiative corrections were included in the inclusive MC via application of radiative weights from tables used in the dilution factor calculations. The tables were prepared for both inclusive and semi-inclusive events and are parametrised in the x_{Bj} and y variables. The MC events were reweighted with radiative corrections (RC) both for comparison with real data and for training of neural networks.

To estimate the upper limit of the expected effect on the high p_T sample the tables for semi-inclusive events were used. The radiative corrections for high p_T events are expected to be smaller then in the semi-inclusive case as the phase space available for the photon emission is largely reduced. The effect of reweighting high p_T events with radiative corrections weight tables was found to be negligible for inclusive variables as well as for average values of the analysing powers and process fractions, as shown in table 11.4. The impact on the hadronic variables is hard to estimate as tables cannot account for change in kinematics of virtual gamma with respect to which the p_T is calculated. Unfortunately a working implementation of RADGEN in LEPTO is currently not available.

11.9 Resolved Photon Processess Contribution

Apart from the three LO processes, also *resolved photon* processes could contribute to the cross-section. A contribution of such processes was found to be significant, of the order of 50%, in the low Q^2 high p_T analysis [11]. The RAPGAP generator [97] was used to estimate the contribution of the resolved photon processes. In RAPGAP the three LO processes and the resolved photon ones have to be generated separately and then weighted with the obtained

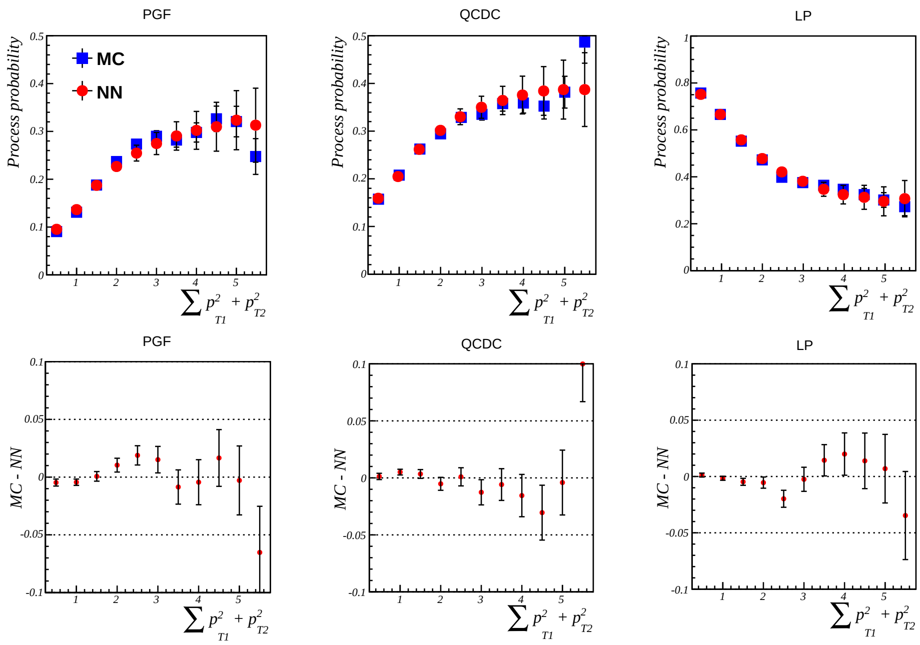

Figure 11.7: Neural network and MC comparison for R_{PGF}, R_{QCDC} and R_{LP} as functions of $\sum p_T^2$. The average of the probability given by the MC (blue squares) and the neural network (red circles) in bins of $\sum p_T^2$ for the three processes is shown in the top row. The differences between the MC and the neural network probabilities are shown in the bottom row.

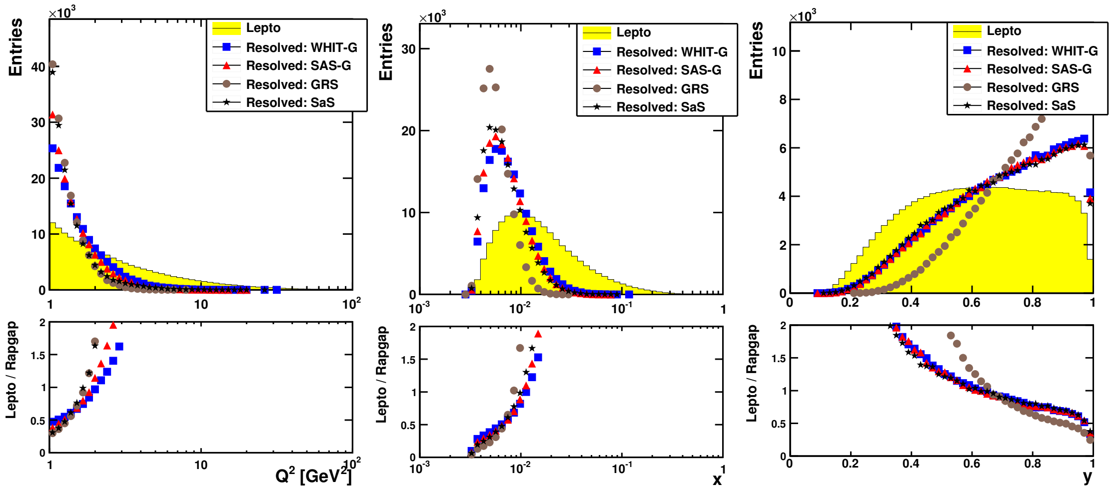

Figure 11.8: Comparison of kinematic distributions of events generated by LEPTO with distributions originating from resolved photon processes obtained from RAPGAP. Different photon PDFs are shown.

cross-sections. Unfortunately the parton distribution functions of the photon are poorly known which leads to variations of obtained cross-section, depending on the selection of PDFs. Thus to estimate the resolved photon contribution a fitting procedure was developed.

The kinematic distributions of events originating from the resolved photon differ significantly from distributions of LEPTO events (Fig. 11.8) This allowed to estimate the fraction of resolved photon events in the high p_T sample. A sum of LEPTO and resolved photon distributions was fitted to the experimental data with one free parameter f, the fraction of

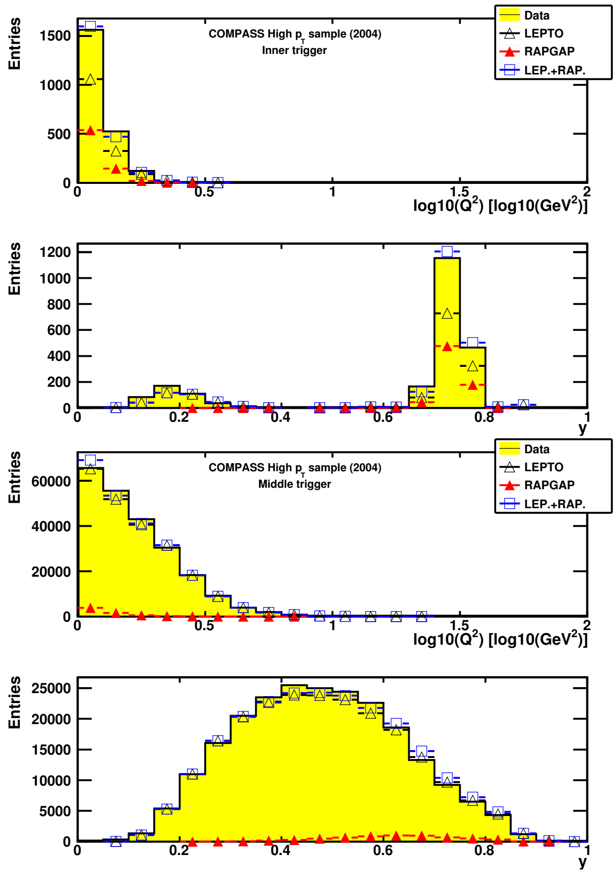

Figure 11.9: Q^2 and y distributions for LEPTO LO and RAPGAP resolved photon simulations compared to the experimental data. The RAPGAP simulations are performed with the photon PDFs of Ref. [98] and with the scale $\mu^2 = m^2 + p_T^2$. The MC distributions are normalised to the fraction obtained from a 2D fit to the data (see text for details). The results are presented for two samples: a) Inner Trigger and b) Middle Trigger. The green circles represent the sum of LEPTO and RAPGAP distributions.

LO events:

$$S = f \cdot \text{LEPTO} + (1 - f) \cdot \textit{Resolved photon} \; . \tag{11.3}$$

The fits were performed in a 2D space (Q^2, y) for nine different photon PDFs [2] and for three different μ^2 scale selections. The three considered scales were the following: $\mu^2 = 4 \cdot m^2 + p_T^2$, $\mu^2 = Q^2 + p_T^2$ and $\mu^2 = \hat{s}$.

In order to account for the spectrometer acceptance, the events generated by LEPTO were processed by a full MC simulation. As we lack interface between RAPGAP and COMGEANT the resolved-photon distributions were weighted with a 2D $\left(Q^2, y\right)$ acceptance obtained from the full LEPTO simulation. The fits were performed for each trigger independently.

Selected fits are presented in figure 11.9. The biggest resolved photon contribution is observed for the IT sample which is consistent with the results of the low Q^2 high p_T analysis [11], where this trigger was dominant. For $Q^2 > 1\,(\text{GeV}/c)^2$, the IT sample corresponds to 0.4% of the whole data and the obtained resolved-photon contribution is well below 1%.

[2] GRS (1), SASGAM (2): the numbers in brackets correspond to the values of the 'INGA' option of the RAPGAP generator [97]. DO-G (311), LAC-G (331), GS-G (341), GRV-G (351), ACFGP-G (361), WHIT-G (381), SaS-G (391): the numbers in brackets correspond to the ID number of a PDF in the LHAPDF library [90].

The values of the fragmentation parameters were tuned to obtain a better description of the experimental data. An artificial compensation for the simulated resolved photon contribution might be introduced by the new tuning. To test this another fit was performed using the distributions obtained from simulations with the default setting of fragmentation parameters. The obtained fraction is $\sim 5\%$; however, given the quality of the fits, it is not possible to judge if such MC simulation would describe data better than the one used for extraction of the final result.

In the low Q^2 analysis, in which the resolved photon events correspond to a half of the sample, the systematic effect due to the lack of knowledge about polarised photon PDFs leads to about 10% relative error on $\Delta G/G$. In our case, $Q^2 > 1(\mathrm{GeV}/c)^2$, the resolved photon contribution can be safely neglected, both with respect to the final result and to the systematic error.

11.10 Simplification of the $\Delta G/G$ Extraction Formula

In the $\Delta G/G$ extraction formula, for sake of simplicity, $\overline{x}'_C$ was assumed to be equal to $\overline{x}_C$. Let us remind that x'_C is the fraction of the nucleon momentum carried by the struck quark in the QCD Compton process for a sample of events with $\overline{x} = \overline{x}_C$. In its turn, x_C is the fraction of the nucleon momentum carried by the struck quark in the QCD Compton process for an inclusive sample.

The impact of this assumption in the equation (8.30) was estimated performing two tests. In the first one, x'_C was assumed to be proportional to x_C, $x'_C = 1.6 \cdot x_C$. In the second x'_C was approximated by using x_C instead of x_{Bj} as an input parameter for the neural network that estimates x_C, therefore extracting $x_C(x_C(x_{Bj}))$. Both tests result in a change of $\Delta G/G$ of 0.024 and 0.035, respectively. For the systematic uncertainty the estimate $\delta(\Delta G/G_{formula})$=0.035 was taken.

11.11 Summary of the Systematic Contributions

The systematic contributions are summarised in table 11.5. The resulting systematic error is 5% larger than the statistical one. In addition the systematic error was evaluated in each bin of x_G (such evaluation is discussed in chap. 12), the results being presented in the same table.

	LEPTO DEF. PS ON CTEQ5L	LEPTO DEF. PS OFF MSTW08	LEPTO DEF. PS ON MSTW08	COMPASS PS ON CTEQ5L	COMPASS PS OFF MSTW08	COMPASS PS ON MSTW08 NO F_L	COMPASS PS ON MSTW08
R_{LO}	0.60	0.56	0.63	0.61	0.60	0.67	0.65
R_{QCDC}	0.23	0.27	0.22	0.22	0.27	0.20	0.21
R_{PGF}	0.18	0.16	0.15	0.16	0.14	0.13	0.14
a_{LL}^{LO}	0.44	0.48	0.47	0.46	0.50	0.51	0.49
a_{LL}^{QCDC}	0.40	0.38	0.40	0.41	0.39	0.41	0.41
a_{LL}^{PGF}	-0.34	-0.30	-0.32	-0.34	-0.30	-0.31	-0.32

Table 11.2: Mean values of analysing power, a_{LL}, and process fractions for all MC samples.

Simulation	$\Delta G/G$	$\delta\Delta G/G$	$\Delta G/G - A^{\mathrm{corr}}/\lambda$
COMPASS_ON_MS	0.125	0.060	0.026
COMPASS_OFF_MS	0.127	0.058	0.019
COMPASS_ON_CQ	0.093	0.052	0.034
COMPASS_ON_MS_NOFL	0.135	0.072	0.041
LEPTO_DEFAULT_ON_MS	0.124	0.048	0.008
LEPTO_DEFAULT_OFF_MS	0.158	0.045	0.014
LEPTO_DEFAULT_ON_CQ	0.111	0.041	0.019

Table 11.3: Results for $\Delta G/G$ using various MCs. See text for details.

	R^{PGF}	R^{LP}	R^{QCDC}	$\langle a_{LL}^{PGF}\rangle$	$\langle a_{LL}^{LP}\rangle$	$\langle a_{LL}^{QCDC}\rangle$
Inclusive	0.07	0.83	0.10	-0.27	0.40	0.38
Inclusive + RC	0.07	0.83	0.10	-0.26	0.39	0.37
Semi-inclusive	0.06	0.85	0.09	-0.27	0.38	0.35
Semi-inclusive + RC	0.06	0.85	0.09	-0.27	0.38	0.35

Table 11.4: Effect of the radiative corrections in inclusive and semi-inclusive MC samples on the process fractions and the analysing powers.

	x_g range			
$\delta(\Delta G/G)$	$[0.04, 0.27]$	$[0.04, 0.12]$	$[0.06, 0.17]$	$[0.11, 0.27]$
MC simulation	0.045	0.077	0.067	0.129
Inclusive asymmetry A_1^d	0.015	0.021	0.014	0.017
NN parametrisation	0.010	0.010	0.010	0.010
f, P_b, P_t	0.004	0.007	0.007	0.010
False asymmetries	0.019	0.023	0.016	0.012
$x_C = x'_C$ in eq. (8.29)	0.035	0.026	0.039	0.057
Total systematic uncertainty	0.063	0.088	0.081	0.143

Table 11.5: Summary of the contributions to the systematic uncertainty of $\Delta G/G$.

CHAPTER 12

RESULTS AND DISCUSSION

One does not leave a convivial party before closing time.

Wiston Churchill.

The gluon polarisation $\Delta G/G$ measurement is presented and some considerations about the physical meaning of this measurement are pointed out.

The $\Delta G/G$ gluon polarisation measured using high p_T hadrons, with $Q^2 > 1\,(\mathrm{GeV}/c)^2$, with data samples from 2002 to 2006 years is

$$\Delta G/G = 0.125 \pm 0.060_{(stat.)} \pm 0.063_{(syst.)}$$

calculated at $x_G^{av} = 0.09$ within a x_G range of $[0.04, 0.27]$ and with a hard scale of $\langle \mu^2 \rangle = 3\,(\mathrm{GeV}/c)^2$.

The measurement of the gluon polarisation through high p_T hadron pairs was performed within the COMPASS muon physics program, using the data from 2002–2004 and 2006 years. The measurement of $\Delta G/G$ as a function of the data taking year and the combined result are shown in figure 12.1 and also summarised in table 12.1.

	number of events	Gluon polarisation $\Delta G/G$
2002	450134	0.087 ± 0.246
2003	1363629	0.158 ± 0.138
2004	2770994	0.082 ± 0.094
2006	2722175	0.164 ± 0.103
total	7306932	0.125 ± 0.060

Table 12.1: $\Delta G/G$ *per* year and integrated results.

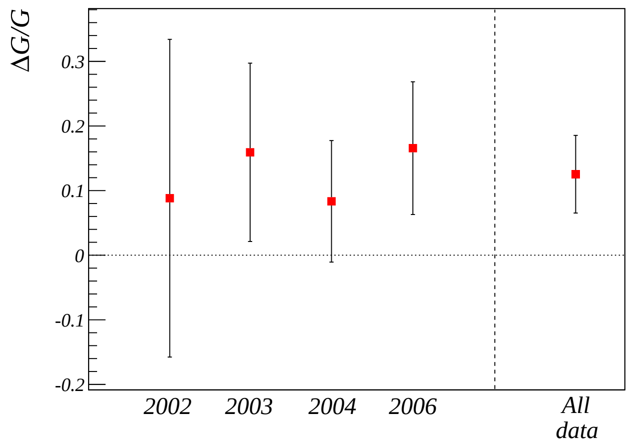

Figure 12.1: Gluon polarisation results per year and combined.

	x_G range			
	$[0.04, 0.27]$	$[0.04, 0.12]$	$[0.06, 0.17]$	$[0.11, 0.27]$
x_G^{av}	0.09	0.07	0.10	0.17
$\Delta G/G$	0.125 ± 0.060	0.147 ± 0.091	0.079 ± 0.096	0.185 ± 0.165

Table 12.2: Gluon polarisation results for the three x_G bins.

The measurement, as described in section 9.4, was performed using a data grouping in order to take into account the stability of the spectrometer. The gluon polarisation was extracted period-by-period as shown in figure 12.4 and compiled in table 12.3.

In order to investigate the x_G dependence on the $\Delta G/G$ measurement, the data is divided into three statistically independent bins of the parametrised x_G variable. These results are given in table 12.2 and also presented in figure 12.2. In the same figure, this new result is compared with other COMPASS results, namely the one obtained for the same measurement performed in the low Q^2 regime [99] and the result obtained from the open charm analysis [47, 100]. Also results from the HERMES [101] and the SMC [102] experiments are shown in figure 12.2. The curves are the NLO QCD global fit to the spin asymmetries of the inclusive and the semi-inclusive DIS world data from the LSS [76] and the DSSV [27, 77] groups.

In figure 12.3, the results shown in figure 12.2 are compared with the parametrisation from the GRVS [103] group assuming three scenarios for ΔG, which according to equation (1.1) is the gluon contribution to the nucleon spin: $\Delta G = 0.2$, the so called minimal scenario; $\Delta G = 0.6$, the so called best fit; and $\Delta G = 2.5$ the so called maximal scenario.

The first and direct conclusion drawn from our $\Delta G/G$ measurement is that it is compatible with a very low gluon polarisation within its x_G range; it is also compatible with all measurements and with the NLO fit curves, which combine data from inclusive and semi-inclusive DIS experiments and theoretical models, as shown in figure 12.2. It is worth noticing the limited range of x_G; therefore, further conclusions outside this range, namely for all x_G would result partially in measurements with absence of consistency.

From the comparison of the results with the three scenarios described in figure 12.3, the conclusion that can be extracted is that low values of the gluon contribution to the nucleon spin, *i.e.* $\Delta G = 0.2$ and $\Delta G = 0.6$ seem to be favoured. Concerning the $\Delta G = 2.5$ curve, the value from the curve at $x_G \approx 0.1$ is more that 4σ apart from the presented measurement in

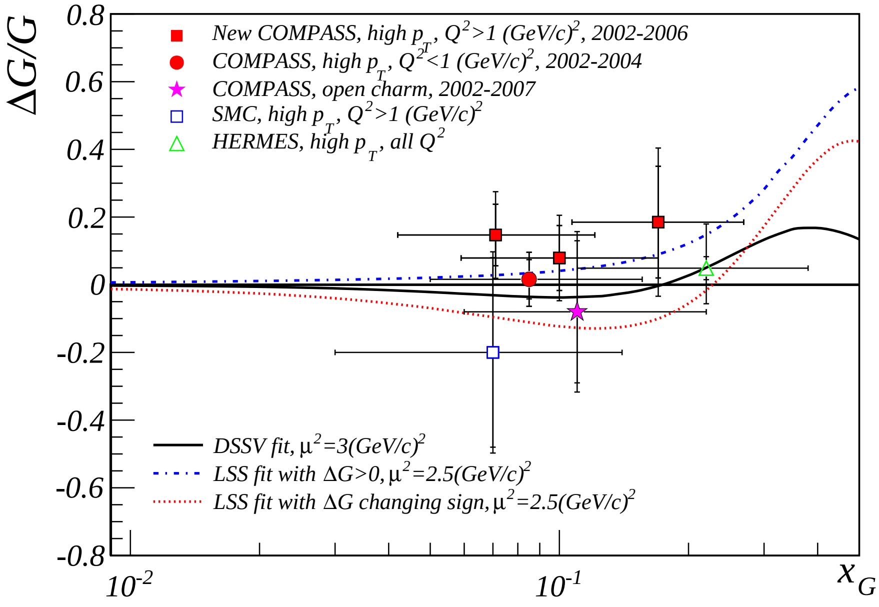

Figure 12.2: $\Delta G/G$ Results from COMPASS [99], SMC [102] and HERMES [101] experiments. Also shown are the QCD fits curves from the LSS [76] and the DSSV [27,77] groups.

the x_G range, meaning that this scenario is very unlikely.

In order to better constrain ΔG, it would be necessary to obtain more measurements in a broader x_G region. This would benefit in two ways: from the experimental point of view, there would be the possibility to cross check with other experiments; from the theoretical/phenomenological side more data would be available leading to a decrease in the uncertainty of the used models. Yet fixed target experiments can access limited x_G ranges and due to its kinematic phase space most of the x_G ranges overlap with each other. Another possibility would be to use experiments in collider machines; in this case the only possibility is to use an electron-proton collider. This would improve significantly the precision of the parton distribution parametrisation at low x. Nevertheless, the programs to start the upgrades for the existing collider machines to cope with this requirement are beyond 2015.

The answer to the question: "what is the contribution from gluons to the nucleon spin?" has no definite answer, so far, unfortunately. From the heuristic expression that relates the nucleon spin with its contributions, namely equation (1.1) one sees that there is room to account a significant contribution from the angular orbital momentum of the parton. Some future physics programs will address this question, namely the study of the Deeply Virtual Compton Scattering (DVCS) process, used to access the so called Generalised Parton Distribution (GPD) functions, used also to measure the orbital momentum of the quarks. Nevertheless, the state of the art concerning the theoretical framework in not yet well established.

		number of events	Gluon polarisation $\Delta G/G$
2002	02P1C	52374	0.927 ± 0.570
	02P2A	82127	0.122 ± 0.504
	02P2D	79528	-0.228 ± 0.495
	02P2E	110714	-0.211 ± 0.421
	02P2F	47087	0.262 ± 0.663
	02P2G	27307	0.746 ± 0.867
	02P3G	50997	-0.497 ± 0.666
2003	03P1A	131079	0.240 ± 0.391
	03P1B	113140	0.677 ± 0.400
	03P1C	128540	-0.248 ± 0.374
	03P1D	128359	0.762 ± 0.384
	03P1E	231559	-0.047 ± 0.280
	03P1F	182412	0.063 ± 0.327
	03P1I	172715	-0.062 ± 0.327
	03P1J	275825	0.083 ± 0.271
2004	04W22	314880	0.228 ± 0.238
	04W23	169089	0.051 ± 0.311
	04W26	198016	0.516 ± 0.295
	04W27	119010	0.150 ± 0.388
	04W28	144574	0.137 ± 0.355
	04W29	148514	-0.157 ± 0.352
	04W30	210282	0.150 ± 0.287
	04W31	216447	-0.353 ± 0.295
	04W32	266225	0.086 ± 0.272
	04W37	307254	-0.137 ± 0.243
	04W38	363844	-0.042 ± 0.214
	04W39	195006	0.470 ± 0.313
	04W40	117853	-0.161 ± 0.407
2006	06W32	12794	0.315 ± 1.297
	06W33	104641	0.100 ± 0.402
	06W34	155940	0.206 ± 0.352
	06W35	60262	-0.359 ± 0.569
	06W36	275872	0.334 ± 0.285
	06W37	256992	-0.118 ± 0.264
	06W40	466235	0.334 ± 0.202
	06W41	147493	0.578 ± 0.370
	06W42	316270	-0.451 ± 0.277
	06W43	374524	0.309 ± 0.233
	06W44	80478	0.097 ± 0.568
	06W45	271029	0.335 ± 0.335
	06W46	199645	-0.112 ± 0.327

Table 12.3: $\Delta G/G$ results *per* period.

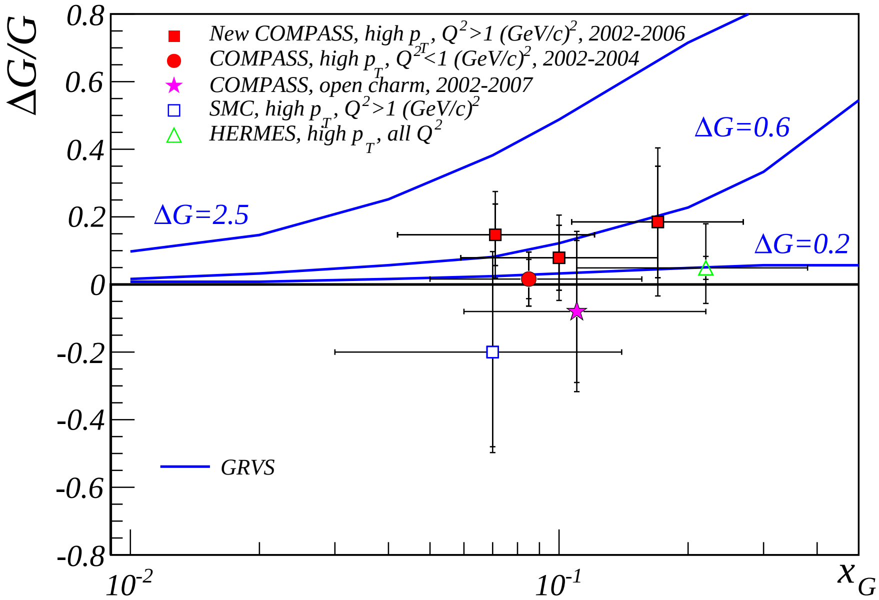

Figure 12.3: $\Delta G/G$ Results from COMPASS [99], SMC [102] and HERMES [101]. Also shown are the QCD fits curves from the GRVS [103] group assuming three different values for ΔG.

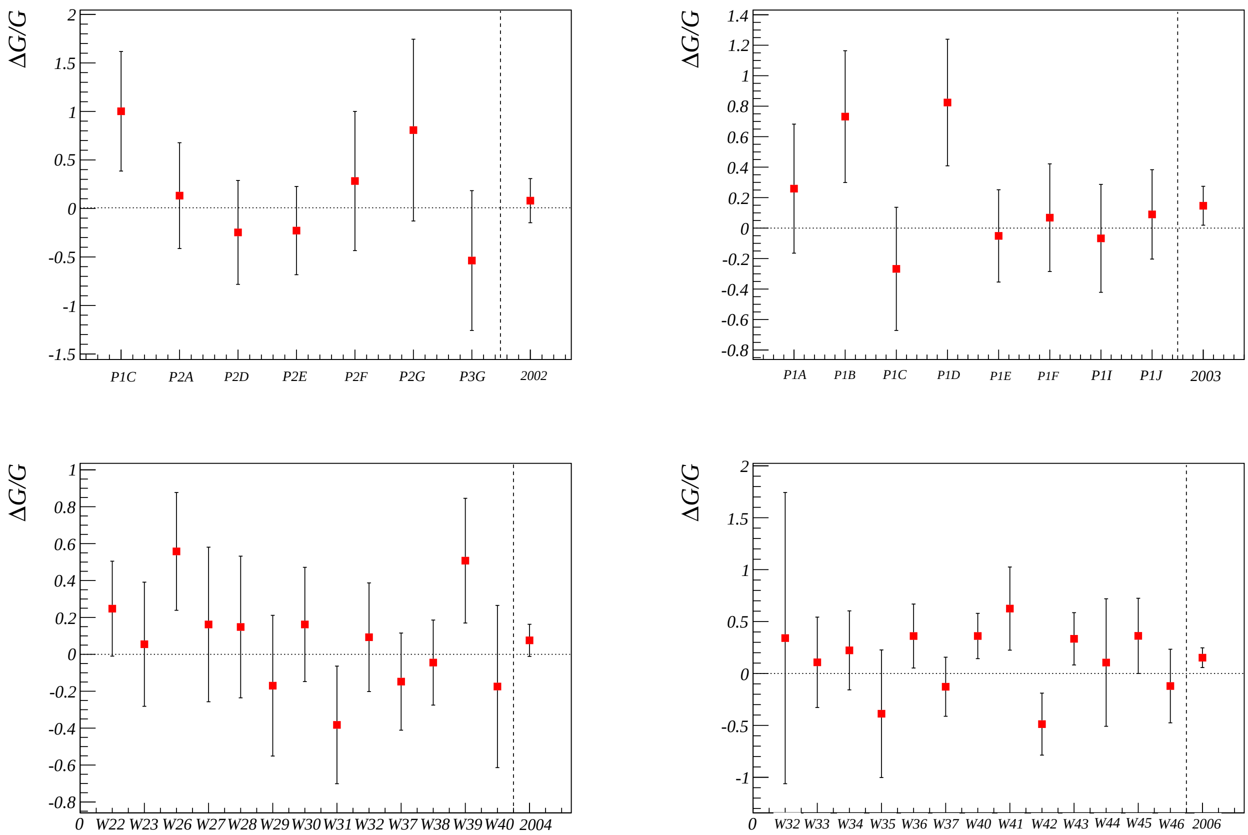

Figure 12.4: The gluon polarisation results are presented *per* period and distributed in four plots related to the data taking year: 2002 (top left), 2003 (top right), 2004 (bottom left) and 2006 (bottom right).**NB. the y-axis of the plot are not at the same scale.**

BIBLIOGRAPHY

[1] J. R. Ellis and R. L. Jaffe, Phys. Rev. D **9** (1974) 1444 [Erratum-ibid. D **10** (1974) 1669].

[2] J. Ashman *et al.*, EMC Collaboration, Phys. Lett. B **206** (1988) 364.
J. Ashman *et al.*, EMC Collaboration, Nucl. Phys. B **328** (1989) 1.

[3] K. Abe *et al.*, E154 Collaboration, Phys. Rev. Lett. **79** (1997) 26 [arXiv:hep-ex/9705012].

[4] K. Abe *et al.*, E143 Collaboration, Phys. Rev. D **58**, (1998) 112003 [arXiv:hep-ph/9802357].

[5] P. L. Anthony *et al.*, E142 Collaboration, Phys. Rev. D **54**, (1996) 6620 [arXiv:hep-ex/9610007].

[6] P. L. Anthony *et al.*, E155 Collaboration, Phys. Lett. B **458** (1999) 529 [arXiv:hep-ex/9901006].

[7] D. Adams *et al.*, SMC Collaboration, Phys. Rev. D **56** (1997) 5330-5358. [arXiv:hep-ex/9702005].

[8] A. Airapetian *et al.*, HERMES Collaboration, Phys. Lett. B **442** (1998) 484 [arXiv:hep-ex/9807015].

[9] V. Y. Alexakhin *et al.*, COMPASS Collaboration, Phys. Lett. B **647** (2007) 8.

[10] R. L. Jaffe, A. Manohar, Nucl. Phys. B **337** (1990) 509-546.

[11] S. Procureur, *Détermination de la polarisation des gluons dans le nucléon par la production de hadrons a grande impulsion transverse a COMPASS*, PhD Thesis, Universite Paris XI, U.F.R. Scientifique d'Orsay, Paris, March 2006.

[12] M. Anselmino, A. Efremov, E. Leader, Phys. Rept. **261** (1995) 1-124. [hep-ph/9501369].

[13] L. N. Hand, Phys. Rev. **129** (1963) 1834-1846.

[14] R. P. Feynman, Phys. Rev. Lett. **23** (1969) 1415-1417.

[15] J. D. Bjorken, E. A. Paschos, Phys. Rev. **185** (1969) 1975-1982.

[16] J. D. Bjorken, Phys. Rev. **179** (1969) 1547-1553.

[17] C. G. Callan, Jr., D. J. Gross, Phys. Rev. Lett. **22** (1969) 156-159.

[18] E. Leader, D. B. Stamenov, Phys. Rev. D **67** (2003) 037503. [hep-ph/0211083].

[19] C. Amsler *et al.*, PDG Collaboration, Phys. Lett. B **667** (2008) 1-1340.

[20] J. Kodaira, S. Matsuda, T. Muta, K. Sasaki, T. Uematsu, Phys. Rev. D **20** (1979) 627.

[21] J. Kodaira, S. Matsuda, K. Sasaki, T. Uematsu, Nucl. Phys. B **159** (1979) 99.

[22] J. Kodaira, Nucl. Phys. B **165** (1980) 129.

[23] J. Ashman *et al.*, EMC Collaboration, Phys. Lett. B **206** (1988) 364.

[24] J. Ashman *et al.*; EMC Collaboration, Nucl. Phys. B **328** (1989) 1.

[25] J. R. Ellis, R. L. Jaffe, Phys. Rev. D **9** (1974) 1444.

[26] S. Bass. *The Spin structure of the proton.* World Scientific, (2007).

[27] D. de Florian, R. Sassot, M. Stratmann, W. Vogelsang, Phys. Rev. D **80** (2009) 034030. [arXiv:0904.3821 [hep-ph]].

[28] A. Airapetian *et al.*, HERMES Collaboration, Phys. Rev. D **71** (2005) 012003. [hep-ex/0407032].

[29] T. Averett. AIP Conf. Proc. **675** (2003) 88.

[30] M. Hirai *et al.*, AAC Collaboration, Phys. Rev. D **69** (2004) 054021. [hep-ph/0312112].

[31] E. Leader, A. V. Sidorov, D. B. Stamenov, Phys. Rev. D **73** (2006) 034023. [hep-ph/0512114].

[32] D. de Florian, R. Sassot, M. Stratmann, Phys. Rev. D **75** (2007) 114010. [hep-ph/0703242].

[33] M. Alekseev *et al.*, COMPASS Collaboration, Phys. Lett. B **680** (2009) 217-224. [arXiv:0905.2828 [hep-ex]].

[34] Y. L. Dokshitzer, Sov. Phys. JETP **46** (1977) 641-653.

[35] V. N. Gribov, L. N. Lipatov, Sov. J. Nucl. Phys. **15** (1972) 438-450.

[36] G. Altarelli, G. Parisi, Nucl. Phys. B **126** (1977) 298.

[37] G. Altarelli, Phys. Rept. **81** (1982) 1.

[38] R. Mertig, W. L. van Neerven, Z. Phys. C **70** (1996) 637-654. [hep-ph/9506451].

[39] W. Vogelsang, Phys. Rev. D **54** (1996) 2023-2029. [hep-ph/9512218].

[40] W. Vogelsang, Nucl. Phys. B **475** (1996) 47-72. [hep-ph/9603366].

[41] W. A. Bardeen, A. J. Buras, D. W. Duke, T. Muta, Phys. Rev. D **18** (1978) 3998.

[42] R. D. Ball, S. Forte, G. Ridolfi, Phys. Lett. B **378** (1996) 255-266. [hep-ph/9510449].

[43] S. L. Adler, Phys. Rev. **177** (1969) 2426.

[44] G. Altarelli and G. G. Ross, Phys. Lett. B **212** (1988) 391.

[45] R. D. Carlitz, J. C. Collins and A. H. Mueller, Phys. Lett. B **214** (1988) 229.

[46] S. L. Adler, W. A. Bardeen, Phys. Rev. **182** (1969) 1517-1536.

[47] C. Franco, *Measurement of the Gluon Polarisation from Open-Charm Production in COMPASS*, Unversidade Técnica de Lisboa, Instituto Superior Técnico, Lisbon, December 2011.

[48] E. S. Ageev *et al.*, COMPASS Collaboration, Phys. Lett. B **633** (2006) 25 [arXiv:hep-ex/0511028].

[49] G. Bunce, N. Saito, J. Soffer, W. Vogelsang, Ann. Rev. Nucl. Part. Sci. **50** (2000) 525-575. [hep-ph/0007218].

[50] P. Abbon *et al.*, Nucl. Instrum. Meth. A **577** (2007) 455.

[51] C. E. Hill, "Talk at the CAS - CERN Accelerator School : Cyclotrons, Linacs and Their Applications, La Hulpe, Belgium, 28 Apr - 5 May 1994", CERN-PS-94-36;

[52] N. Doble, L. Gatignon, G. von Holtey, F. Novoskoltsev, Nucl. Instrum. Meth. A **343** (1994) 351-362.

[53] A. Abragam, *The Principles of nuclear magnetism* (The Clarendon Press , Oxford, 1961).

[54] A. Meier, ^{6}*LiD fur da Polarisierte Target des* COMPASS-*experiments*, PhD Thesis, Ruhr-Universitat Bochum, Germany, 2001.

[55] J. Kyynaeraeinen, Nucl. Instrum. Meth. A **356** (1995) 47.
D. Adams *et al.* [Spin Muon Collaboration], Nucl. Instrum. Meth. A **437** (1999) 23.

[56] G. Mallot.*The Spin Structure of the Nucleon from the SMC Experiments*. Habilitation Thesis, Fachbereich Physik de Johannes Guttenberg-Universität Mainz, (1993).

[57] C. Bernet, A. Bravar, J. Hannappel, D. von Harrach, R. Hermann, E. Kabuss, F. Klein, A. Korzenev *et al.*, Nucl. Instrum. Meth. A **550** (2005) 217-240.

[58] E. Albrecht, G. Baum, R. Birsa, F. Bradamante, A. Bressan, A. Chapiro, A. Cicuttin, P. Ciliberti *et al.*, Nucl. Instrum. Meth. A **553** (2005) 215-219. And therein references.

[59] J. Pyrlik, et al., Nucl. Instrum. Meth. A **446** (2000) 299.

[60] LHCb Collaboration, LHCb technical design report, CERN/LHCC/2000-37 (2000).

[61] E. Albrecht, et al., Nucl. Instrum. Meth. A **488** (2002) 110.

[62] S. Dalla Torre, G. Menon and F. Tessarotto, *Geometrical description of RICH-1 central region in RICH*, COMPASS RICH internal note, 2005.

[63] G. Baum, et al., Nucl. Instrum. Meth. A **502** (2003) 315.

[64] T. Ypsilantis, et al., Nucl. Instrum. Meth. A **343** (1994) 30.

[65] P. Abbon, *et al.*, Nucl. Instrum. Meth. A **587** (2008) 371-387.

[66] R. Brun and F. Rademakers, Nucl. Instrum. Meth. A **389** (1997) 81-86. See also http://root.cern.ch/.

[67] `http://www.rubyonrails.org/`

[68] A. Bravar, D. von Harrach, A. Kotzinian, Phys. Lett. B **421** (1998) 349-359. [hep-ph/9710266].

[69] K. Kowalik, *Selection of the photon gluon fusion process by requiring high-p_T hadrons in muon nucleon scattering*, PhD Thesis, Soltan Institute for Nuclear Studies, Warsaw, 2004.

[70] S. Hedicke, *Determination of the gluon polarisation in the nucleon using hadron pairs with high transverse momentum at COMPASS*, PhD Thesis, Albert-Ludwigs-Universität Freiburg, November 2005.

[71] O. A. Rondon-Aramayo, Phys. Rev. C **60** (1999) 035201.

[72] A. A. Akhundov, D. Y. Bardin, L. Kalinovskaya and T. Riemann, Fortsch. Phys. **44** (1996) 373 [arXiv:hep-ph/9407266].

[73] B. Adeva *et al.*, SMC Collaboration, Nucl. Instrum. Meth. A **343** (1994) 363.

[74] D. Adams *et al.*, SMC Collaboration, Nucl. Instrum. Meth. A **443** (2000) 1.

[75] J.-M. Le Goff, *Asymmetry extraction*, COMPASS internal note, 2004.

[76] E. Leader, A. V. Sidorov, D. B. Stamenov, Phys. Rev. D **82** (2010) 114018. [arXiv:1010.0574 [hep-ph]].

[77] D. de Florian, R. Sassot, M. Stratmann, W. Vogelsang, Phys. Rev. Lett. **101** (2008) 072001. [arXiv:0804.0422 [hep-ph]].

[78] M. Alekseev *et al.*, COMPASS Collaboartion, Eur. Phys. J. C **52** (2007) 255.

[79] *CORAL*, `http://coral.web.cern.ch/coral/`.

[80] *Data production status webpage*, `http://na58dst1.home.cern.ch/na58dst1/dstprod.html`.

[81] *PHAST*, `http://ges.home.cern.ch/ges/phast/index.html`.

[82] R. Brun *et al.*, CERN Program Library W5013, 1994.

[83] G. Ingelman, A. Edin and J. Rathsman, Comput. Phys. Commun. **101** (1997) 108 [arXiv:hep-ph/9605286].

[84] B. Andersson, G. Gustafson, G. Ingelman, T. Sjostrand, Phys. Rept. **97** (1983) 31-145.

[85] B. Andresson, *The Lund model* (Cambridge Univ. Press , Cambridge, 1989).

[86] T. Sjostrand, P. Eden, C. Friberg, L. Lonnblad, G. Miu, S. Mrenna and E. Norrbin, Comput. Phys. Commun. **135** (2001) 238 [arXiv:hep-ph/0010017].

[87] A. Hillenbrand, in proc. of 11th International Workshop of Deep inelastic Scattering (DIS 2003), 2003.

[88] K. Klimaszewski, *Determination of the gluon polarisation in the gluon from events with high-p_T hadrons pairs in COMPASS experiment*, PhD Thesis, Soltan Institute for Nuclear Studies, Warsaw, June 2010.

[89] A.D. Martin, W.J. Stirling, R.S. Thorne, G. Watt, Eur. Phys. J. C **63** (2009) 189-285.

[90] *LHAPDF*, `http://projects.hepforge.org/lhapdf/`

[91] R. Sulej, K. Zaremba, K. Kurek and E. Rondio, Measur. Sci. Tech. **18** (2007) 2486.

[92] M. Stolarski, *Spin structure of the nucleon at low x and low Q^2 in the COMPASS experiment at CERN*, PhD Thesis, Faculty of physics, Warsaw University, Warsaw, 2006.

[93] P. Bordalo, *et al.*, *Determination of $\Delta G/G$ for $Q^2 > 1(GeV/c)^2$ from 2002-2006 high p_T data*, COMPASS note, (2010).

[94] A. Airapetian *et al.*, Phys. Lett. B **684** (2010) 114-118.

[95] M. Stolarski, *COMPASS Analysis Meeting*, November 2008.

[96] Y. Bedfer, *et al.*, *Determination of $\Delta G/G$ for $Q^2 > 1(GeV/c)^2$ from 2002-2004 high p_T data*, COMPASS note, 2008.

[97] J. Hannes, Comp. Phys. Commun. 86 (1995) 147–161.

[98] GRS, M. Gluck *et al.*, Phys. Rev. D54 (1996) 5515–5522

[99] C. Bernet, *et al.*, *Measurement of $\Delta G/G$ in the production of high p_T hadron pairs at low Q^2 (2004 data)*, COMPASS note, (2006).

[100] M. Alekseev, *et al.*, "Leading and Next-to-Leading Order Gluon Polarisation in the Nucleon and Longitudinal Double Spin Asymmetry from Open Charm Muoproduction" to be sumbitted to Phys. Rev. D.

[101] A. Airapetian *et al.*, HERMES Collaboration], Phys. Rev. Lett. **84** (2000) 2584.

[102] B. Adeva *et al.*, SMC Collaboration, Phys. Rev. D **70** (2004) 012002.

[103] M. Glück, E. Reya, M. Stratmann, and W. Vogelsang, Phys. Rev. D **63** (2001) 094005.